題目(和文)	
Title(English)	Estimation Method on Thermophysical Properties of Building Surfaces Based on Multi-spectral Remote Sensing and Surface Energy Balance Simulation
著者(和文)	Xi Xu
Author(English)	Xi Xu
出典(和文)	学位:博士（工学）, 学位授与機関:東京工業大学, 報告番号:甲第12002号, 授与年月日:2021年3月26日, 学位の種別:課程博士, 審査員:淺輪 貴史,中村 芳樹,山中 浩明,松岡 昌志,大風 翼,小林 秀樹
Citation(English)	Degree:Doctor (Engineering), Conferring organization: Tokyo Institute of Technology, Report number:甲第12002号, Conferred date:2021/3/26, Degree Type:Course doctor, Examiner:,,,,,
学位種別(和文)	博士論文
Type(English)	Doctoral Thesis

Doctoral Thesis

Estimation Method on Thermophysical Properties of Building Surfaces Based on Multi-spectral Remote Sensing and Surface Energy Balance Simulation

Xi Xu

Major in Urban Design and Built Environment,
Department of Architecture and Building Engineering,
School of Environment and Society,
Tokyo Institute of Technology

2021

Content

CHAPTER 1: INTRODUCTION

1. Background

Due to the increase of population and people's needs for a comfortable and convenient life, urban development leads to the replacement of natural surfaces by buildings and paved roads. It essentially alters the urban surface energy balance, which results in increasing surface and air temperature (Fig.1). Compared to a rural area, it contributes to the overheating in urban surface and air, resulting in an increase in the surface temperature (T_s) and sensible heat flux (Q_H) in urban areas [1]. During the daytime, solar irradiance dominantly drives the urban surface energy balance [2]. Urban surfaces are exposed to radiance, part of which is stored in the urban surfaces and causes a higher T_s than that found in most rural areas in the meanwhile, part of which is conductively transferred into the ground and the internal surfaces of buildings, while the surplus is shed as Q_H into the cooler ambient air. The Q_H emitted by roofs may create micro-thermals that disturb the stability of the lowest overlying atmosphere. The Q_H emitted from wall external surfaces is not usually as large as that from the roof. However, the Q_H released by a fully irradiated wall for only a few hours may influence the air flow and dispersion in the surrounding environment [1]. At night, the building surfaces cool fairly rapidly, expending much of the heat stored during the daytime. The transport of the nocturnal Q_H, with a much lower magnitude than that of the daytime, is often released into the atmosphere from many urban surfaces, which is a unique urban feature compared to rural surfaces. The diurnal uniqueness of the urban surface energy balance contributes to the urban heat island (UHI) in both the surfaces and the air, influencing the habitats' comfort, raising the mortality rate owing to intense pollution and heat, and increasing building energy demand [3]. Consequently, lowering the surface temperature and the sensible heat flux released can effectively mitigate the UHI effects and reduce such problems [4].

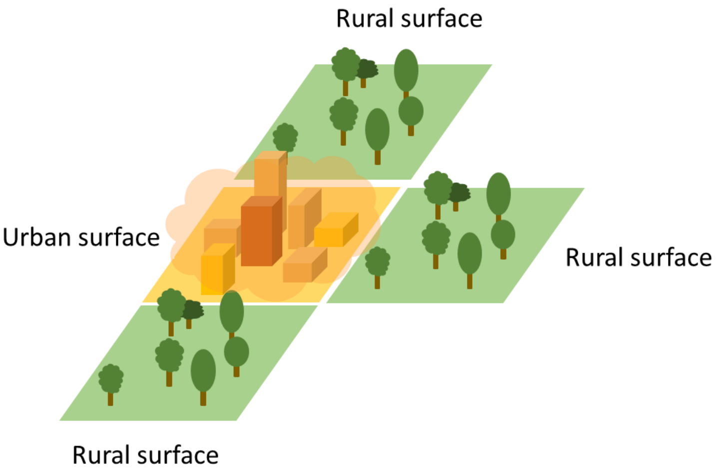

Figure 1. Overheating in urban area caused by the altered surface materials.

Therefore, for the sustainable urban developments, it is important for urban area to gain knowledge on the interaction of the urban surfaces and the atmosphere, in order to identify areas with severe outdoor thermal conditions and to examine the potential technologies and scenarios to mitigate UHI. The surface energy balance (SEB) model, such as ENVI-met [5], SOLENE [6–8] and THERMORender [9–11] (Fig.2), is able to handle the complexity of simulating the heat exchanges between buildings and the atmosphere in the surface layer[3]. These models can identify areas with severe outdoor thermal conditions [12,13], examine potential scenarios and technologies for the UHI mitigation [14–16], and can be coupled with building energy models for a more accurate prediction of energy demands [17–19]. The selection of urban thermophysical properties, including both optical and thermal properties, is important to the simulation quality [20]. They are often used to simulate synthetic landscapes assuming standardized building forms, construction materials, and vegetation types[21,22]. Although studying the effect of certain characteristics on the microclimate using assumed world urban landscape and surface information can be useful, the simulation of real world urban landscapes with actual surface information is very desirable for urban planning purposes in practice[23]. Hence, to collect the input building surface data in the real world is thus important for a practical project.

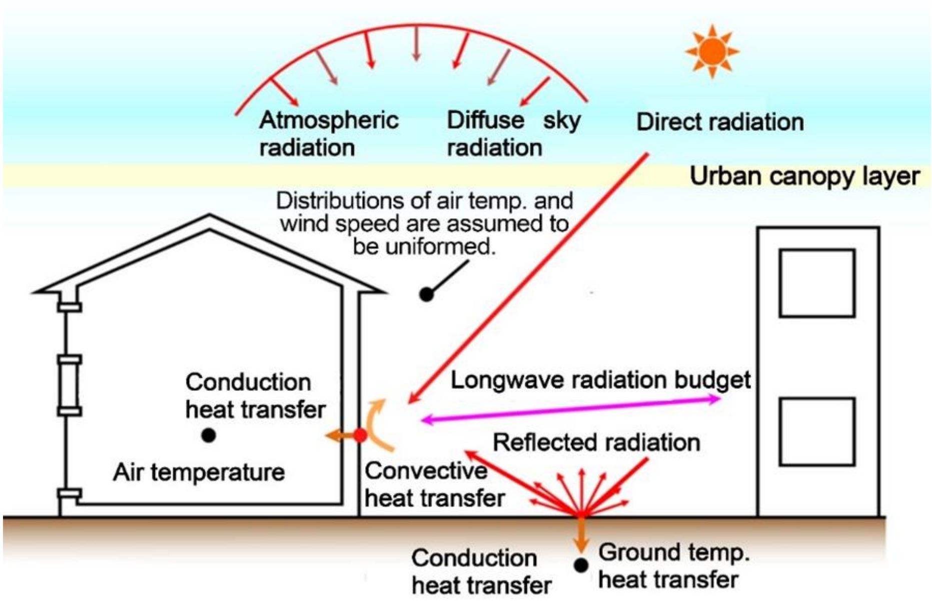

Figure 2. Surface heat balances in the THERMORender model

The easier way is to collect the documented information of building surface from the government or the developers. However, there exists a problem with the data quality and availability of urban surfaces, especially in developing countries [24]. The urban surface-atmosphere heat and radiative exchanges can be studied at various climate scales corresponded to urban morphological units, including meso-, local and micro scales[1]. Obtaining the urban surface data should be corresponded to the study scale. Satellite/airborne remote sensing (RS) and in-situ measurements are widely applied to derive or estimate the urban/ building surface information for the meso- and micro scales, respectively. However, regarding the local scale such as the block or neighborhood scales, there exists the gap to obtain the urban surface data between in-situ and spaceborne/airborne observations. Because the former is generally time-consuming, labor-intensive, provides limited points of each surface, and cannot easily access certain surfaces (e.g., roofs), whereas regarding the latter: spatial resolution of the satellite RS is not sufficient (e.g. even with Sentinel 2, which has a 10 m spatial resolution[25,26], small structures show mixed pixels[27]); and airborne RS requires high labor and financial cost[28], and there is a lack of vertical surface data[29].

2. State-of-the-art

2.1 Thermophysical properties

Albedo quantifies the capacity of an urban surface to reflect solar radiation, which is a driving factor of the surface energy balance (SEB) [1,30]. Large natural surfaces in urban areas have been replaced by construction materials, such as asphalt for roads and concrete for buildings, increasing air and surface temperatures and resulting in the urban heat island (UHI) phenomenon[31]. Albedos are involved in radiative heat exchanges and tie the urban climate to the surface cover[32,33]. Thus, modifying urban surfaces with high-albedo materials or coatings and their effects on surface cooling, UHI mitigation, and in-/outdoor thermal comfort has been widely studied in recent years, revealing their benefits [5,6].

The thermal behavior of urban surfaces results from not only the radiation budget on the exterior surfaces but also heat conduction through the surfaces and convective heat transfers at both the exterior and interior surfaces of buildings. The thermal properties of the urban surface (e.g., heat capacity and thermal conductivity), influencing all the above-mentioned heat transfers, contribute to its heat exchanged with the inside of a building affecting the energy demand, and with the atmosphere forming the urban climate. The effects of modifying the other thermophysical properties of building surfaces (e.g., roofs and walls) were investigated primarily by focusing on indoor thermal comfort and energy consumption [35–38], whereas the effects with the regard to the atmosphere were investigated less, which study target focused on solely the ground pavement [39].

2.2 Existing satellite/airborne RS methods on estimating thermophysical properties

At a mesoscale (i.e., city and region), the satellite remote sensing (RS) provides a common source of surface data, especially the surface albedo which quantifies the capacity of an urban surface to reflect solar radiation as a driving factor of the surface energy balance (SEB) [1,30]. Satellite RS techniques have been widely applied for estimating land surface albedo at a mesoscale[40–42]. Among these studies, some have integrated them with SEB modelling. For example, a regional-scale SEB model, COSMO-CLM, uses several satellite RS-based data sets such as land cover (e.g. by GlobalLand2000) and leave area index (LAI) (e.g. by MODIS) [43]. However, at a local scale (e.g. block and neighborhood), few studies have derived the urban surface parameters by airborne (e.g., aircraft and airships) RS. For example, Liu et al. use hyperspectral airborne data in the reflective and thermal wavelengths to estimate high-resolution land surface temperature [44]. Moreover, some among these studies have derived the airborne RS-based land cover information and surface parameters and used them for SEB modelling. For instance, Xu et al.[45] used airborne hyperspectral imagery from the operative modular imagine spectrometer (OMIS), along with a survey map and meteorological data, to derive the land cover, surface temperature, albedo, vegetation fraction and emissivity to map spatial variations in turbulent sensible heat flux based on the simple SEB model with single facet as local-scale Urban Meteorological parameterization scheme (LUMPS) and atmospheric radiation measurement (ARM) program. Similarly, Heldens et al. [29] have derived the land cover, albedo, LAI/LAD and high quality object height data and integrated them into the ENVI-met model, revealing that three-dimensional SEB simulation with multi facet for local scale can be supported by remote sensing products, but with an assumption of the thermophysical properties of the urban vertical surfaces which differentiations were ignored.

2.3 Existing in-situ measurement-based methods

It is common to collect the thermophysical properties of the urban surface by in situ measurement at the microscale, since its maximum typical urban unit is a canyon (typical horizontal length scale is 30m*200m [1]). One of the important thermophysical property, albedo/reflectance, can be directly observed in situ by using pyranometers/ spectroradiometers[46–48] (Fig.3). In addition, the thermal characteristics of the building envelopes, such as thermal transmittance and resistance (R-value), can be accessed by in-situ methods. The thermal transmittance/resistance have shown to be the most critical parameter affecting the building heat loss and thus its energy performance[49–51]; hence it is necessary to assess it carefully for the purpose of effective energy saving[52]. Heat flow meter method (HFM)[53–55], simple hot box-heat flow meter method (SHB-HFM)[52,56], quantitative infrared thermography method (QIRT)[57–59] as the main in-situ methods to access the heat transmittance of the building wall surface have been widely studied for years. The rationale schematic and required equipment are shown in Table.1.

Figure 3 Albedo and reflectance observed directly in situ using pyranometers (left) and spectroradiometers (right), respectively.

Table 1 In-situ methods widely used to determine thermal transmittance (refers to [52,56])

	Rationale schematic	***Equipment required***	***Limitations for larger-scale adoption***
Heat flow meter method (HFM) ***ISO 9869***	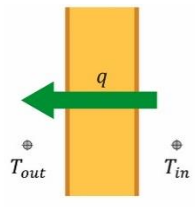	Thermometers Heat flux plates A data logger A weather station*(ASTM C1060) Infrared camera*(ISO 6781)	Need access to the building interior and indoor furniture limits probe locations; Building occupier behavior affects measurements; Metrological errors related to the heat flux plate; Limited use in warm areas or summer; Long test duration, more than 2 weeks in some cases.
Simple hot box-heat flow meter method (SHB-HFM)	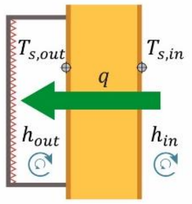	A simple hot box Heat flux plates Thermometers A data logger Infrared camera*	Need access to the building interior; Devices can only be used on the ground floor (auxiliary structure required for higher floors, increasing the cost); Use in winter has not been studied. Metrological errors related to the heat flux plate and surface thermometers;
Quantitative infrared thermography method (QIRT)	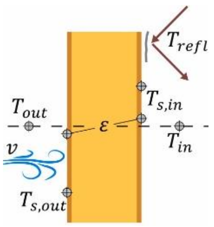	An infrared camera A hot-wire anemometer An infrared reflector A tape with known emissivity	Need access to the building interior; Metrological errors related to the infrared camera and the anemometer; Limited use in warm areas or summer.

***Optional**

The standard heat flow method (HFM), a direct contact measurement method being commonly applied, has been standardized as described in international standard ISO 9869[54] and ASTM[60,61]. Average (steady-state) method and dynamic methods are applied for data analysis procedures in ISO 9869[54]. **To carry out the measurements for a single homogeneous building envelope requires several equipment** mainly including (a) one heat flux sensor (two are needed for both internal and external surface when applying some dynamic analysis methods) to detective the conductive heat flux through the building envelope; (b) two high-precision thermocouples or thermistors with a maximum error of 0.2 degrees; (c) a data logger to store the measured data. Other equipment (e.g., a weather station[62] or an infrared camera[63]) can be used during the test to ensure that the environmental condition is appropriate and the building envelope is in an appropriate state of repair. Following the ISO 9869, **the standard HFM has often shown to rely on long measurement periods**[53,64,65] **of up to more than a month**[66]. Regarding the light walls, after at least 72 hours of monitoring, the measurement may stop if the termination criteria have been met[54,67] but should be performed at night and before the sunset to avoid the influence of direct solar radiation[54]. Whereas regarding the heavy walls, the minimum measurement periods should be extended as not less than 96 hours[54]. 6 days was found to be enough for satisfying the convergence criteria based on ISO 9869[54] for the hollow reinforced precast concrete walls[68]. In some cases, even 36 days of monitoring had not been sufficient to measure the U-value of the walls[66], especially the walls with heavy thermal mass demanding more time to stabilize the average heat flux and temperature gradient. It may cause more climatic fluctuations included in the results increasing the error probability[56]. In addition, the measurement period varies in terms of the consistency of the conditions during the measurement and temperature gradients along two sides of the walls. **The performance of HFM mainly depends on operation and meteorology**[52]**.** Many criteria for siting the equipment should be followed to avoid incorrect measurement, such as the placement of heat flux sensor should be at 1.5m height above the floor, more than 1.3m from the heating equipment like fan coils or radiators, and generally between windows and corners to get rid of the thermal bridge effects. It has been found that the heat flux sensor could change the thermal flux by up to 30%, which is the main contributor to cause errors in the thermal behavior of building envelope and thus the estimation of thermal transmittance and resistance. Strong and stable temperature gradients along two sides are required to give reliable results. The test conduction or the data selection was thus recommended to be when (a) the temperature difference between interior and exterior was more than 10 degrees; (b) not rain fell; (c) the wind speed was 0-1m/s; and (4) controlled use of the heating system. However, regarding the walls with low U-values, a temperature difference of more than 19 degrees was found to be required, which is difficult to be achieved in a warm climate. Moreover, as prescribed in ISO 9869, **considering the dynamic effect of thermal mass of unknown building components**

requires sampling and endoscopic inspection by drilling, which is commonly not allowed by the occupants of the buildings. In addition to be reliable, a desirable in-situ method should be non-destructive to be applied during the building inspections as well.

The non-contact in-situ measurement method mainly relates to the infrared thermography method (IRT). Fokaides et al.[69] applied infrared thermography to determine U-value in building envelopes in Cyprus based on steady-state models, which requires steady climate conditions such as indirect solar radiation, low wind speed, and complete evacuation of the building. Later, this method was studied by Aversa et al. to assess actual dynamic thermal behavior of building components. Considering the assumptions which may be far from actual circumstances, such as the emissivity of the surface, Albatici et al.[59] improved this method by measuring the wind velocity and surface emissivity, demonstrating this method can be reliable to determine thermal transmittance of normal heavy walls. **Performing a QIRT usually requires the following equipment and material** including (a) an infrared camera; (b) a hot-wire anemometer to measure the wind speed near the wall; (c) two temperature probes to measure the internal and external air temperature; (d) a tape with known emissivity provided by the manufacturer and (e) a contact thermometer used to determine the emissivity[52]. **This method requires very specific environmental condition, which should be similar to steady state**[57,59,69]. A stable heat transfer state is required to be achieved for 3-4 hours prior to the monitoring with a minimum temperature gradient along two sides of 10 degrees[57,59,69,70], while it is well known that for the heavy constructions with a high thermal mass, such short period is not sufficient[56]. The tests should ideally be carried out in winter since it is difficult to achieve a strong thermal gradient in summer[69]. Other climatological parameters, such as wind speed and wind combined with a clear sky and solar irradiance, also strongly affect the QIRT performance[71,72]. Hence, the tests are recommended to be performed 2 hours before sunrise and when (a) the temperature gradient along two sides is 7-16 degrees (or more than 10 degrees[57,59,69,70]); (b) the wind speed is less than 1m/s; (c) no rain falling; (d) it is cloudy or no exposure to direct radiation (to avoid thermal inertia effects).

3. Existing gap

The thermal behavior of urban surfaces results from not only the radiation budget on the exterior surfaces but also heat conduction through the surfaces and convective heat transfers at both the exterior and interior surfaces of buildings. Although albedo is a driving factor of the thermal behavior of the urban surface, the thermal properties of the urban surface (e.g., heat capacity and thermal conductivity), influencing all the above-mentioned heat transfers, contribute to its heat exchanged with the inside of a building affecting the energy demand, and with the atmosphere forming the urban climate. However, unlike the wide investigations about modifying urban surfaces with high-albedo materials or coatings and their effects on surface cooling, UHI mitigation, and in-/outdoor thermal comfort[5,6], thermal properties (e.g., thermal conductivity and heat capacity)' effects on the heat exchanged between the building surface and the atmosphere has not yet been studied enough and systematically. Moreover, in addition to modifying the albedo, the effects of modifying the other thermophysical properties of building surfaces (e.g., roofs and walls) were investigated primarily by focusing on indoor thermal comfort and energy consumption [35–38], whereas the effects with the regard to the atmosphere were investigated rarely. **Overall, as shown in Fig.4 there is a first research gap in systematically exploring the effects of thermophysical properties, especially the rare-investigated thermal properties, of building surfaces on the radiative and heat exchanges between the building surface and the atmosphere.**

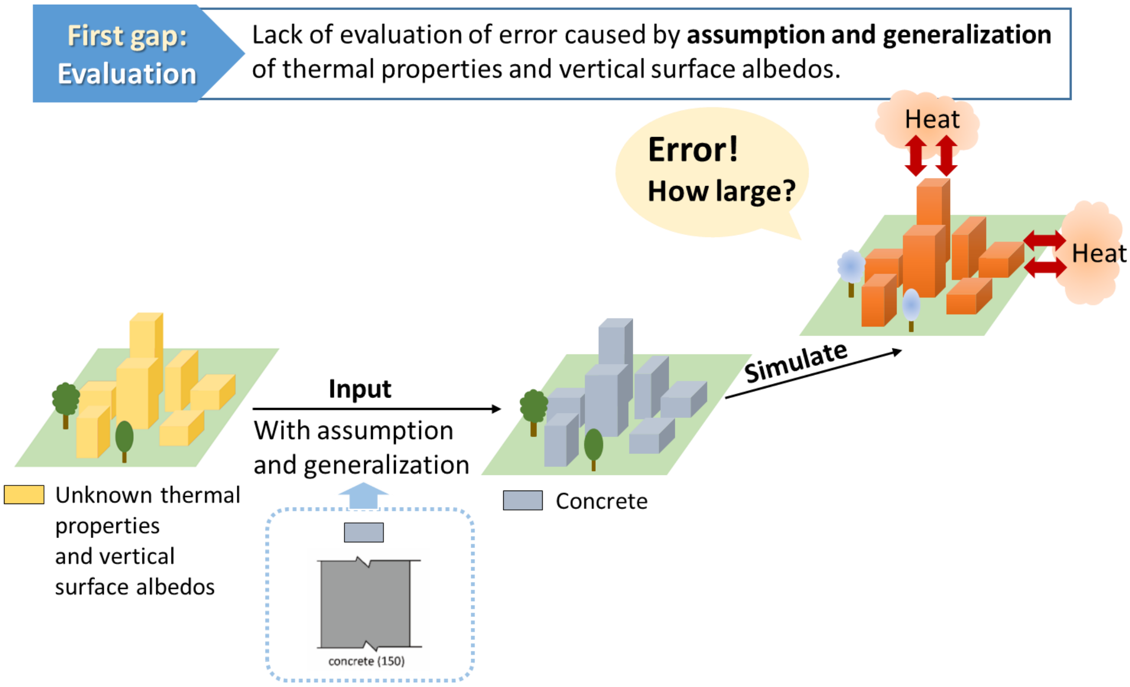

Figure 4. The first research gap

In addition to the albedo well-known as a driving factor on the building surface-atmosphere radiative exchanges, if the thermal properties are also important on surface thermal and radiative behavior, which cannot be ignored in SEB model-based simulations as well as albedo, a time- and labor-saving method to obtain the actual thermal properties of urban surfaces is necessary to guarantee the quality of SEB modeling.

Based on the literature reviews on the existing satellite/airborne RS and in-situ measurement methods for estimating thermophysical properties of urban surfaces as shown in section 2.2 and 2.3, there are clear limitations of these methods to be applied for a block and neighborhood scale (included in local scale). Regarding the satellite/airborne RS-based method, their clear limitations to be adopted for local scale are as follows:

(1) The estimation of very high-spatial resolution surface information and parameters from satellite/airborne observations is challenging. Regarding satellite RS, even with Sentinel 2, which has a 10 m spatial resolution[25,26], small structures show mixed pixels[27]. Regarding airborne observation, taking the land surface temperature as an example, its estimation with very high resolution is very challenging, so the very fine scale of 1 or 2m level is usually not considered. Moreover, the airborne RS requires high labor and financial cost[28].

(2) There is a lack of thermal properties of urban surfaces derived by RS products. Few studies have derived the surface materials and albedo by RS and integrated them with SEB modeling[29,43], but the thermal properties (e.g., the U value and heat capacity as the input required in Envi-met [29]) of urban surfaces were usually assumed and generalized with the ignorance of their differentiations [7,11,25,26].

(3) The surface information and parameters in these studies are derived from airborne sensors, causing that they are limited to be used for the single-facet SEB models (upper of Fig.5) like Xu et al.'s[45]. Otherwise, the uniformed material should be assumed for all vertical urban surfaces for SEB modeling in terms of multiple facets (lower of Fig.5), like Heldens et al[29]. It causes the neglection of differentiation of material composition of urban vertical surfaces. The raising area of urban vertical surfaces, resulted from the increasing high-rise buildings, have important influence in urban surface energy as well, especially within street canyons that complex heating process involves multiple reflection of the solar radiation and long-wave radiation. It may influence more if considering the contribution of cool selective paint[34] or green infrastructure[74] as the UHI mitigation/indoor energy saving strategies applied on the urban vertical surface.

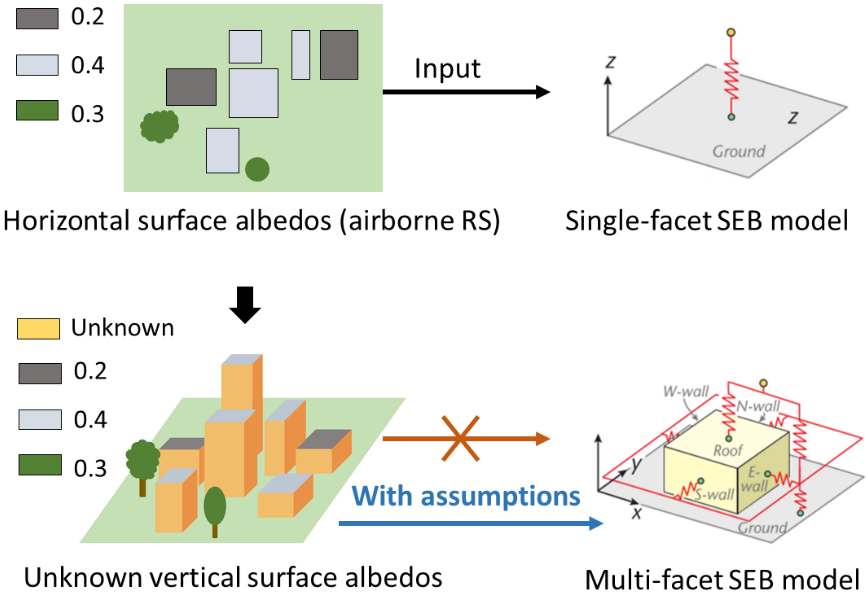

Figure 5. Airborne RS-based data limited to be used for single-facet SEB modeling or with the assumption of vertical surface data for multi-facet SEB modeling

Regarding the in-situ methods as introduced in Section 2.1, their relatively long measurement period under steady weather condition, multi equipment, and strict operation required for in situ monitoring campaigns are the main obstacles for a larger-scale adoption [75–78] (Table 1):

(1) Many pieces of equipment required in the current in-situ measurement methods for monitoring a single wall. For example, to carry out the HFM method for a single homogeneous building envelope requires the following equipment at least: (a) one or two heat flux sensor (two are needed for both internal and external surface when applying some dynamic analysis methods); (b) two high-precision thermocouples or thermistors; (c) a data logger to store the measured data. Some other equipment (e.g., a weather station[62] or an infrared camera[63]) were also recommended in some studies. Regarding the QIRT method, it usually requires: (a) an infrared camera; (b) a hot-wire anemometer to measure the wind speed near the wall; (c) two temperature probes to measure the internal and external air temperature; (d) a tape with known emissivity provided by the manufacturer and (e) a contact thermometer used to determine the emissivity. Considering the labor needed to take proper care of the equipment, intensive labor and cost would be needed for a scale larger than a building.

(2) The criteria to install the probes used in the current in-situ measurement method is strict, since it may lead to a large measurement error. For example, up to 26% by a random location of heat flux plates in the most widely used heat flow method (HFM) [55].

(3) The specific requirement of weather and environmental condition. For example, the monitoring of the QIRT

method requires very specific environmental condition, which should be similar to steady state. It is recommended to be performed 2 hours before sunrise and when (a) the temperature gradient along two sides is 7-16 degrees (or more than 10 degrees[57,59,69,70]); (b) the wind speed is less than 1m/s; (c) no rain falling; (d) it is cloudy or no exposure to direct radiation (to avoid thermal inertia effects). Such specific environmental conditions required by the current in-situ measurement methods are difficult to be satisfied.

(4) Long period is required for the mostly common-used HFM. Following the ISO 9869, the standard HFM has often shown to rely on long measurement periods[53,64,65] of up to more than a month[66]. Regarding the light walls, after at least 72 hours of monitoring, the measurement may stop if the termination criteria have been met[54,67] but should be performed at night and before the sunset to avoid the influence of direct solar radiation[54]. Whereas regarding the heavy walls, the minimum measurement periods should be extended as not less than 96 hours[54].

Overall, considering the clear limitations of these methods to be applied for a block and neighborhood scale, **there exists the second research gap of a time- and labor-saving method to obtain the thermophysical properties of the building surfaces between in-situ and spaceborne/airborne observations (Fig.6).**

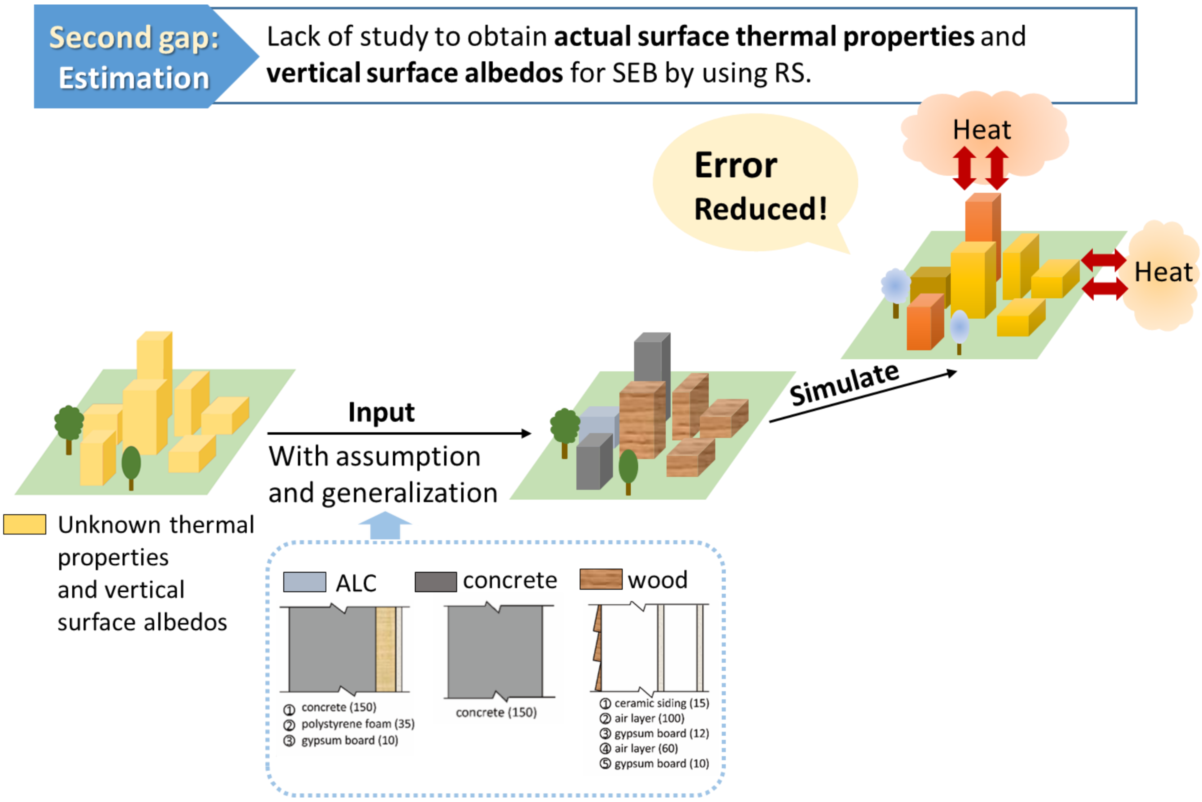

Figure 6. The second research gap

4. Research objective and main content

In order to bridge the gaps as proposed above, this thesis firstly investigated the effects of thermophysical properties of building surfaces on the surface temperatures and sensible heat flux in order to evaluate their influence on urban surface-atmosphere heat exchanges. Based on the findings that assuming and generalizing the thermal properties cause nonnegligible errors in SEB modeling, **the main objective of this thesis is to propose a new estimation method on thermophysical properties (i.e., albedo, thermal conductivity, and heat capacity) of building surfaces which can be applicable and efficient at a block or neighborhood scale (Fig.7).** The flow chart of chapter contents in this thesis is shown in Fig.8.

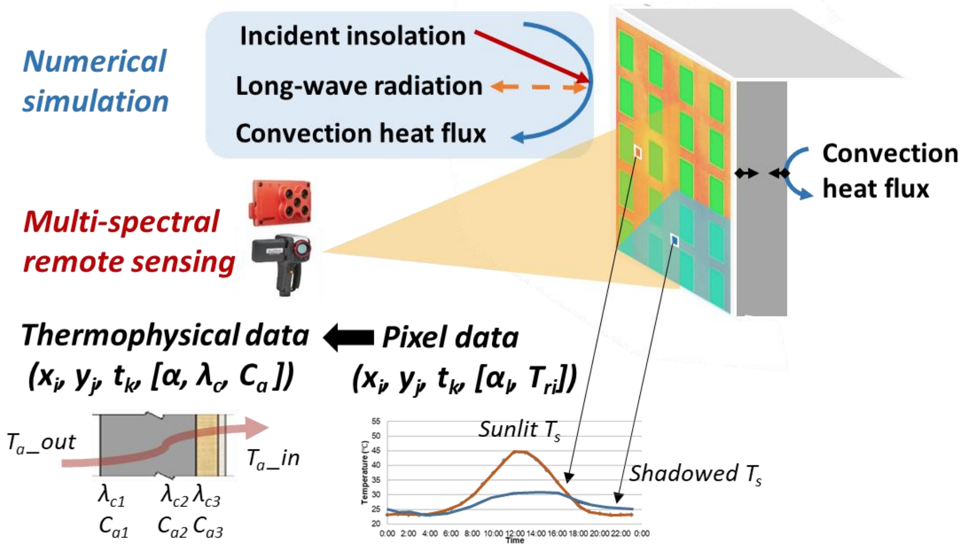

Figure 7. Estimation method on thermophysical properties of building surfaces proposed in this thesis

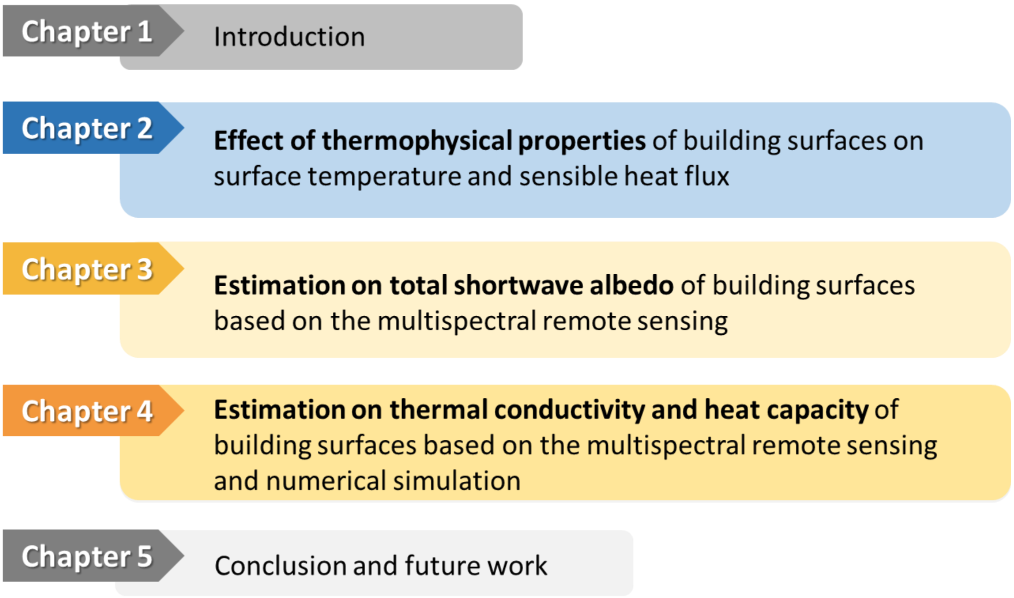

Figure 8. Flow chart of chapter contents in this thesis

Chapter 2: Taking a block in university campus in Yokohama city, Japan as a study area, Chapter 2 estimated the effect of thermophysical properties of building wall and roof surface in terms of the surface temperature and sensible heat flux, demonstrating that a non-negligible temperature difference behaved by building surface with different thermophysical properties. Meanwhile, the SEB model sensitivities of the building surface temperature in terms of the thermophysical properties were also studied.

Chapter 3: Based on the established datasets of various at-surface solar irradiances and spectral albedos, Chapter 3 developed the technique process and three narrow-to-broadband (NTB) conversion models were developed to estimate the total shortwave albedo of the building surface based on the multispectral RS (ground-based in this research), and evaluated their performance as well as the camera capacity to estimate broadband albedo. In addition, the sensitivities of models to the solar conditions and the surface material class were analyzed. These models were also validated using independent sample surfaces covered by different construction materials.

Chapter 4: Chapter 4 proposed an estimation method on the thermal properties (i.e., thermal conductivity and heat capacity) of the building surface based on multispectral RS and SEB model-based simulation. Taking a concrete building in a block in a university campus (Yokohama city, Japan) as a target building, the multispectral images and hourly infrared thermal images from sunrise to sunset of the target building were taken, and meanwhile the indoor air temperature and weather data were measured in site. Typical combinations of thermal properties of building surface were characterized by clustering based on a database established here. These typical cases were input as possible thermal properties of the target building in SEB simulation with other boundary conditions of the measured indoor air temperature and weather data, and the estimated albedo of the target building (Chapter 2). Among these them, the case which simulated radiant surface temperatures of target building revealing the most consistent with the measured temperatures (retrieved from hourly infrared images) was regarded as the one closest to actual condition, and its thermal properties were regarded as the estimated results.

CHAPTER 2: EFFECT ON THERMOPHYSICAL PROPERTIES OF BUILDING SURFACES ON TEMPERATURE AND SENSIBLE HEAT FLUX

1. Introduction

A comfortable climate is important for both the personal well-being and to attract citizens to urban open spaces [79]. Owing to urbanization, natural surfaces replaced by paved roads and buildings alter the surface energy balance, resulting in an increase in the surface temperature (T_s) and sensible heat flux (Q_H) in urban areas [1]. During the daytime, solar irradiance dominantly drives the urban surface energy balance [2]. Urban surfaces are exposed to radiance, part of which is stored in the urban surfaces and causes a higher T_s than that found in most rural areas in the meanwhile, part of which is conductively transferred into the ground and the internal surfaces of buildings, while the surplus is shed as Q_H into the cooler ambient air. The Q_H emitted by roofs may create micro-thermals that disturb the stability of the lowest overlying atmosphere. The Q_H emitted from wall external surfaces is not usually as large as that from the roof. However, the Q_H released by a fully irradiated wall for only a few hours may influence the air flow and dispersion in the surrounding environment [1]. At night, the building surfaces cool fairly rapidly, expending much of the heat stored during the daytime. The transport of the nocturnal Q_H, with a much lower magnitude than that of the daytime, is often released into the atmosphere from many urban surfaces, which is a unique urban feature compared to rural surfaces. The diurnal uniqueness of the urban surface energy balance contributes to the urban heat island (UHI) in both the surfaces and the air, influencing the habitats' comfort, raising the mortality rate owing to intense pollution and heat, and increasing building energy demand [3]. Consequently, lowering the surface temperature and the sensible heat flux released can effectively mitigate the UHI effects and reduce such problems [4].

Modifying urban surfaces with high-albedo materials or coatings and their effects on surface cooling, UHI mitigation, and in-/outdoor thermal comfort has been widely studied in recent years, revealing their benefits [5,6]. The thermal behavior of urban surfaces results from not only the radiation budget on the exterior surfaces but also heat conduction through the surfaces and convective heat transfers at both the exterior and interior surfaces of buildings. The thermal properties of the urban surface (e.g., heat capacity and thermal conductivity), influencing all the above-mentioned heat transfers, contribute to its heat exchanged with the inside of a building affecting the energy demand, and with the atmosphere forming the urban climate. However, their effects on the heat exchanged between the building surface and the atmosphere has not yet been studied systematically. We therefore considered three gaps in previous studies.

First, in addition to modifying the albedo, the effects of modifying the other thermophysical properties of building surfaces (e.g., roofs and walls) were investigated primarily by focusing on indoor thermal comfort and energy consumption [35–38], whereas the effects with the regard to the atmosphere were investigated less. The effects from modifying heat capacity and thermal conductivity were individually investigated for ground pavement [39]; however, the studied thermal property values were specific and limited to guarantee the universality of the findings, and these results could not be applied to a building surface owing to the differences in surface heat transfer. Additionally, because the conduction of heat through a surface depends on both thermal conductivity and heat capacity, the combined effects will differ from the accumulation of their individual effects (accumulated effect). Overall, there is a research gap in systematically exploring the individual and combined cooling effects of modifying thermal properties for building surfaces.

Second, the impact of thermal properties as a variable affecting the performance of a high-albedo strategy [80] was mostly neglected in existing studies; moreover, their values were sometimes not documented [81,82]. A high-albedo strategy can reduce the heat transfer to the building and the atmosphere [83]. The influence of thermal properties and the performance of cool roofs on indoor energy consumption has been widely studied [73,84,85], but only few specific scenarios of thermal mass and insulation were considered in evaluating the effect that cool roofs have on the atmosphere [80,86]. A systematic account of thermal properties for investigating the effect of a high-albedo strategy on the atmosphere is still lacking.

Third, the assumption and generalization of thermal properties may influence the accuracy of surface energy balance (SEB) models. SEB models, such as ENVI-met [5], SOLENE [6–8], and THERMORender [9–11], explore the interaction between buildings and the atmosphere at the surface layer [3]. These models can identify areas with severe outdoor thermal conditions [12,13], examine potential scenarios and technologies for the UHI mitigation [14–16], and can be coupled with building energy models for a more accurate prediction of energy demands [17–19]. The selection of urban optical and thermal properties is important to the simulation quality [20]. In addition to a study that assumes standardized building parameters [21,22], collecting the input building material data in the real world is a tedious job because of the large number of diverse materials used in urban constructions. Few studies have derived the surface materials and albedo by remote sensing [29,87], but the thermal properties of urban surfaces are usually assumed and generalized [15,16,39,73]. SEB model's sensitivities to the albedo and emissivity have been analyzed, showing that they clearly alter the model quality [20]. However, SEB model-based simulation errors caused by the assumption and generalization of thermal properties have been rarely discussed, and this may affect the decision of tailored UHI mitigation solutions and the boundary conditions to accurately predict building energy demand.

To bridge the above three gaps by attaining more universal results, the effects of the thermal properties of building surfaces on the heat exchange with the environment is systematically studied by a numerical simulation. A case study is thus carried out on a typical summer day with clear sky conditions in a city block in Yokohama city, Japan. A SEB model and input parameters (meteorological data and physical properties) are introduced and validated with a simulation-to-measurement comparison. The thermal properties studied are determined from a database of commonly used wall and roof surface materials in urban areas in Japan. The effects that both individual and combined modifications of the thermal properties of walls and roofs have on the surface heat exchange are investigated, as well as the thermal behavior of roofs before and after applying a high-albedo strategy with various thermal properties. The results are discussed in terms of the external surface temperature (T_s) and sensible heat flux (Q_H) emitted by the surface which represents the heat exchange between the building surface and the atmosphere; with regards to three issues: (a) the effect of modifying the thermal properties of surface materials, (b) the impact of various thermal properties on the cooling effect of the high-albedo strategy, and (c) the sensitivity of the SEB model to thermal properties and the simulation error that is caused by the assumption and generalization of the thermal properties.

2. Methodology

2.1 Simulation model

The SEB model (THERMORender) developed by Asawa et al. (2008) was applied in this chapter [10]. The 3D T_s distribution in the test area was calculated by using an energy balance simulation model. First, 3D spatial geometries of buildings, trees, and other structures, as well as two-dimensional (2D) ground surfaces, were divided into mesh cells of a regular 400-mm size. For each surface cell, in which the normal vector of the surface and component materials with a multilayer were stored, the energy balance and unsteady heat conduction were calculated. The energy calculation equations used are shown as follows.

(1) Energy balance of each surface

$$R_S + R_L + Q_H + Q_E - Q_G = 0$$

$$R_S = (1-\alpha)(\cos\theta \cdot I_{DR} + F_{sky} I_{SR} + I_{RR})$$

$$R_L = F_{sky} R_{La} + R_{Lw} - \varepsilon_s \sigma {T_s}^4$$

$$= F_{sky}\left(R_{La} - \varepsilon_s \sigma {T_s}^4\right) + \left(R_{Lw} - F_w \varepsilon_s \sigma {T_s}^4\right)$$

$$F_{sky} + F_w = F_{sky} + \sum_{i=1}^{n} F_i = 1,$$

$$R_{La} = \varepsilon_s \sigma {T_a}^4 \left(\left(a + b\sqrt{e}\right)\left(1 - \frac{c}{10} m\right) + \frac{c}{10} m\right),$$

$$R_{Lw} = \varepsilon_s \sum_{i=1}^{n} F_i \varepsilon_{wi} \sigma {T_{wi}}^4,$$

$$Q_H = \alpha_c (T_a - T_s),$$

$Q_E = \mathrm{l\beta k}(X_a - X_s)$ (wet surface, vegetated surface, in this chapter $Q_E = 0$),

$$Q_G = -\lambda \frac{\partial T}{\partial x}$$

(2) One-dimensional (1D) unsteady heat conduction (inside of each surface)

$$\frac{\partial T}{\partial t} = \frac{\lambda}{C_\rho} \frac{\partial^2 T}{\partial x^2}$$

(3) Boundary condition for building interior

$$-\lambda \frac{\partial T}{\partial x} = \alpha_o (T_{sr} - T_r)$$

The quantity of direct solar radiation I_{DR} received by a cell was simulated by using the ray-tracing method. The reflected solar radiation I_{RR} on each surface included specular reflection and isotropic diffuse reflection, both of which were considered as the first reflection. The specular reflective radiation was calculated by conducting a ray-tracing simulation toward the direction of the specular reflection. Diffuse reflective radiation was estimated under the assumption of an isotropic diffuse reflection following Lambert's cosine law, and the quantity of the diffuse reflective radiation received by a cell was calculated by performing a multitracing simulation toward the surrounding cells. The specular reflectance was only applied to the glass materials of windows, and diffuse reflectances were set for all other materials.

The quantity of sky solar radiation I_{SR} received by a cell was estimated by multiplying the sky view factor of the cell by the quantity of sky solar radiation for unobstructed sky conditions derived from the meteorological data. The sky view factor was calculated by conducting a multi tracing simulation from the cell toward upper hemispherical directions. The quantity of atmospheric radiation R_{LA} received by a cell was also estimated by the sky view factor and the quantity of atmospheric radiation calculated by Brunt's formula. The sky radiance distribution was ignored for both shortwave and longwave diffuse radiation from the sky, and was assumed to be uniform in this calculation. The exchange of longwave radiation with the surroundings was also calculated.

In reality, 3D transient heat conduction occurs on the building surfaces. However, this factor here was simplified to 1D transient heat conduction. This assumption is considered to be valid in the simulation results, because T_s and Q_H were averaged for each surface unit. The T_s and sectional distribution of the temperature in the building envelopes and the ground were calculated using the 1D transient heat conduction equation and the estimated energy balance for a diurnal circle. The backward difference method was employed for the 1D transient heat conduction with a time integration in increments of 5 minutes. The Q_H was calculated by multiplying the convective heat transfer coefficient (CHTC) with the difference between T_s and the ambient temperature. The CHTC was estimated by the Jürges equation [88]，which may introduce an uncertainty of +/- 15-20% [89–91]. The air temperature and wind speed on the surfaces of the building were assumed to be uniform. This simplification may appear drastic; however, it is required. Once the model is coupled with a computational fluid dynamics simulation, the computational load significantly increases, causing difficulty in conducting systematic simulations in many cases. This simplification will be checked in the validation section. The latent heat flux (Q_L) was not calculated for the building surfaces.

2.2 Theoretical calculation on thermal properties of multilayer surface

The theoretical calculation method used in this chapter is based on ISO 6946 [92] and is a simple calculation using reliable technical information or database without the requirement of physical testing. However, compared to the actual value of the thermal properties by the measured method (e.g., ISO 9869-1 [54]), this method may introduce roughly a +/- 5-20% uncertainty in each thermal property due to the influence from construction and workmanship, the omission of thermal contact resistance, and the use of the standardized and generalized thermal resistance of the air layer [93].

2.2.1 Coefficient of thermal conductivity λc [W m-2 K-1]

Since layers of building surfaces are assumed to be tightly laminated, the thermal contact resistance can be ignored. $\delta i\ [m]$ is the thickness of each target layer. In addition to air layers, the thermal resistance per unit surface area (R_i [m^2 K W^{-1}]) and thermal conductivity (λ_i [W m^{-1} K^{-1}]) of each target layer are related via [Eq. (1)]:

$$R_i = \delta_i/\lambda_i \qquad (1)$$

The thermal resistance per unit surface area for each air layer (R_a) was given the standardized value of 0.09 m^2 K W^{-1} here. Material with an extremely low-emissivity (e.g., aluminum foil with an emissivity of 0.2) emits lower longwave radiation, and was therefore rarely used to line air layers in Japan, meaning that no exceptional thermal resistances need to be examined here. The difference in resistance between horizontal and vertical air spaces is also ignored owing to its slight influence on both the radiative and the convective heat transfer within an air layer. According to the analogy between electrical and thermal resistance, the total thermal resistance per unit surface area (R [m^2 K W^{-1}]) of n layers of engineering materials and m layers of air spaces can be calculated as in Eq. (2):

$$R = \sum_{i=1}^{n} R_i + mR_a \qquad (2)$$

Based on Eq. (1) and (2), the total thermal resistance per unit surface area of a multilayer component is determined via the relation to the conductivity and thickness of each target layer [Eq. (3)]:

$$R = \sum_{i=1}^{n} (\delta_i/\lambda_i) + mR_a \qquad (3)$$

Therefore, the total conductivity coefficient (λ_c [W m^{-2} K^{-1}]) of the multilayer component of a building surface is calculated as the weighted mean of the conductivity of each layer, where the weight is inversely proportional to the thickness of each target layer [Eq. (4)]:

$$\lambda_c = 1/R = 1/(\sum_{i=1}^{n} (\delta_i/\lambda_i) + mR_a) \qquad (4)$$

2.2.2 Areal heat capacity C_a [kJ m-2 K-1]

$C_{\rho i}$ [kJm^{-3}K^{-1}] and C_{ai} [kJm^{-3}K^{-1}] are the volumetric and areal specific heat capacities of a target layer, respectively. The total specific heat capacity (C_a [kJ m^{-2} K^{-1}]) of a unit-area multilayer urban surface can be calculated by the following equation [Eq. (5)]:

$$C_a = \sum C_{ai} = \sum (\delta i * C_{\rho i}) \qquad (5)$$

2.3 Study building and simulation condition

A case study was conducted on a university campus in Yokohama city, Japan. The test area was approximately 174 m × 148 m, enclosed on four sides as a repeated unit within the school (Fig. 1). The test building was three floors and of a straight type, with offices and experimental rooms inside. The values of the physical properties for the study area are listed in Table 1 in order to reproduce the actual material.

Based on weather data observed by the Japan Meteorological Agency's weather station at Yokohama (open online: *https://www.data.jma.go.jp*), July 9 was selected as a typical summer day in 2017 for simulations. The sky was clear and sunny, and in the middle of sunny days. The meteorological conditions are displayed in Fig. 2. The indoor air was assumed to have a constant temperature of 26 ºC with air conditioning.

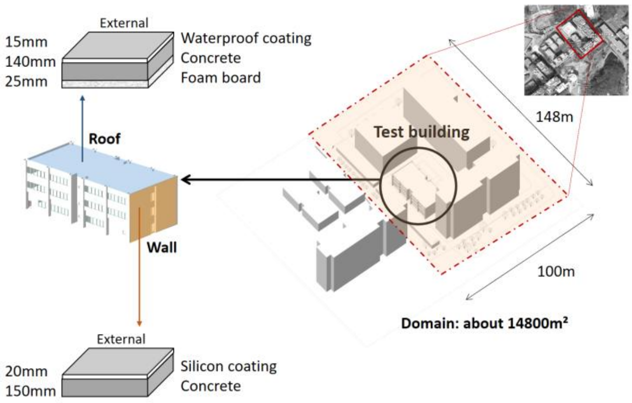

Figure 1. Test area and target building

Table 1. Physical properties of test building and ground materials (see nomenclature)

	δ [mm]	α [-]	ε [-]	λ_c [W m^{-2} K^{-1}]	C_a [kJ m^{-2} K^{-1}]
Test building wall	***170***	***0.4***	***0.95***	***5.06***	***325***
Silicon coating	20	0.4	0.95	7.50	32
concrete	150	-	-	5.40	285
Test building roof	***180***	***0.3***	***0.95***	***0.86***	***282***
Waterproof coating	15	0.3	0.95	0.67	15
Concrete	140	-	-	5.79	266
Foam board	25	-	-	1.2	0.75
Ground	***1130***	***0.3***	***0.90***	***0.61***	***1820***
Asphalt pavement	130	0.3	0.90	5.38	260
Mortar	200	-	-	7.5	320
Gravel	400	-	-	1.5	600
Soil	400	-	-	1.5	640

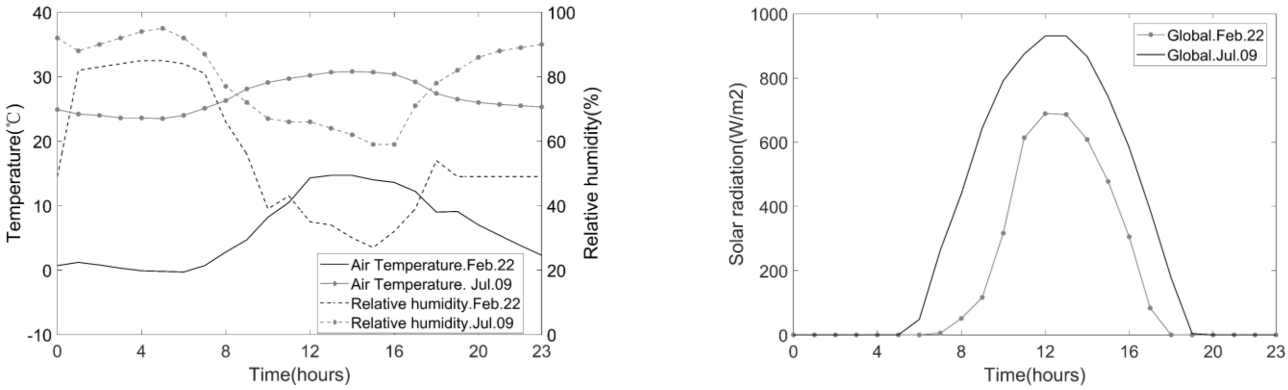

(a) Ambient temperature and relative humidity **(b) Global solar radiation**

Figure 2. Reference meteorological conditions at the study site

2.4 Input property parameter of building surface for simulation cases

In order to discuss the effects of modifying the thermal and optical properties systematically, synthetic values were set for the simulation cases. To confirm the universality and applicability of the simulation results, the input thermal and optical properties for the surface materials were sourced from a database of commonly used building surface materials in an urban area of mainland Japan, and within the documented range of engineering materials (termed as the “civil engineering range” in the following thesis). Notice that the “civil engineering range” in this thesis does not have the scientific evidence to give its quantitative definition. According to a classification method by Hoyano et al. (2007)[94], 63 and 76 components were included for roof and wall surfaces from the database, respectively. Note that this database contained information for existing buildings that were mainly constructed before 2000. Thicker insulation (50–100 mm) is required in more recent constructions owing to Japan’s Regulation of Building Energy Efficiency. However, considering the climate of mainland Japan is subtropical climate, this database may not be applicable for other countries and regions with different climate and preference of building materials.

2.4.1 Control case

To determine a control case for the thermal properties, K-means clustering was applied to classify the roof/wall components from the abovementioned database into 10 clusters and to plot each cluster center (Fig. 3) depending on the Euclidean distance calculated by the values of the normalized thermal properties. Fig. 3 (a) shows that the most commonly used wall constructions have low thermal conductivity and heat capacity, such as ALC panel/steel/ceramic siding with layers of insulation and air used in commercial and residential buildings, and the components for wooden houses. Their cluster centers are 0.68 Wm^{-2}K^{-1} (λ_c) and 44744 Jm^{-2}K^{-1} (C_a). As shown in Fig. 3 (b), the roof components with low heat capacity and thermal conductivity (wooden construction and tile/asphalt/steel covered with layers of insulation and air) are as widely used as those with low heat capacity and high thermal conductivity (tile/steel covered with a thin layer of asphalt and a layer of plywood). Their centers are 0.72 $Wm^{-2}K^{-1}$ (λ_c) and 49740 $Jm^{-2}K^{-1}$ (C_a), and 11.3 $Wm^{-2}K^{-1}$ (λ_c) and 27745 $Jm^{-2}K^{-1}$ (C_a), respectively. The thermal conductivity of the roof and wall constructions is rarely allocated at a medium value (around 6 $Wm^{-2}K^{-1}$ and 7 $Wm^{-2}K^{-1}$, respectively). Hence, the control case was set at 1 $Wm^{-2}K^{-1}$ (λ_c) and 50 $kJm^{-2}K^{-1}$ (C_a) for both the wall and roof.

(a) Wall surface

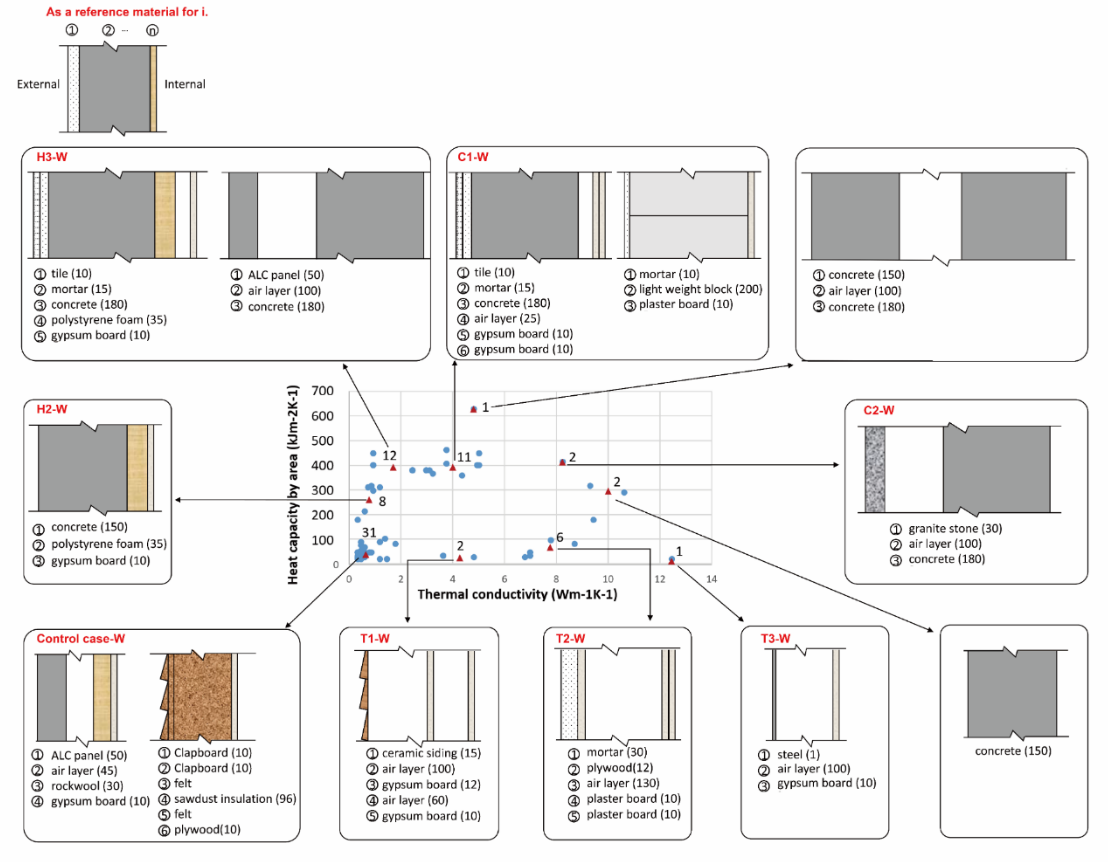

(b) Roof surface

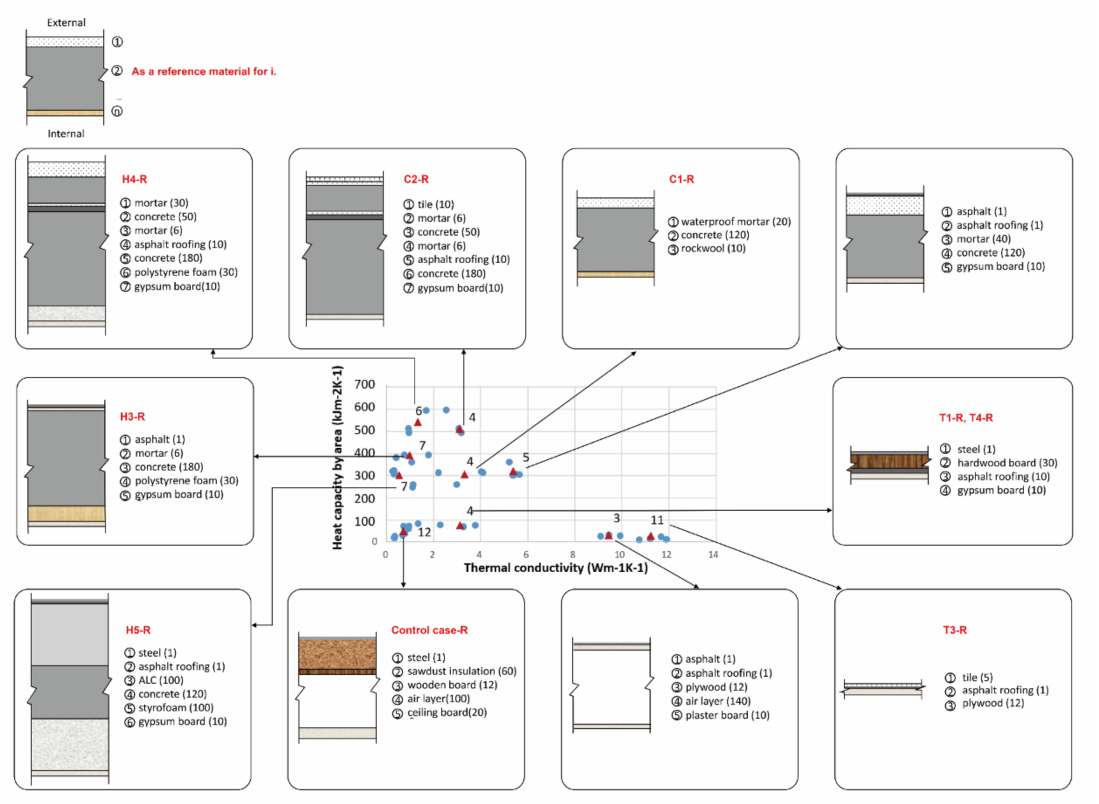

Figure 3. Distributions of thermal properties of commonly used wall (a) and roof (b) components

In terms of the optical properties, the commonly used exterior covering materials for urban surfaces (concrete, asphalt, stone, tile, etc.) usually have a 0.2–0.3 albedo if the coating color is not light [40,41]. Most building materials have high emissivities between 0.9 and 0.95 [97]. Hence, the control case here for the roof and wall surfaces was set to 0.2 for the albedo and 0.9 for the emissivity.

2.4.2 Cases involving individual modifications of thermal properties

Cases of individual modifications of thermal properties were simulated as shown in Table 2. For walls, the studied values of thermal properties were referred from Fig. 3 (a). For a roof as shown in Fig. 3 (b), even if there is no typical material with a thermal conductivity of a medium value (6–8 $Wm^{-2}K^{-1}$), the materials with a medium thermal conductivity of 8 $Wm^{-2}K^{-1}$ were assumed to simulate the uniform modification.

Modifications of the optical properties were also studied as a comparison. The albedo of commonly used surface materials with light-color coating is 0.4–0.5. Many reflective materials and white coatings have an albedo of 0.7–0.8 [40,41]. For example, Takebayashi (2007) monitored a roof surface with an albedo of 0.74 in Japan [98]. Hence, the studied albedos were set as 0.5 and 0.8. Few engineering materials (e.g., asbestos slate, silver-gray slate, and zinc-iron plate) have an emissivity lower than around 0.8 [99], so a low emissivity of 0.8 was set.

Table 2. Simulations for individual modification of thermal properties for roof and wall surfaces

Modification	Case	α [-]	ε [-]	λ_c [W m^{-2} K^{-1}]	C_a [kJ m^{-2} K^{-1}]	Reference materials λ_c [W m^{-2} K^{-1}] / C_a [kJ m^{-2} K^{-1}] Layers from exterior to interior [mm]	
						Roof	**Wall**
	Control Case-R/W	0.2	0.9	1	50	0.8 / 41 Layers shown in Fig. 3 (b)	0.9 / 43 Layers shown in Fig. 3 (a)
Albedo	A1-R/W	0.5	0.9	1	50	Light-color paint	Light-color paint
	A2-R/W	0.8	0.9	1	50	White paint	White paint
Emissivity	E1-R/W	0.2	0.8	1	50	Low-emissivity coating	Low-emissivity coating
Thermal conductivity	T1-R/W	0.2	0.9	4	50	3.3 / 71 Layers shown in Fig. 3 (b)	3.7 / 32 Layers shown in Fig. 3 (a)
	T2-R/W	0.2	0.9	8	50	None	8.7 / 78 Layers shown in Fig. 3 (a)
	T3-R/W	0.2	0.9	12	50	11.2 / 34 Layers shown in Fig. 3 (b)	12.5 / 15 Layers shown in Fig. 3 (a)
Heat capacity	H1-R/W	0.2	0.9	1	100	1.3 / 86 Asphalt 1 Asphalt roofing 10 ALC 100 Gypsum board 10	1.2 / 82 Granite stone 30 Air layer 15 Rock wool 30 Gypsum board 10
	H2-R/W	0.2	0.9	1	250	1.1 / 249 Asphalt 1 Mortar 6 Concrete 120 Polystyrene foam 30 Gypsum board 10	1.0 / 295 Layers shown in Fig. 3 (a)
	H3-R/W	0.2	0.9	1	400	0.8 / 395 Layers shown in Fig. 3 (b)	0.9 / 396 Layers shown in Fig. 3 (a)
	H4-R	0.2	0.9	1	550	0.9 / 515 Layers shown in Fig. 3 (b)	

2.4.3 Cases for combined modification of thermal properties

As presented in Table 3, H3-W, H4-R, T1-W/R, and T2-W (section 3.1) as previously simulated were used as individual modifications, and H5-R and T4-R were added for the roof surface. Four cases (C series) were simulated as combined modifications of both the heat capacity and thermal conductivity. The reference materials are commonly used in urban areas in Japan.

Table 3. Simulations for combined modification of thermal properties for roof and wall surfaces

Modification	Case	α [-]	ε [-]	λ_c [W m^{-2} K^{-1}]	C_a [kJ m^{-2} K^{-1}]	Reference materials λ_c [W m^{-2} K^{-1}] / C_a [kJ m^{-2} K^{-1}] Layers
	Control Case-R/W	0.2	0.9	1	50	Table 2
Heat capacity	H3-W	0.2	0.9	1	400	Table 2
	H5-R	0.2	0.9	1	300	0.3 / 312 Layers shown in Fig. 3 (b)
	H4-R	0.2	0.9	1	550	Table 2

Thermal conductivity	T1-W/R	0.2	0.9	4	50	Table 2
	T2-W	0.2	0.9	8	50	Table 2
	T4-R	0.2	0.9	3	50	3.3 / 71 Layers shown in Fig. 3 (b)
Combined modification	C1-W	0.2	0.9	4	400	3.8 / 404 Layers shown in Fig. 3 (a)
	C2-W	0.2	0.9	8	400	8.3 / 414 Layers shown in Fig. 3 (a)
	C1-R	0.2	0.9	3	300	3.0 / 261 Layers shown in Fig. 3 (b)
	C2-R	0.2	0.9	3	550	3.2 /495 Layers shown in Fig. 3 (b)

2.4.4 Cases to simulate impact of thermal properties on cooling effects of high-albedo strategy

As shown in Table 4, the studied values of the thermal properties for roof surfaces were derived from 10 cluster centers [shown in Fig. 3 (b)]. The simulated albedos before (B-case) and after the high-albedo modification (M-case) were 0.2 and 0.8, respectively.

Table 4. Simulations for high-albedo strategy applied for roofs with various thermal properties

Modification	**Case**	α **[-]**	ε [-]	λ_c [W m^{-2} K^{-1}]	C_a [kJ m^{-2} K^{-1}]	**Cluster center** λ_c **[W m^{-2} K^{-1}] /** C_a **[kJ m^{-2}·K^{-1}]**
Before modification	B1-R *(Control Case-R)*	0.2	0.9	1	50	0.7 / 50
	B2-R *(H5-R)*	0.2	0.9	1	300	0.5 / 299
	B3-R *(H3-R)*	0.2	0.9	1	400	1.0 / 387
	B4-R *(H4-R)*	0.2	0.9	1	550	1.3 / 536
	B5-R	0.2	0.9	3	100	3.1 / 74
	B6-R	0.2	0.9	3	300	3.3 / 302
	B7-R	0.2	0.9	3	500	3.1 / 504
	B8-R	0.2	0.9	5	300	5.4 / 317
	B9-R	0.2	0.9	10	50	9.5 / 30
	B10-R	0.2	0.9	11	50	11.2 / 28
High albedo	M1-R	0.8	0.9	1	50	Same to B1-R
	M2-R	0.8	0.9	1	300	Same to B2-R
	M3-R	0.8	0.9	1	400	Same to B3-R

M4-R	0.8	0.9	1	550	Same to B4-R
M5-R	0.8	0.9	3	100	Same to B5-R
M6-R	0.8	0.9	3	300	Same to B6-R
M7-R	0.8	0.9	3	500	Same to B7-R
M8-R	0.8	0.9	5	300	Same to B8-R
M9-R	0.8	0.9	10	50	Same to B9-R
M10-R	0.8	0.9	11	50	Same to B10-R

3. Simulation validation

The SEB model and calculation mesh size were validated by a simulation-to-measurement comparison in terms of the radiant temperature and shadow-sunlight transitions. The measurement was conducted on February 24, 2018, a windless winter day with a clear sky. The meteorological data were as shown in Fig. 2, observed in the field by a radiometer, thermometer, and anemometer. With clear-sky conditions, the partition between the direct and diffuse components was calculated using Erbs' model [100] for the target day.

By using a handheld thermal infrared camera (InfReC Thermo GEAR, Nippon Avionics Co., Ltd., Japan) and a multispectral camera (Rededge-M, MicaSense Inc., USA), hourly infrared and multispectral images for each façade were captured from sunrise to sunset and at around midnight. We averaged the measured radiant temperatures of façade surfaces excluding windows, branches, pipes, and air-conditioner outdoor units. As measured by the thermal infrared camera, the relationship between the radiant temperature T_{ri} of a target i and its actual surface temperature T_{si} is as follows [Eq. (6)]:

$$L_b(T_{ri}) = \varepsilon L_b(T_{si}) + (1-\varepsilon) L_b(T_w) \tag{6}$$

where T_w is the average temperature of the surrounding buildings and ground, and $L(T) = \varepsilon L_b(T)$. L_b is the radiant heat flux from a black body, whose emissivity (ε) close to 1, to its surroundings. It depends on the target temperature (T) and spectral wavelength (in this chapter, the thermal infrared wavelength) expressed by Kirchhoff's law. The average of the measured radiant temperature for each façade is directly applied for the comparison. According to the hourly multispectral images, the time when measured areas of the SW, SE, and NW façades starts being sunlit and shadowed can be clearly observed. The measured area of the NE façade is without sunlight, and only some other parts are slightly sunlit in the morning because they are mainly under the shadow of a south-facing building.

Two simulations were carried out on February 24, 2018, with mesh sizes of 200 mm and 400 mm. The basic simulation outputs were the instantaneous surface temperatures of facets based on an iterative computation of an energy flux budget. This computation involves the reflection on all facets, and ε of the surface material and simulated T_s are known; therefore, the simulated radiant temperatures can be obtained for the comparison based on Eq. (6).

As shown in Fig. 4, the thinner mesh provides values closer to those measured, but the difference is negligible. Considering a reasonable time for computation (about 100 min for 400 mm, and 400 min for 200 mm), the grid resolution of 400 mm was selected to allow for an accurate simulation. A fairly good agreement is generally observed in Fig. 4; in particular, the shadow-sunlight transitions are reproduced quite well. The radiant temperatures are simulated with a high r^2 above 0.90, indicating a strong correlation with the values measured. This is also verified by the mean absolute errors (MAEs) and root mean square errors (RMSEs) for four façades, which are usually around 1.0 ºC and 1.3 ºC and are not greater than 1.3 ºC and 1.67 ºC, respectively.

The simulated value of the NE façade, which received the least direct solar radiation, reveals the smallest difference from the observed value, which is in agreement with existing validations of the SOLENE model [21,33]. Most of the noon and afternoon radiant temperatures of the SE and NE façades are overestimated by up to about 2.0 ºC, while those of the SW and NW façades appear to be more satisfactory. This is probably caused by Erbs' model [100] as applied to the solar radiation partitioning that overestimates the received solar radiation on the east-oriented vertical surfaces from noon through the afternoon. An adapted coefficient should be applied to improve the radiation model while accounting for the geographical and climatic conditions of the study site.

Only the NW-façade temperature overshot from sunrise to noon by up to 3.4 ºC (10:00) as a maximum error. Its comparison to the NE façade from 06:00 to 12:00, when all temperatures were supposed to be close since they did not receive orientation-based direct solar radiation, suggests that this difference was caused by reasons other than the model performance. This may be owing to the reflected radiative contributions of windows on the opposite façade (SE orientation) because windows are not modeled in the façades of surrounding buildings as a simplification.

Indeed, a multispectral image of the NW façade taken at 10:00, presenting obvious window-shaped areas with higher brightness, reinforces this hypothesis. Meanwhile, it is confirmed that the simplifications of uniform distributions of the air temperature and wind speed on the building surfaces in the simulation are valid under weather conditions with a low wind velocity [101].

The reason to validate on a winter day rather than a summer day was a priority to test the influence of low solar elevation angles on the simulation accuracy. Among the SEB-based models validated in different cases [16–

18,30,42,43], the simulated evolution of a case in France is in excellent agreement with the measured data for July 15, whereas a clear underestimation (up to 8 K) is observed for February 25 when the solar elevation angle was low [8]. On winter days, the solar elevation angle is lower than in summer, and the proportion of direct solar radiation received by the façade is larger than in summer, so its surface temperature variation appears more sensitive to solar radiation. Meanwhile, the temperature difference between the indoor and ambient air on winter days (around 15 ºC) is larger than that on summer days (less than 10 ºC) in Yokohama city. This can better test the simulation accuracy of heat conduction and convection.

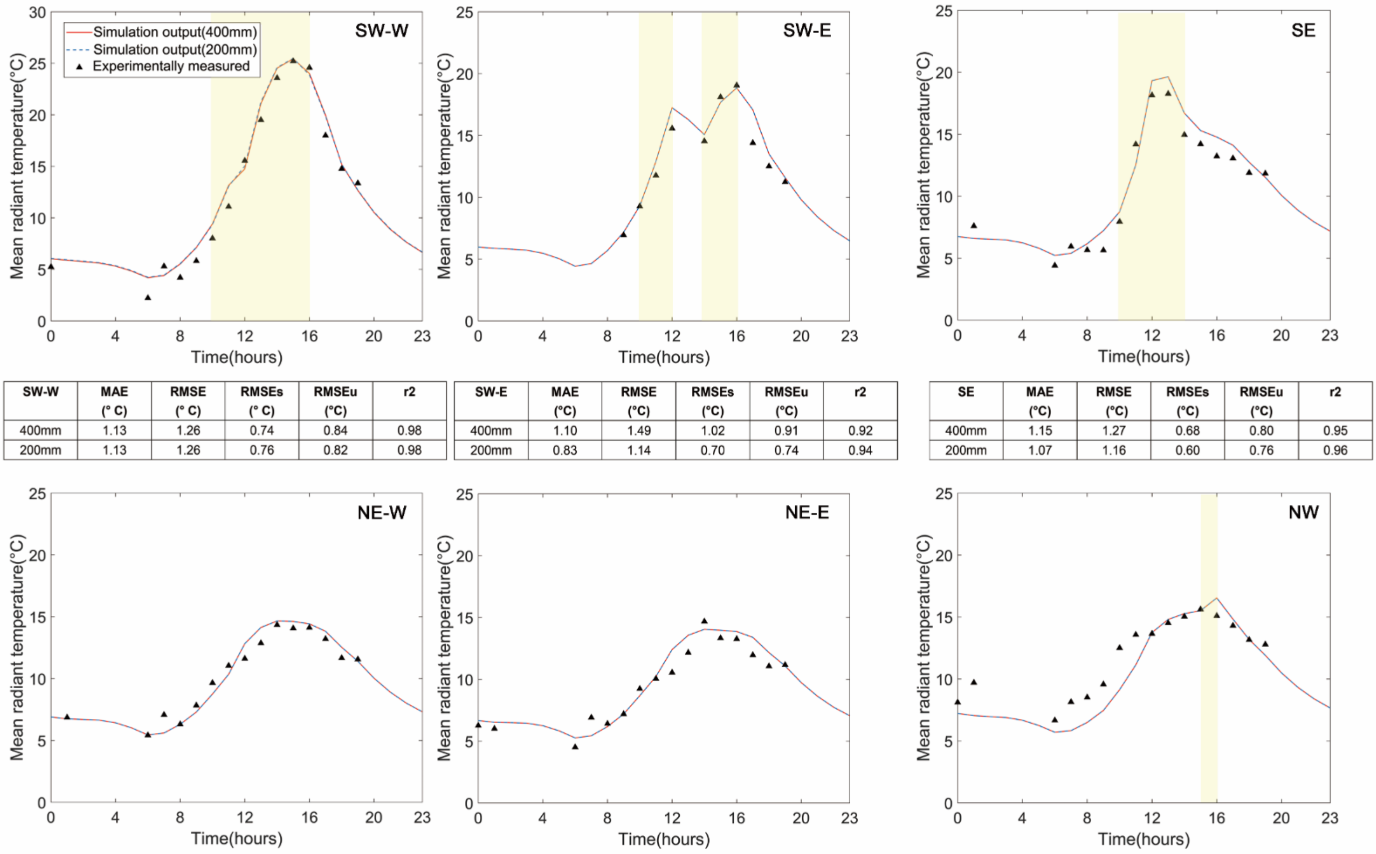

SW-W	MAE (° C)	RMSE (° C)	RMSEs (° C)	RMSEu (°C)	r2
400mm	1.13	1.26	0.74	0.84	0.98
200mm	1.13	1.26	0.76	0.82	0.98

SW-E	MAE (°C)	RMSE (°C)	RMSEs (°C)	RMSEu (°C)	r2
400mm	1.10	1.49	1.02	0.91	0.92
200mm	0.83	1.14	0.70	0.74	0.94

SE	MAE (°C)	RMSE (°C)	RMSEs (°C)	RMSEu (°C)	r2
400mm	1.15	1.27	0.68	0.80	0.95
200mm	1.07	1.16	0.60	0.76	0.96

NE-W	MAE (°C)	RMSE (°C)	RMSEs (°C)	RMSEu (°C)	r2
400mm	0.71	0.88	0.53	0.51	0.97
200mm	0.60	0.75	0.38	0.54	0.97

NE-E	MAE (°C)	RMSE (°C)	RMSEs (°C)	RMSEu (°C)	r2
400mm	0.92	1.12	0.77	0.60	0.94
200mm	0.74	0.92	0.37	0.66	0.94

NW	MAE (°C)	RMSE (°C)	RMSEs (°C)	RMSEu (°C)	r2
400mm	1.28	1.67	0.98	0.88	0.91
200mm	1.27	1.64	0.95	0.87	0.92

Mesh size	MAE (°C)	RMSE (°C)	RMSEs (°C)	RMSEu (°C)
400mm	1.09	1.33	0.80	0.78
200mm	1.00	1.21	0.67	0.75

Figure 4. SEB modeling performance in terms of hourly radiant temperature and error analysis compared to measurement. Yellow band indicates period of being sunlit.

SW: southwest, NE: northeast, NW: northwest, SE: southeast. i-W: west side of i, i-E: east side of i. MAE: mean absolute error, RMSE: root mean square error, RMSEs: systematic RMSE, RMSEu: unsystematic RMSE, r2: coefficient of determination.

To further evaluate the model quality, the model is compared with the validation results of SOLENE. A validation case on July 28 in an industrial area of Guerville, France, exhibits an RMSE of 0.61–2.57 ºC for the daily T_s at different heights of the S façade, and 0.79–1.38 ºC for those on the N façade [20]. The maximum errors for both the S and W façades are around 5 ºC at a height of 2.6 m at noon. Another validation case, conducted on a summer day and a winter day in the center of Toulouse, France, reveals an average RMSE of the daily T_r for the four façade orientation groups (N-NE, E-SE, S-SW, and W-NW) as 1.6, 2.3, 2.7, and 2.6 ºC, respectively [8]. It is not very strict to compare the error values since the above validations were determined under different meteorological conditions and urban geometry. However, the generally lower RMSE, MAE, and maximum error for the simulated temperatures in the THERMORender model demonstrate that its performance is sufficient.

Overall, the THERMORender model can explore the effects of building external surfaces in terms of the diurnal variations of the surface temperature and energy budget. For better simulation accuracy, an improved model of diffuse solar fractions, considering geographical and climatic conditions in Japan, is applied to the following simulations.

4. Simulation results

4.1 Individual modifications of thermal properties

4.1.1 Roof

The simulation results of Case-R from Table 2 are shown in Fig. 5. Fig. 5 (a) shows the control case and albedo modification cases (Ai-R); and (b), (c), and (d) are the same except for the emissivity (Ei-R), thermal conductivity (Ti-R), and heat capacity (Hi-R). Fig. 5 illustrates that for the roof, increasing α cools the external surface considerably. An increase of 0.3 in α led to a reduction of up to about 9 ºC in Ts at noon. Nonnegligible cooling effects were detected for an increasing thermal conductivity and heat capacity. For an increase from 1 to 8 Wm-2K-1 (λc), the maximum cooling and warming effects were about 2.8 ºC around 12:00 and 0.4 ºC during the night. Further cooling by increasing λc from 8 to 12 W m-2 K-1 was only 0.7 ºC at 12:00, which is not as significant as those from 1 to 4 Wm-2K-1 (about 1.6 ºC) and 4 to 8 Wm-2K-1(about 1.3 ºC).

The daytime cooling effect when increasing C_a is lower than that when increasing λ_c within a typical civil engineering range, whereas its warming effect is greater. Increasing C_a also delays the time for the peak temperature at noon. The maximum cooling and warming effects of a C_a modification, within a typical civil engineering range in Japan, were about 3.0 ºC and 2.0 ºC, respectively. A modification to ε has a relatively insignificant impact. The warming effect when decreasing an ε of 0.1 was up to about 0.8 ºC.

The simulated Q_H released by the roof is shown in Fig. 6. Similar to the results of T_s, the reduction in Q_H is primarily driven by α modifications and remains scarcely influenced by the ε modification from a practical viewpoint. In terms of the noontime Q_H (12:00–13:00), the mitigation effects of an extreme increase in λ_c and C_a within a typical civil engineering range were around 1/3 and 1/4 of that of an α increase of 0.3, respectively.

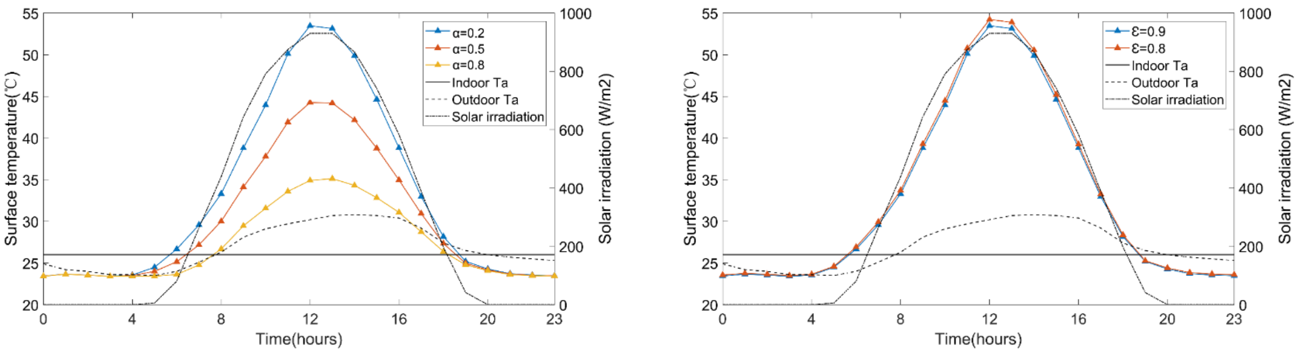

(a) α [-]

(b) ε [-]

(c) λ_c [Wm^{-2}K^{-1}]

(d) C_a [kJm^{-2}K^{-1}]

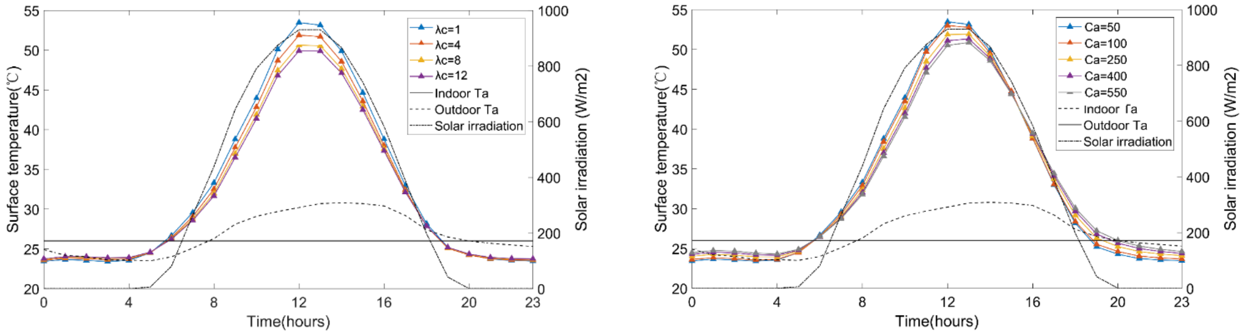

Figure 5. Simulated surface temperatures of roofs with various (a) albedo, (b) emissivity, (c) thermal conductivity, and (d) heat capacity

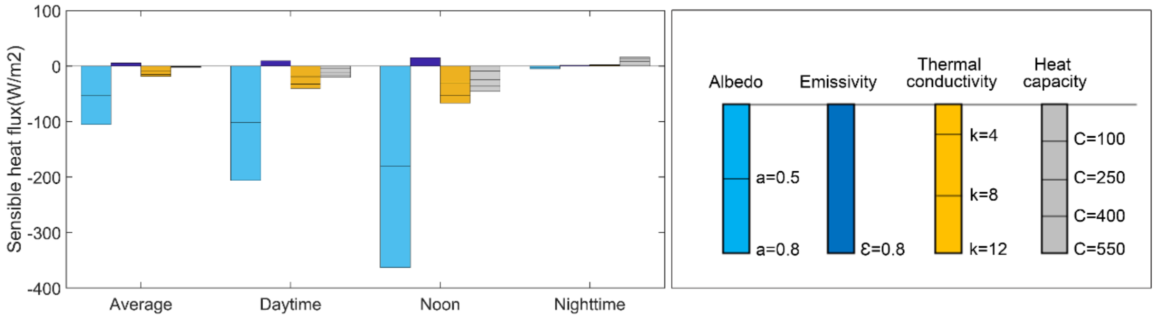

Figure 6. Simulated QH released by roof external surface

4.1.2 Wall

The simulation results of Case-W from Table 2 are shown in Fig. 7. The first row of Fig. 7 (a–d) reveals the diurnal variation of the average surface temperature of four façades, the second row is the same as the first row for the SW and NE façades, and the third row shows the results for the SE and NW façades. Since the SW and NE façades are dominant in the total area of the building façades, the diurnal variation of the average surface temperature of the four façades seems to be a compromise between those of the SW and NE façades. Only one strong increasing curve reaches its peak value at around 14:00 for the SW façade, mainly owing to the contribution of solar radiation. Hence, the best modification to reduce the peak value is to increase α, whose behavior is far from other modifications.

For the NE façade, its summer diurnal variation is quite different from the winter one (section 2.4) because the higher solar elevation angle allows it to be sunlit. This removes the shadow of the building at the south side in the morning, causing an extra peak value at 10:00 in addition to that at 13:00 in winter, which is mainly owing to the increase in ambient air temperature. Different peak reason influences the effects of surface modifications. The α modification is superior in reducing the first peak value, but its contribution to the second one is negligible, whereas the contributions of modifying λ_c and C_a are close to reducing these two peak values.

The contribution of an increase in λ_c and C_a on the temperature reduction does not significantly depend on the façade orientations. The maximum differences in the daytime reductions among the four façades are about 0.1 ºC and 0.2 ºC, respectively. Conversely, the façade orientations significantly affect the cooling effect of an α increase. The maximum difference in the peak reduction was 3.3 ºC between the SW (5.1 ºC at 14:00) and NE (1.8 ºC at 9:00) façades. As another optical property, the cooling effect of increasing ε is also influenced by the orientation, and the maximum effect appears on the SW façade as well. Meanwhile, increases in λ_c and C_a have a nocturnal warming effect of up to about 0.3 ºC and 0.5 ºC on average for the four façades, respectively.

(a) *α* [-]

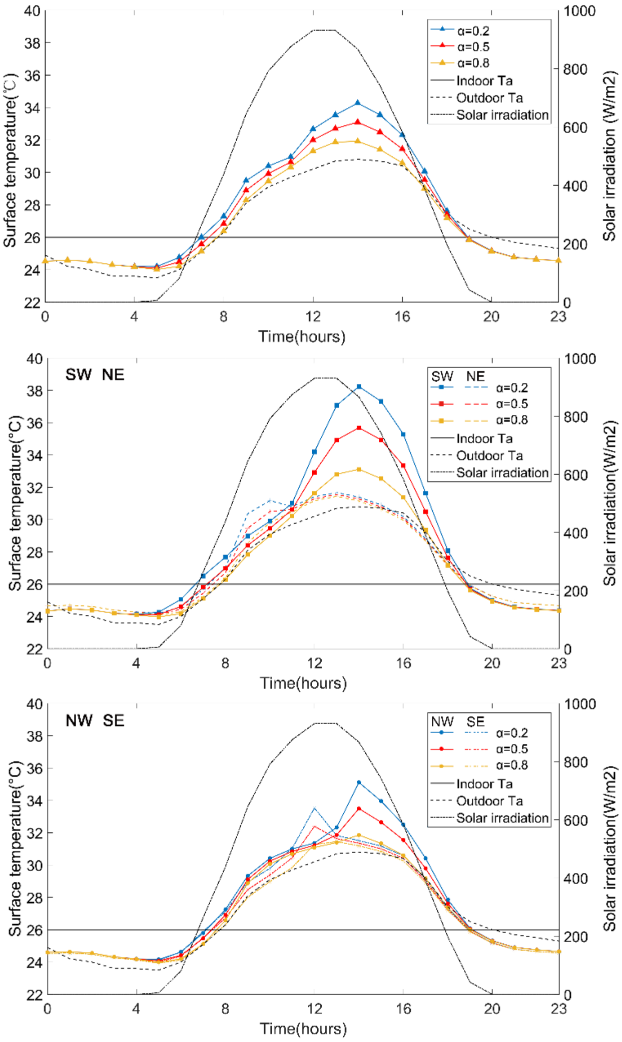
Surface temperature(℃)
Solar irradiation (W/m2)
Time(hours)
α=0.2
α=0.5
α=0.8
Indoor Ta
Outdoor Ta
Solar irradiation
SW NE
NW SE
40
38
36
34
32
30
28
26
24
22
1000
800
600
400
200
0
0
4
8
12
16
20
23

(b) *ε* [-]

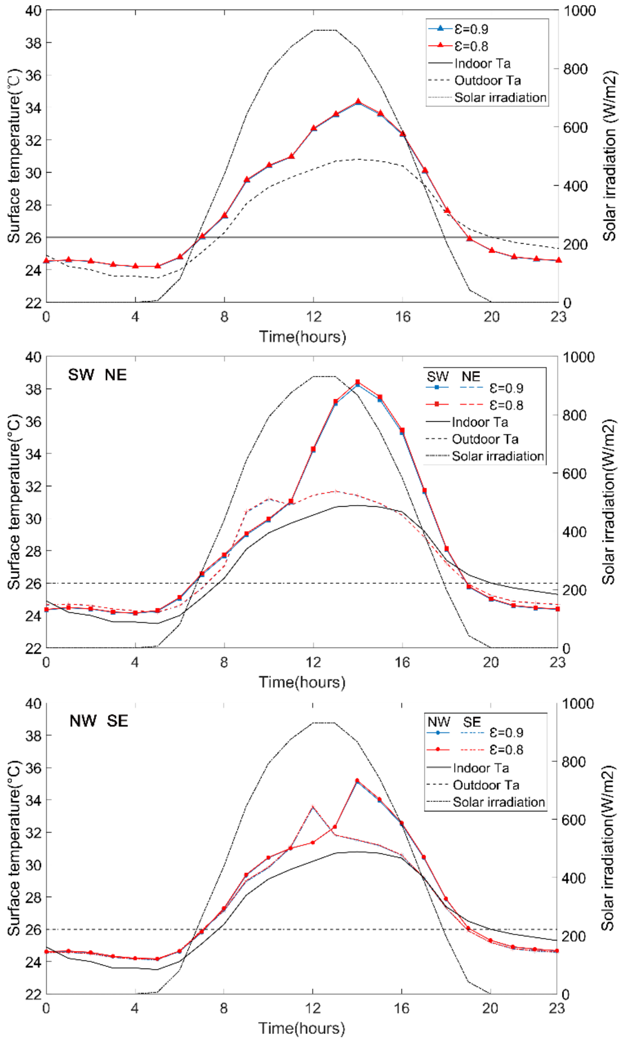
Surface temperature(℃)
Solar irradiation (W/m2)
Time(hours)
Ɛ=0.9
Ɛ=0.8
Indoor Ta
Outdoor Ta
Solar irradiation
SW NE
NW SE
40
38
36
34
32
30
28
26
24
22
1000
800
600
400
200
0
0
4
8
12
16
20
23

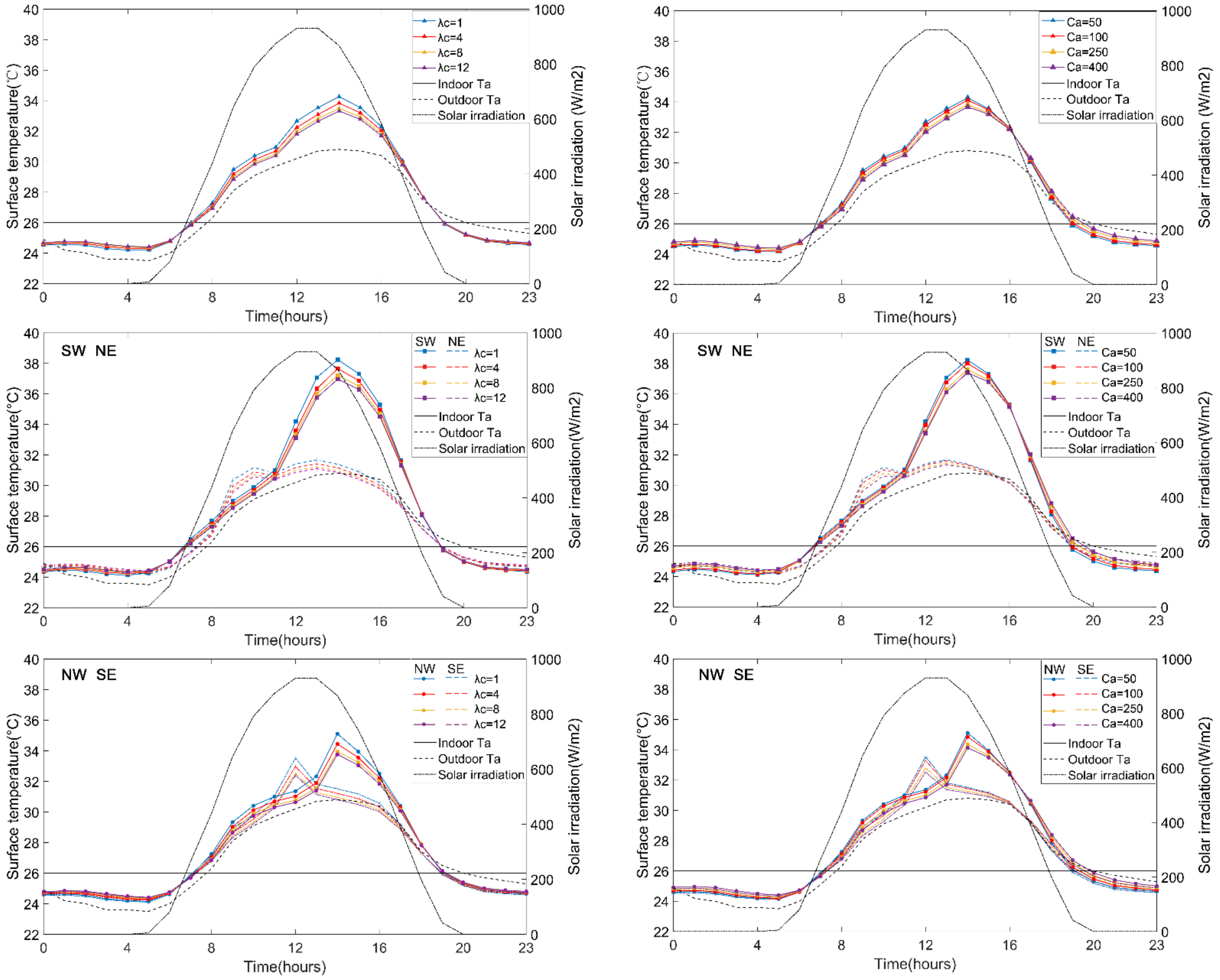

(c) λ_c [Wm^{-2}K^{-1}] **(d)** C_a [kJm^{-2}K^{-1}]

Figure 7. Simulated surface temperatures of walls with various (a) albedo, (b) emissivity, (c) thermal conductivity, and (d) heat capacity for average four façades and individual façade

In terms of Q_H as shown in Fig. 8, the UHI mitigation effect of a large increase in λ_c was apparently close to that of an increase of 0.3 in α during the daytime and at noon, but lower than that for the daily average owing to its nocturnal warming effect. A large increase in C_a shows about 54% and 68% of the mitigation effect of a large increase in λ_c during the daytime and at noon, respectively. However, this also exhibited a slightly larger nocturnal warming effect. The amount of sensible heat flux emitted by the SW façade accounts for most of the total emitted by the façades, while that emitted by the NE façade accounts for the least. The α modification plays the main role in influencing Q_H for most of the façades, whereas for the NE façade, the reduction in Q_H at noon is dominantly driven by a largely increasing λ_c and C_a, which are more than twice of and obviously more than the effect of the largely increasing α, respectively.

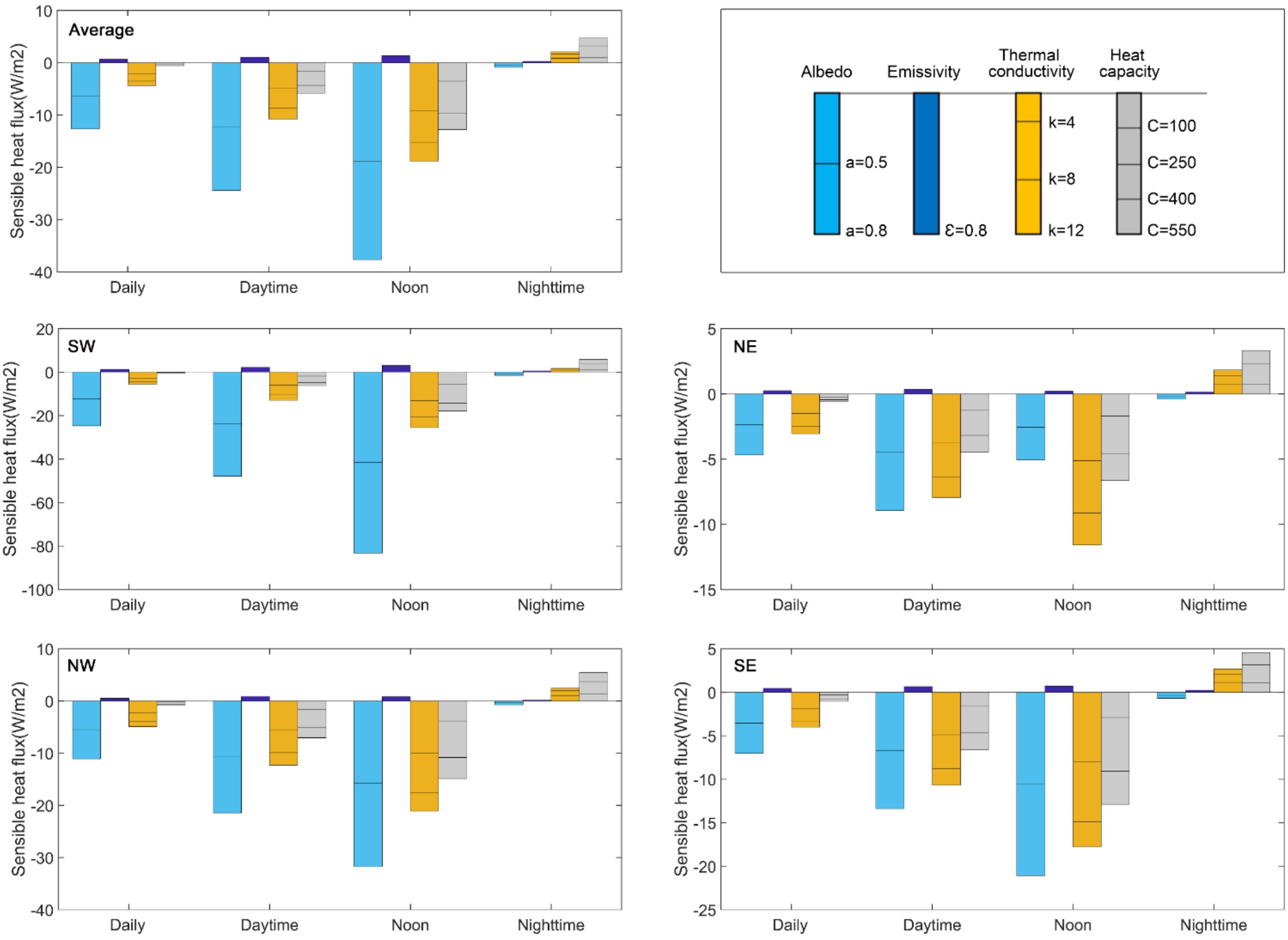

Figure 8. Simulated Q_H released by façade

4.2 Combined modifications of thermal properties

Fig. 9 shows the simulated accumulated and combined effects of modifying the thermal properties on the emitted sensible heat fluxes. The cases are listed in Table 3. As shown in Fig. 9, a nonsignificant difference is illustrated between the combined effect and the accumulated effect for the daily average reduction of Q_H released by building surfaces. For the roof, the combined effects of C1-R and C2-R are separately 18% and 26% higher than the accumulated ones in reducing the daytime Q_H, whose ratios increase to 31% and 38% at noon, respectively. Their nocturnal warming effects are 58% and 55% higher, respectively. For the wall (C1-W and C2-W), the daytime combined cooling effects are separately 40% and 46% higher than the accumulated ones, and their ratios remain similar at 41% and 49% at noon, respectively. Their nocturnal combined warming effects are 63% and 80% higher, respectively.

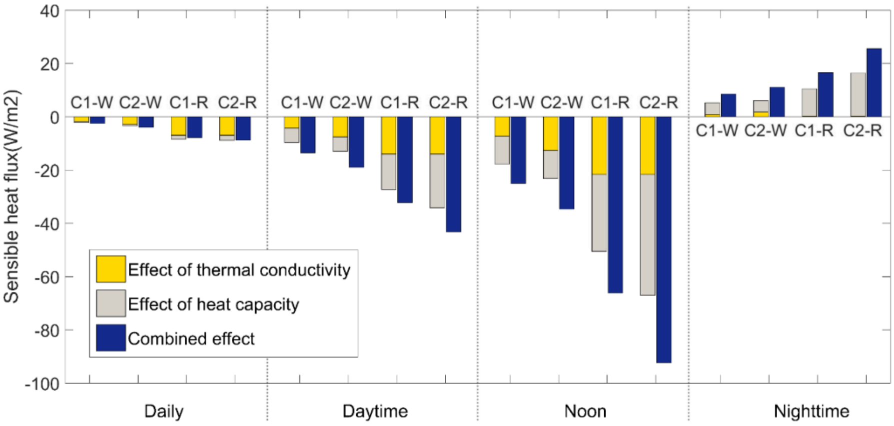

Figure 9. Simulated accumulated and combined effects on Q_H

In addition, as shown in Fig. 10 (left), in summer, the combination of H2-W with a relatively low thermal conduction of 1 $Wm^{-2}K^{-1}$ and medium heat capacity of 250 $Jm^{-2}K^{-1}$ showed a similar performance on the hourly surface temperature and its temporal variation as T1-W with a medium thermal conduction of 4 $Wm^{-2}K^{-1}$ and relatively low heat capacity of 50 $Wm^{-2}K^{-1}$. However, the surface temperature difference turned larger by about 0.2-0.3 ºC at night with a Whereas, in winter, T1-W revealed an obviously higher surface temperatures than the H2-W with an average of about 1.3 ºC and up to about 2 ºC.

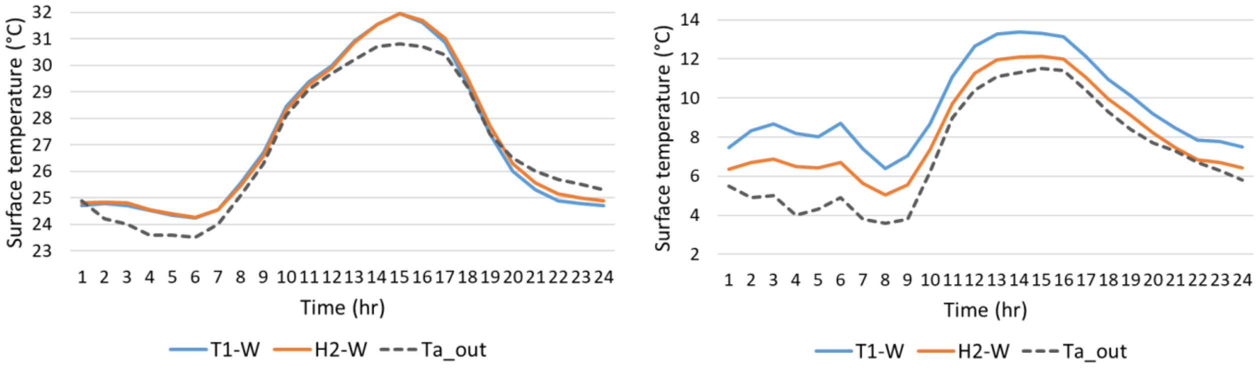

Figure 10 Simulated combined effects as a compromise in summer (left) and an accumulation in winter (right) on surface temperatures

4.3 Impact of thermal properties on cooling effects of high-albedo roof

Fig. 11 shows the results after applying high-albedo strategies to the roofs with various combinations of thermal properties. The effects of a high-albedo strategy on Q_H are shown as the lower scatters (Table 4, calculated by the M*i* Q_H to minus corresponding B*i* Q_H), and the effects of the thermal properties are shown as the upper scatters (Table 4, calculated by the M1–10 Q_H to minus M1 Q_H). As shown in the lower scatters, nonnegligible differences of Q_H exist among 10 typical roof constructions when applying a high-albedo coating. M1-R, with the smallest λ_c and C_a, shows the best effect after applying a high-albedo strategy to reduce the daytime Q_H, whereas the worst daily effect appears for M10-R. The worst daytime effect appears in M8-R with the median λ_c (5/11 W m^{-2} K^{-1}) and C_a (300/550 kJ m^{-2} K^{-1}).

The maximum daily, daytime, noon, and nighttime Q_H reductions are 14 (15%), 26 (15%), 66 (23%), and 14 Wm^{-2} (344%) larger than the minimum ones, respectively. Meanwhile, their standard deviations, compared to the mean values of the 10 cases, are 10, 14, 21, and 5 W m^{-2}, respectively. On the other hand, as shown in the upper scatters, M1-R shows the worst daytime performance contributed by the thermal properties, while the largest daily and daytime cooling effects appear in M10-R and M8-R, respectively.

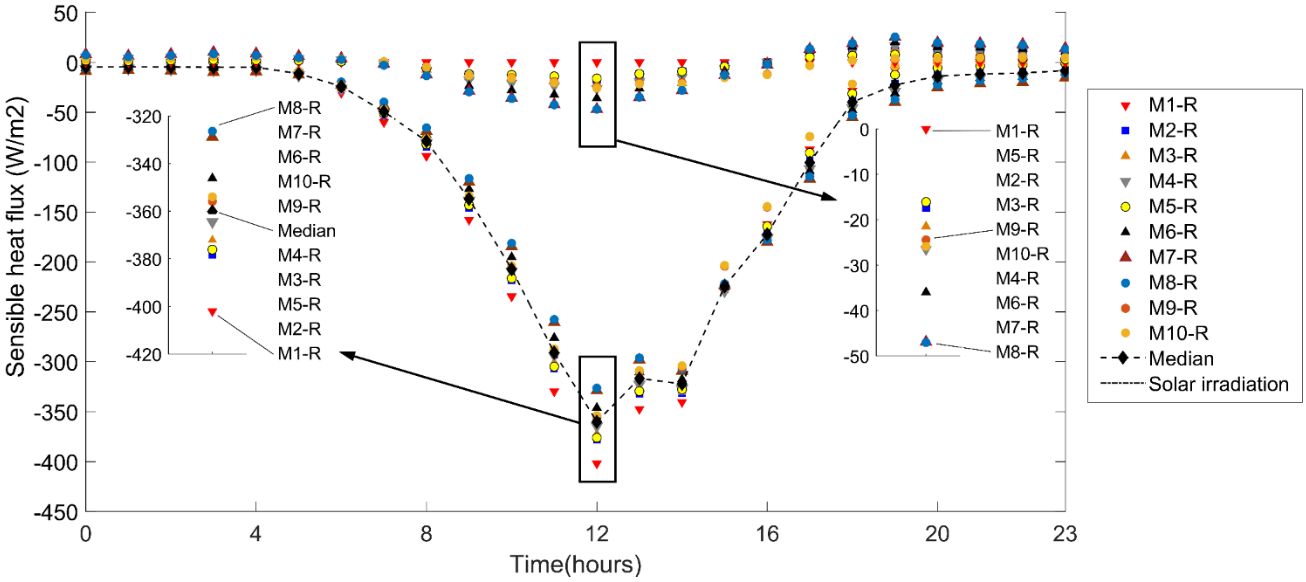

Figure 11. Effects on Q_H owing to high-albedo strategy (lower scatters) and owing to various combinations of thermal properties (upper scatters)

5. Discussion

5.1 Effect of individual modification of thermal properties

The results in section 4.1.1 reveal that the thermal performance of a roof depends on thermal and optical properties, and the determinant one is the albedo. This confirms the potential of a high-albedo roof for UHI mitigation in temperate zones during the summer [98]. Compared to the albedo, modifying a roof's thermal properties has only a limited effect in cooling the surface. This is in agreement with a pavement modification case by Yang et al. (2016) [39]. Because the ground and roof are both horizontally exposed to receive a large amount of direct solar radiation in the summer. However, the studied thermal property values in Yang et al.'s case are specific: the increase in λ_c is only 3 W m^{-2} K^{-1} but reaches 630 kJ m^{-2} K^{-1} for C_a.

However, a more systematic and objective selection of the thermal property values here leads to an improvement in the universality of the study, and suggests that the studied thermal properties within a typical practical range do not affect the findings. On the other hand, the cooling effects when increasing the thermal conductivity and heat capacity cannot be negligible for the heat transferred to the atmosphere. This may lead to a risk that as well accepted, an increase in the thermal conductivity of a building surface leads to a greater energy consumption for the cooling and heating loads. However, as concluded by Gagliano et al. (2015), to further improve the thermal insulation (i.e., to further lower the thermal conductivity), besides a first insulation layer, does not provide considerate effects on indoor energy savings but worsens the environmental thermal stress [104].

This is similar to one of our findings: that an initial increase in thermal conductivity (from 1 to 4 $Wm^{-2}K^{-1}$) provides a greater effect to reduce the heat released to the atmosphere, compared to a further increase in the thermal conductivity (from 4 to 8 $Wm^{-2}K^{-1}$, and from 8 to 12 $Wm^{-2}K^{-1}$). Hence, it is largely possible to obtain a compromise in the thermal conductivity modification between the performances of the environmental thermal stress and building energy consumption. Unlike the results for the roof, those shown in section 4.1.2 demonstrate that the thermodynamic behavior of most façades is not solely determined by the albedo, but the surface cooling abilities of modifying the thermal conductivity and heat capacity are secondary.

As an exception for the NE façade, which receives the least solar radiation, a thermal conductivity modification plays the main role and is followed by modifying the heat capacity to reduce the emitted sensible heat flux. This can be more than twice that and obviously more than that owing to the albedo modification. An increase in thermal properties releases more sensible heat fluxes during the night; however, accounting for their larger mitigation effects during the daytime, their average daily sensible heat fluxes emitted to the atmosphere are reduced. To be more specific, the daytime surface cooling effect of an albedo modification largely depends on the façade orientation [Fig. 7 (a)], and its ability to reduce the peak temperature for the same façade can be widely different owing to the peak formation [Fig. 7 (a) for the NE façade]. By contrast, the daytime surface cooling benefit of modifying the heat capacity and thermal conductivity do not significantly depend on the façade's orientation.

Similarly, in future studies, a wall modification by increasing its thermal conductivity also needs a discussion of the trade-off relation between the cooling effect for the surrounding atmosphere and the building cooling load.

5.2 Effect of combined modification of thermal properties

The results in section 4.2 reveal that increasing the heat capacity and thermal conductivity at the same time appears to enlarge their individual abilities to cool surfaces during the daytime, and remain close cooling effects to the control case for the daily average. However, the enlarging scales (130%–150% at noon) reveal variables among the various combined modification cases. This may be caused by the balance between the ability to conduct thermal energy and the heat storing ability of a building surface. The effects and risks of individually increasing the thermal conductivity were discussed above. However, appropriately increasing the thermal conductivity can be a powerful aid when enlarging the daytime cooling effect by increasing the heat capacity for building surface modification.

As shown in Fig.10 (left), the combined effect of modifying both thermal conductivity and heat capacity can cause a compromise due to the warming effect of decreased thermal conductivity and the cooling effect of increased heat capacity in summer, and vice versa. However, as shown in Fig.10 (right), due to the opposite effect, a cooling effect, of the decreased thermal conductivity in winter, the accumulated cooling effects of the decreased thermal conductivity and increased heat capacity caused their combined effect as a compromise in summer disappeared. The main reason causes the large difference occurs in opposite seasons is due to the extra cooling/heating source in terms of the season provided by the air conditioning, and the larger air temperature difference along with the indoors and outdoors in winter. If there is no extra cooling/heating source, this large difference may not occur in the winter season because of the same heat diffusivity in two seasons.

5.3 Impact of thermal properties on effect of high-albedo strategy

The results in section 4.3 indicate that during the daytime, the surface cooling effect of a high-albedo strategy (lower scatters, Fig. 11) applied to roofs with various thermal properties is almost negatively correlated to the cooling ability of the thermal properties (upper scatters, Fig. 11). This is especially obvious around noon (Fig. 11), and implies that applying a high-albedo strategy reduces more daytime heat to the atmosphere when the daytime cooling effect contributed by the thermal properties of the roof surface is lower. In other words, the daytime cooling effect of the combination of thermal properties appears to be higher when the albedo contributes less.

Y. Yang et al. (2018) concluded that heavyweight roofs with higher λ_c applied to a high-albedo strategy reveal a higher mitigation than lightweight roofs with lower λ_c [105]. Our finding corresponds with Y. Yang et al.'s results, and we further explore this with a combination of thermal properties. The relatively balanced combination of thermal properties (e.g., M8-R, M7-R, and M6-R) shows a higher daytime cooling ability than the unbalanced ones (e.g., M10-R, M9-R, and M4-R). This also confirms that the combined cooling effect is crucially influenced by the balance condition to conduct thermal energy and heat storing ability, as discussed in section 4.2.

On the other hand, the largest difference between the Q_H reductions among typical roof constructions (maximum: M1-R; minimum: M8-R) for the daytime, noon, and summer season are 26 W m^{-2}, 66 W m^{-2}, and 30 kWh m^{-2} y^{-1}, respectively. According to Y. Yang et al. (2018), the difference can be much larger for a tropical climate, in which the maximum reduction of a cool surface applied on a higher-λ_c roof reaches about 500 W m^{-2} higher than the minimum one during 11:00–17:00 [105]. These can be regarded as possible errors when estimating the potential effects of applying a high-albedo strategy owing to the ignorance of the thermal properties. This may lead to a different decision regarding a solution for optimal UHI mitigation.

For example, compared to the green roofs, the cool roofs with assumed U-values were verified by V. Costanzo et al. (2016) to be preferred when minimizing the released heat flux [15]. These results showed that the reductions in the summer by cool roof-1 (0.65 in reflectance) and cool roof-2 (0.8 in reflectance) were close and about 50 kWhm^{-2}y^{-1} higher than the performance of a green roof. The error caused by ignoring the influence of the U-values in their study may have significantly affected the results. The above comparative discussions highlight that the impact of the thermal properties on estimating the cooling effect of a high-albedo surface strategy cannot be ignored. An accurate effect estimation prior to decision-making among potential solutions will support the development of tailored solutions to minimize the UHI effect.

5.4 Impact of thermal properties on sensitivity and error of SEB modeling

The results in section 4.1 also reveal the sensitivity of the simulated T_s to the thermal properties. For the SOLENE model, the sensitivity to the albedo for walls is 1–2 K/0.1 ($\Delta\alpha$) at noon during the summer [8]. As shown in Fig. 9, the sensitivity to albedo for the walls in our study, which appears to be lower, is up to 0.43 ºC/0.05 ($\Delta\alpha$)

(1/12 of the civil engineering range) for the SW façade at 14:00, and much lower at 0.1 ºC/0.05 ($\Delta\alpha$) for the NE-façade peak value. The sensitivity to a $\Delta\lambda_c$ of 1 $Wm^{-2}K^{-1}$ (1/11 of the civil engineering range) and a ΔC_a of 50 $kJm^{-2}K^{-1}$ (1/10 of the civil engineering range) are both close to 0.1 ºC, and the difference owing to the orientation is slight. This is close to the sensitivity to α for a shaded façade. In terms of the roof at 12:00 (Fig. 7), the sensitivity to λ_c and C_a is about 1/3 and 1/5 of that to α (1.5 ºC/0.05). To conclude, even when the simulated surface temperature is more sensitive to the albedo, its T_s sensitivity to the thermal properties is nonnegligible.

The results in section 4.3 were used to estimate the error of the simulated Q_H caused by assuming and generalizing the thermal properties. The simulated Q_H released by typical roofs with albedos of 0.2 and 0.8 are shown at the left and right of Fig. 12, respectively. The proportion of the largest difference among high-albedo roofs is larger than that among the low-albedo cases, and can be used to estimate the largest error percentage. As the albedo increases, the solar irradiation absorbed by the surface decreases, resulting in a Q_H that is more sensitive to thermal properties.

Two extreme scenarios were assumed: the assumed thermal properties agreed with the actual, and the opposite assumption (assuming B/M1-R for the actual B/M8-R) caused maximum errors of 18(67%), 44 (96%), and 90 W/m^2 (72%) for the daily, daytime, and noon observations, respectively (Table of Fig. 12).In addition, a more realistic scenario was assumed, i.e., the input thermal properties were generalized to be a typical combination from the database for the roof (section 2.4.1). Meanwhile, the actual properties were also from the database, with an equal amount of each typical combination. The maximum RMSE appears when a combination with an extreme Q_H is assumed (dashed line in Fig. 12), while the minimum appears with a median Q_H (dashed-dotted line in Fig. 12).

Since the typical albedo range is 0.2–0.8, the RMSE ranges of low- and high-albedo cases can be regarded as those for SEB modeling caused by generalizing the thermal properties on a clear summer day for a temperate climate. As shown in the table of Fig. 12, the daily, daytime and noon RMSEs are 1.4–12.1 (6%–41%), 5.4–29.6 (7%–50%), and 10.7–57.6 W/m^2 (7%–38%), respectively. It can be inferred that a larger error may appear for a wall because its Q_H is more sensitive to thermal properties, as discussed in section 3.1, especially for a façade receiving little solar radiation. These findings indicate that the selection of thermal properties for SEB modeling is key to the simulation quality and reliability [20] with a quantitative estimation.

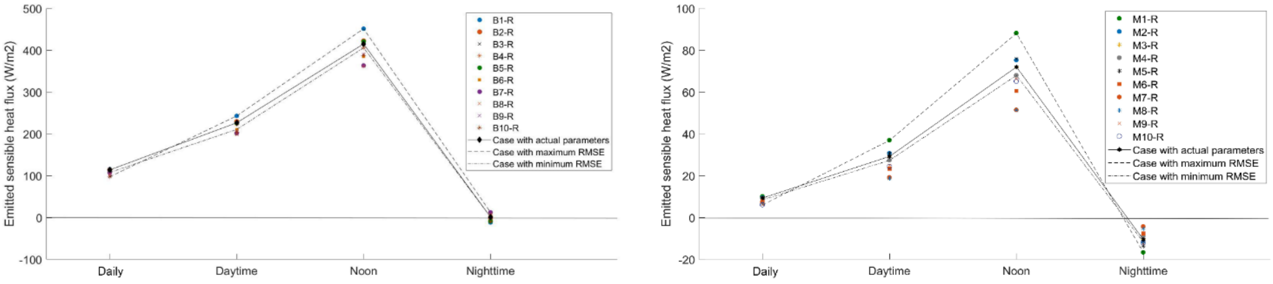

	Evaluation	**Daily**	**Daytime**	**Noon**
Extreme scenario: (assume B8-R for the actual B1-R)	Maximum error (W/m^2)	**18**	**44**	**90**
	Maximum error percentage (%)	**19**	**22**	**25**
More realistic scenario: (generalized to be a common-used combination among B1-R~B10-R)	Maximum RMSE (W/m^2)	**12.1**	**29.6**	**57.6**
	Maximum percent RMSE (%)	**12**	**12**	**13**
	Minimum RMSE (W/m^2)	**6.2**	**15.1**	**28.5**
	Minimum percent RMSE (%)	**6**	**7**	**7**

	Evaluation	**Daily**	**Daytime**	**Noon**
Extreme scenario: (assume M8-R for the actual M1-R)	Maximum error (W/m^2)	**4.1**	**18.1**	**36.7**
	Maximum error percentage (%)	**67**	**96**	**72**
More realistic scenario: (generalized to be a common-used combination among M1-R~M10-R)	Maximum RMSE (W/m^2)	**2.5**	**11.7**	**23.3**
	Maximum percent RMSE (%)	**41**	**50**	**38**
	Minimum RMSE (W/m^2)	**1.4**	**5.4**	**10.7**
	Minimum percent RMSE (%)	**17**	**20**	**16**

Figure 12. Simulated QH by typical roof components with albedo of 0.2 (left) and 0.8 (right), and quantitative difference measures with assumed and generalized thermal properties in terms of error, error percentage, RMSE, and percent RMSE

6. Summary

A measurement-to-simulation comparison was carried out to validate an SEB-based model THERMORender. The results showed good agreement, especially for shadow-sunlight transitions. With an RMSE of 1.33 and an MAE of 1.09, this was allowed to be used in this chapter as a reliable model.

A simulation was performed on a typical summer day in order to estimate the effects of thermal property modifications of urban surfaces (roofs and walls) on surface temperatures and emitted sensible heat fluxes to the atmosphere, compared with those of optical property modifications, and to explore their impact on the evaluation of a high-albedo strategy applied to a roof.

The studied parameters input to the simulations were crucial in determining the practicality and objectiveness of the results. An important contribution was the appropriate selection of the input thermos-physical properties for surface materials, based on a database established here to characterize the regular thermal properties of commonly used surface materials for building walls and roofs in urban areas in Japan. The main findings are as follows:

a) Compared to albedo modification, the effects of individual modifications of thermal properties were limited for the roof but nonnegligible for wall surfaces. For wall surfaces, the cooling effects of increasing thermal conductivity and heat capacity within an civil engineering range were close to and above 50% of the effects of an increasing albedo of 0.3 during the daytime, respectively.

b) The appropriate combined modification of thermal properties can enlarge the accumulated cooling effects of individual modifications. At noon, the cooling effect of the combined modification reached 30%–50% higher than that of the accumulated modifications. In the other hand, the combined modification of thermal properties can also reduce or even eliminate their single effects, which depends on how to modify the thermal properties. However, this combined effect would not be a compromise but an accumulated cooling or warming effect in the opposite season, and vice versa.

c) Roof thermal properties should be considered when evaluating the cooling effect of high-albedo coatings applied to existing roofs. When cool coatings (increased albedo of 0.6) were applied to roofs with various typical combinations of thermal properties, the maximum reductions of the emitted sensible heat fluxes for the daily, daytime, and noon observations were 14 (15%), 26 (15%), and 76 W m^{-2} (23%) higher than the minimum ones, respectively.

The above simulation results were used to estimate the sensitivity of the surface temperature to the thermal property and the error range of the simulated sensible heat flux to the atmosphere, which is determined by the assumption and generalization of the thermal properties for the roof surface. The main findings were obtained as follows:

d) Even when the simulated temperature is more sensitive to the albedo, its sensitivities to the thermal properties are nonnegligible. For shaded façades, sensitivity to the thermal conductivity and heat capacity is close to the sensitivity of the albedo; meanwhile, they are up to about 1/3 and 1/5 of the sensitivity to the albedo for the roof, respectively.

e) The significance of the error caused by the assumption depends on the difference between the assumed and actual thermal properties. In addition to the extreme scenarios of correct and opposite assumptions, the RMSE ranges of the predicted sensible heat fluxes caused by the generalization of the daily, daytime, and noon observations were 6%–41%, 7%–50%, and 7%–38%, respectively.

As a summary, first, the results of this chapter indicate that urban surface thermal properties are important to study urban surface-atmosphere heat exchange which error caused by their assumption and generalization cannot be ignored in SEB model-based simulations. It thus proves the importance to estimate actual thermal properties of building surfaces for SEB modeling. Second, the sensitivities of SEB-based simulated Ts to thermophysical properties are estimated and analyzed, providing quantitative supports for the further development of the estimation method: (a) determining the acceptable error for estimating albedo (0.03 as albedo error causing a ΔT_s of about 0.1 ºC); (b) providing possible accordance to conduct clustering for typical combinations of thermal properties (1/4 and

1/3 of civil engineering range of λ_c and C_a *causing a* ΔT_s of 0.3 ºC, however, a finer clustering was conducted in Chapter 4 in order to explore the sensitivities of the developed estimation method). Third, the effect of emissivity within civil engineering range is negligible compared with other thermophysical properties (albedo, thermal conductivity, and heat capacity), supporting the assumption of emissivity in the estimation method developed in this thesis. Last but not the least, combination may compromise the effect of individual modification of λc and Ca, but this combined effect would not be a compromise but an accumulated cooling or warming effect in the opposite season, and vice versa, revealing the possible problem (two very different combinations of thermal properties showing similar performance on surface temperatures, which cannot be distinguished) and potential solution (to conduct measurement once more in opposite season) of the estimation method developed in this thesis.

CHAPTER 3: ESTIMATION ON TOTAL SHORTWAVE ALBEDO OF BUILDING SURFACES BASED ON MULTISPECTRAL REMOTE SENSING

1. Introduction

As introduced in Section 2.1 of Chapter 1 and further evaluated by simulated results (Fig.5 and 7) in Chapter 2, albedo could be a driving factor of the surface energy balance (SEB) [1,30], especially for the building surfaces receiving a high solar radiation. The first step to develop the estimation method on thermophysical properties of building surfaces in this thesis is to obtain the urban surface albedo.

Albedo and reflectance can be obtained in situ using pyranometers and spectroradiometers[46–48]. Satellite remote sensing (RS) techniques have been widely applied for estimating land surface albedo[40–42]. However, while studying the urban microclimate at local and neighborhood scales, in-situ "point" measurements and satellite RS have their limitations. The former is time-consuming, labor-intensive, provides limited points of each surface, and cannot easily access certain surfaces (e.g., roofs), whereas the spatial resolution of the latter is not sufficient (e.g. even with Sentinel 2, which has a 10 m spatial resolution[25,26], small structures show mixed pixels[27]). A few studies have contributed in filling a gap between ground measurements and satellite RS by airborne (e.g., aircraft and airships) RS, such as the study on the high spatial- and spectral-resolution hyperspectral airborne data to estimate broadband albedo[106]. However, airborne RS requires high labor and financial cost[28], and there is a lack of vertical surface data[29]. Rapid development of unmanned aerial vehicles (UAVs) equipped with spectral cameras has enabled obtaining both horizontal and vertical urban surface albedo with fine spatial resolution to further bridge the gap between in-situ and spaceborne/airborne observations. Few studies recently applied UAV-based hyperspectral RS to retrieve land surface albedo[107]. Satellite and airborne hyperspectral RSs with sophisticated sensors like Airborne Hyperspectral Scanner (AHS) are applied in a broad range of fields like agriculture and forestry[108], but the UAV-hyperspectral RS is in its early stages and is yet to become widespread due to its high cost (>100,000 USD) and operational issues (limited flight duration due to the heavy weight and battery performance, and geometric correction) [109]. Although consumer-grade digital cameras are inexpensive and easy-to-operate, they are inadequate for accurately estimating the total shortwave (SW) albedo due to the lack of near infrared (NIR) bands[27,110]. Compared to the UAV-hyperspectral- and consumer-grade digital camera, a multispectral camera is relatively inexpensive, robust, and widely used, thus achieving an applicability–cost balance[110]. Multispectral images provide the surface reflectance at limited bands with narrow-wavelength bandwidths in each pixel and depend on the spectral responses of camera channels (e.g., 5 bands for a RedEdge camera). However, monitoring surface energy budget and modeling their efforts require broadband albedos[111], such as the total SW albedo that is crucial to SEB modeling[20,112]. Therefore, estimating broadband albedo from narrowband spectral reflectance at the sensor viewing angle is critical, and requires three processes in general[27,113,114]: (1) radiometric calibration converting digital numbers to surface directional reflectance, accounting for atmospheric and solar conditions as well as sensor noise (response of the photo-sensitive items is included), (2) surface bidirectional reflectance distribution function (BRDF) modeling to convert surface directional albedo at the viewing angle into hemispheric albedo, and (3) narrow-to-broadband (NTB) conversion of albedo. Though it is ideal to conduct the BRDF modeling[115,116], it requires measurements at multiple illuminations and multi-angular observations, involving elaborate preparation and post-processing[116–118]. The study of Nakaohkubo et al. (2008)[119] has demonstrated that the reflections of many materials commonly used for the building surface, including wooden slat, sand tile, asphalt, ceramic siding, cement board (flat/textured surface), and granite polished by burner, are near isotropic when incident angle of illumination is not very large. It is unnecessary to adopt the BRDF modeling for heterogeneous surfaces[26,27], and it is common to assume the target surface as Lambertian and that the reflectance is near isotropic from different viewing and solar/illumination angles[27,120]. Hence, in this paper, we focused on the third process, NTB conversion, following the same assumptions as those for isotropic reflection.

The models for NTB conversions for spaceborne sensors have been widely proposed and improved over the years, such as the Advanced Very High Resolution Radiometer (AVHRR)[41,121–123], Advanced Spaceborne Thermal Emission and Reflection Radiometer (ASTER)[41], Landsat-7 Enhanced Thematic Mapper Plus (ETM+)[41], Moderate Resolution Imaging Spectroradiometer (MODIS)[41,115,124,125], Sentinel-2A[26,126], and Visible Infrared Imaging Radiometer Suite (VIIRS)[124,127,128]. Liang explored the easy-to-use NTB model for universal application over different surface cover types for common sensors by regressing the conversion coefficients based on extensive radiative transfer simulations and spectral reflectance database[41,113]. A further conversion, proposed by Tasumi et al. [125], utilized a physics-based approach to integrate narrowband reflectance viewed at nadir with weighting coefficients representing the solar radiation fraction within each sensor spectral band. Recently, a few studies retrieved broadband albedo from Sentinel-2 Multispectral Instrument (MSI) bands with a 10 m pixel size using the same coefficients as those for ETM+ proposed by Liang[41], whereas Li et al. [126] calculated the NTB coefficients for Sentinel-2 MSI based on Liang[41]'s regression strategy. Bonafoni et al. [26] compared the model using Li et al. [126]'s coefficients and the one based on Tasumi et al [125].'s physics-based strategy.

UAV-based RS has been studied only recently as an alternative to estimate albedo [27,120]. Cao et al. [27] directly adopted Landsat 8 NTB coefficients, as provided by Wang et al.[115], using a consumer-grade digital camera on board a UAV. Appropriate NTB conversion models are needed for UAV-based multispectral cameras as directly adopting existing NTB coefficients would be difficult due to the different bandwidths and central wavelengths of the sensor channels (Fig.1), and the existing models developed for satellite/high-altitude observation and large homogeneous rural/vegetated/snow zones may not be suitable for local and neighborhood scales and to the urban complex texture. Meanwhile, an advantage of UAV-based observation is the capture of vertical surface data, which brings more uncertainty in adopting the existing models developed solely for horizontal surfaces.

The aim of this chapter was to obtain NTB conversion models for UAV/ground-based multispectral cameras and urban surfaces. Based on the measured spectral reflectances of urban surfaces and simulated at-surface solar spectral irradiances under various conditions (season, solar zenith angle, and horizontal/vertical surface), we simulated datasets of extensive spectral albedos of urban surfaces. Based on the built datasets of various at-surface solar irradiances and spectral albedos, we developed three NTB conversion models following published methodologies (Model_reg following Liang[41], Model_phy following Tasumi et al.[125], and Model_phy_reg as an improvement of Model_phy) for three common UAV-based multispectral cameras for urban surfaces, and evaluated their performance as well as the camera capacity to estimate broadband albedo. In addition, the models' sensitivities to the solar conditions (season, solar zenith angle, and horizontal/vertical surface) and the surface material class were analyzed. These models were also validated using independent sample surfaces covered by different construction materials.

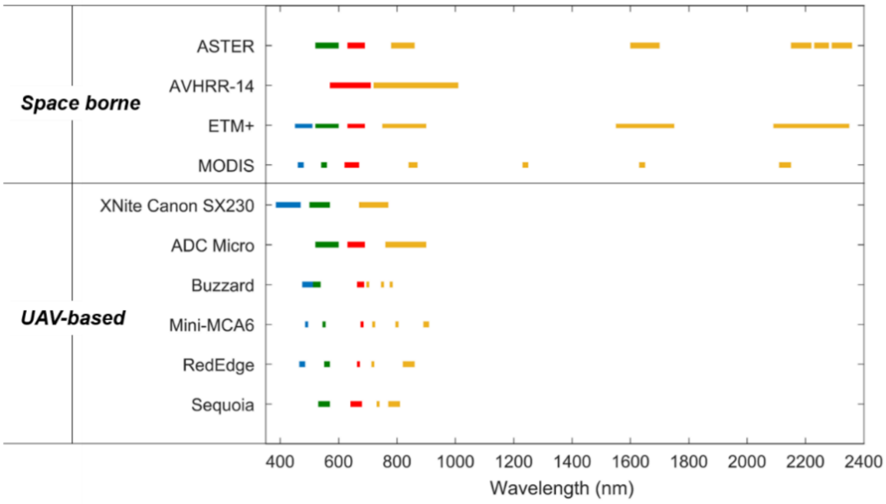

Figure 1. Spectral bands of commonly used spaceborne and UAV-based multispectral sensors/cameras.

2. Materials and Methods

2.1. Study cameras and urban surface materials

As shown in the lower part of Fig.1, UAV-based multispectral sensors can be categorized based on their bandwidths[110]: one with narrow spectrum range, such as the Mini-MCA6 (Tetracam Inc., Chatworth, CA, USA) with narrow bandwidths (bands 1–5 are 10 nm, band 6 is 20 nm), and the other with a wider spectrum range, such as the ADC Micro (Tetracam Inc., Chatworth, CA, USA) with a minimum bandwidth of 60 nm. The Mini-MCA6 has twice the number of bands as that of ADC Micro. Their typical characteristics are representatives of commonly used UAV-based cameras. In addition, the RedEdge (Rededge-M, MicaSense Inc., USA), which has a median band number and bandwidth between Mini-MCA6 and ADC Micro, was also studied.

ADC-Micro, Mini-MCA6, and RedEdge were thus selected for the study. Their bands, spectral ranges, and other main parameters are shown in Table 1.

Table 1. Main parameters of studied multispectral cameras.

Sensor	Blue band/B (nm)	Green band/G (nm)	Red band/R (nm)	Red-Edge band/RE (nm)	NIR band /NIR1 (nm)	NIR band /NIR2 (nm)	Resolution (pixels) /Weight (g)
ADC Micro	-	520–600	630–690	-	760–900	-	2018*1536/ 200
Mini-MCA6	485–495	545–555	675–685	715–725	795–805	890–910	1280*1024/ 700
RedEdge	465–485	550–570	663–673	712–722	820–860	-	1280*960/ 150

Concrete, asphalt, tile, wall coating, stone, brick, and wooden slat were selected as these are the commonly used building materials for urban surfaces in Japan[11,129].

2.2. Technical process

The technical process is shown in Fig.2, which also provides a workflow of developing the NTB conversion formulae and the steps for estimating broadband albedo through UAV-based multispectral imagery. The crucial step is building sample groups to develop conversion formulae and validate their applicability. This requires datasets of various spectral reflectance and at-surface solar spectral irradiance, as both narrowband and broadband albedos are not the sole measures of physical properties (e.g., absolute reflectance), but also depend on the atmospheric conditions through the at-surface solar fluxes, influencing the NTB conversion’s weighting function. Therefore, we measured spectral reflectance of various urban surfaces using a spectroradiometer from a nadir position (section 2.3.1 for details) and simulated the at-surface solar spectral irradiances under various conditions (section 2.4.1). Based on the obtained solar irradiance and spectral reflectances, the broadband and narrowband albedos were calculated (section 2.4.1 and 2.4.2) and segregated in two sample groups. Sample_D, composed of 2424 samples from 101 urban surfaces and 24 at-surface solar spectral irradiances (season, solar zenith angle, and horizontal/vertical surface), was used to develop three conversion models for each camera based on the published conversion strategies. Sample_V included 23 independent urban surfaces and was used to validate the conversion models. Meanwhile, in order to validate the models’ applicability to UAV-based multispectral imagery, the narrowband and broadband albedos of Sample_V were also derived from a RedEdge camera (section 2.3.2 and 2.4.3) and the conversion models (developed in section 3.3). The reason why not solely use the multispectral data for validating the models was to avoid the possible errors/biases caused by multispectral RS images (e.g., camera (radiometric aberration and camera setting), platform (whether the camera is pointing nadir and at the target), and the environment (sky, wind, and illumination conditions)[130]). The in-situ measurement, radiative transfer simulation, and related calculations are described in the following sections.

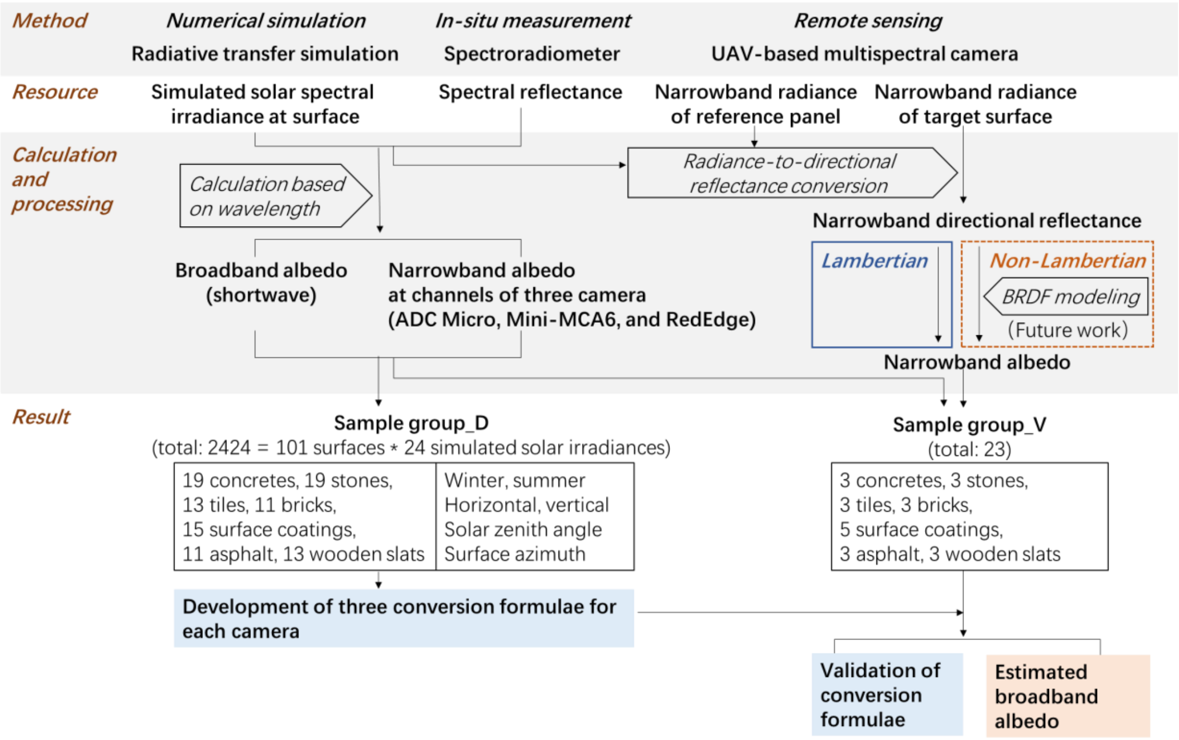

Figure 2. Technical process used to develop conversion models and to validate their applicability.

2.3. In-situ measurement and ground-based remote sensing

2.3.1. In-situ measurement of spectral reflectance

If the surface is tough without dominating three-dimensional structures and assumed to be Lambertian, the nadir-viewing reflectances are numerically equal to the spectral albedos[26,41,113,131]. The spectral reflectances of target surfaces were measured at nadir using a spectroradiometer (ASD FieldSpec4, ASD Inc., USA) under an artificial illumination and were adopted as spectral albedos. The ASD FieldSpec4 detects light continuously over the visible (VIS) and near-infrared (VNIR) to short-wave infrared (SWIR) wavelengths with a 25° field of view (FOV) and a spectral resolution of 3 nm at VNIR (350–1000 nm in wavelength) using a silicon detector, and 10 nm for two sets of SWIR bands, ranging from 1001–1800 nm and 1801–2500 nm, using a detector made of thermoelectric-cooled indium gallium arsenide (InGaAs). We conducted the measurements under an artificial illumination provided by an ASD Contact Probe (ASD Inc., USA) to reduce errors associated with stray light, allowing our measurements to be carried out at any time of the day.

The target surfaces comprised of 22 concrete, 22 stone, 16 tile, 14 brick, 20 surface coating, 14 asphalt, and 16 wooden slat coverings. Among them, 19 concrete, 19 stone, 13 tile, 11 brick, 15 surface coating, 11 asphalt, and 13 wooden slat surface specimens formed Sample_D as shown in Fig.3, and were measured in the central Nagoya city, Japan (Lat./Lon.: 35° 10’ 26’’ N/136° 54’ 28’’ E) in October, 2012. The other samples formed Sample_V, and were measured in a university campus in Yokohama city, Japan (Lat./Lon.: 35° 30’ 45’’ N/139° 29’ 04’’ E) during January–February, 2020. The mean spectral reflectance of the surface specimens within each material class for Sample_D was calculated as the typical spectral reflectance within each material class and is represented by black curves in Fig.3. We also measured spectral reflectance for a grey reference panel (RP, approximately 49% reflectivity, MicaSense Inc., USA) for calibrating the multispectral images.

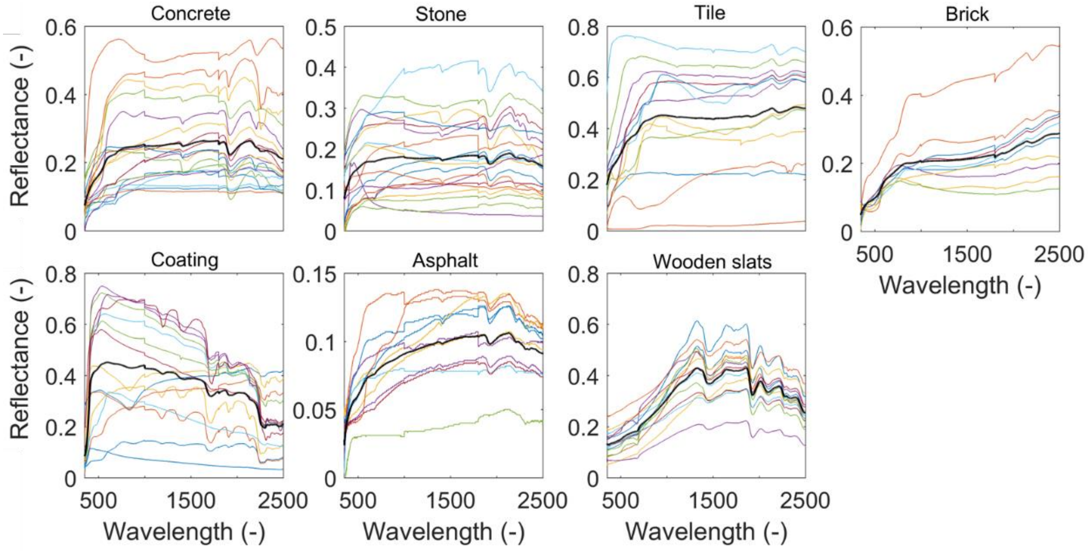

Figure 3. Spectral reflectances of urban surface specimens and the typical spectral reflectance within a single construction material class.

Fig.3 reveals that the spectral reflectance showed similar spectral variation within a single class, mainly due to similar chemical/mineralogical constituents. For example, concrete is composed of silica, carbonates, and a few other minerals. However, its spectral radiative response is dominantly driven by siliceous and calcareous minerals. As shown in Fig.3, regardless of the higher or lower reflectance in general, all SW spectra of the concrete class revealed an increase in reflectance up to 600 nm and a strong absorption at around 1950 nm. The latter indicates that H_2O is related to the absorption of the gypsum component, corresponding to Kotthaus et al.'s finding[132]. Asphalt is often used for road surfaces and comprises various natural bitumen composed of solid or semi-solid hydrocarbon mixtures, causing an increasing reflectance with longer wavelengths[133] (Fig.3). As shown in Fig.3, most tiles, which usually consist of clay-based ceramics, showed an increasing reflectance up to around 600/800 nm and absorption at around 1950 nm. As compared to the spectral reflectance of a single material class[132], most construction material classes showed similar spectral variation. However, certain spectral reflectance of the brick and tile in [132] showed different spectral features. These exceptions, mainly composed of concrete/cement, which exhibited similar spectral features as those of concrete. Thus, their spectral variation could additionally be captured by our NTB conversion models.

2.3.2. Ground-based multispectral remote sensing

Although we aimed to estimate broadband albedo using the UAV-base multispectral camera, as a first step, we used a handheld RedEdge camera and observed from the ground-level during the solar noon (11:00–15:00) of February 12–15, 2020 in the campus at Yokohama City, Japan. The experience of ground-based multispectral RS and developed workflow formed the foundation for the next step, the UAV-mounted observation. The camera was placed around 1 m just above the horizontal surface or far from the vertical surface, with the same orientation with respect to the sun as the target surface. In the meantime, the multispectral images of the RP were taken. Notably, RP was placed at the same position and orientation as the target surface to guarantee similar solar and observation angles and the illumination received as the target surface.

2.4. Calculation of broadband and narrowband albedos

2.4.1. Calculation of total shortwave albedo (broadband albedos)

The total SW wavelength range was selected as 350–2500 nm. This covered almost all the solar radiation at surface as the downward fluxes beyond this range were negligible. Based on the spectral albedo, the total SW albedos (α_{SW}) can be calculated by integrating the spectral reflectance (ρ) and multiplying the spectral irradiance of solar radiation (R_s) with the wavelength (λ_i) within the SW range.

$$\alpha_{SW} = \int_{350}^{2500} \rho(\lambda_i)\, R_s(\lambda_i)\, d\lambda \Big/ \int_{350}^{2500} R_s(\lambda_i)\, d\lambda \tag{1}$$

The Simple Model of Atmospheric Radiative Transfer of Sunshine software (SMARTS 2.9.5, National Renewable Energy Laboratory, US) offers fast and accurate predictions on how the distribution of solar power for each wavelength of light traveling from the sun is modified by atmospheric changes[134,135]. Users can construct text files with dozens of lines of text and numbers to specify input atmospheric conditions and to output simulated cloud-free spectral irradiances, including direct beam, hemispherical diffuse, circumsolar, and total on a tilted/horizontal receiver surface. The SMARTS model has been widely applied over a large number of scientific and technologic disciplines[136], and its performance was validated with typical differences within 2% when compared to the sophisticated models (MODTRAN, SBDART, COART, and LibRadtran), and mostly within 5% as the instrumental uncertainty when compared to spectroradiometric measurements[137,138]. Therefore, we used the SMARTS model to simulate cloud-free solar spectral irradiance at the target surfaces. The simulation for Sample_D was conducted by keeping the study site location and suggested UAV-based RS conditions (clear-sky and near solar noon (late noon for vertical surfaces)) fixed, while the season, solar zenith angle (SZA), and horizontal/vertical urban surface were varied (Table 2). As the rough surfaces like soils showed almost no changing values of albedo at SZAs lower than 75°[139], UAV-based RS is suggested in late solar noon for the vertical surface rather than the noon to avoid the high incident angle (> 75°) of the illumination with respect to vertical surfaces, which would not bring much error caused by the Lambertian assumption. The study site is located at 35° 30’ 45’’ N and 139° 29’ 04’’ E, where the SZA near summer noon (11:00–14:00) ranges between 0°–30° and is close to 40° for late noon (14:00–15:00). The winter near-noon (11:00–14:00) SZA is approximately 40°–70°, and 70°–80° around 15:00. The reference atmosphere for simulating was either mid-latitude winter or summer standard atmosphere with corresponding conditions (Table 2).

Table 2. The conditions used while simulating solar spectral irradiances.

Case	**Horizontal/ vertical surface**	**Season**	**Solar zenith angle**	**Surface azimuth (°)**	***Case***	**Horizontal /vertical surface**	**Season**	**Solar zenith angle**	**Surface azimuth**
Rs_1	Horizontal	Winter	40°	-	***Rs_13***	Vertical	Winter	70°	50°
Rs_2	Horizontal	Winter	50°	-	***Rs_14***	Vertical	Winter	70°	140°
Rs_3	Horizontal	Winter	70°	-	***Rs_15***	Vertical	Winter	70°	230°
Rs_4	Horizontal	Winter	80°	-	***Rs_16***	Vertical	Winter	70°	320°
Rs_5	Horizontal	Summer	0°	-	***Rs_17***	Vertical	Summer	30°	50°
Rs_6	Horizontal	Summer	10°	-	***Rs_18***	Vertical	Summer	30°	140°
Rs_7	Horizontal	Summer	20°	-	***Rs_19***	Vertical	Summer	30°	230°
Rs_8	Horizontal	Summer	30°	-	***Rs_20***	Vertical	Summer	30°	320°
Rs_9	Vertical	Winter	50°	50°	***Rs_21***	Vertical	Summer	40°	50°
Rs_10	Vertical	Winter	50°	140°	***Rs_22***	Vertical	Summer	40°	140°
Rs_11	Vertical	Winter	50°	230°	***Rs_23***	Vertical	Summer	40°	230°
Rs_12	Vertical	Winter	50°	320°	***Rs_24***	Vertical	Summer	40°	320°

The simulation input for Sample_V accounted for the ground-based RS dates (February 12–15, 2020) and duration (11:00–14:00), and the mid-latitude winter standard atmosphere was selected as the reference atmosphere, the SZA was set at 50°, and the surface tilt angle and azimuth were set according to the actual conditions (Table 3).

Table 3. Samples used for validation.

Sample	**Horizontal/Vertical surface**	**Surface azimuth**	***Sample***	**Horizontal/Vertical surface**	**Surface azimuth**
Concrete_1	Vertical	50°	***coating_1***	Horizontal	-
Concrete_2	Horizontal	-	***coating_2***	Horizontal	-
Concrete_3	Vertical	230°	***coating_3***	Vertical	140°
Stone_2	Horizontal	-	***coating_4***	Vertical	140°
Stone_1	Horizontal	-	***coating_5***	Vertical	320°

Stone_3	Horizontal	-	***Asphalt_1***	Horizontal	-
Tile_1	Vertical	50°	***Asphalt_2***	Horizontal	-
Tile_2	Vertical	230°	***Asphalt_3***	Horizontal	-
Tile_3	Vertical	140°	***Woodenslabs_1***	Horizontal	-
Brick_1	Horizontal	-	***Woodenslabs_2***	Horizontal	-
Brick_2	Horizontal	-	***Woodenslabs_3***	Horizontal	-
Brick_3	Horizontal	-			

2.4.2. Calculation of narrowband albedo based on spectral reflectance

The simulated solar irradiances and the measured spectral reflectances were normalized to have a 1 nm spectral resolution. The Nth narrowband albedo can be calculated by integrating spectral reflectances and solar spectral irradiance within the band spectral range corresponding to the ones captured by the study sensors, as shown in Eq. (2).

$$\alpha_N = \int_{\mathrm{a\_N}}^{\mathrm{b\_N}} \rho(\lambda_i) R(\lambda_i)\, d\lambda \Big/ \int_{\mathrm{a\_N}}^{\mathrm{b\_N}} R(\lambda_i)\, d\lambda \tag{2}$$

where α_N is narrowband albedo of the target surface, $\rho(\lambda_i)$ and $R(\lambda_i)$ are the surface spectral reflectance and at-surface solar spectral irradiance at wavelength λ_i (nm), respectively, and a_N and b_N are the lower- and upper-wavelength limits, respectively, corresponding to band N. For example, the RedEdge camera can capture narrowband albedos of five bands; band wavelengths are shown in Table 1 as 465–485 (Blue), 550–570 (Green), 663–673 (Red), 712–722 (Red-Edge), and 820–860 (NIR). These band wavelength limits were input into Eq. (2) to calculate the narrowband albedos.

2.4.3. Calibration of multi-spectral images to convert raw pixel values to albedo

RedEdge images were processed in Python3, OpenCV, numpy, matplotlib, and the standalone exiftool, and manipulated using Python wrapper, following the RedEdge user manual[140]. Optical and natural vignette, exposure, and row correction were conducted to convert raw pixel values to radiances. The calibration formula for calculating

the spectral radiance (L, W/m2/sr/nm) for the ith band is described in Eq. (3). The pixel and black level value were normalized by dividing their raw digital number by 2^N, where N is the number of image bits (e.g., 2^N=65536 for 16-bit images).

$$L_i(x,y) = V_i(x,y)\,\frac{a_{1,i}}{g_i}\,\frac{p_i(x,y) - p_{BL,i}}{t_{e,i} + a_{2,i}y - a_{3,i}t_{e,i}y} \tag{3}$$

where $V_i(x, y)$ is the vignette polynomial function for pixel location (x, y), $a_{1,i}$, $a_{2,i}$, and $a_{3,i}$ are radiometric calibration coefficients, $P_i(x, y)$ is the normalized raw pixel value for pixel location (x, y), $P_{BL,i}$ is the normalized dark level value, g_i is the sensor gain, $t_{e,i}$ is the image exposure time [s], and x and y are the pixel column and row number, respectively. The $V_i(x, y)$ can be described as:

$$V(x, y) = 1/(1 + k_{0,i}r_i + k_{1,i}{r_i}^2 + k_{2,i}{r_i}^3 + k_{3,i}{r_i}^4 + k_{4,i}{r_i}^5 + k_{5,i}{r_i}^6) \tag{4}$$

where $k_{0,i}$ through $k_{5,i}$ represent polynomial correction coefficients and r_i is the distance of the pixel (x, y) to the vignette centers, estimated using:

$$r_i = \sqrt{(x - c_{x,i})^2 + (y - c_{y,i})^2} \tag{5}$$

where $c_{x,i}$ and $c_{y,i}$ are the coordinates of vignette center for the ith band. The $L_i(x, y)$ can be calculated using Eqs. (3)–(5).

Different from the absolute reflectance retrieval given by RedEdge user manual, we conducted a radiance-to-directional reflectance conversion by calculating its calibration factor using the multispectral image of RP (Section 2.3.2) with known spectral reflectances (Section 2.3.1). After being converted into radiance using Eqs. (3)–(5), the RP directional reflectance in each band was calculated following Eq. (2) with band spectral ranges as input and simulated close-to-actual solar irradiance on RP (Section 2.4.1). The radiance-to-directional reflectance factor for the band i (F_i) is estimated as:

$$F_i = \rho_{\Omega i}/avg(L_{\alpha,i}(x1 - x2,\ y1 - y2)) \tag{6}$$

where $\rho_{\Omega i}$ is the directional reflectance and $avg(L_{p,i}(x1 - x2,\ y1 - y2))$ is the average radiance of the pixels inside the RP, $(x1 - x2,\ y1 - y2)$, for band i.

Multiplying the factor Fi converts all radiance values into the surface directional reflectance including the calibration of the spectral response of the camera channel for the i-th band. As the selected urban surfaces are quite rough, homogeneous, without dominating 3D structures, and the multispectral RS was conducted near midday (late midday for vertical surfaces) ensuring a relatively large solar elevation angle, we assumed them as approximately Lambertian surfaces. Their directional reflectances were thus numerically equal to the surface albedos. This process can be applied to each of the five bands individually.

2.5. Variable selection for the sensitivity analysis

Broadband albedo also depends on the solar conditions through downward fluxes influencing the weighting function of the NTB conversion. Gul et al. showed that the variation in albedo with changing cloud conditions (overcast, partly cloudy, and clear) for sand, cement slabs, and white tiles was less than 0.05 [141]. Liang et al. concluded that the broadband albedos are relatively stable unless the SZA is extremely large [41], and the asphalt surface albedo is not prone to solar elevation [113]. Considering the suggested near-solar noon time and clear skies for UAV-based RS, we did not investigate the developed conversion models' sensitivity to overcast skies, but analyzed their dependency to SZAs, the ranges for which were calculated for solar noon (late noon for vertical surface) in winter or summer. Accounting for the fine spatial resolution and accessibility to measure the vertical surface of UAV-based RS, the models' sensitivity to the construction material class and its applicability to the vertical surface albedo were also investigated. Therefore, season, SZA, horizontal/ vertical surface, and construction material class were selected to analyze model sensitivity.

3. Model development

3.1. Conversion model

The NTB conversion models for Sample_D followed published algorithms (Liang's [41] and Tasumi et al.'s [125]) to estimate the total SW albedo for ADC Micro, Mini-MCA6, and RedEdge.

3.1.1. Model by applying regression-based strategy (Liang's)

Using spectral reflectance database and radiative transfer simulations, Liang [41] investigated the coefficients for NTB conversion for typical spaceborne sensors using regressions derived from extensive sampling under various atmospheric and surface covers. The conversion models following Liang's strategy were established by the linear regression using the Least Squares Method named "Model_reg", and are shown in Eqs. (7)–(9).

- ADC Micro:

$$\alpha_{\_Mic\_reg} = 0.7028G - 0.4155R + 0.6222NIR + 0.009 \tag{7}$$

- Mini-MCA6:

$$\alpha_{\_MCA6\_reg} = 0.3668B - 0.0449G + 0.2183R + 0.2105RE - 0.5914NIR1 + 0.7708NIR2 + 0.0075 \tag{8}$$

- RedEdge:

$$\alpha_{\_RedE\_reg} = 0.3973B - 0.0102G + 0.0454R - 0.1017RE + 0.6116NIR + 0.0075 \quad (9)$$

3.1.2. Model by applying physics-based strategy (Tasumi et al.)

The other easy-to-use conversion models follow Tasumi et al.'s strategy[125] used for Landsat and MODIS data under cloud- and snow-free, low-haze conditions, and sensor viewing angles not more than 20°. For each study camera, the broadband albedo of target surface was estimated by integrating narrowband albedos across the SW spectrum as below.

$$\alpha = \sum \alpha_{\_N}\ w_{\_N} \quad (10)$$

where $\alpha_{\_N}$ is the albedo for Nth band and $w_{\_N}$ is the weighting coefficient, estimated as:

$$w_{\_N} = \int_{\mathrm{a\_N}}^{\mathrm{b\_N}} R(\lambda_i)\, d\lambda \Big/ \int_{350}^{2500} R(\lambda_i)\, d\lambda \quad (11)$$

where $R(\lambda_i)$ is the at-surface solar irradiance at wavelength λ_i (nm) and a_N and b_N denote the waveband range of band N. The conversion models following Tasumi et al.[125] are named "Model_phy", assuming that reflectances in the missing wavelength regions are estimated by linear interpolation of adjacent bands' albedos. The weighting coefficients listed in Table 4 are based on the simulated 24 at-surface solar irradiances (Table 2) and spectral ranges of camera channels (Table 1).

Table 4. Physical weighting coefficients for sensors and solar irradiance (Rs_i).

Sensor	**ADC Micro**			**Mini-MCA6**						**RedEdge**				
Variable*	***0.9141***			***0.9193***						***0.9282***				
Channel	***G***	***R***	***NIR***	***B***	***G***	***R***	***RE***	***NIR1***	***NIR2***	***B***	***G***	***R***	***RE***	***NIR***
Rs_1	0.3632	0.1462	0.4950	0.2197	0.1440	0.1208	0.0697	0.0892	0.3695	0.2157	0.1510	0.1076	0.0904	0.4459
Rs_2	0.3571	0.1472	0.4999	0.2153	0.1430	0.1207	0.0704	0.0912	0.3722	0.2113	0.1497	0.1077	0.0917	0.4503
Rs_3	0.3382	0.1477	0.5180	0.2039	0.1375	0.1185	0.0724	0.0964	0.3843	0.2000	0.1433	0.1059	0.0948	0.4668
Rs_4	0.3225	0.1438	0.5372	0.1998	0.1280	0.1121	0.0737	0.1012	0.3982	0.1957	0.1330	0.1003	0.0967	0.4847
Rs_5	0.3850	0.1515	0.4682	0.2333	0.1519	0.1265	0.0702	0.0907	0.3405	0.2291	0.1595	0.1127	0.0915	0.4184
Rs_6	0.3843	0.1515	0.4689	0.2329	0.1517	0.1264	0.0702	0.0907	0.3412	0.2287	0.1593	0.1126	0.0914	0.4191
Rs_7	0.3839	0.1517	0.4690	0.2325	0.1518	0.1266	0.0703	0.0909	0.3410	0.2283	0.1594	0.1127	0.0916	0.4191
Rs_8	0.3830	0.1522	0.4694	0.2317	0.1519	0.1268	0.0704	0.0914	0.3409	0.2275	0.1594	0.1130	0.0919	0.4194

Rs_9	0.6459	0.1233	0.2345	0.4828	0.1603	0.1100	0.0519	0.0598	0.1477	0.4741	0.1744	0.0963	0.0672	0.1992
Rs_10	0.3516	0.1503	0.5024	0.2068	0.1458	0.1236	0.0716	0.0923	0.3729	0.2030	0.1526	0.1102	0.0932	0.4520
Rs_11	0.3345	0.1513	0.5186	0.1914	0.1443	0.1238	0.0726	0.0941	0.3868	0.1878	0.1506	0.1106	0.0945	0.4674
Rs_12	0.6328	0.1283	0.2427	0.4654	0.1643	0.1145	0.0540	0.0621	0.1525	0.4570	0.1782	0.1003	0.0698	0.2060
Rs_13	0.6124	0.1301	0.2612	0.4518	0.1598	0.1127	0.0573	0.0670	0.1644	0.4431	0.1731	0.0990	0.0742	0.2221
Rs_14	0.2918	0.1541	0.5581	0.1578	0.1375	0.1227	0.0762	0.1022	0.4168	0.1548	0.1423	0.1099	0.0997	0.5042
Rs_15	0.2764	0.1544	0.5732	0.1448	0.1355	0.1224	0.0768	0.1037	0.4301	0.1420	0.1398	0.1097	0.1006	0.5187
Rs_16	0.5997	0.1347	0.2695	0.4357	0.1631	0.1166	0.0593	0.0693	0.1694	0.4272	0.1762	0.1025	0.0767	0.2290
Rs_17	0.6675	0.1247	0.2116	0.4953	0.1680	0.1143	0.0493	0.0573	0.1283	0.4867	0.1827	0.0997	0.0643	0.1778
Rs_18	0.6504	0.1321	0.2216	0.4714	0.1743	0.1210	0.0521	0.0605	0.1336	0.4632	0.1889	0.1056	0.0680	0.1859
Rs_19	0.3977	0.1523	0.4546	0.2426	0.1551	0.1280	0.0698	0.0897	0.3282	0.2382	0.1631	0.1139	0.0909	0.4052
Rs_20	0.5086	0.1439	0.3519	0.3422	0.1641	0.1254	0.0622	0.0770	0.2422	0.3362	0.1750	0.1107	0.0811	0.3085
Rs_21	0.6709	0.1232	0.2097	0.5006	0.1664	0.1127	0.0489	0.0569	0.1270	0.4918	0.1812	0.0982	0.0638	0.1762
Rs_22	0.6478	0.1331	0.2233	0.4685	0.1747	0.1217	0.0527	0.0612	0.1343	0.4602	0.1893	0.1063	0.0687	0.1872
Rs_23	0.3800	0.1544	0.4703	0.2261	0.1542	0.1289	0.0712	0.0921	0.3407	0.2220	0.1617	0.1149	0.0928	0.4199
Rs_24	0.4766	0.1472	0.3807	0.3128	0.1622	0.1269	0.0646	0.0811	0.2656	0.3072	0.1723	0.1122	0.0843	0.3354

Variable*: the value used to multiply the weighting coefficients for each camera in Model_phy_reg.

3.1.3. Conversion formulae by improving physically based methodology

After verifying the accuracy of Model_phy, we found that the estimated results were linearly correlated to the measured results, though the difference increased as the albedos increased (see Section 3.2 and Fig.4). To improve accuracy, we multiplied the weighting coefficients for each camera with a value of approximately 0.9 (second row of Table 4), calculated by the linear regressions without intercepts, and developed an improved model named" Model_phy_reg".

3.2. Performance evaluation

We used the SW albedos calculated by the measured spectral reflectance and simulated solar irradiance (Section 2.4.1) to evaluate the models developed (Fig.4) for the three cameras, with the measures of R-square (R^2), Root Mean Square Error (RMSE), Residual Standard Error (RSE), and Mean Bias Error (MBE) (Table 5).

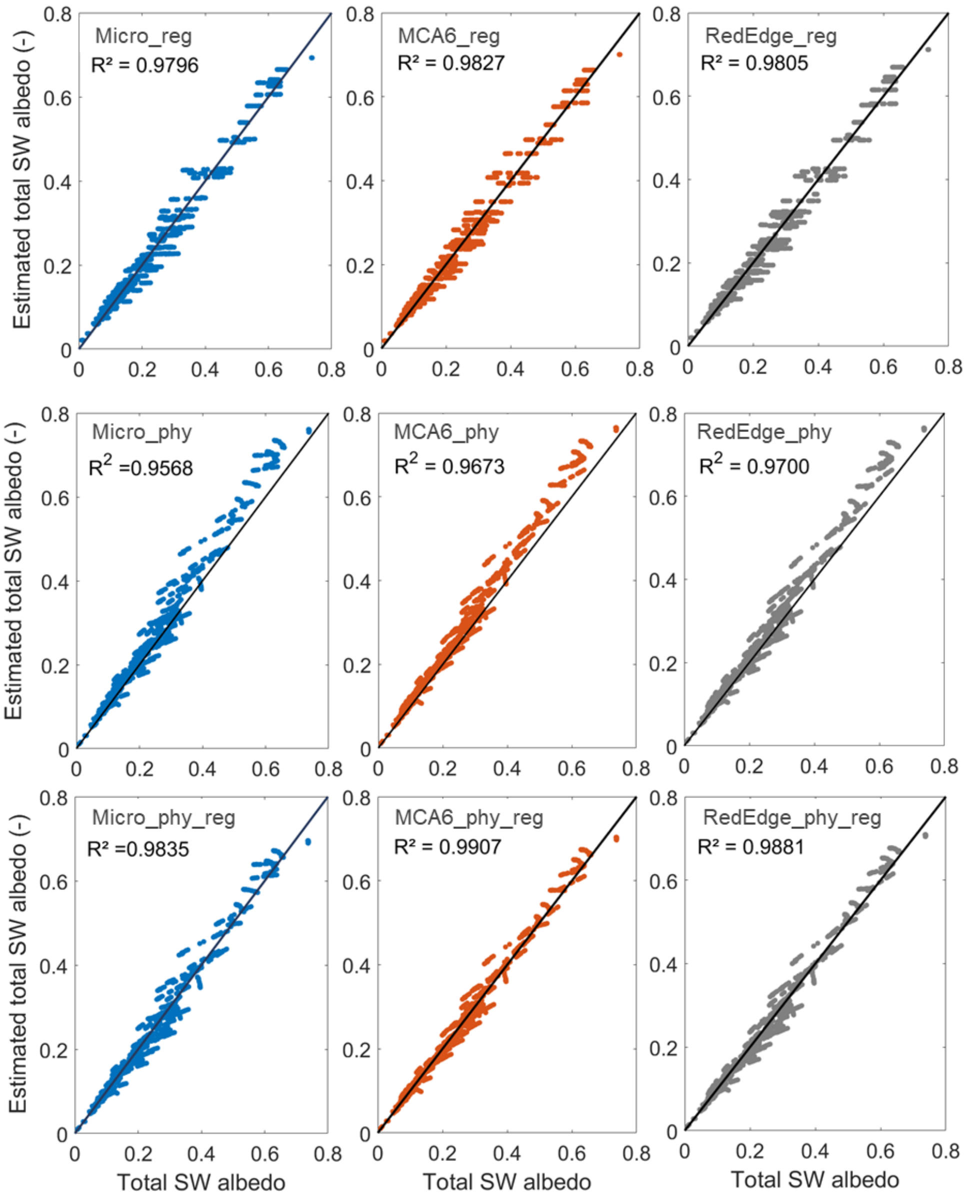

Figure 4. ASD measurement-based simulated total SW albedo (horizontal axis) and estimated values (vertical axis) retrieved by narrowband albedos of ADC Micro (first column), MCA6 (second column), and RedEdge (third column) applying Model_reg (first row), Model_phy (second row), and Model_phy_reg (third row).

Table 5. Measures of R^2, RMSE, RSE, and MBE.

		R^2	RMSE	RSE	MBE
Regression-based (Model_reg)	**ADC Micro**	0.9796	0.0227	0.0227	7.42691E−16
	Mini-MCA6	0.9827	0.0209	0.0209	4.29695E−16
	RedEdge	0.9805	0.0222	0.0222	5.70368E−16
Physically based (Model_phy)	**ADC Micro**	0.9568	0.0330	0.0330	0.0189
	Mini-MCA6	0.9673	0.0287	0.0287	0.0182
	RedEdge	0.9700	0.0275	0.0275	0.0152
Improved physically based (Model_phy_reg)	**ADC Micro**	0.9835	0.0204	0.0204	−0.0022
	Mini-MCA6	0.9907	0.0153	0.0153	−0.0016
	RedEdge	0.9881	0.0173	0.0173	−0.0022

As shown in Fig.4, the three models performed well, with a generally low RMSE of up to 0.033. Model_phy_reg was the most accurate among the three models, as shown in the third row of Fig.4, with a highest R^2 (0.98–0.99) and a lowest RMSE of approximately 0.02. This was closely followed by Model_reg with RMSE values that were 0.002–0.005 higher. Model_phy had the lowest accuracy among the three models, with an RMSE approximately 0.01 higher and R^2 0.01–0.02 lower. RSE is a variant of the RMSE adjusted for the number of predictors in the model. Its difference from RMSE was negligible as shown in Table 5, due to the large number of surface spectral albedos (2424) used for developing models and small number of predictors (narrow bands).

The Mini-MCA6 camera performed the best with Model_reg and Model_phy_reg, whereas the RedEdge camera performed the best with Model_phy. When applying the best algorithm (Model_phy_reg), Mini-MCA6 showed the highest R^2 of approximately 0.99 and the lowest RMSE of approximately 0.015, which was closely followed by RedEdge with an RMSE only 0.002 higher. The ADC Micro showed the lowest performance with an RMSE of approximately 0.02.

4. Result

4.1. Sensitivity analysis

4.1.1. Sensitivity to the season and SZA

The RMSEs of the three model-based albedos with respect to the seasons and SZAs are shown in Fig.5. Most models performed slightly better with summer solar irradiances (first column, Fig.5), except for Model_phy used for ADC Micro, which had the poorest performance indicated by a higher RMSE. Regarding the summer SZAs (first row, Fig.5), the performances of Model_phy and Model_phy_reg were similar, whereas Model_reg performed slightly better with the 20° SZA. As the winter SZAs increased from 40° to 70° (second row, Fig.5), the accuracy of Model_reg and Model_phy_reg reduced marginally, whereas that of Model_phy improved, as shown by the difference in RMSE of up to 0.005.

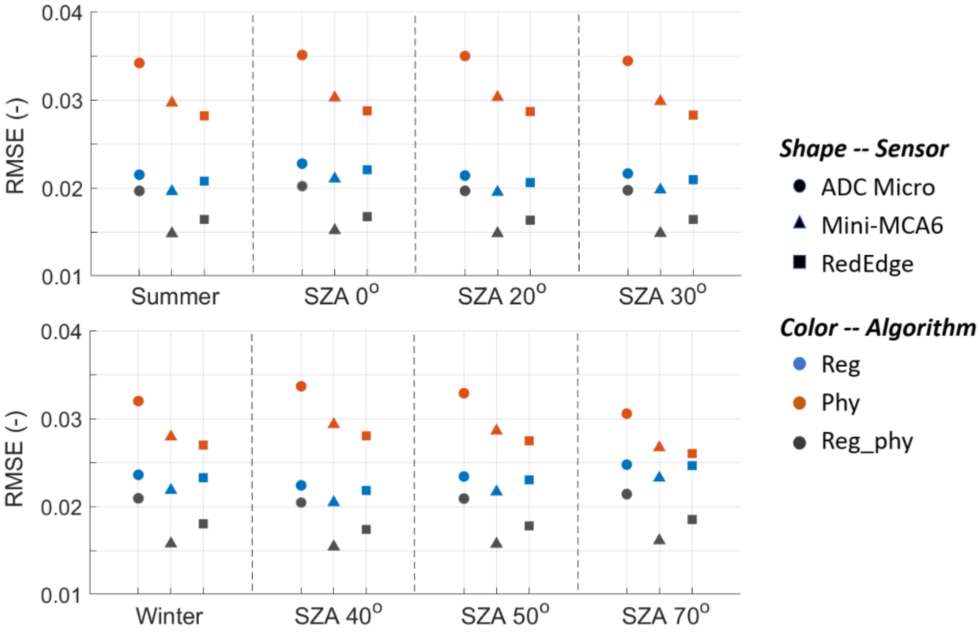

Figure 5. RMSEs of the three model-based estimated total SW albedos with respect to the season and SZA.

4.1.2. Sensitivity to the horizontal/vertical surface

The sensitivity of the NTB models to the vertical/horizontal surface and azimuth (if vertical) was evaluated using RMSE, and the results are shown in Fig.6.

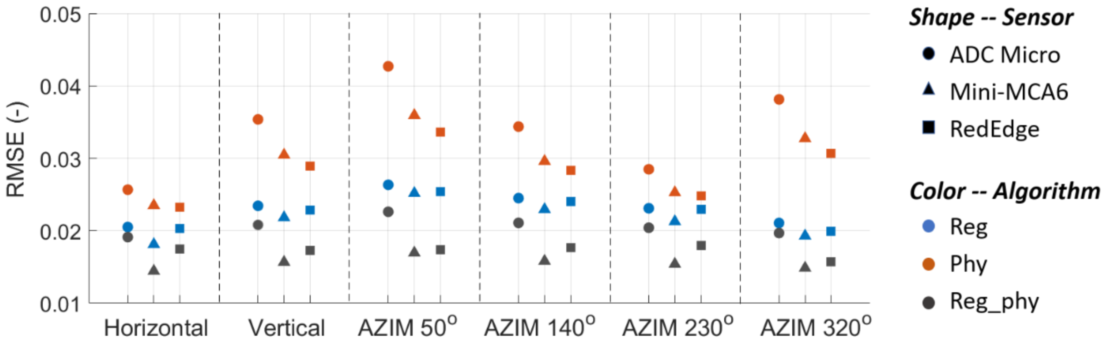

Figure 6. RMSEs of the three models-based estimated albedos with respect to the axial and orientation of target surface.

As shown in the first two columns (from left) in Fig.6, most models showed higher accuracies when applied to the horizontal surface than the vertical surface: Model_phy performed significantly better with an RMSE value that was 0.006–0.01 lower, the RMSE value of Model_reg was 0.0025–0.0037 lower, and Model_phy_reg performed slightly better with RMSE value lower by 0.0017 and 0.0012 for ADC Micro and Mini-MCA6, respectively, except for RedEdge which performed marginally lower.

In terms of the vertical surface azimuth, as shown in the last four columns of Fig.6, Model_phy demonstrated the best and worst performances with 230°- and 50°-azimuth surfaces, respectively, where the largest RMSE gap ranged between 0.009–0.014. Model_reg and Model_phy_reg performed the best and worst with the 320°- and 50°-azimuth vertical surface, respectively. The difference in RMSE for Model_reg was 0.005–0.006. As compared to the other two models, Model_phy_reg was less sensitive to the various surface azimuths, and the largest RMSE difference was between 0.002–0.0029.

4.1.3. Sensitivity to the class of materials

Considering the difference in albedo among construction materials (e.g., overall low albedo of asphalt), we used the RMSE percentage of the estimated SW albedos to better evaluate the models' dependencies on the material classes. The results, as shown in Fig.7, showed that the RMSE percentages of models applied to the urban surfaces were almost less than 15%, except for Model_phy and Model_reg applied to concrete and asphalt, respectively.

Regarding Model_reg, the best material class as the application target is the coating, whereas the worst and close-to-worst classes were asphalt and wooden slats, respectively, where the largest difference in RMSE percentage was approximately 11%. Model_phy's best application target was the wooden slat, whereas the worst was the coating for Mini-MCA6 and RedEdge, and concrete for ADC Micro, where the difference in RMSE percentage was up to 8%. Model_phy_reg's application on most construction materials showed an RMSE percentage less than 11%, except for asphalt and wooden slat. Their best and worst applications were stone and wooden slat, respectively, where the RMSE percentage difference was up to 9%.

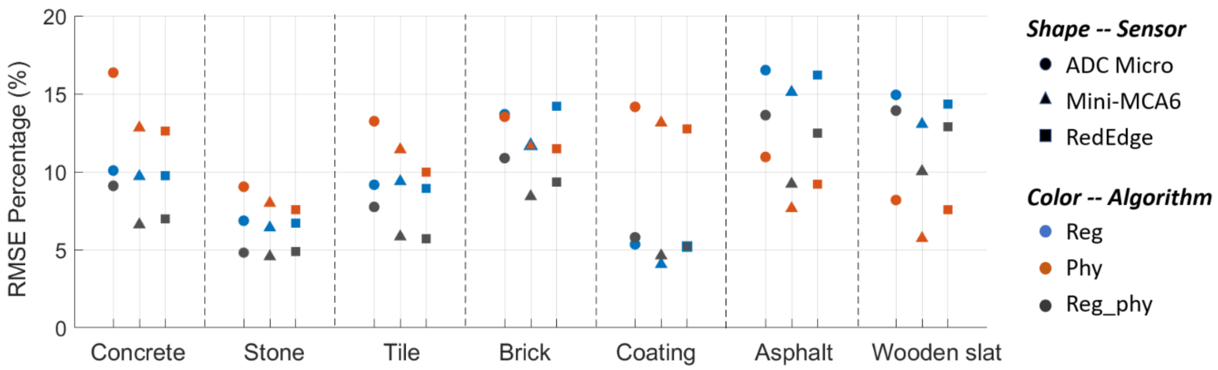

Figure 7. RMSE percentages of the three model-based estimated albedos with respect to the surface material class.

The worst application targets of Model_reg and Model_phy_reg were asphalt and wooden slat (Fig.7). Their capacity to capture spectral variations of different surface materials can be improved by developing custom models for each cover type, such as categorizing land cover into snow, soil, and vegetation for spaceborne RS [123,142]. The weighting coefficients of Model_phy remained unchanged unless the at-surface solar irradiance varied. We thus customized Model_reg and Model_phy_reg individually for the asphalt and wooden slat samples, as shown in Eqs. (12)–(17), in order to explore the potential for improving NTB conversion while considering different surface materials.

- Custom Model_reg for asphalt:

$$\alpha_{\_Mic\_reg} = 0.5011G - 0.6705R + 1.0308NIR + 0.0023 \tag{12}$$

$$\alpha_{\_MCA6\_reg} = 0.3276B - 0.0196G + 0.2205R - 0.2433RE - 0.1853NIR1 + 0.8345NIR2 + 0.0004 \tag{13}$$

$$\alpha_{\_RedE\_reg} = 0.3595B - 0.0451G - 0.8113R + 0.6996RE + 0.6437NIR + 0.0001 \tag{14}$$

- Custom Model_reg for wooden slat:

$$\alpha_{\_Mic\_reg} = -0.2058G + 0.5498R + 0.5912NIR + 0.0075 \tag{15}$$

$$\alpha_{\_MCA6\_reg} = 1.0432B - 1.0292G - 0.0135R + 2.9212RE - 3.8306NIR1 + 1.8782NIR2 + 0.01618 \tag{16}$$

$$\alpha_{\_RedE\_reg} = -0.8996B + 3.8407G + 0.2938R - 4.6087RE + 2.4312NIR + 0.007 \tag{17}$$

The general and customized regression-based weighting coefficients for sensors as shown in Eqs. (7)–(9), (12)–(17) were also summarized in Table 6.

Table 6. General and customized regression-based weighting coefficients.

Sensor	**ADC Micro**				**RedEdge**					
Channel	**G**	**R**	**NIR**	**Cons-tant**	**B**	**G**	**R**	**RE**	**NIR**	**Cons-tant**
General	0.7028	-0.4155	0.6222	0.009	0.3973	-0.0102	0.0454	-0.1017	0.6116	0.0075
Asphalt	0.5011	-0.6705	1.0308	0.0023	0.3595	-0.0451	-0.8113	0.6996	0.6437	0.0001
Wooden slat	-0.2058	0.5498	0.5912	0.0075	-0.8996	3.8407	0.2938	-4.6087	2.4312	0.007

Sensor	**Mini-MCA6**						
Channel	**B**	**G**	**R**	**RE**	**NIR1**	**NIR2**	**Constant**
General	0.3668	-0.0449	0.2183	0.2105	-0.5914	0.7708	0.0075
Asphalt	0.3276	-0.0196	0.2205	-0.2433	-0.1853	0.8345	0.0004
Wooden slat	1.0432	-1.0292	-0.0135	2.9212	-3.8306	1.8782	0.01618

Instead of the general variables of ***0.9141, 0.9193, and 0.9282*** (second row of Table 4) to develop Model_phy_reg for ADC Micro, Mini-MCA6, and RedEdge, respectively, the custom formulae applied ***0.9856, 0.9714, and 1.0021***, calculated by the regression for the asphalt samples, and ***1.0291, 0.9979, and 1.0388*** for the wooden slat samples.

A comparison of the general and custom NTB models is shown in Fig.8. It demonstrates that the customization resulted in an improvement in RMSE by approximately 1–4% for Model_reg and 3–6% for Model_phy_reg. The best conversion formulae for the asphalt and wooden slat are the custom Model_phy_reg used for Mini-MCA6, achieving a lowest RMSE percentage of 6.5% and 5.7%, respectively.

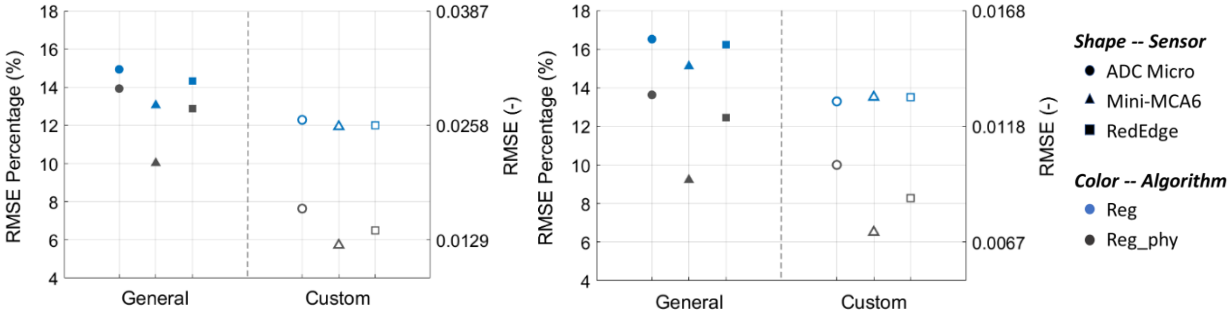

Figure 8. RMSE percentages of the general and custom NTB models-based estimated albedos of asphalt (left) and wooden slat (right).

4.2. Validation of conversion models

As mentioned in Section 2.2, avoiding the influence of the error caused by multispectral RS, the ASD measurement- and RedEdge image-based narrowband albedos were compared, as shown in Fig.9, and the accuracy of the estimated total SW albedos was evaluated, as shown in Fig.10.

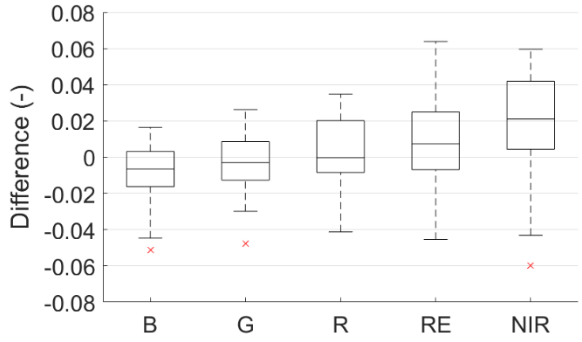

Figure 9. Difference between the narrowband albedos derived from RedEdge multispectral images and ASD measurement.

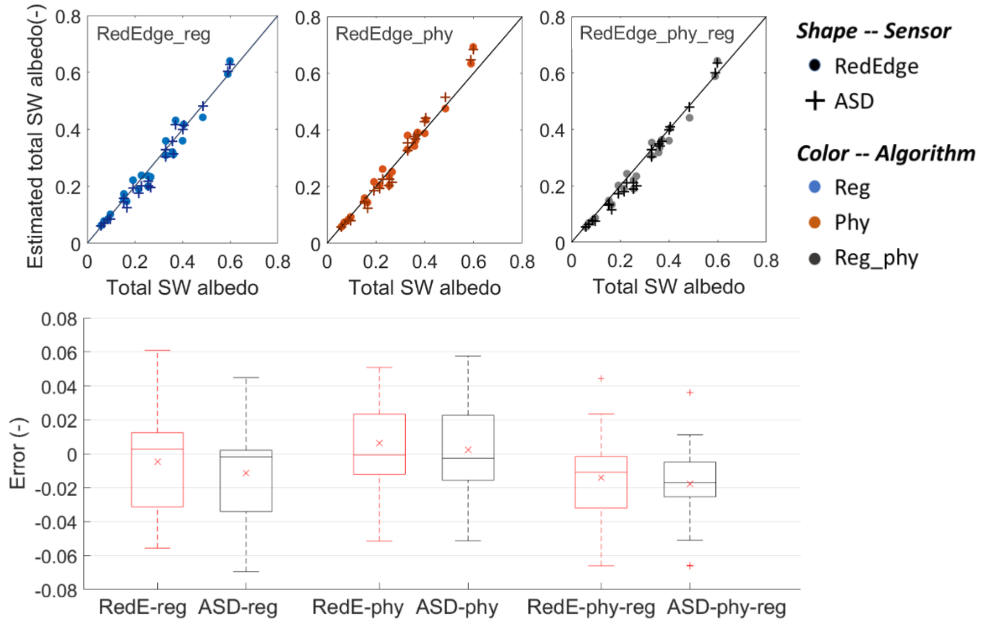

	R^2 RedEdge/ASD	RMSE RedEdge/ASD	RSE RedEdge/ASD	MBE RedEdge/ASD (red cross marks in the boxplot above)
Model_reg	0.959/0.962	0.0304/0.0293	0.0354/0.0341	−0.0049/−0.0113
Model_phy	0.960/0.954	0.0300/0.0322	0.0349/0.0375	0.0063/0.0023
Model_phy_reg	0.966/0.963	0.0279/0.0290	0.0325/0.0337	−0.0142/−0.0179

Figure 10. Validation results of the three models estimated from RedEdge images- and ASD measurement-based narrowband albedos.

As shown in Fig.9, the difference between the ASD measurement- and RedEdge image-based narrowband albedos ranged between −0.01–0.02, and the most inconsistency appeared for the albedos at the NIR region. This inconsistency caused a marginal difference in the estimated total SW albedos (Fig.10).

The results estimated from ASD measured data, as shown in the table of Fig.10, demonstrated that the developed models performed well with an R^2 above 0.95 and an RMSE of approximately 0.03. Model_reg and Model_phy_reg showed marginally better accuracy, with the RMSE of approximately 0.003 lower than that of Model_phy. Considering that the value range of most errors is located as shown in the boxplots in Fig.10, half of the errors were located from −0.026 to −0.005 for Model_phy_reg, from −0.037 to 0.002 for Model_reg, and between −0.017 to 0.024 for Model_phy, indicating that the error distribution of Model_phy_reg was less dispersed. The scatterplots in Fig.10 show that Model_reg and Model_phy_reg may underestimate the surfaces with a lower albedo (lower than 0.03) but overestimate the higher-albedo (above 0.6) surfaces, whereas Model_phy performed better when applied to the low-albedo surfaces but probably overestimated when the albedo was above 0.4, and the overestimation may increase as the surface albedo increases.

The results obtained from the RedEdge image (Fig.10) show that their accuracy is similar to the values estimated from ASD measured data with a difference of less than 0.006 in R^2 and up to 0.0022 in RMSE.

The suitability of the developed models to estimate the vertical surface albedos was also investigated, and the results are shown in Fig.11. The results estimated from the ASD measured data solely for vertical surfaces, as shown in Fig.11, indicated a small difference as compared to the accuracy performance shown in Fig. 10. Model_reg and Model_phy_reg performed slightly better, with an RMSE reduction of less than 0.008, whereas Model_phy had the worst performance with an RMSE of around 0.01 higher. The results estimated from the RedEdge image (Fig.11) indicated that their performances were inferior as compared to the ones estimated from the ASD measured data, especially for Model_reg with a difference of around 0.08 in R^2 and 0.016 in RMSE.

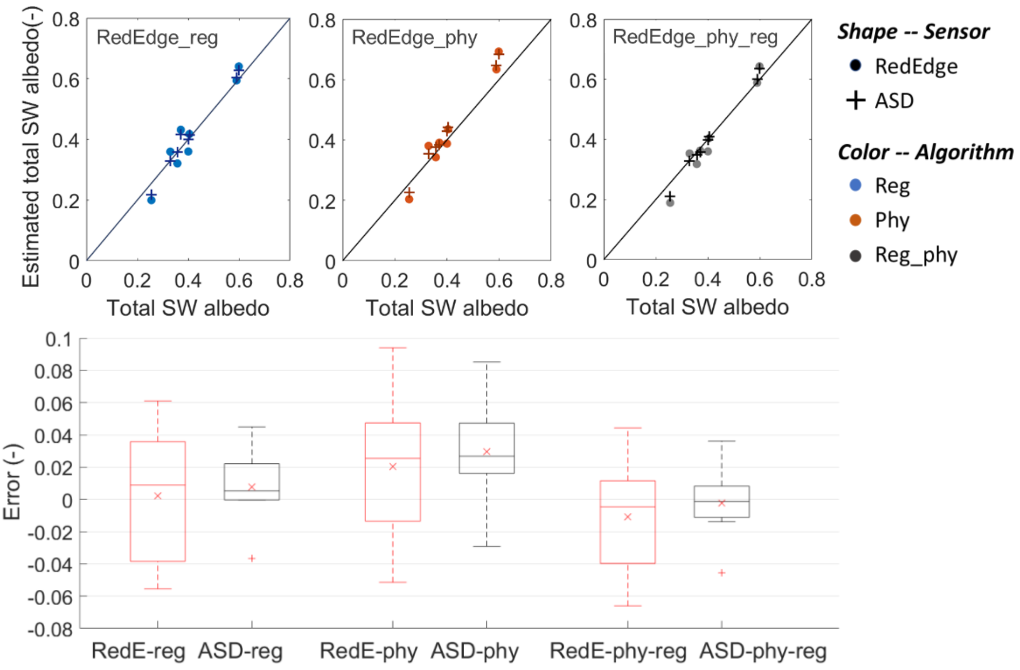

	R^2	RMSE	MBE
	RedEdge/ASD	**RedEdge/ASD**	**RedEdge/ASD**
Model_reg	0.878/0.956	0.0397/0.0238	0.0022/0.0077
Model_phy	0.827/0.856	0.0471/0.0430	0.0201/0.0295
Model_phy_reg	0.902/0.963	0.0355/0.0218	−0.0110/−0.0023

Figure 11. Validation results for the samples of vertical urban surfaces.

5. Discussion

5.1. Performance evaluation

Model_reg and Model_phy_reg showed higher accuracies, suitable for SEB modeling, with RMSEs of approximately 0.02 for Sample_D (Section 3.2). As compared to the performance of another physics-based conversion model against Sentinel-2A products in urban Perugia with an RMSE of approximately 0.02[26], Model_phy's RMSE value was higher by 0.01 (Fig.4). This may be due to the close-to-visible wavelength for NIR channel (< 1000 nm) and narrower bandwidth of spectral bands provided by UAV-based cameras, whereas the spectral bands provided by spaceborne sensors (e.g., Landsat, MODIS, Sentinel-2 MSI, etc.), to which the physics-based models are well-adapted to, could better capture the spectral variation of albedo. This resulted in an overall overestimation of SW albedos (second row, Fig.4). The degree of overestimation depends on the weighting coefficient of narrowband albedo at NIR (where the albedo is usually higher than those at VIS), which was largest for ADC Micro and smallest for RedEdge, causing that the overestimation was highest for ADC Micro and lowest for RedEdge.

We compared the model performances with those from previous studies, and found that the relatively low RMSEs (less than 0.033) were sufficient. To retrieve the SW albedos from Landsat 8 OLI (7 bands) data, Baldinelli et al.[131] obtained RMSE values of 0.058 and 0.039 for one regression with physics-based constraints and the other without constraints, respectively. Bonafoni et al.[26] computed the regression coefficients by applying Tasumi's[125] strategy and directly adopted Li's[126] coefficients for Setinel-2 MSI (6 bands), with RMSE values of 0.023 and 0.025, respectively. Liang's models for common spaceborne sensors revealed a high accuracy with RSE ranging between 0.01–0.02[41].

As shown in Fig.4 and Table 5, ADC Micro had the lowest accuracy as compared to the other cameras. This corresponds to our expectation and the previous study that less bands would influence the efficiency of converting narrowband to broadband albedos[41]. Mini-MCA6 performed best with Model_reg and Model_phy_reg whereas RedEdge performed better with Model_phy. However, their performances were similar, with the difference in RMSE less than 0.002. Their similar performance indicates that the advantage offered by Mini-MAC6's plural bands at NIR region is not dominant to the accuracy of estimating albedo, as compared to RedEdge with the single band at NIR. Though the changes in spectral reflectance are largely in the VIS wave range, these become relatively stable in the NIR wave range. Meanwhile, spectral solar irradiance decreased from the VIS to NIR wave. Its peak was observed at around 500 nm and decreased gradually towards a longer wave range. In addition to the efficiency of the narrowband albedos to estimate albedo, the data quality, processing complexity[110], and the weight (which may influence the battery consumption of the platform and thus the available flight time) should also be considered while selecting a multispectral camera. For example, when applying the best NTB model (i.e., Model_phy_reg), the RedEdge had reduced efficiency while estimating narrowband albedos and lower spatial image resolution than Mini-MCA6, but was lighter and had a wider FOV, which may contribute to a longer flight time, reduced flight rounds, and less images to capture than the Mini-MCA6 to estimate albedos of the same area, resulting in easier and timely post-processing.

5.2. Sensitivity analysis

As shown in Fig.5, the performance of the developed models was not much prone to solar irradiance with respect to the season and possible SZAs within the season if the UAV multispectral RS was conducted near solar noon (late solar noon for vertical surface) and under clear skies. These results confirm Liang's finding that broadband albedos are relatively stable unless the SZA is quite large, based on the albedo dependences of snow, deciduous forest[41], and asphalt[113], and are suitable for urban surfaces covered by other common construction materials.

As shown in Fig.6, compared to Model_phy, the accuracies of Model_reg and Model_phy_reg were less dependent on whether surfaces are horizontal or vertical. Regarding the application to vertical surfaces with respect to various azimuths, Model_phy_reg was much less sensitive than Model_reg and Model_phy. It can be further concluded that Model_phy_reg had the least sensitivity to the applications on vertical surfaces and various azimuths.

As shown in Fig.7, different conversion models for different cameras have their own advantages with the respect to the material class, due to differences in their capacity to capture spectral variations which would cause diverse efficiency values with respect to certain spectral variations within the material class. Among them, Model_reg and Model_phy_reg could not be well-adopted to estimate the albedo of the asphalt and wooden slat surfaces. Fig.8 demonstrates the potential improvement room of a few percent in RMSE for Model_reg and Model_phy_reg due to the customization accounting for the surface material class, which was a non-negligible improvement for the case study with high requirement of estimating the albedo. It was also observed that to improve the NTB conversion accuracy, the category method of the surface cover[123,142] was also suitable for the construction material class and could be downscaled to neighborhood scales.

5.3. Model validation

The difference between the ASD measurement-based and RedEdge image-based narrowband albedos reveals the most inconsistent at NIR band (Fig.9), which may be caused by the Lambertian surface assumption that did not consider the BRDF effect, which would have a strong influence on the NIR region, as concluded by France[143]. This inconsistency caused a minor difference in the estimated total SW albedo, as shown in Fig.10, but did not influence model validation. As discussing the error caused by ground-based multispectral RS is beyond our scope here, the results shown in Fig.9 and Fig.10 were used to demonstrate that the developed models are applicable to the multispectral RS data in practice if adopting the appropriate observation protocols and post-processing. The following discussions are mainly based on the results derived from the ASD measurement-based narrowband albedos.

As shown in Fig.10, the three developed models were applicable to the independent and separate samples including both vertical and horizontal surfaces, various construction materials, and multispectral RS data with low RMSEs of around 0.03, meeting the desired accuracy of SW albedo (around 0.05) for SEB modeling. Comparing the performances of the three models for sample_D (Fig.4), the performance ranking of models applied for Sample_V

(Fig.10) showed a general consistency, but with an RMSE increase lower than 0.012, indicating that no significant difference in the developed models' accuracies was caused by the random and independent samples.

The studies directly applying the coefficients of Liang's and others' NTB formulae to the samples which are not used to develop the models can be regarded as model validations, where the results are supposed to show a larger error. Compared to these studies, our developed models were quite reliable with a relatively low RMSE and MBE. An average RSE of generally 0.02 for most spaceborne sensors was observed in the validation cases of Liang's models[113]. Fitted RMSEs of 0.075 and 0.081 were shown in [131] as the results of the accuracy assessment conducted by directly using Liang's and Tasumi's models for Landsat 8 OLI data for estimating the albedo in urban contexts. Cao et al.[27] observed that the MBE was about 0.01 for the validation of Landsat VIS band albedo conversion algorithm given by Wang[115], applied to a UAV-based RS.

When the model validation was applied to the vertical surface (Fig.11), as compared to the general validation results shown in Fig.10, Model_reg and Model_phy_reg showed lower RMSE values than Model_phy, demonstrating that they are less sensitive to the vertical or horizontal nature of the surface.

It can be concluded that the developed models are suitable and show a relatively stable performance when applying to the separate and independent samples. However, it is not clear yet if these models only work well for Sample_V in our validation site, for which further validations are needed to draw a more general conclusion. Model_phy_reg performed better as compared to the other two models, as indicated by the RMSE values and the denser distribution of errors, revealing that Model_phy_reg is the most stable and robust among the three models. It further suggests that the physical constraints used to develop the NTB conversion model may contribute to its applicability and robustness, which is suggested to be further applied for developing NTB conversion models for other multispectral cameras that were not analyzed in this chapter (e.g., Buzzard Camera six, Parrot Sequoia+, and Sentera Quad).

The technical process and method to develop the NTB conversion model herein could be applied to other cameras. The differences among Liang's strategy of empirical regression (Model_reg), Tasumi's strategy based on the albedo physics (Model_phy), and the improved physical strategy (Model_phy_reg) lead to different requirements to develop the models. For developing Model_reg, the sample quality and quantity would decide how general and applicable the model is. Although more samples involving diverse material and illumination conditions may result in a more compelling empirical model, the typical nature of the material and a reasonable application limit for illumination conditions (e.g., noontime as the limit used here) would efficiently reduce the workload but guarantee the model performance. Although no database of samples is required to develop the Model_phy, the specific surface orientation and solar condition of the application case should be known, which would decide the conversion coefficients of Model_phy. The specific surface orientation and solar condition of the application case should also be known for developing Model_phy_reg. However, the sample quantity would influence the Model_phy_reg much less than Model_reg, which mainly decides the variable (term explanation as shown in Table 4) with respect to the camera for Model_phy_reg.

Regarding the selection of the NTB conversion models developed here, it should depend on the similarity of the application case and Sample_D (used to develop the models) and the demand for accuracy and efficiency. If the application case is similar to the Sample_D cases considering the surface orientation, material class, and the solar condition under which it is based, Model_reg is recommended due to its high time and workload efficiency. This is because it can be adopted directly without the variation of conversion coefficients due to the illumination, unless the application priority is the accuracy (Model_phy_reg with higher accuracy as a preference). Whereas, if there is a large difference between the application case and the Sample_D, the applicability of Model_reg should be further validated by the target case before using the Model_reg, or it may lead to a larger error due to its development strategy of empirical regression. Instead, the Model_phy_reg is more recommended to be applied in this situation, as its coefficients were decided based on the albedo physics, which would guarantee its accuracy and robustness, but with a larger workload for calculating the different conversion coefficients depending on the urban surface orientation and solar condition. However, the calculation of conversion coefficients based on the usual regular and limited surface orientation in a block or a neighborhood and fast- and easy-to-use SMARTS simulation would not be too complicated and time-consuming.

5.4. Limitation

The Lambertian assumption may be not valid for different surface covers [131]. The Lambertian assumption of the procedure to simulate spectral albedos allows us to develop models based on extensive spectral albedos under different solar conditions rather than the time-consuming and labor-intensive direct measurements of albedos using albedometers. The Lambertian assumption was used for two purposes: to obtain the spectral albedos equaling the ASD measured spectral reflectances, and to obtain the narrowband albedos equaling the narrowband reflectances derived from RedEdge images. For the first purpose, all the target urban surfaces used here are quite rough, homogeneous, without dominating 3D structures, and the ASD measurements were conducted with a near-90° elevation angle to the surfaces and with an artificial illumination to guarantee the measurement environment close to be in the laboratory, which are essential and crucial to give a Lambertian surface approximation similar to the actual situations[26,41,113,131]. For the second purpose, the albedos estimated from RedEdge images should be considered as the Lambertian-equivalent since we did not model the BRDF effect. However, apart from the characteristics of the urban surfaces mentioned above, the RS exercises were conducted to guarantee both the illumination and observation facing the target surface with a small incident and observation angle which would keep the error margin due to Lambertian assumptions relatively low. Besides, it would not impact our discussion (Section 5.3) as the findings were mainly derived from the ASD measured data rather than the RedEdge images. However, estimating albedos from UAV-based multispectral RS requires radiometric calibration, surface BRDF modeling (if non-Lambertian surface), and NTB conversion. The NTB conversion models developed here mainly deal with the last process, where the accuracy would be affected by the first two processes. In the future application of developed models, it is suggested that the BRDF effect be incorporated to retrieve the narrowband albedos from multispectral observation.

The developed models in this chapter could only be applied to the midday period (late midday for vertical surface in summer), clear sky, and the location in the mid-latitude region as they work well when applied to the validation samples. However, more samples and conditions are needed to further test the applicability of the models.

6. Summary

The aim of this chapter is to provide applicable and easy-to-use NTB conversion models for UAV-based multispectral cameras and urban textures. Based on the obtained dataset of various at-surface solar spectral irradiances and spectral reflectances of urban surfaces, we simulated extensive spectral albedos of urban surfaces (Sample_D) and thus developed three NTB conversion formulae following published methodologies (Model_reg following Liang[41], Model_phy following Tasumi et al.[125], and Model_phy_reg as an improvement of Model_phy) for three common UAV-based multispectral cameras for urban surfaces covered by construction materials. Their accuracy and sensitivities to solar conditions and construction material class were evaluated, along with the albedo retrieval capacity of three multispectral cameras. The main findings are as follows.

1. The performances of the three developed NTB conversion models are acceptable for SEB modeling (RMSE < 0.033).
2. ADC Micro had the poorest performance. Mini-MCA6 performed the best with Model_reg and Model_phy_reg and the RedEdge performed better with Model_phy. However, their performances were similar (RMSE

difference < 0.002). Data quality, processing complexity, and weight should also be considered while selecting a UAV-based multispectral camera.

3. The developed models were not prone to the solar irradiance corresponding to the season and possible SZAs within the season if the multispectral observation was taken near the solar noon (late solar noon for vertical surface) and under clear sky.
4. Model_phy_reg was least sensitive to the vertical surfaces with various azimuths, as compared to other two models.
5. The developed models performed differently for the construction material class with the RMSE percentage difference of up to 11%. The worst application targets of Model_reg and Model_phy_reg were the asphalt and wooden slat surfaces.
6. The potential for improving the customized NTB conversion models for different surface material classes could be a few percent, which is non-negligible for a case study with a high requirement to estimate albedo.

These conversion formulae were validated by independent and separate Sample_V. The main findings are presented below.

7. The developed models could estimate the total SW albedo with the fitted RMSEs of approximately 0.03, thus meeting the desired accuracy of SW albedo (approximately 0.05) for SEB modeling.
8. The model performances for Sample_V were consistent with those of Sample_D, indicating that the model performances were relatively stable when applied to an independent and random dataset.
9. Model_phy_reg's performance was the most accurate, stable, and robust, suggesting that the physical constraint used to develop the NTB conversion model may contribute to its applicability and robustness.

All the urban surfaces studied here meet the essential and crucial conditions of Lambertian surface approximation. In the future application of the developed conversion models, it is suggested that the BRDF effect be modelled to retrieve the narrowband hemispherical albedos from UAV-based multispectral observation. It is suggested to select the appreciate NTB conversion model developed herein depending on the similarity between the application case and the samples used to develop the models in this chapter and the demand for accuracy and efficiency (time and workload). The developed models and technical process could contribute to the wider and further application of UAV/ground-based multispectral RS on the microclimate monitoring and SEB modeling at neighborhood or local scales. For example, before adopting the UHI mitigation strategy, quantifying the actual albedo is important to predict the strategy's performance (e.g., outdoor thermal environment and indoor energy consumption) through SEB modeling; after applying the strategy like the cool roof to mitigate UHI effect, monitoring the variation of albedo would support the decisions on whether to clean the dust or to repaint the roof.

CHAPTER 4: ESTIMATION ON THERMAL CONDUCTIVITY AND HEAT CAPACITY OF BUILDING SURFACES BASED ON MULTISPECTRAL REMOTE SENSING AND SURFACE ENERGY BALANCE SIMULATION

1. Introduction

The assumption and generalization of thermal conductivities and heat capacities of building surfaces may cause a RMSE in SEB and Jurges CHTC model-based predicted sensible heat flux of up to 58 W/m2 and 38% during the noon time (Chapter 2)[144]. It reveals that error due to assumption and generalization cannot be ignored to simulate external surface temperature and sensible heat flux based on SEB modeling. Hence, to obtain actual thermal conductivities and heat capacities of building surfaces is in an important need for SEB modeling and to study the urban surface-atmosphere heat exchange. Due to the limitations of in-situ measurement method and satellite/airborne RS method to be applied for estimating thermal properties at a local scale as introduced in Chapter 1, this chapter aims to develop a new estimation method on thermal conductivities and heat capacities of building surfaces, filling a gap of the estimation method at a block and neighborhood scale.

Rapid development of unmanned aerial vehicles (UAVs) equipped with multispectral cameras has shown the potential to obtain the thermophysical properties of both horizontal and vertical urban surface with fine spatial resolution to further bridge the gap between in-situ and spaceborne/airborne observations. An estimation method on urban surface albedo based on UAV-based multispectral camera including the method process and narrow-to-broadband models have been proposed and validated in Chapter 3, establishing the foundation for the further study to estimate thermal properties of building surfaces. With the estimated surface albedos, the method of further estimation on thermal properties of opaque building surfaces was proposed in this chapter, coupling the use of multispectral RS and SEB model-based simulation. Taking a concrete building in a block in a university campus (Yokohama city, Japan) as a target building, the multispectral and hourly infrared thermal images from sunrise to sunset of the target building were taken, and meanwhile the indoor air temperature and weather data were measured in site. Typical cases of the combinations of thermal properties of building surface were characterized by clustering based on a database established here. These cases were input as possible thermal properties of the target building in SEB simulation with other boundary conditions of the measured indoor air temperature and weather data, and the estimated albedo of the target building (Chapter 3). Among these cases, the one which simulated radiant surface temperatures of target building revealing the most consistent with the measured temperatures was regarded as the one closest to actual condition, and its thermal properties were regarded as the estimated results. The point-to-point, grid-to-grid, and region-to-region comparisons were carried out to evaluate which case performed the closest to actual ones. The accuracy of this developed method was evaluated, and the sensitivities of the assumption of indoor air temperatures and the main limitations of this method were also analyzed. In addition to use the measured global solar radiation to simulate the at-surface radiation, another approach of the simulation based on multispectral brightness-radiation correlation and heat transfer model was proposed as an implement to be potentially applied for the conditions under an overcast or partly cloudy sky.

2. Methodology

2.1 Studied area and target wall surface

The studied area was also selected on the same university campus as stated in Section 2.3 of Chapter 2 in Yokohama city, Japan. The studied area was approximately 100 m × 120 m, enclosed on four sides as a repeated unit within the school (Fig. 1). G3 building as the studied building was eleven floors and of a straight type, with offices and experimental rooms inside. Its NW-oriented wall external surface was selected as the studied building surface.

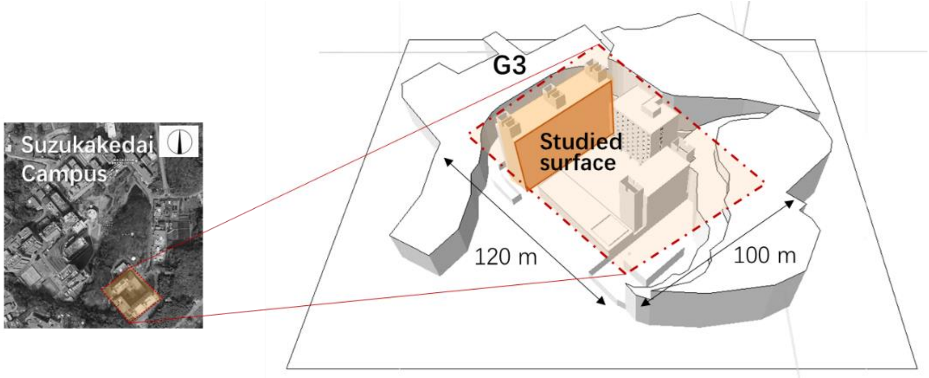

Figure 1. The studied area and building wall surface

As shown in Fig.2, ten points distributed uniformly on G3 NW-oriented wall external surface were selected as the studied points on the target building surface. Their sunlit and shadowed conditions change through the temporal variation, which is shown in Fig.3. Two of them, L5 and R4, were a bit different from others' distribution rule. It is due to that the originally planned location for L5 cannot be used for comparison with the infrared images taken in this chapter since it was hidden by the G4 building. Regarding the R4, its location was selected to be higher than the originally planned one, because the originally planned location on G3 NW-oriented wall reveals the thermal anomalies suggested by the obvious sudden variation of spatial distribution of surface temperature shown in the infrared image taken in this chapter. These ten points were termed as L1_5 and R1_5 in the following thesis, and their simulation results were compared with their measured surface temperature in Section 3.1.

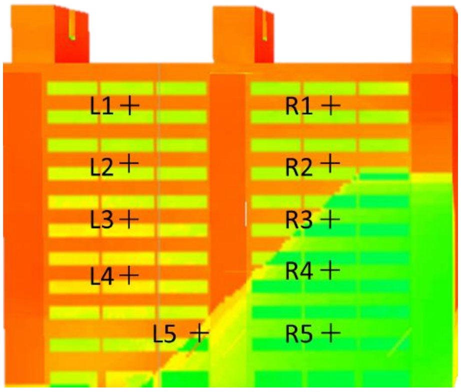

Figure 2. The studied ten points on G3 NW-oriented wall surface.

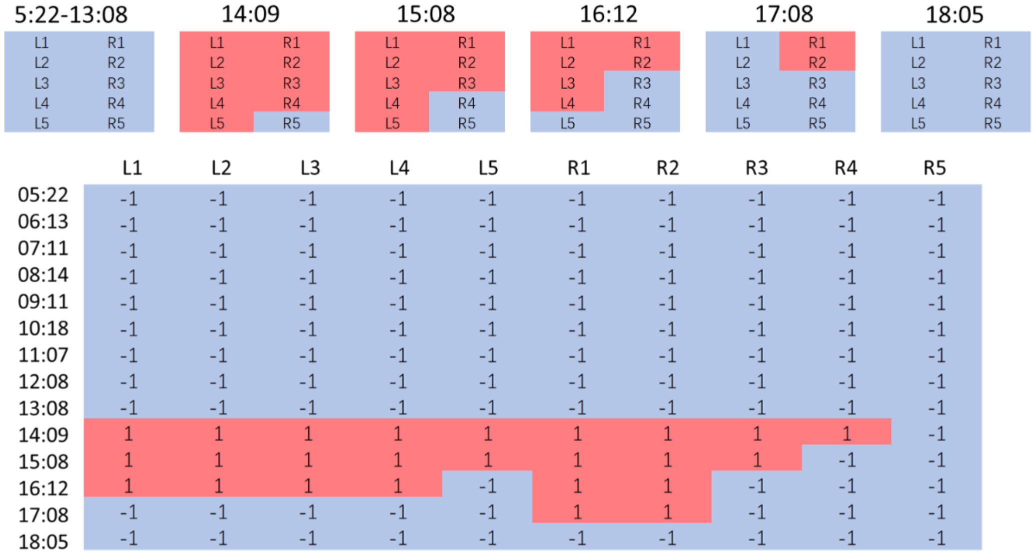

	L1	L2	L3	L4	L5	R1	R2	R3	R4	R5
05:22	-1	-1	-1	-1	-1	-1	-1	-1	-1	-1
06:13	-1	-1	-1	-1	-1	-1	-1	-1	-1	-1
07:11	-1	-1	-1	-1	-1	-1	-1	-1	-1	-1
08:14	-1	-1	-1	-1	-1	-1	-1	-1	-1	-1
09:11	-1	-1	-1	-1	-1	-1	-1	-1	-1	-1
10:18	-1	-1	-1	-1	-1	-1	-1	-1	-1	-1
11:07	-1	-1	-1	-1	-1	-1	-1	-1	-1	-1
12:08	-1	-1	-1	-1	-1	-1	-1	-1	-1	-1
13:08	-1	-1	-1	-1	-1	-1	-1	-1	-1	-1
14:09	1	1	1	1	1	1	1	1	1	-1
15:08	1	1	1	1	1	1	1	1	-1	-1
16:12	1	1	1	1	-1	1	1	-1	-1	-1
17:08	-1	-1	-1	-1	-1	1	1	-1	-1	-1
18:05	-1	-1	-1	-1	-1	-1	-1	-1	-1	-1

Figure 3. Temporal variation of sunlit and shadowed conditions of ten points

In addition to the above-mentioned point-to-point comparison of 10 points, a grid-to-grid comparison was also conducted for the target surfaces to avoid the influence of the point selection and to figure out the error distribution in order to analyze the cause of error. Four moments on the studied day from sunrise to sunset were selected: 05:22, 09:11, 13:08, and 18:05. Different from the mesh size for simulation (i.e., 400mm), the grid size used for comparison is about 100mm*100mm, leading to a large grid number of 27000-30000. The process to conduct this grid-to-grid comparison is shown in Fig. 4. After following this process, the results of the grid-to-grid comparison were shown in section 3.1.

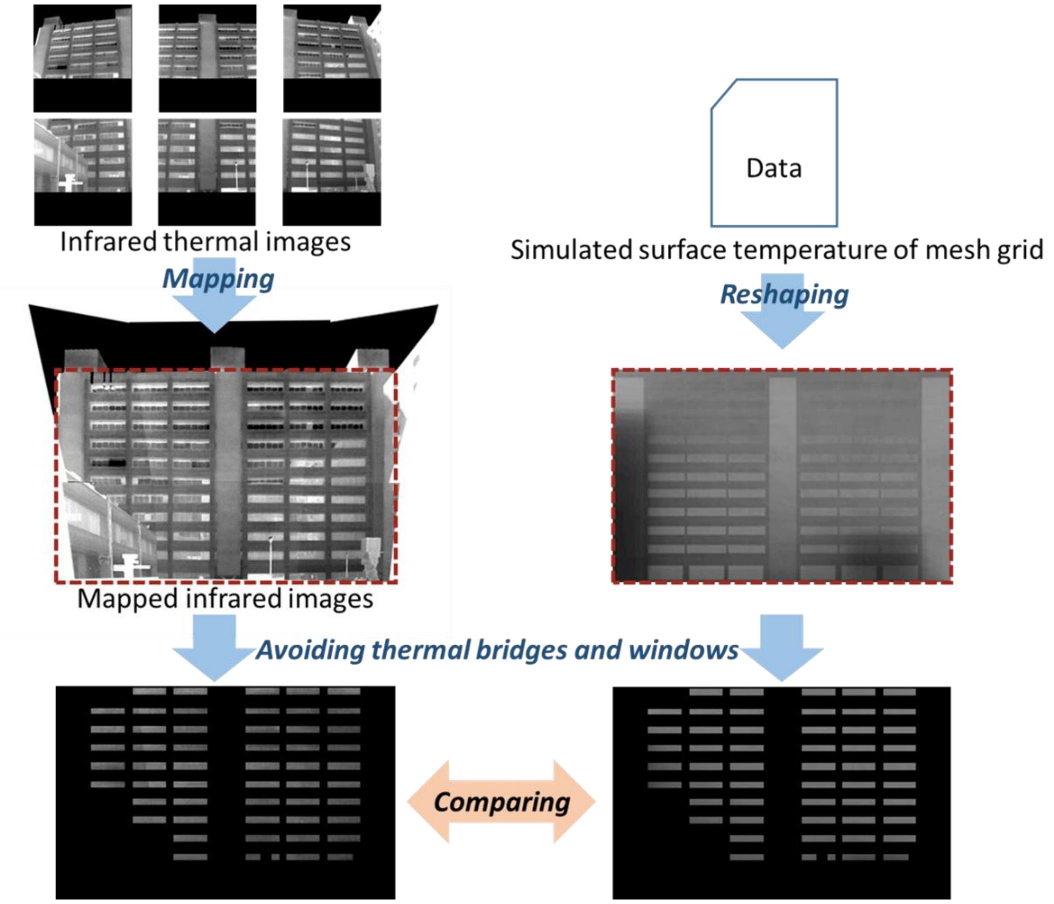

Figure 4. Process to conduct grid-to-grid comparison of G3 NW wall surface between the infrared image and 2D spatial distribution of the simulated temperature for the target moments

As shown in Fig.5, five small regions being either sunlit or shadowed on G3 NW-oriented wall external surface were also selected as the studied regions on the studied building surface, which were used termed as Shadowed_L, Sunlit_L, Shadowed_R, Sunlit_R, and Sunlit_R2 region in the following thesis. The simulation results of these five small regions were compared with their measured surface temperature averaged within the region in Section 3.2.

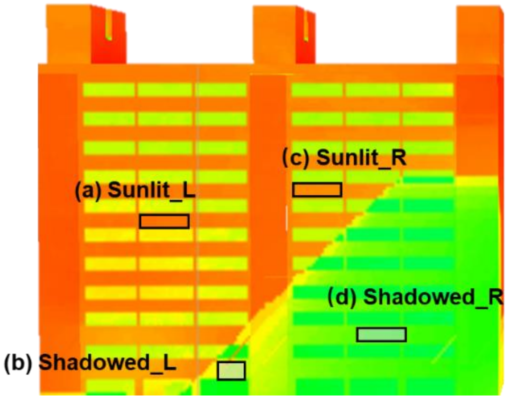

Figure 5. The studied four small regions on G3 NW-oriented wall surface.

2.2 Technical process

The thermal properties (i.e., thermal conductivity and heat capacity) of the building surface were estimated based on multispectral RS and SEB model-based simulation. Taking a concrete building in a block in a university campus (Yokohama city, Japan) as a target building, the multispectral and hourly infrared thermal images from sunrise to sunset of the target building were taken, and meanwhile the indoor air temperature and weather data were measured in site. 17 typical combinations of thermal properties of building surface were characterized by clustering based on a database established here. These 17 cases were input as possible thermal properties of the target building in SEB simulation with other boundary conditions of the measured indoor air temperature and weather data, and the estimated albedo of the target building (Chapter 2). Among these 17 cases, the case which simulated radiant surface temperatures of target building revealing the most consistent with the measured temperatures (retrieved from hourly infrared images) was regarded as the one closest to actual condition, and its thermal properties were regarded as the estimated results.

2.3 Measurement

2.3.1 Ground-based multispectral remote sensing and in-situ measurement

The ground-based multispectral RS was carried out on a typical summer day as the target day, August 01, 2018. The sky was clear and sunny, and in the middle of sunny days. By using a handheld thermal infrared camera (InfReC Thermo GEAR, Nippon Avionics Co., Ltd., Japan) and a multispectral camera (Rededge-M, MicaSense Inc., USA), hourly infrared and multispectral images for G3 NW-oriented wall surface were captured from sunrise to sunset and at around midnight. As measured by the thermal infrared camera, the relationship between the radiant temperature and actual surface temperature is shown as Eq. (6) in Section 3 of Chapter 2.

Meanwhile, the meteorological data on August 01, 2018 as the target day were collected using an anemometer (KANOMAX Climomaster anemometer 6501-00, Kanomax USA, Inc., USA) and a coupled sensor (T&D TR-72nw-S, T&D Co., Japan) for measuring and recording temperature and humidity observing at 1.5m height which are located in the central open space of the study area, and a weather station (Davis Vantage Pro2, Davis Instruments Co, USA) settled on a nearby roof in order to guarantee the complete exposure to global solar radiation (at an observing height of approximately 10m from the ground, and at a distance of about 150m from the study area). These observed meteorological data are shown in Fig. 6. In addition, the indoor air temperature was observed by using a thermometer (T&D TR-72nw-S, T&D Co., Japan) located on low (second), middle (fifth), and high floors (ninth) of G3 building, which results are shown in Fig.7.

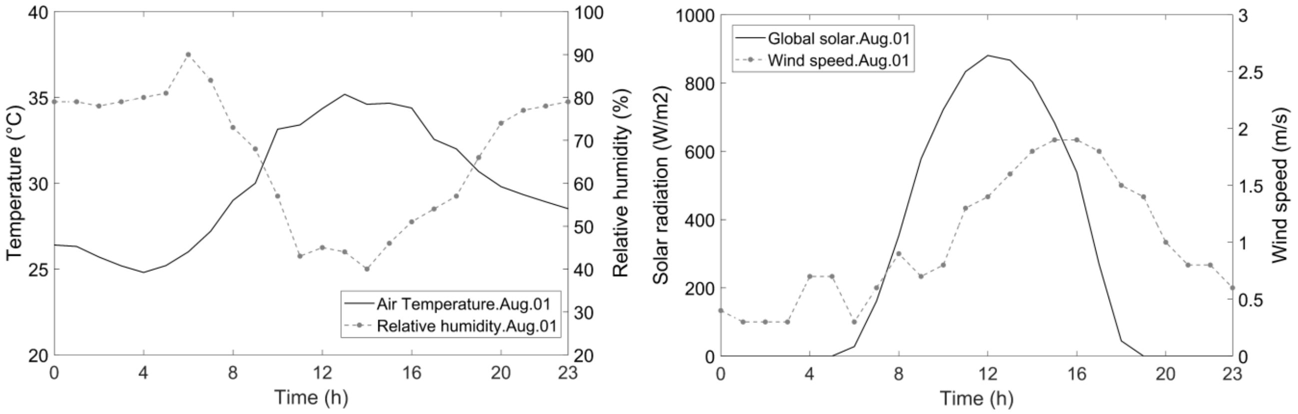

Figure 6. Meteorological conditions on August 01

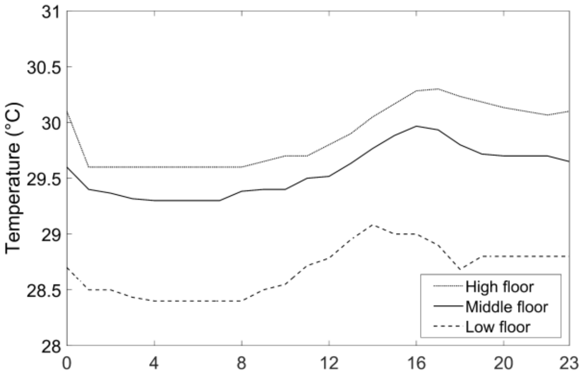

Figure 7. Indoor temperature in G3 building in terms of high, middle, and low floors

2.3.2 Measurement to study brightness-radiation correlation

84 samples were taken to study the brightness-radiation correlation. As shown in Fig.8, the reference panel was placed horizontal and very near the pyranometer to guarantee similar solar and observation angles and the illumination received as the pyranometer.

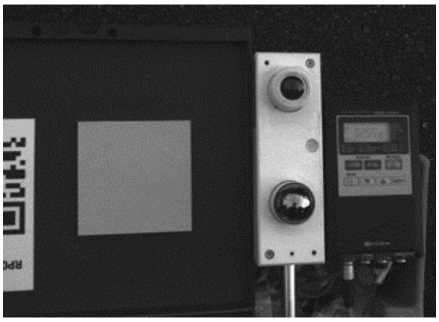

Figure 8. Placement of reference panel and pyranometer with a data logger

2.4 Numerical simulation

2.4.1 Simulation cases

To determine the simulation cases for the thermal properties, K-means clustering was applied to classify the roof/wall components from the abovementioned database (Section 2.4 and Fig.3 in Chapter 2) into typical combinations of thermal properties depending on the Euclidean distance calculated by the values of the normalized thermal properties.

Before conducting the K-means clustering, the elbow method was applied to figure out the optimal number of clusters. As shown in the left of Fig.9, it reveals that the error decreases as the K, cluster number, increases sharply until. The K of 17 was thus selected to carry out the K-means clustering, and the mean and maximum standard deviation in each cluster under being clustered by 17 was shown in the right of Fig.9.

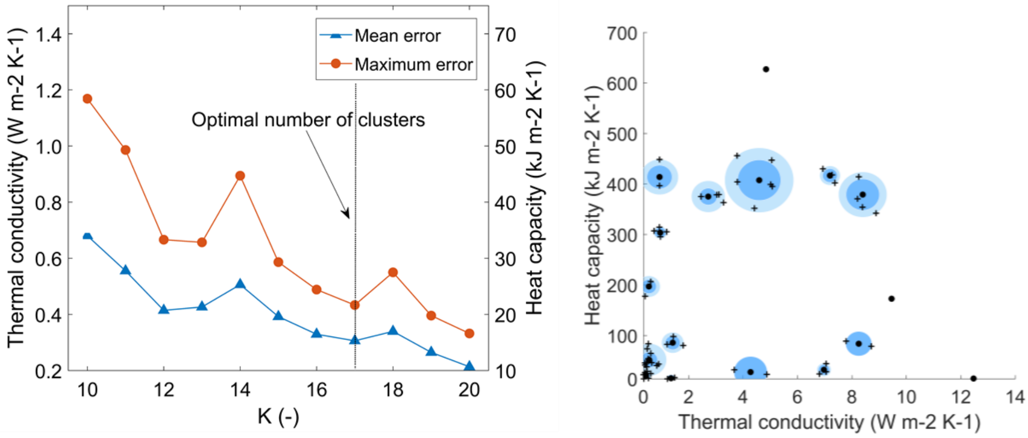

Figure 9. Optimal cluster number (K) based on Elbow method (left), and mean and maximum standard deviation in each cluster under being clustered by the optimal cluster number, 17 (right).

As shown in the right of Fig.9, the corresponding thermal property values of 17 cluster centers were selected as the typical combinations of thermal properties which were input as the simulation cases (Table 1).

Table 1. Typical cases to simulate based on the more specific clustering

Typical case	λ_c **[W m^{-2} K^{-1}]**	C_a **[kJ m^{-2}K^{-1}]**	**Reference materials Layers from exterior to interior [mm]**
TC_1	0.44	20.43	Ceramic siding (20) Air layer (20) Glass wool 16K (100) Air layer (60) Gypsum board (10)
TC_2	0.54	196.99	Mortar (30) Plywood board (20) Glass wool (70) Concrete (70) Gypsum board (12)
TC_3	0.55	51.88	ALC (50) Air layer (45)

			Rock wool (30) Gypsum board (10) Rock wool (30) Air layer (200) Gypsum board (10)
TC_4	0.93	413.77	Tile (10) Mortar (15) Concrete (180) Polystyrene foam (35) Gypsum board (10)
TC_5	0.96	303.55	Concrete (150) Polystyrene foam (35) Gypsum board (10)
TC_6	1.36	15.26	Plywood (20) Air layer (100) Soft board (6)
TC_7	1.42	85.66	Granite (30) Air layer (45) Rock wool (30) Gypsum board (10)
TC_8	2.72	375.03	ALC (50) Air layer (100) Concrete (180)
TC_9	4.28	27.47	Ceramic siding (15) Air layer (100) Gypsum board (12) Air layer (60) Gypsum board (12)
TC_10	4.59	407.45	Mortar (10) Light weight block (200) Plaster board (10)
TC_11	4.85	627.13	Concrete (150) Air layer (100) Concrete (180)
TC_12	6.97	32.05	Ceramic siding (15) Air layer (130) Plaster board (10) Air layer (60) Gypsum board (10)
TC_13	7.19	416.67	Tile (20) Concrete (230)
TC_14	8.25	83.63	Mortar (30) Plywood (12) Air layer (130) Plaster board (20)
TC_15	8.40	378.95	Concrete (220)
TC_16	9.46	172.71	Mortar (7) Light-weight block (94) Plaster board (7)
TC_17	12.47	14.73	Steel (1) Air layer (100) Gypsum board (10)

Considering the efficiency to figure out the target thermal combination which is closest to the actual thermal behavior of the target G3 NW-oriented wall surface, more general clustering can be conducted to reduce the possible typical thermal combinations needed to be simulated. K-means clustering was carried out for the 80 thermal combinations in the established database with a K value of 4, and these 4 general clusters were shown in Fig.10 and their corresponding cases of thermal combinations (Table 2) were simulated. The GC case with the smallest simulated-measured temperature difference was the general cluster which the target thermal combination belongs to. After the determination of which general cluster (GC cases) the target thermal combination belongs to, the specific clusters (TC cases) included in this cluster are the possible target thermal combinations needed to be further simulated. Based on this process, the needed number of simulation cases can be effectively reduced into the half of total number of typical cases. Instead of the total of 17 typical cases, 8, 7, 7, and 8 cases are required to simulate if the target thermal combinations belong to GC_1, 2, 3, 4, respectively.

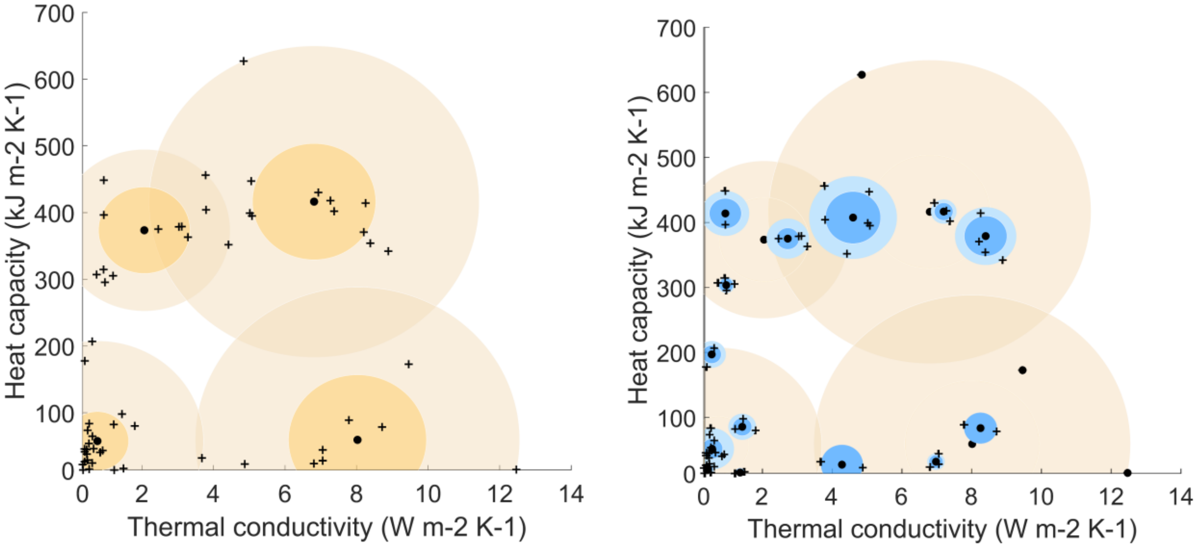

Figure 10. General cluster with the general cases(left) and the typical cases included in each of them(right)

Table 2. General cases to simulate based on the more general clustering

General case	λ_c [W m^{-2} K^{-1}]	C_a [kJ m^{-2}K^{-1}]	Reference materials Layers from exterior to interior [mm]
GC_1 (TC_1)	0.44	20426	Ceramic siding (20) Air layer (20)

			Glass wool 16K (100) Air layer (60) Gypsum board (10)
GC_2 (TC_8)	2.72	375032	ALC (50) Air layer (100) Concrete (180)
GC_3 (TC_13)	7.19	416667	Concrete (220)
GC_4 (TC_14)	8.25	83629	Mortar (30) Plywood (12) Air layer (130) Plaster board (20)

Considering that the indoor air temperature may not be easily measured when applying this proposed estimation method in practice, the sensitivity of indoor air temperature was also simulated and analyzed. 28 ºC, 29 ºC, and 30 ºC as the constant indoor air temperature were input as IC_1, IC_2, and IC_3 case, respectively.

2.4.2 THERMORender model-based simulation

The THERMORender model based on surface energy balance model developed by Asawa et al. [10] was applied, and this model was described in the Section 2.1 in Chapter 2.

Regarding the August 01, 2018 conducting the multispectral RS as the target day, the meteorological data observed in the study area as shown in Fig.4 were input into THERMORender simulation (Section 2.4). With clear-sky conditions, the partition between the direct and diffuse components was calculated using Nagata's decomposition model[145] for the target day. The indoor air temperature observed on the middle floor of G3 building, as shown in Fig.7, was input into THERMORender simulation (Section 2.4).

Simulation cases were carried out with mesh sizes of 400 mm. In addition, the case with the best simulation result, which is consistent with the measured surface temperature, was also simulated with a mesh size of 200mm to test the sensitivity of the mesh size on the simulation accuracy.

2.4.3 Simulation based on multispectral brightness-radiation correlation and heat transfer model

(1) Estimation on at-surface shortwave radiation based on multispectral brightness-radiation correlation

The separation model (e.g., Nagata's[145] and Erbs[100] model) used in THERMORender is to split the input hourly global horizontal solar radiation into its direct and diffuse components, which usually starts from the clear-sky model to the subsequent cloudy sky model[146] and reliable cloud condition should be obtained. The direct and diffuse fraction of solar radiation in clear sunny day can be well predicted, and thus the at-tilt surface radiation;

whereas they are difficult to be estimated when it is in a cloudy-sky day due to that the real-time information of rapid variation of cloud cover is hard to obtain[147]. In order to adopt the estimation method on thermal properties proposed here to the cloudy days, another simulation method is developed based on multispectral brightness-radiation correlation and heat transfer model.

With the assumption of the Lambertian surface, the narrowband radiation within each band of multispectral camera reflected by the surface can be calculated by multispectral brightness. The detailed calculation equations are shown in follows. First, radiant intensity I_θ(W/sr) and brightness L_θ (W/m^{2}sr) can be expressed by equations (1) and (2), respectively.

$$I_\theta = d\Phi/d\Omega \qquad (1)$$

$$L_\theta = I_\theta/dS \cdot \cos\theta \qquad (2)$$

Where the $d\Phi$ is the element of radiant flux, $d\Omega$ is the element of solid angle, dS is the element of the area of the surface reflecting (can be regarded as emitting) the radiation, and θ is as shown in Fig.11.

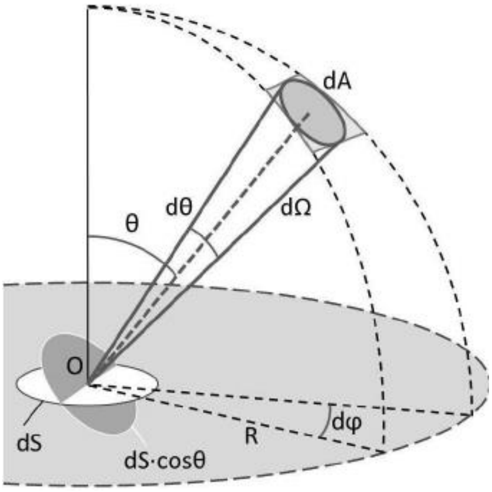

Figure 11. Solid angle and radiance (online: https://math.stackexchange.com/questions/3121489/can-there-be-two-adjacent-solid-angles)

Based on equation (1) and (2), the $d\Phi$ can be calculated based on equation (3), and thus the the Φ can be calculated by equation (4).

$$d\Phi = I_\theta \cdot d\Omega = L_\theta \cdot \cos\theta \cdot dS \cdot d\Omega = L_\theta \cdot \cos\theta \cdot dS \cdot \sin\theta \cdot d\theta \cdot d\varphi \qquad (3)$$

$$\Phi = L\int_0^S dS \int_0^{2\pi} d\varphi \int_0^{\pi/2} \cos\theta \cdot \sin\theta \cdot d\theta = \pi \cdot L \cdot S \qquad (4)$$

Where φ is as shown in Fig.11. Hence, the radiant exitance, M, can be calculated based on the brightness by equation (5).

$M = \Phi/S = \pi \cdot L$ (5)

In our case, the radiation for wavelength i, $R(\lambda_i)$, reflected by the Lambertian surface can be regarded as the radiant exitance in λ_i from the surface, which equation is as:

$R(\lambda_i) = M_i = \pi \cdot L_i$ (6)

Following the above steps, the correlation study can be turned to the conversion from narrowband radiation within each band of multispectral camera to the total shortwave radiation, which is similar to the narrow-to-broadband conversion on albedo estimation as shown in Chapter 3.

SMARTS as introduced in Section 2.4.1 of Chapter 3 was applied to simulate the hourly (05:00-18:00) at-surface solar spectral irradiance with the input of the same location (Lat./Lon.: 35° 30’ 45’’ N/139° 29’ 04’’ E) and azimuth (320º) as G3 NW surface with a height of 4m and 40m on August 1, 2018. Based on these hourly spectral irradiances, the total simulated solar radiation, R_{sw_s}, can be calculated by integrating the simulated spectral irradiance of solar radiation (R_{s_s}) with the wavelength (λ_i) within the SW range [Eq. (7)], which is termed as simulated total solar radiation in this dissertation; whereas the hourly narrowband solar radiation was calculated by integrating solar spectral irradiance within the band spectral range corresponding to the ones captured by the studied camera, as shown in Eq. (8), termed as simulated narrowband solar radiation.

$$R_{sw\_s} = \int_{350}^{2500} R_{\_s}(\lambda_i)\, d\lambda \qquad (7)$$

$$R_{N\_s} = \int_{\mathrm{a_N}}^{\mathrm{b_N}} R_{\_s}(\lambda_i)\, d\lambda / (\mathrm{b_N} - \mathrm{a_N}) \qquad (8)$$

where R_{N_s} is simulated average solar radiation of the target surface within band N, $R_{\_s}(\lambda_i)$ is the at-surface solar spectral irradiance at wavelength λ_i (nm), and $\mathrm{a_N}$ and $\mathrm{b_N}$ are the lower- and upper- wavelength limits, respectively, corresponding to band N of the studied camera. Five band wavelengths captured by the RedEdge camera are shown in Table 1 of Chapter 3 as 465–485 (Blue), 550–570 (Green), 663–673 (Red), 712–722 (Red-Edge), and 820–860 (NIR). These band wavelength limits were input into Eq. (1) to calculate the narrowband solar radiation. The physics-based methodology which was described in Section in Chapter 3.1.2 was adopted to estimate the total solar radiation according to the above-simulated narrowband solar radiation. For the study camera of RedEdge camera, the total solar radiation of target surface was estimated by integrating narrowband solar radiations across the SW spectrum as Eq. (9), assuming that radiation in the missing wavelength regions are estimated by linear interpolation of adjacent bands’ radiations, which is termed as estimated total solar radiation.

$$R_{sw\_e} = \sum R_{N_s} \cdot ((\mathrm{b_N} - \mathrm{a_N}) + 0.5 \cdot (\mathrm{a_N} - \mathrm{b_{N-1}}) + 0.5 \cdot (\mathrm{a_{N+1}} - \mathrm{b_N})) \qquad (9)$$

Where N= [1, 2, 3, 4, 5]. When N=1, $\mathrm{b_{N-1}}$=350; and when N=5, $\mathrm{a_{N+1}}$=2500.

The result of the simulated and estimated total solar radiation is shown in Fig.12. The regression model was developed as below.

$$R_{sw\_e\_reg} = 1.2551 \cdot R_{sw_e} + 20.647 \qquad (10)$$

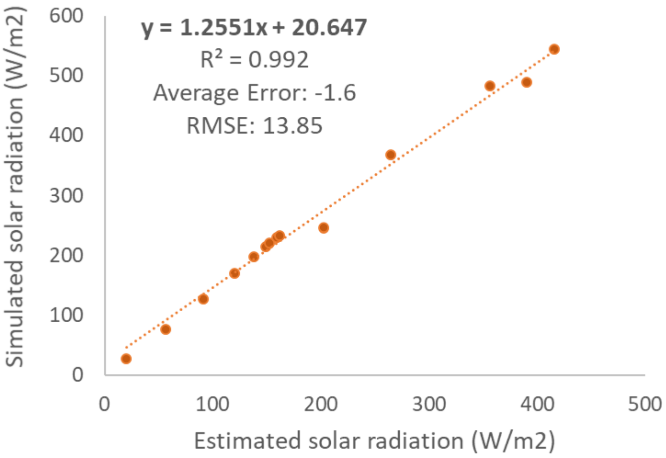

Figure 12. The simulated and estimated total solar radiation

With the adoption of this regression model, compared with the simulated solar radiation, the average error is only about -1.6W/m^2 and RMSE is about 13.85 W/m^2.

Based on the measurement as described in Section 2.2.2, the average radiation for each wavelength within a band of multispectral can be calculated based on the average brightness of this band captured by RedEdge camera following the Eq. (6). After that, the narrowband shortwave radiation of band *N* can be calculated by applying Eq. (8). With the input of narrowband shortwave radiation of band *N*, the total shortwave radiation was estimated following Eq. (9), which is termed as estimated shortwave radiation. Compared with the measured total shortwave radiation, the result of the estimated total shortwave radiation is shown in Fig.13 and another regression model was developed as below.

$$R_{sw\_e\_reg} = 1.3056 \cdot R_{sw_e} + 20.155 \qquad (12)$$

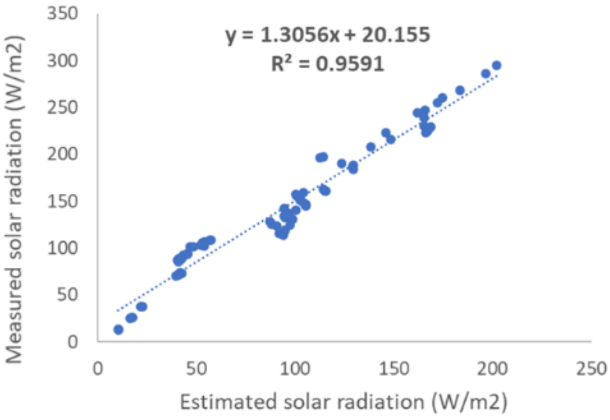

Figure 13. The measured and estimated total shortwave radiation

As shown in Fig.13, it generally reveals a linear relation but the regression model was easily affected by the sample selections due to the measurement error (e.g., horizontal placement of RP and pyranometer, at-nadir observation by using multispectral camera, and varying radiation affecting readings from data logger) and limited number of samples. However, we found a very small difference between these two regression models, Eq. (10) and (12). The better fitted model of Eq. (10) was thus applied.

After following Eq. (10), the estimated shortwave radiations reflected by the studied four small regions (Fig.5) are shown in Fig.14.

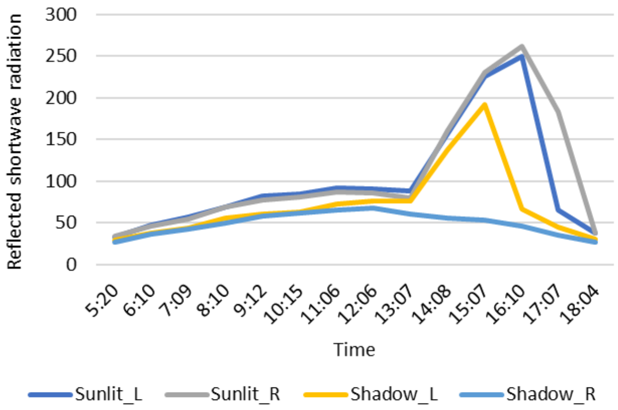

Figure 14. Shortwave radiation reflected by the studied small regions on G3 NW wall surface

Considering the RMSE of about 0.03 for estimating total albedo based on the narrowband albedos obtained by multispectral camera (Chapter 3), the error propagation can be calculated when adopting the developed Eq. (10) to estimate the at-surface shortwave radiation in this chapter case.

The probably value range of the G3 wall albedo is 0.6±0.03 (i.e., 0.57-0.63). The absorbed solar radiation can be calculated by Eq. (11).

$$R_{sw\_abs} = R_{sw\_ref} \cdot (1-\alpha)/\alpha \qquad (11)$$

In the case of G3 wall, if the G3 wall albedo of 0.6 is overestimated, the variable $(1-\alpha)/\alpha$ is ranged 0.667-0.7544, causing the shortwave radiation is probably underestimated (termed as $R_{sw\_abs\_under}$); while if the albedo of 0.6 is underestimated, this variable is ranged 0.587-0.667, causing the shortwave radiation is probably overestimated (termed as $R_{sw\_abs\_over}$). Fig.14 shows the temporal variation of the shortwave radiation reflected by 5 small regions being either sunlit or shadowed which were estimated following the Eq. (10). As shown in Fig.14, the minimum and maximum of the reflected shortwave radiation on G3 wall is respectively about 26 W/m^2 and 230 W/m^2, so the radiation error with the overestimated albedo (higher by 0.03) is ranged from -2.27 to -23 W/m^2 and that with the underestimated albedo (lower by 0.03) is ranged from 2.08 to 21 W/m^2. As shown in Fig.14, the small regions on G3 wall with the maximum and minimum reflected shortwave radiation are Sunlit_R and Shadowed_R regions, respectively. Fig.15 shows the temporal variation of the absorbed shortwave radiation and the overestimated and underestimated ones respectively caused by an under- and overestimated albedo in Sunlit_R (left Fig.15) and Shadowed_R region (right Fig.15) estimated here. It demonstrates that the error is small with a radiation difference of less than 9 W/m^2 when the target surface region is shadowed or with a shortwave radiation reflected by itself of lower than 100 W/m^2.

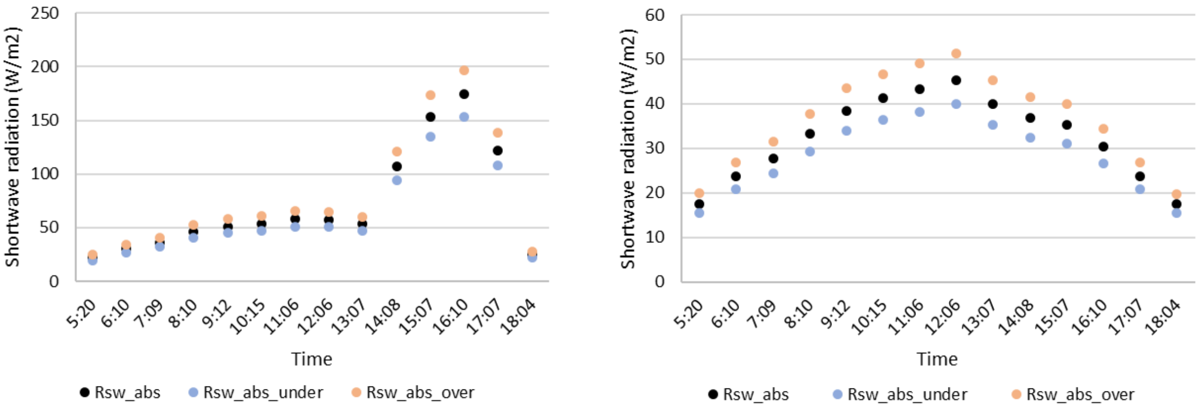

Figure 15. Temporal variation of the absorbed shortwave radiation and the overestimated and underestimated ones in Sunlit_R (left) and Shadowed_R region (right).

(2) Estimation on at-surface longwave radiation

The atmospheric longwave radiation budget on the studied region of G3 wall surface can be calculated based on the emissivity of G3 wall surface, sky temperature, air temperature, and sky view factor ($\emptyset_{sky}$) following the Planck's equation [Eq.(12)] and (13) below.

$$f(\lambda,T) = \frac{C_1}{\lambda^5 \cdot (e^{C_2/\lambda \cdot T} - 1)} \qquad (12)$$

Where the constant C_1 equals 1.191042×10^8 $(W/m^2/sr/um^{-4})$, C_2 equals 1.4387752×10^4, λ is the wavelength (um), and T is the blackbody temperature (K).

$$L_{at} = \varepsilon_{G3} \cdot \emptyset_{sky} \cdot \pi \cdot \int_4^{1000} f(\lambda,T) d\lambda \qquad (13)$$

Where the global atmospheric radiation, L_{at}, was calculated based on Planck's equation with air temperature (T_a) for wavelength 4-7um and 15-1000um, and sky temperature (T_{sky}) derived from hourly infrared images for 8-14um. Hence the Eq.(13) can be converted into Eq.(14) below.

$$L_{at} = \varepsilon_{G3} \cdot \emptyset_{sky} \cdot \pi \cdot (\int_4^8 f(\lambda,\ T_a) d\lambda + \int_8^{14} f\big(\lambda,\ T_{sky}\big) d\lambda + \int_{14}^{1000} f(\lambda,\ T_a) d\lambda) \qquad (14)$$

The following process was used to calculate the sky view factor (SVF): (a) Exportation of panorama images from Vectorworks 3D model; (b) Conversion of the panorama images into orthographic projection images; (c) SVF calculation using a Rayman model-based software[148]. The panorama images and SVF monochromes (screenshots from Rayman) for the selected regions on G3 NW wall surface are shown in Fig.16. Their sky view factors calculated are shown in Table 8.

Table 3. Sky view factor of the selected regions on G3 NW wall surface

Region on G3 NW wall	Sky view factor (%)
Sunlit_L	33.3
Sunlit_R	47
Sunlit_R2	38
Shadowed_L	26.5
Shadowed_R	24.1

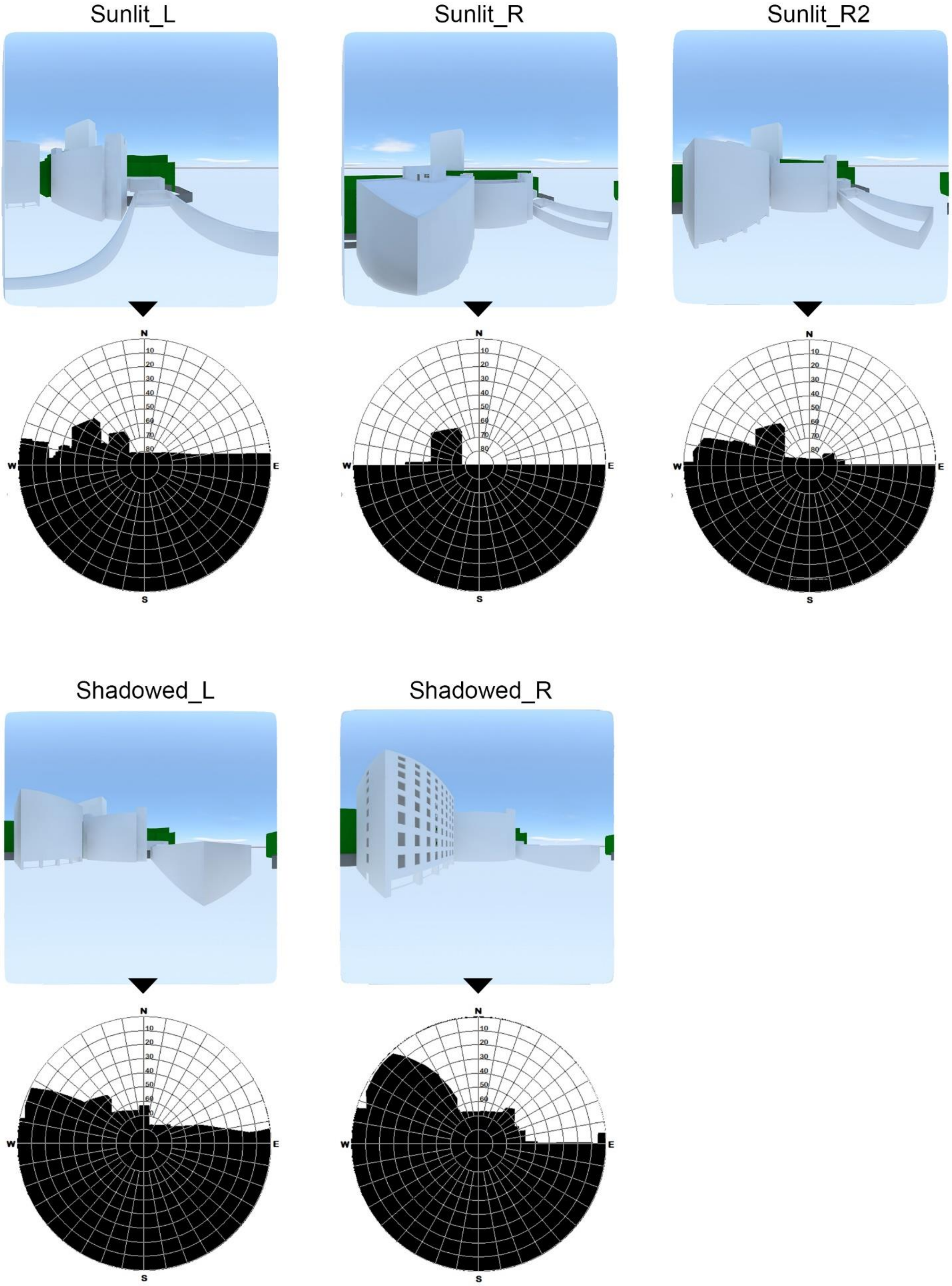

Figure 16. Panorama images and SVF monochromes (screenshots from Rayman software [148]) of the selected regions on G3 NW wall surface

The environmental longwave radiation budget on the studied region of G3 wall surface was calculated following the Eq. (15) below.

$$L_{en} = \varepsilon_{G3} \cdot \sigma \cdot (\sum \varepsilon_{i \cdot en} \cdot \emptyset_{i \cdot en} \cdot {T_{si \cdot en}}^4 - {T_{s \cdot G3}}^4) \qquad (15)$$

Where σ was Stefan-Boltzmann constant, and the $\varepsilon_{i \cdot en}$, the emissivity of the *i*-th surface of the surrounding environment, was assumed to be the same due to the commonly high emissivities for construction materials [97] and plants[149]. The air temperature was assumed approximating the surface temperature of the surrounding environment. The total view factor of all the surfaces of the surrounding environment can be calculated according to the sky view factor, i.e., $1 - \emptyset_{sky}$. Hence, the Eq. (15) can be written as Eq. (16) below.

$$L_{en} = \varepsilon_{G3} \cdot \sigma \cdot (\varepsilon_{en} \cdot (1 - \emptyset_{sky}) \cdot {T_a}^4 - {T_{s \cdot G3}}^4) \qquad (16)$$

Where ε_{G3} (emissivity of G3 wall surface) was set as 0.95, and the emissivity of the surfaces of the surrounding environment, ε_{en}, was approximated to be 1.

The longwave radiation budget on the studied regions on G3 wall surface, L_{total}, can be calculated as the accumulation of L_{at} and L_{en} [Eq. (17)].

$$L_{total} = L_{at} + L_{en} \qquad (17)$$

2.4.4 Influence of error of estimated albedos in simulation results and estimating thermal properties

The estimated shortwave radiations reflected by the studied four small regions are shown in Fig.2.

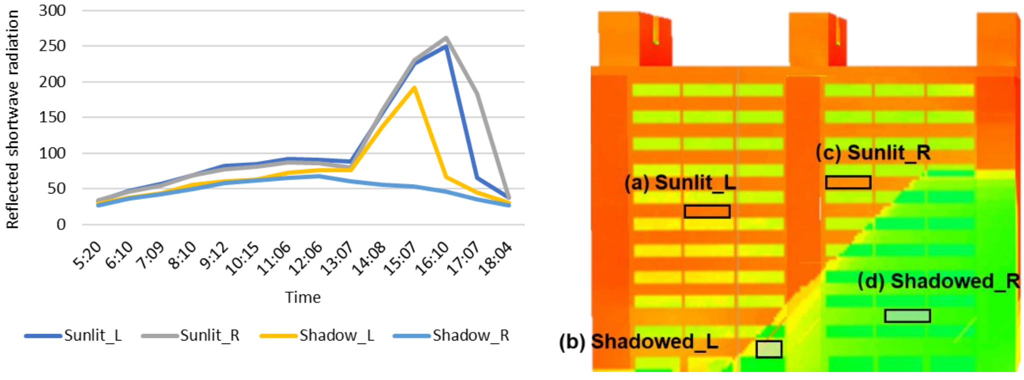

Figure 17. Shortwave radiation reflected (left) by the studied small regions on G3 NW wall surface (right)

As shown in Fig.17, the small regions on G3 wall with the maximum and minimum reflected shortwave radiation are Sunlit_R and Shadowed_R regions, respectively. Considering the RMSE is about 0.03 for the estimated albedo of 0.6 for studied wall surface, the absorbed shortwave radiation when albedo is over overestimated (0.57) or underestimated (0.63) for R_sunlit and R_shadowed regions is shown in Fig.18.

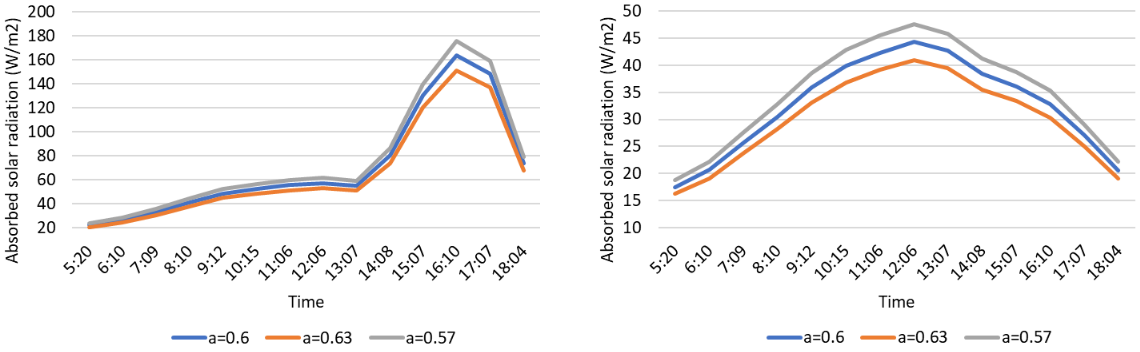

Figure 18. Absorbed solar radiation when albedo is overestimated (0.57) or underestimated (0.63) for R_sunlit and R_shadowed regions.

By inputting these absorbed solar radiations into the correct case TC_13 (Section 4.1), the simulated surface temperatures are shown in Section 3.3.

2.5 Theoretical method on thermal properties

The estimated values of thermal properties obtained by our method here were validated by a theoretical method based on ISO 6946, with the known composition and thermal properties of layers for the target wall surfaces. $\delta i\ [m]$ is the thickness of each layer. The areal thermal resistance for each air layer (Ra) was given the standardized value of 0.09 m2 K W-1 here, and the number of air layers is m. Therefore, the total conductivity coefficient (λc [W m-2 K-1]) of the multilayer component of a building surface is calculated by Eq. (10):

$$\lambda_c = 1/A = 1/(\sum_{i=1}^{n}(\delta_i/\lambda_{ci}) + mAR_a) \qquad (10)$$

Cρi [kJ m-3 K-1] and Cai [kJ m-3 K-1] are the volumetric and areal specific heat capacities of a layer, respectively. The total areal specific heat capacity (Ca [kJ m-2 K-1]) of a multilayer building surface can be calculated by Eq. (11):

$$C_a = \sum C_{ai} = \sum(\delta i * C_{\rho i}) \qquad (11)$$

As stated in ISO9869-1, assuming that the theoretical value is accurate, the results are representative if the theoretical and in-situ measured values are less than 20% different. We also used this standard to validate the estimated values.

3. Result

3.1 THERMORender simulation result

Compared with the measurement-based surface radiant temperature, the results of the simulated surface radiant temperature (Section 2.5) of the studied 10 points on G3 NW wall surface, L1-5 and R1-5 (Fig.2), for case GC_1-4 are shown in Fig.19 and 20. Their mean bias error (MBE), mean absolute error (MAE), and root mean square error (RMSE) are shown in Table 4.

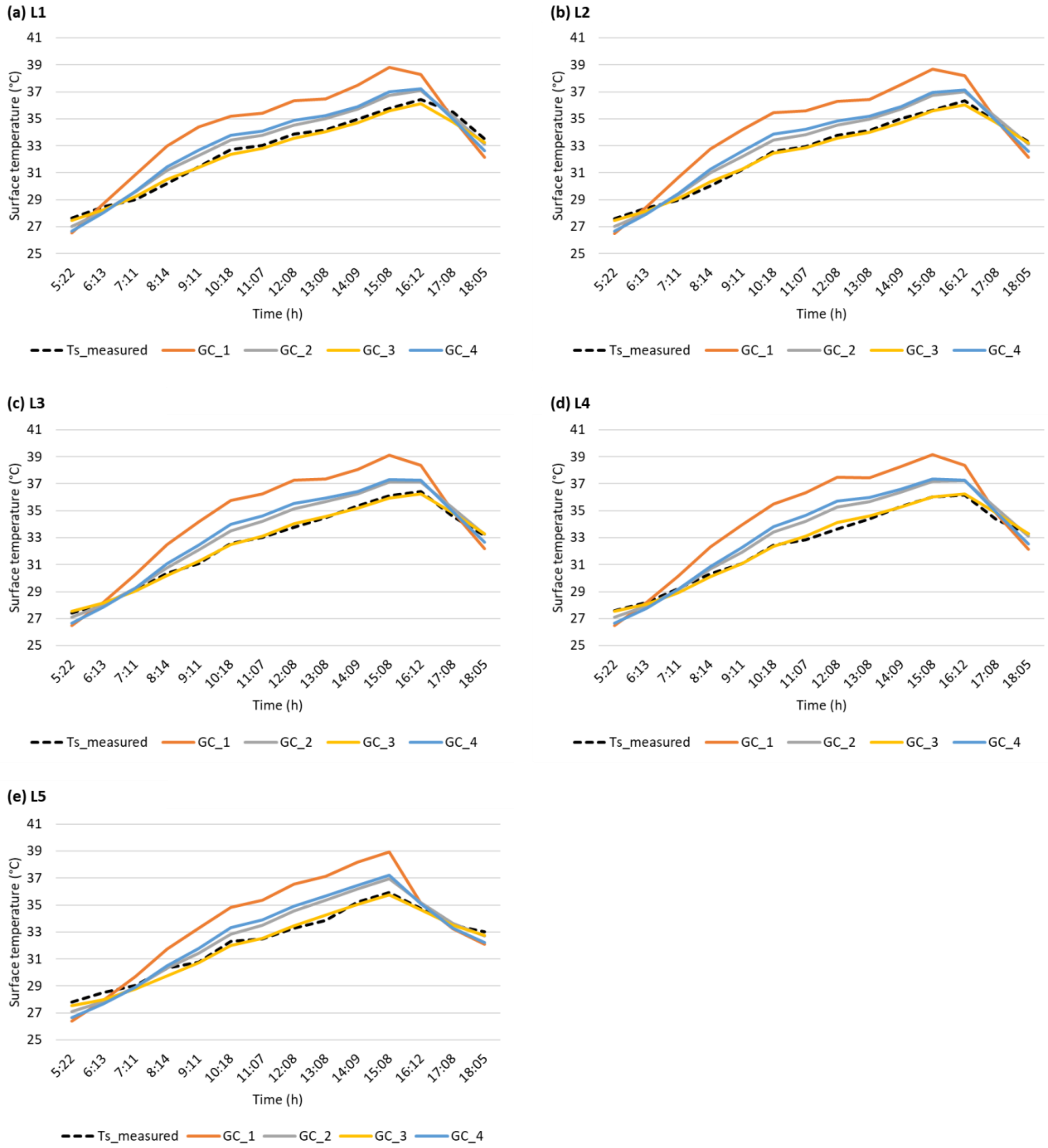

Figure 19. Measurement-simulation comparison for the case GC_1, 2, 3, 4 (shown in Table 2) in terms of the L1-5

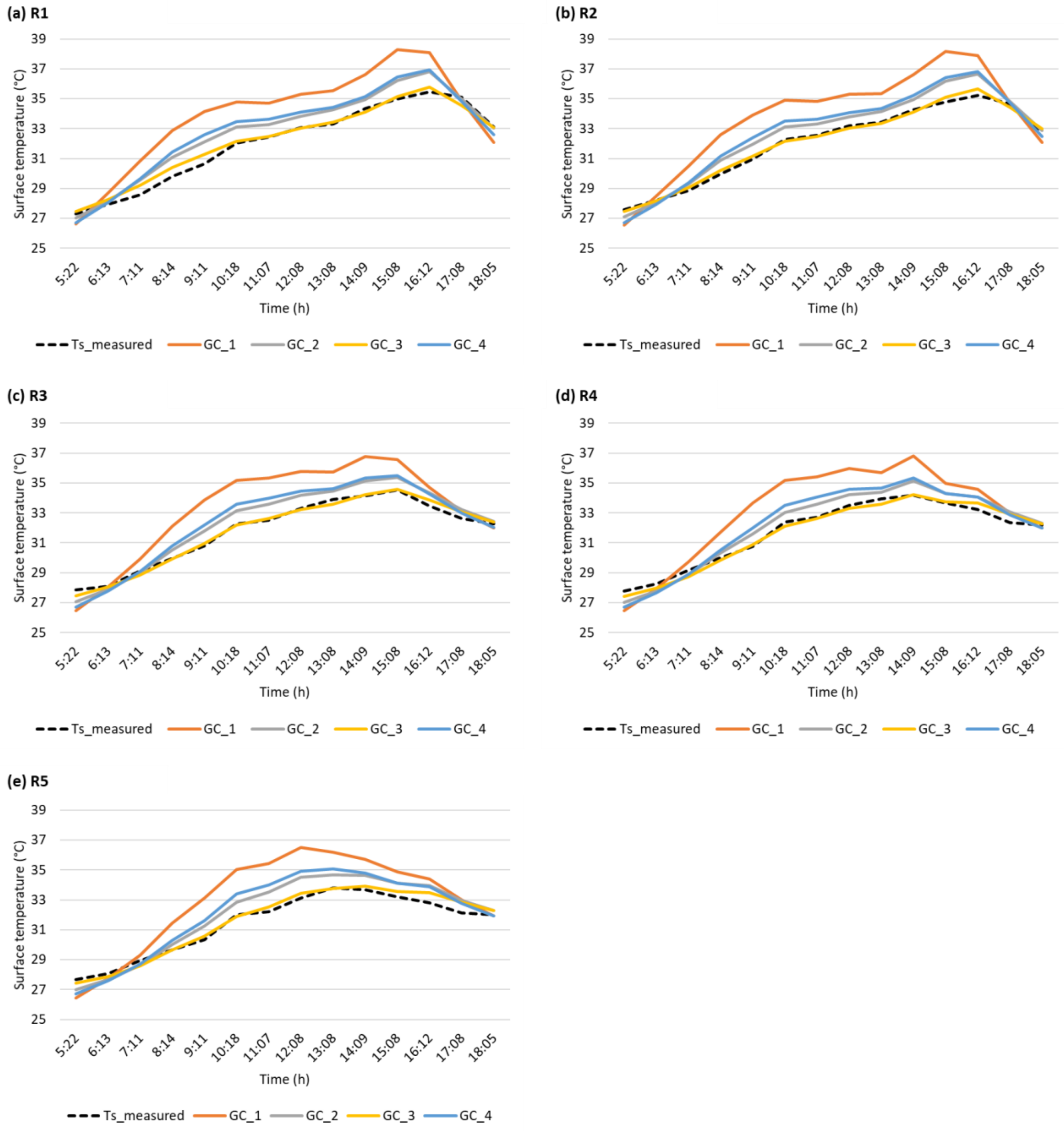

Figure 20. Measurement-simulation comparison for the case GC_1, 2, 3, 4 (shown in Table 2) in terms of the R1-5

Table 4. Mean bias error (MBE), mean absolute error (MAE), and root mean square error (RMSE) of the simulated surface radiant temperatures of case GC_1, 2, 3, 4.

Studied region	**Case**	**MBE (ºC)**	**MAE (ºC)**	**RMSE (ºC)**
L_1	GC_1	1.560	1.987	2.165
	GC_2	0.436	0.673	0.703
	GC_3	-0.189	0.260	0.301
	GC_4	0.533	0.942	0.973
L_2	GC_1	1.660	1.979	2.206
	GC_2	0.538	0.683	0.739
	GC_3	-0.072	0.146	0.176
	GC_4	0.636	0.926	0.999
L_3	GC_1	1.806	2.083	2.366
	GC_2	0.663	0.721	0.836
	GC_3	0.025	0.137	0.149
	GC_4	0.751	0.972	1.096
L_4	GC_1	1.839	2.164	2.466
	GC_2	0.685	0.830	0.951
	GC_3	0.056	0.169	0.231
	GC_4	0.770	1.077	1.212
L_5	GC_1	1.406	1.863	2.171
	GC_2	0.409	0.670	0.794
	GC_3	-0.151	0.243	0.296
	GC_4	0.494	0.938	1.078
R_1	GC_1	1.809	2.088	2.309
	GC_2	0.737	0.801	0.925
	GC_3	0.164	0.288	0.361
	GC_4	0.857	1.053	1.174
R_2	GC_1	1.654	1.905	2.140
	GC_2	0.599	0.691	0.795
	GC_3	0.043	0.180	0.206
	GC_4	0.716	0.929	1.040
R_3	GC_1	1.474	1.719	1.983
	GC_2	0.514	0.676	0.744
	GC_3	0.009	0.185	0.232
	GC_4	0.602	0.850	0.956
R_4	GC_1	1.363	1.623	1.869
	GC_2	0.396	0.618	0.664
	GC_3	-0.062	0.248	0.294
	GC_4	0.505	0.803	0.879
R_5	GC_1	1.533	1.764	2.060
	GC_2	0.606	0.798	0.871
	GC_3	0.161	0.291	0.352
	GC_4	0.728	0.974	1.099

Fig.19 and 20 reveal that the simulated radiant temperatures of case GC_3 were the closest to the measured ones with a very small differences, which was followed by GC_2 and GC_4; whereas, the GC_1's results demonstrate the largest difference from the measured radiant temperatures. To be more specific as shown in Table 4, the MAE and RMSE for L1-5 and R1-5 were ranged 0.137-0.291^{o}C and 0.149-0.361^{o}C for case GC_3, respectively, which were obviously smaller than the 0.618-0.801^{o} C (MAE range) and 0.664-0.925^{o} C (RMSE range) for GC_2 as the second closest case to the measured temperatures with a difference of at least about 0.37^{o} C for both MAE and RMSE, and up to about 0.67 and 0.72 ^{o} C for MAE and RMSE, respectively. When comparing with the GC_1, the error differences were ranged about 1.4-2 ^{o} C and 1.5-2.2 ^{o} C for MAE and RMSE, respectively.\

Based on the above results, the general cluster (GC cases) the target thermal combination belongs to can be determined as GC_3, four specific clusters of TC_13, TC_15, TC_10, and TC_11 included in GC_3 are the possible target thermal combinations needed to be further tested. In terms of the case TC_13, TC_15, TC_10, and TC_11, the point-to-point (L1-5 and R1-5 as shown in Fig.2) comparison between the simulation results and the measured surface radiant temperatures were shown in Fig. 21 and Fig. 22, and their MBE, MAE, and RMSE were shown in Table 5.

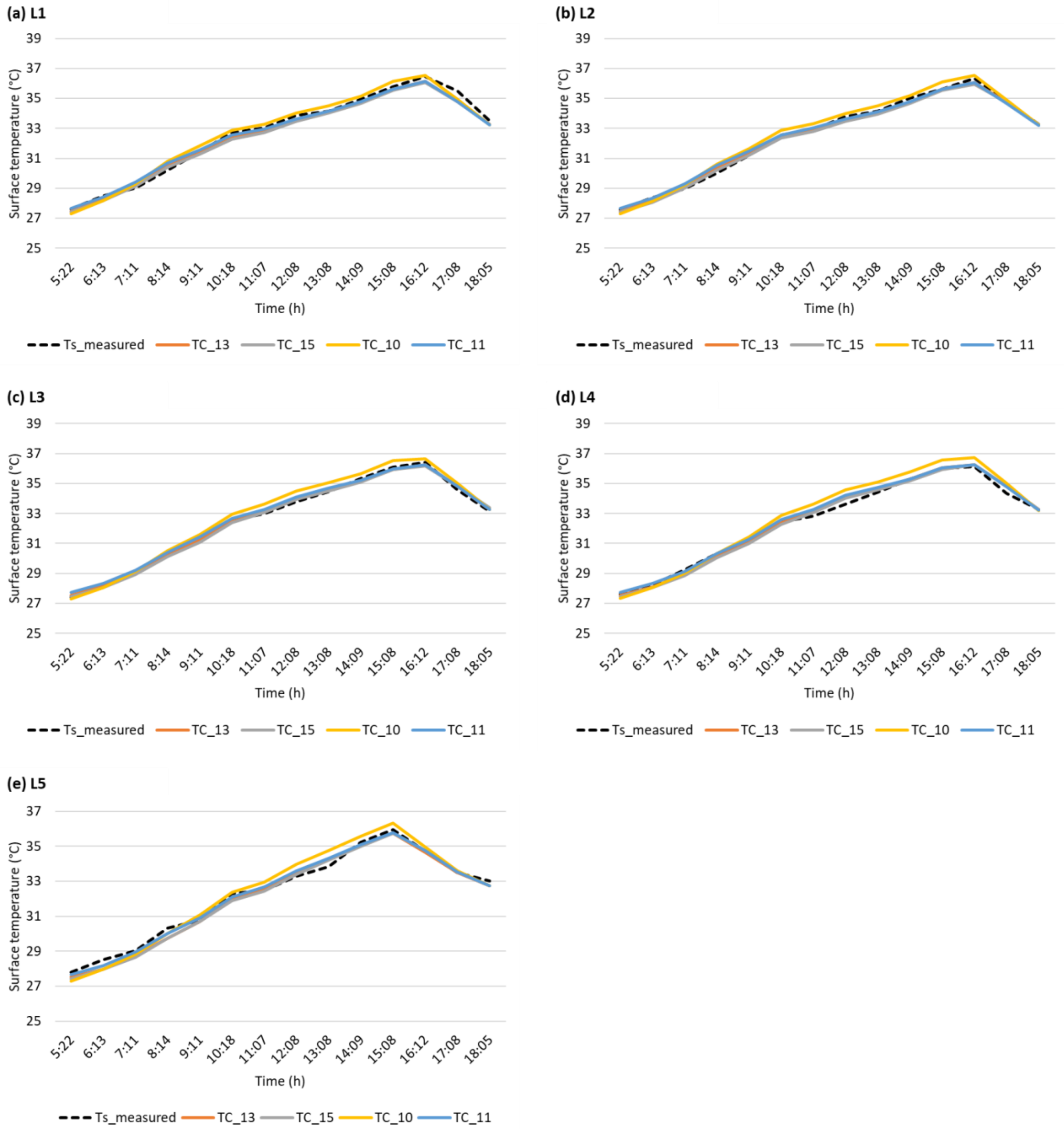

Figure 21. Measurement-simulation comparison for the case TC_13, 15, 10, 11 (shown in Table 2) in terms of the L1-5 (shown in Fig.2)

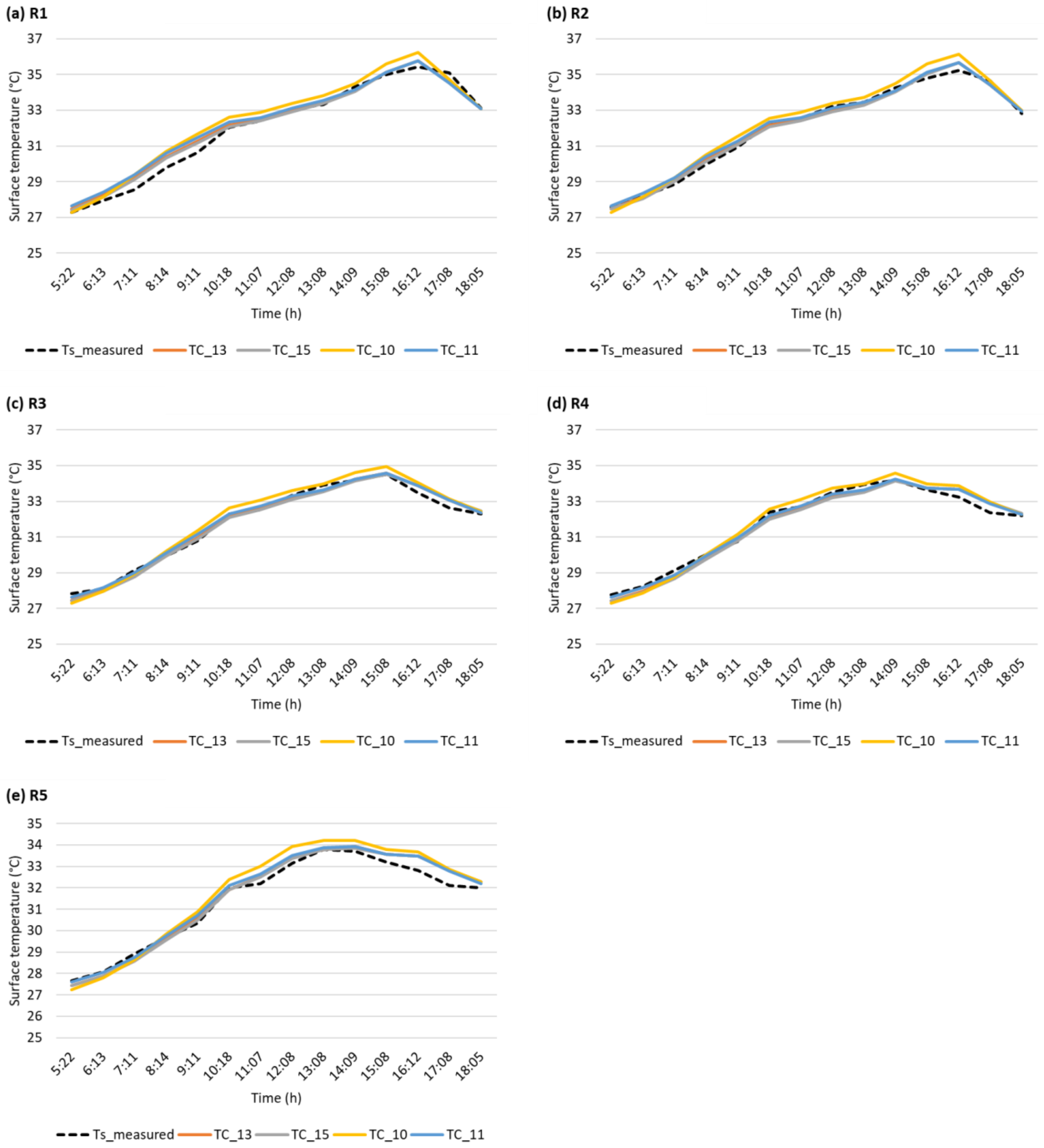

Figure 22. Measurement-simulation comparison for the case TC_13, 15, 10, 11 (shown in Table 2) in terms of the R1-5 (shown in Fig.2)

Table 5. MBE, MAE, and RMSE of the simulated surface radiant temperature of case TC_13, 15, 10, 11.

Studied region	Case	MBE (ºC)	MAE (ºC)	RMSE (ºC)
L_1	TC_13	-0.189	0.260	0.3011
	TC_15	-0.254	0.297	0.335
	TC_10	0.088	0.309	0.336
	TC_11	-0.083	0.231	0.301
L_2	TC_13	-0.072	0.146	0.176
	TC_15	-0.136	0.174	0.212
	TC_10	0.205	0.289	0.320
	TC_11	0.025	0.155	0.210
L_3	TC_13	0.025	0.137	0.149
	TC_15	-0.041	0.146	0.170
	TC_10	0.308	0.337	0.400
	TC_11	0.136	0.195	0.214
L_4	TC_13	0.056	0.169	0.231
	TC_15	-0.001	0.196	0.236
	TC_10	0.339	0.442	0.518
	TC_11	0.162	0.185	0.252
L_5	TC_13	-0.151	0.243	0.296
	TC_15	-0.180	0.261	0.316
	TC_10	0.121	0.383	0.445
	TC_11	-0.032	0.200	0.232
R_1	TC_13	0.164	0.288	0.361
	TC_15	0.104	0.259	0.327
	TC_10	0.427	0.482	0.573
	TC_11	0.266	0.380	0.469
R_2	TC_13	0.043	0.181	0.206
	TC_15	-0.013	0.200	0.215
	TC_10	0.313	0.364	0.445
	TC_11	0.141	0.207	0.254
R_3	TC_13	0.009	0.185	0.233
	TC_15	-0.041	0.202	0.256
	TC_10	0.237	0.364	0.405
	TC_11	0.091	0.177	0.225
R_4	TC_13	-0.062	0.248	0.294
	TC_15	-0.114	0.292	0.336
	TC_10	0.144	0.322	0.375
	TC_11	0.010	0.189	0.238
R_5	TC_13	0.161	0.291	0.352
	TC_15	0.130	0.275	0.338
	TC_10	0.364	0.506	0.552
	TC_11	0.236	0.268	0.339

**** Background of orangey color indicates the minimum error value among TC_13, 15, 10, and 11.***

As shown in Fig. 21 and 22, the TC_10 reveals smaller temperatures in the morning and larger peak temperatures which peak times for the target points can be observed to be a bit earlier than TC_13, 15, and 11 especially in Fig. 19(e). Whereas, the simulated surface radiant temperatures and their temporal variation TC_13, 15, and 11 in terms of the target points were observed significantly close based on Fig. 21 and 22. To be more specific, Table 5 reveals that daily average MAEs and RMSEs from sunrise to sunset of the TC_10 were generally larger than the other cases by 0.1-0.25 and 0.1-0.28, respectively, except for the points of L1 and R4 with much smaller MAE and RMSE differences. As shown in Table 5, TC_13 reveals smallest RMSEs for L1-L4 and R2 as the TC case with most points among 10 target points dominating the smallest RMSEs, which was followed by TC_11 with smallest RMSEs for L5, R3, and R4; whereas the TC_15 reveals smallest RMSEs for R1 and R5.

However, to better estimate the general performance of these 4 TC cases (i.e., TC_13, 15, 11, and 10) included in GC_3, the histograms of the hourly absolute error (AE) of the simulated surface temperatures for L1-5 and R1-5 compared with measured ones in terms of the TC_13, 15, 11, and 10 were shown in Fig. 23. Meanwhile, the RMSE, MBE, and frequency of the AE in terms of the case TC_13, 15, 10, 11 were shown in Table 6.

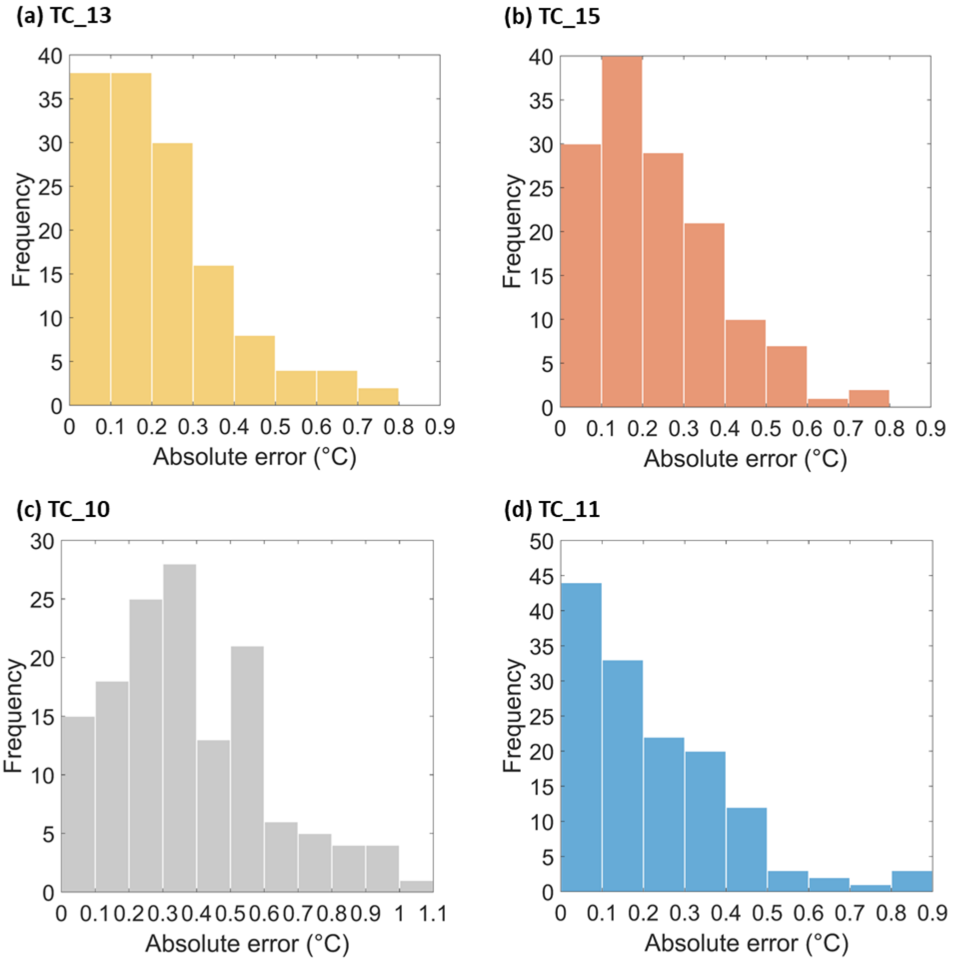

Figure 23. Histogram of the absolute error of the simulated surface temperatures compared with measured ones in terms of TC_13, 15, 11, and 10

Table 6. RMSE, MBE, and frequency of the MAE in terms of the case TC_13, 15, 10, 11.

Case	RMSE (ºC)	MAE (ºC)	Frequency of the AE <0.2	Frequency of the AE <0.3	Frequency of the AE >0.5	Frequency of the AE >0.7
TC_13	0.269	0.215	76	106	10	2
TC_15	0.281	0.230	70	99	10	2
TC_10	0.445	0.380	33	58	41	14
TC_11	0.284	0.219	77	99	9	4

As shown in Fig. 23 and Table 6, regarding the relatively low hourly AE lower than 0.2, the TC_13 reveals the largest AE number of 106, followed by TC_15 and 11 with the same AE number of 99, whereas the smallest AE number of 58 occurred on TC_10. In terms of the relatively high hourly AEs, the TC_13 and 15 reveal the same smallest number for hourly AEs above 0.5 and 0.7 as 10 and 2, respectively, which was followed by the TC_10 with a number of 9 and 4 for AEs above 0.5 and 0.7, respectively; whereas, the largest number of 41 and 14 occurred on TC_10 for hourly AEs above 0.5 and 0.7 as 10 and 2, respectively. As shown in Table 6, considering all the hourly errors, the TC_13 reveals the generally lowest RMSE and MAE of about 0.269 and 0.215, respectively, closely followed by TC_15 and TC_11 with the RMSEs of about 0.28 and MAEs of respectively 0.23 and 0.219. Whereas, the TC_10 was with the highest RMSE and MAE of about 0.445 and 0.38, respectively.

Following the process as shown in Fig. 4, the results of the grid-to-grid comparison were shown in Fig.24-27 with respect of the target moment of 05:22 (sunrise time: 04:50), 09:11, 13:08, and 18:05 (sunset time: 18:46) on August 01, 2018, respectively. The histograms of the grid-to-grid comparison-based errors for the target moments of 05:22, 0911, 13:08, and 18:05 were shown in Fig. 28, and their mean error (ME), MBE, and RMSE were shown in Table 7.

(a) TC_13

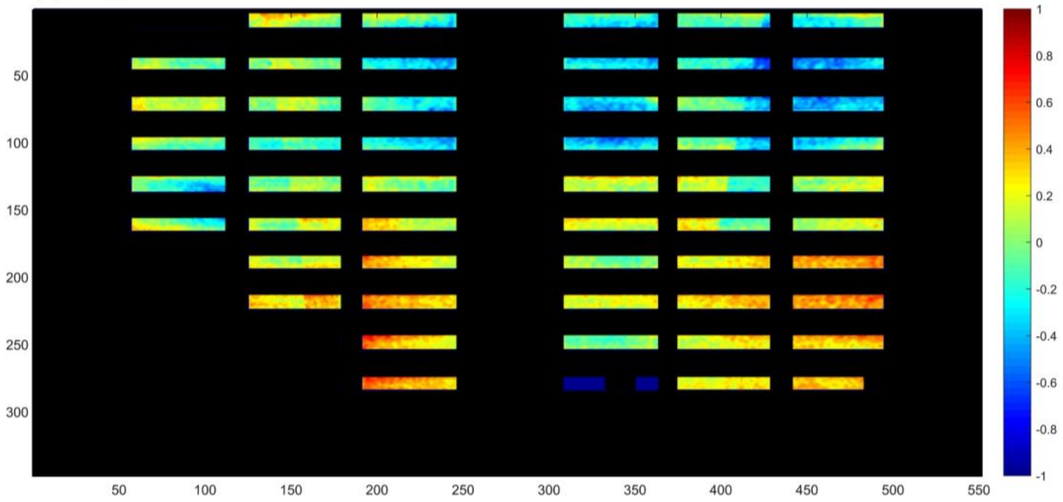

(b) TC_15

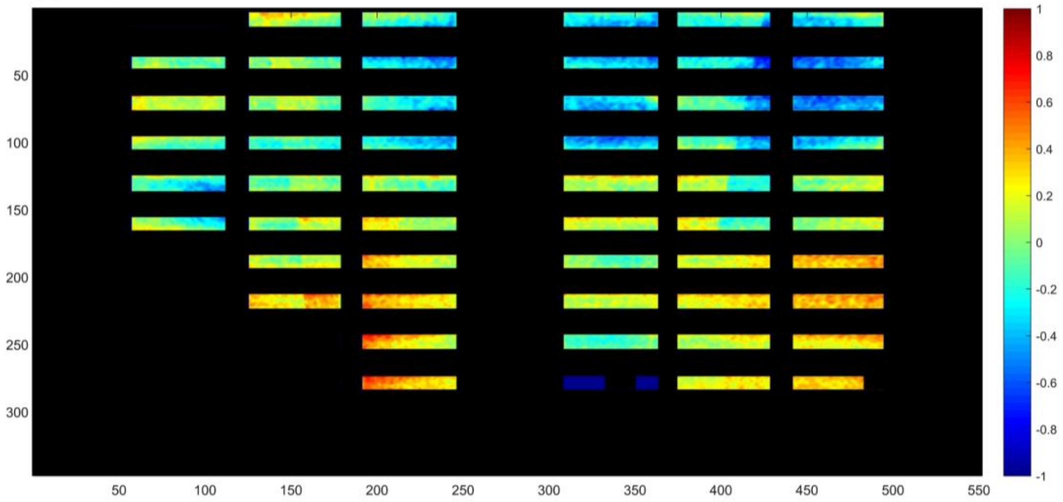

(c) TC_11

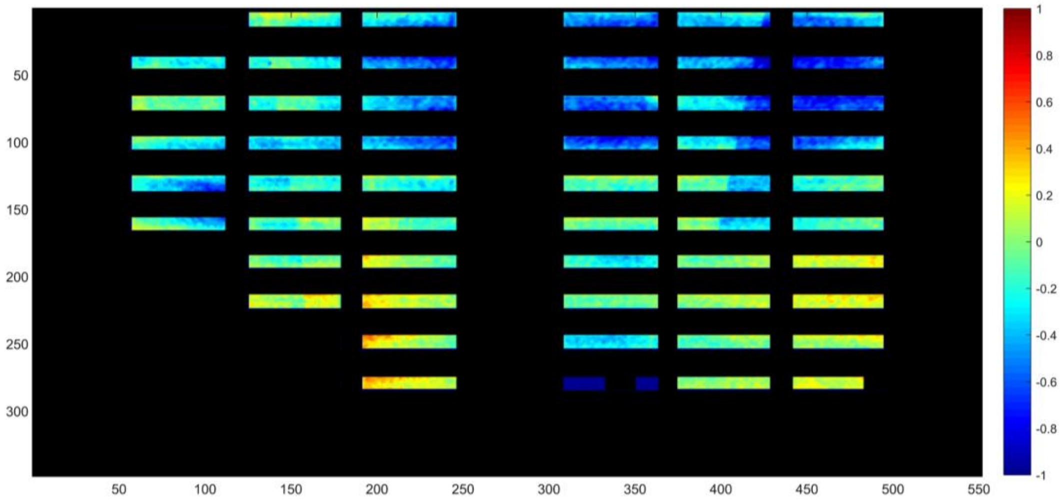

Figure 24. Grid-to-grid comparison of G3 NW wall surface between the infrared image and 2D spatial distribution of the simulated temperature for the target moment of 05:22

(a) TC_13

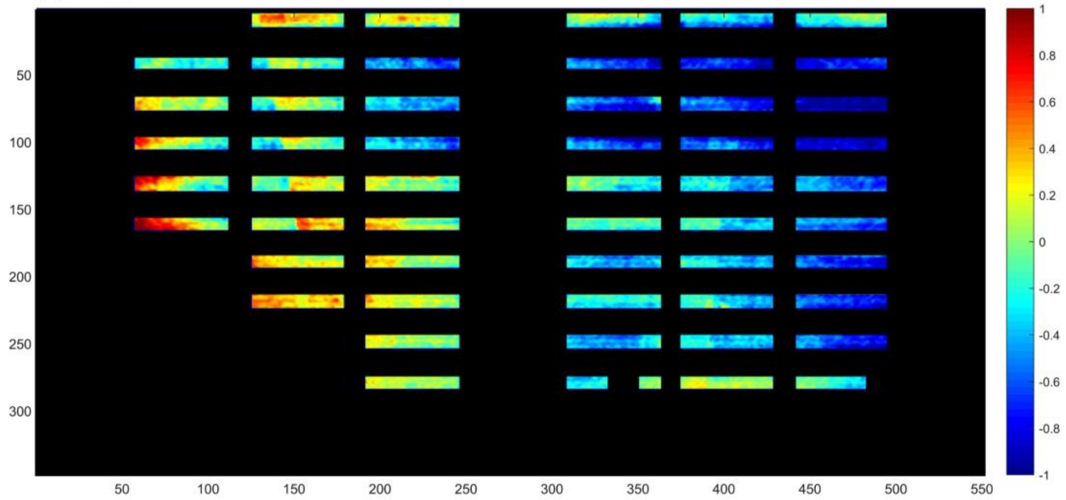

(b) TC_15

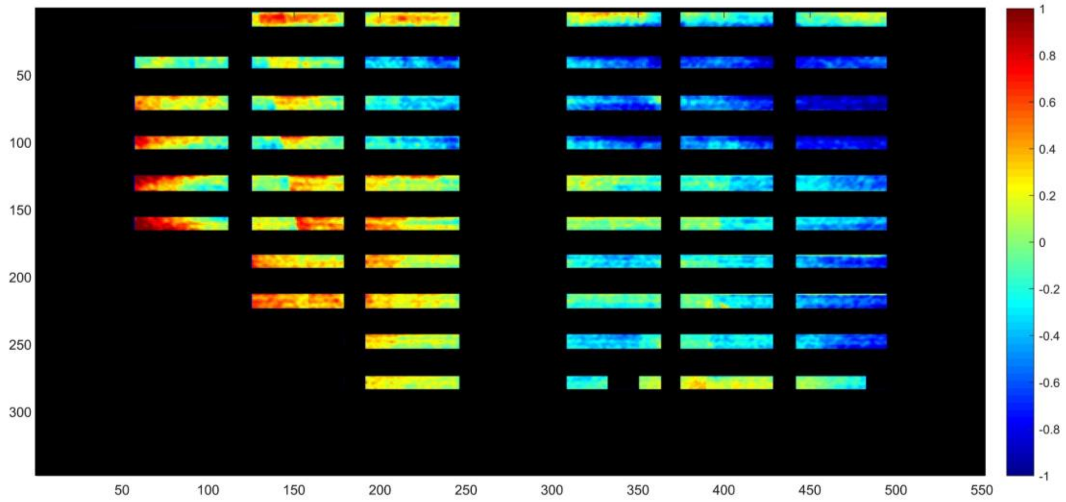

(c) TC_11

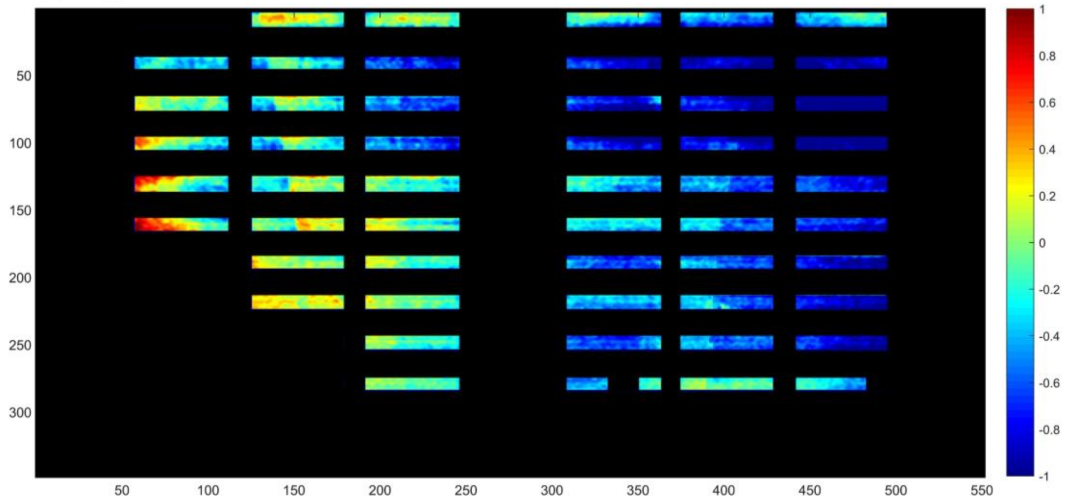

Figure 25. Grid-to-grid comparison of G3 NW wall surface between the infrared image and 2D spatial distribution of the simulated temperature for the target moment of 09:11

(a) TC_13

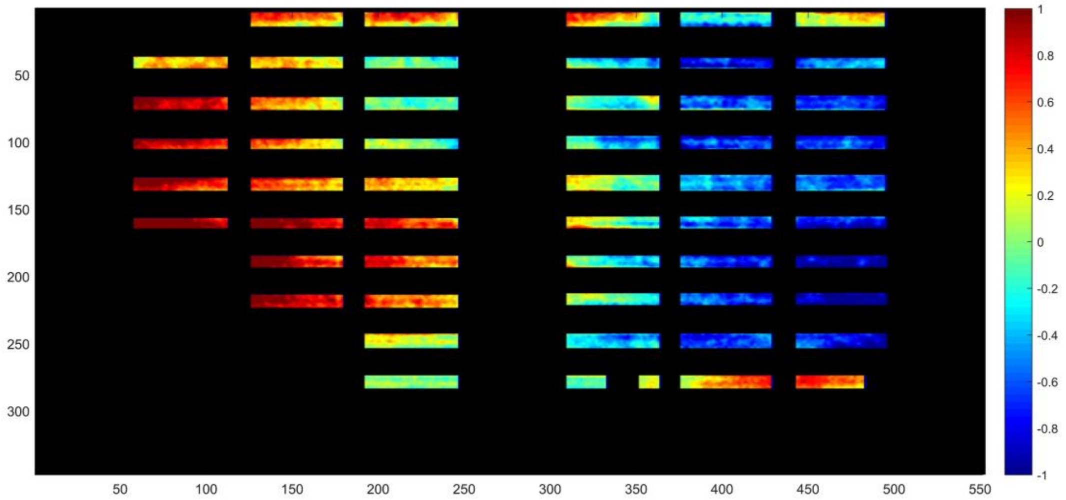

(b) TC_15

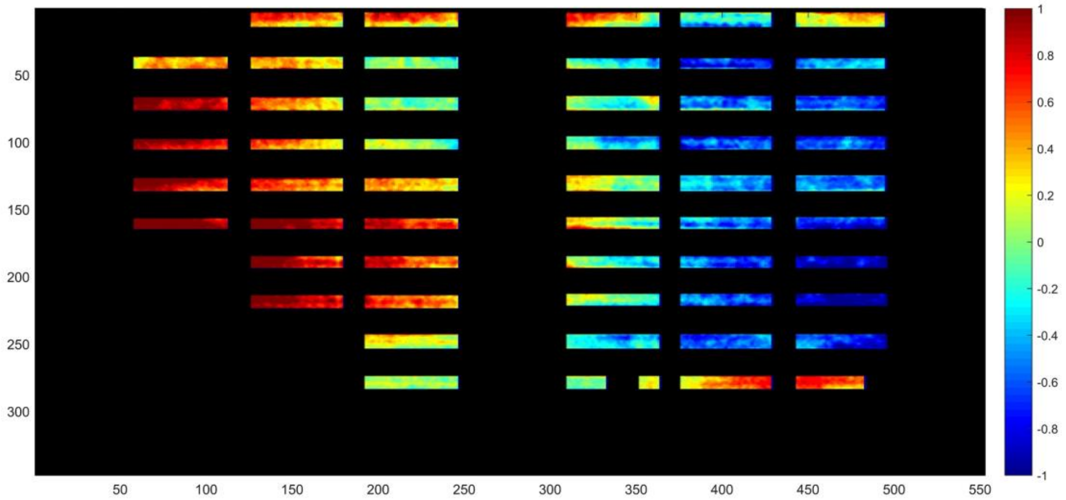

(c) TC_11

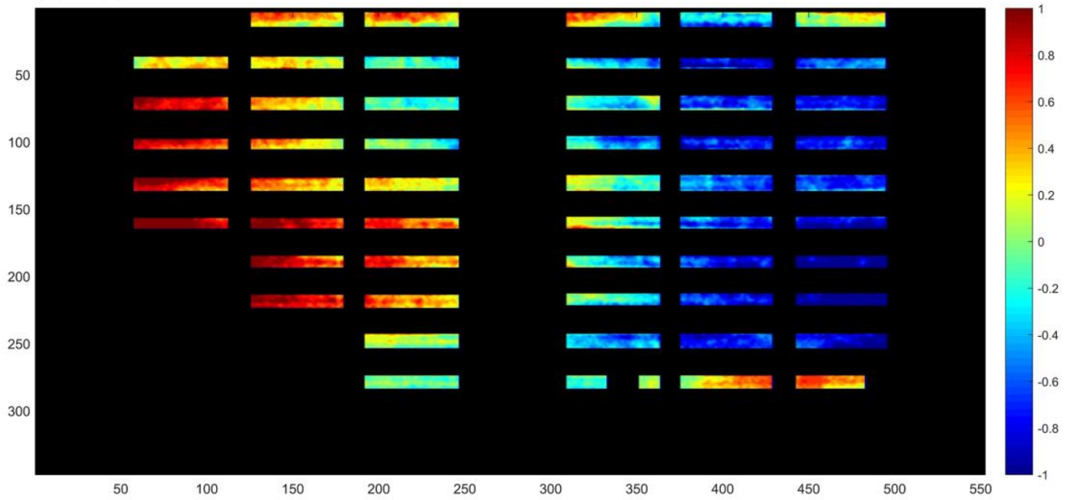

Figure 26. Grid-to-grid comparison of G3 NW wall surface between the infrared image and 2D spatial distribution of the simulated temperature for the target moment of 13:12

(a) TC_13

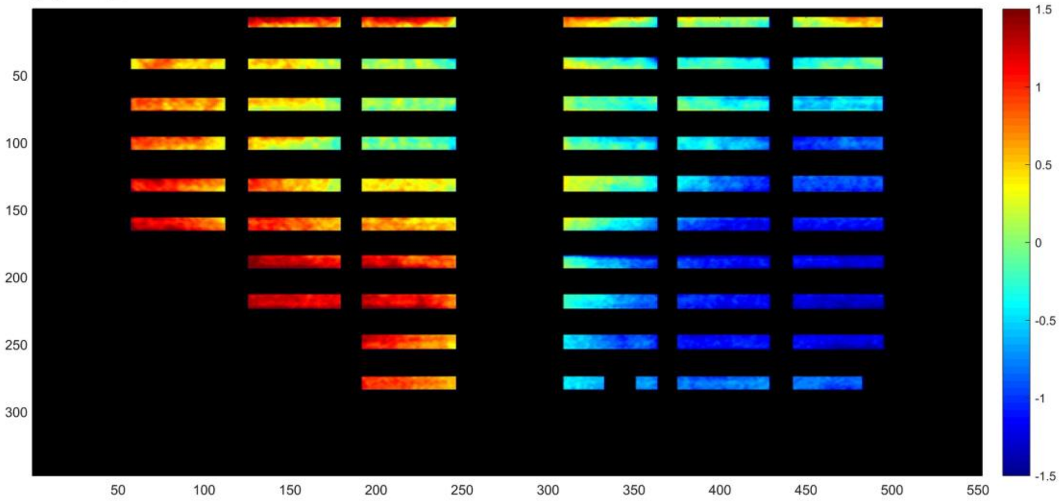

(b) TC_15

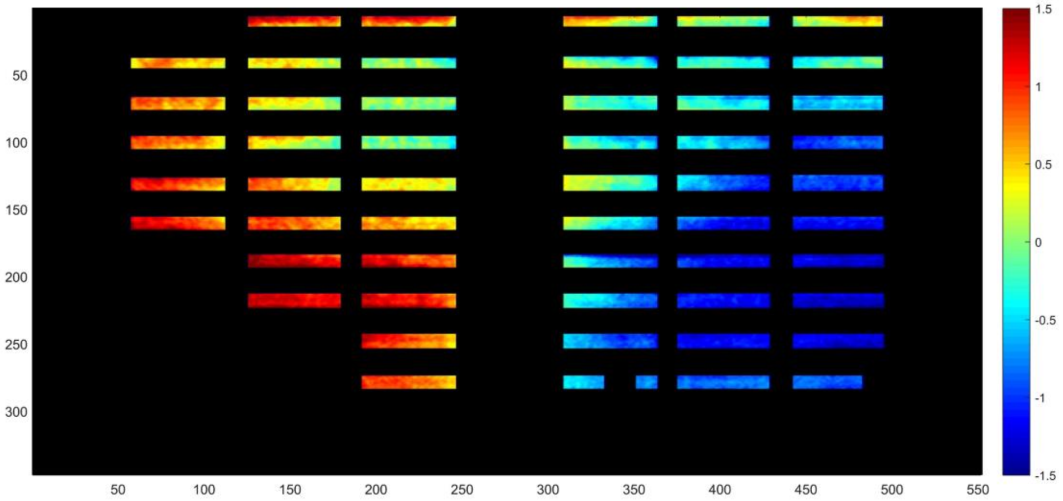

(c) TC_11

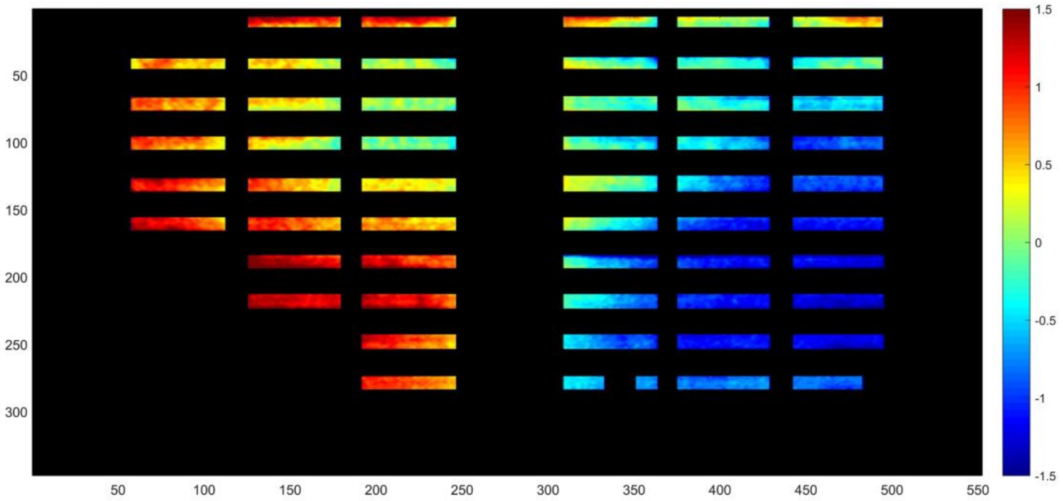

Figure 27. Grid-to-grid comparison of G3 NW wall surface between the infrared image and 2D spatial distribution of the simulated temperature for the target moment of 18:05

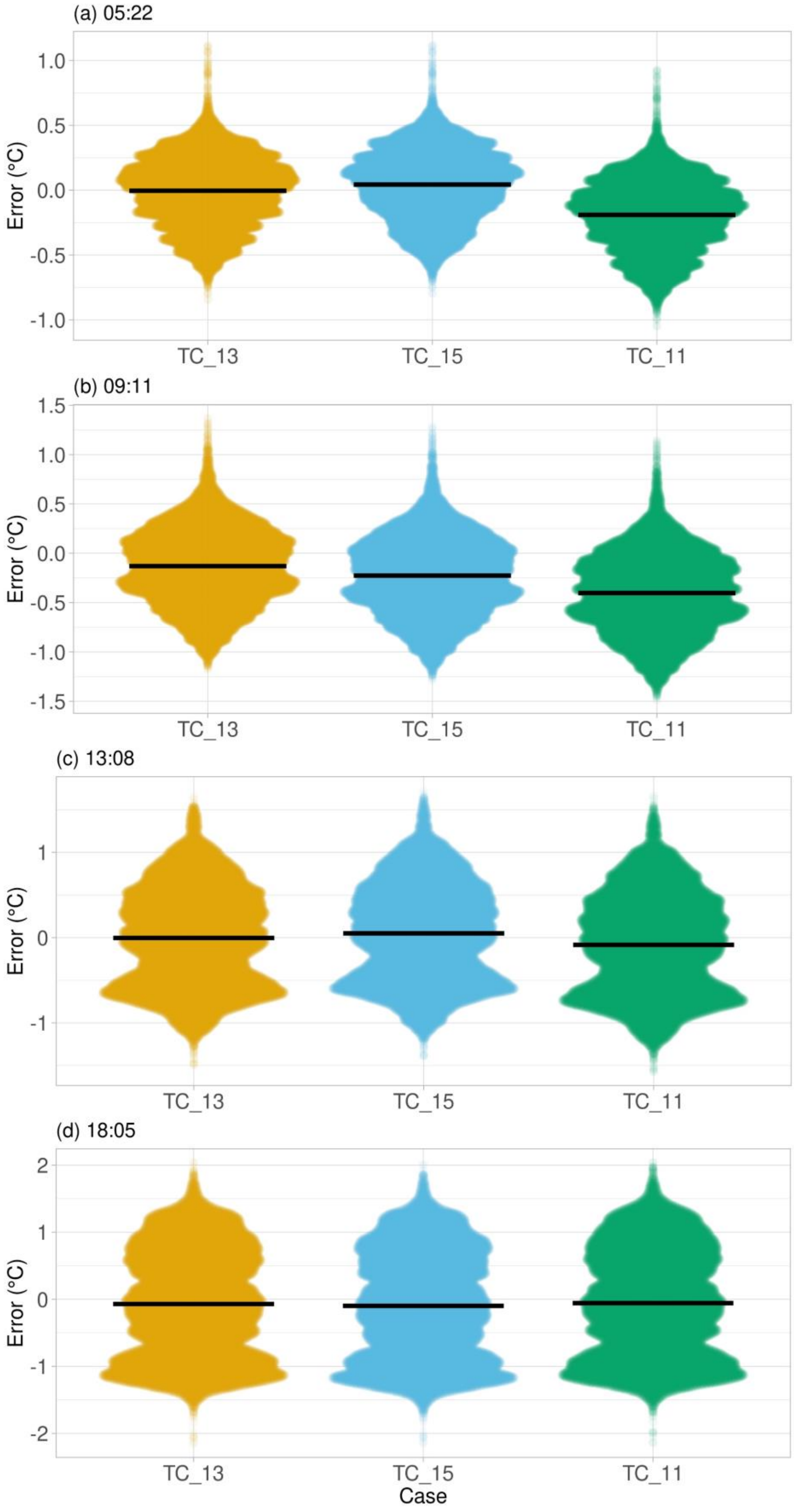

Figure 28. Histogram of the grid-to-grid comparison-based error for the target moments of 05:22, 0911, 13:08, and 18:05

Table 7. Mean error (ME), MBE, and RMSE in terms of the case TC_13, 15, 11.

	ME			MAE			RMSE		
	TC13	**TC15**	**TC11**	**TC13**	**TC15**	**TC11**	**TC13**	**TC15**	**TC11**
05:22	-0.004	0.043	-0.190	0.221	0.226	0.263	0.270	0.273	0.333
09:11	-0.130	-0.227	-0.403	0.332	0.365	0.466	0.409	0.453	0.568
13:08	-0.004	0.050	-0.085	0.494	0.491	0.502	0.581	0.579	0.594
18:05	-0.071	-0.098	-0.058	0.698	0.707	0.700	0.809	0.813	0.811

As shown in Fig. 24, the 2D distributions of the errors of the simulated surface radiant temperatures for the target moment of 05:22 reveals that the simulated surface radiant temperatures were generally close to the measured ones, but were a bit smaller and larger than the measured ones for the upper and lower sides of target wall surface, respectively. As shown in Fig. 25-27, the 2D distributions of the errors of the simulated surface radiant temperatures for the target moments of 09:11, 13:08, and 18:05 reveal that the simulated surface radiant temperatures were close to the measured ones in the middle region (higher middle region for 13:08, and 18:05) of the target wall surface with the errors mostly within the range from -0.5 to 0.5 ^{o}C, but they were generally larger than the measured ones for the lower left side of the target wall surface and smaller than the measured ones for the lower right side, especially obvious for the target moment of 18:05 as shown in Fig.27. As shown in Table 7, TC_13 demonstrates the closest-to-0 ME and smallest MAEs and RMSEs expect for the target moment of 13:08, when the smallest MAE and RMSE occurred for TC_15. However, as shown in Table 7, the largest gap among the MAEs and RMSEs of TC_13, 15, and 11 was very small for the target moments of 05:22, 13:08, and 18:05, which was up to respectively 0.04 ^{o}C and 0.06 ^{o}C, whereas a bit larger for the 09:11 with the gap of about 0.13 ^{o}C and 0.16 ^{o}C. Regarding the error values, the 18:05 was the moment revealing the largest MAEs and RMSEs regarding these three cases (TC_13, 15, and 11), followed by the moment of 13:08; whereas the 05:22 was the one demonstrating the smallest MAEs and RMSEs. In addition, the edges of the infrared thermal images used for mapping can be observed obviously in Fig. 24 and 25 for the target moments of 05:22 and 09:11.

Meanwhile, the sensitivities of the mesh size and indoor air temperature on the simulated temperatures were also tested based on the THERMORender simulations. The simulated surface radiant temperatures of the IC_1, IC_2, and IC_3 compared with those of the TC_13 and the measured ones in terms of the points of L1-5 and R1-5 (Fig.2) were shown in Fig.29 and Fig. 30, and the MBE, MAE, and RMSE regarding the target points were shown in Table 8.

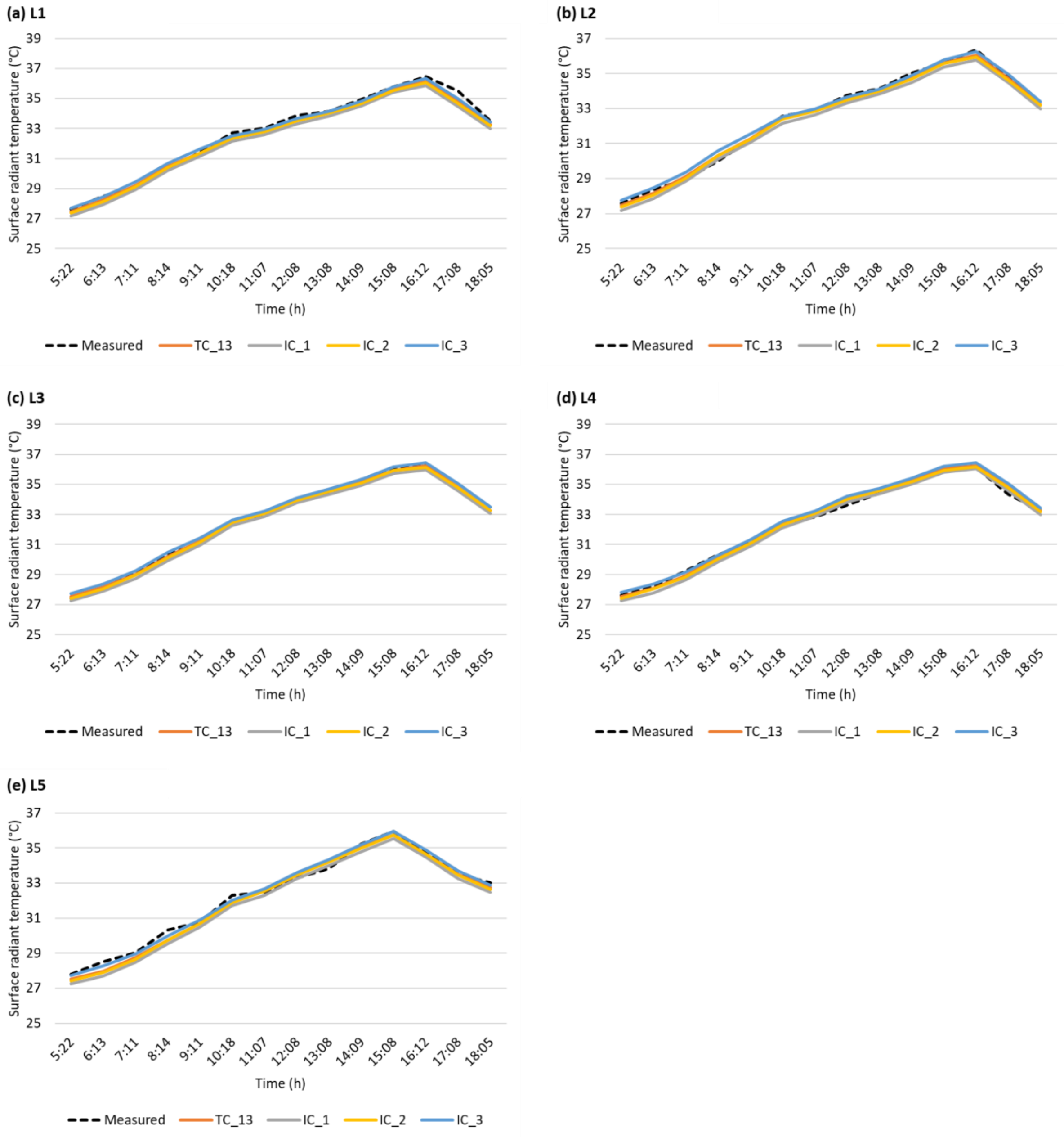

Figure 29. Measurement-simulation comparison for the case TC_13, 15, 10, 11 (shown in Table 2) in terms of the L1-5

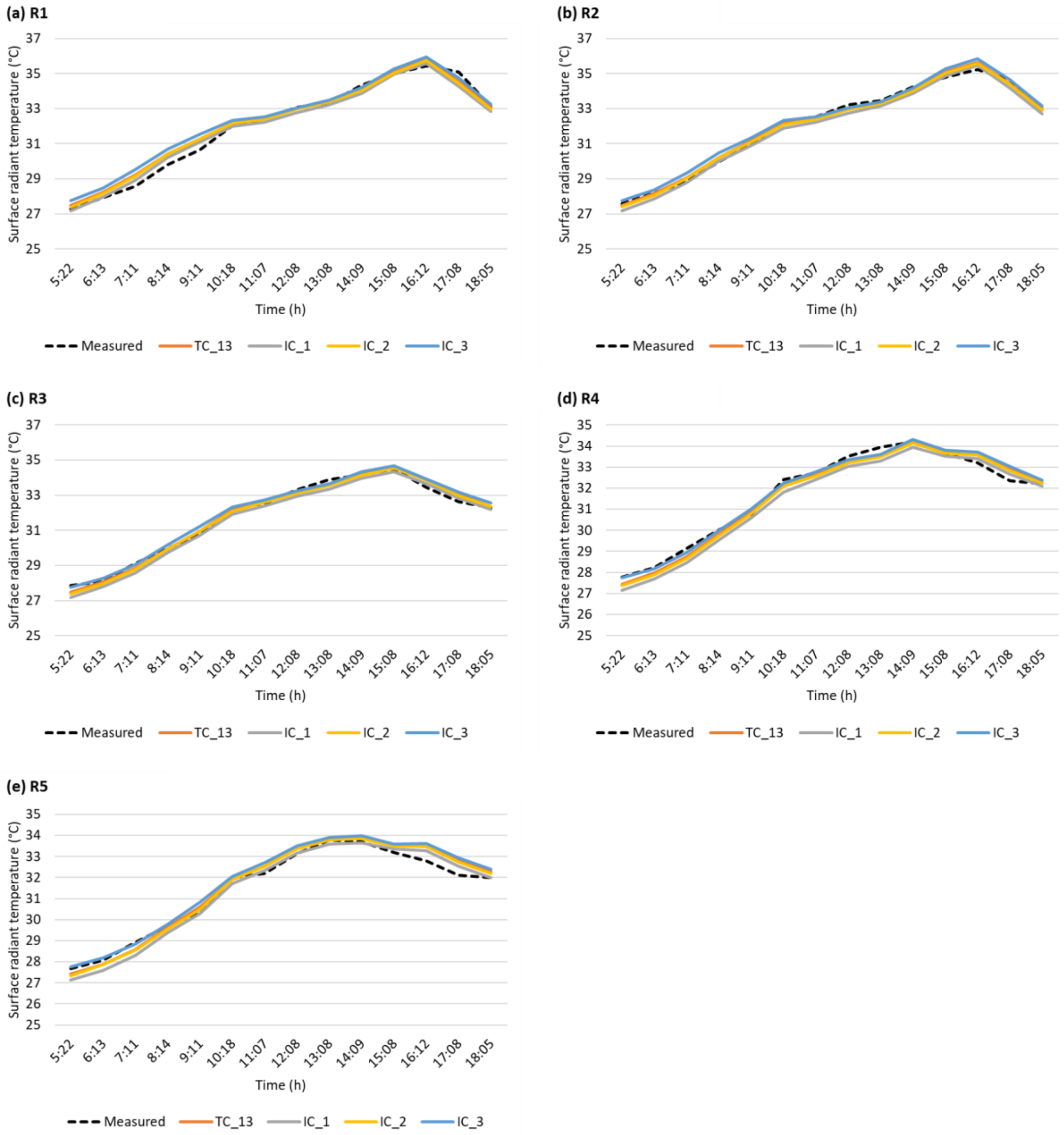

Figure 30. Measurement-simulation comparison for the case TC_13, 15, 10, 11 (shown in Table 2) in terms of the R1-5

Table 8. MBE, MAE, and RMSE of the simulated surface radiant temperatures of case TC_13, 15, 10, 11.

Studied region	Case	MBE (ºC)	MAE (ºC)	RMSE (ºC)
L_1	TC_13	-0.189	0.260	0.301
	IC_1	-0.441	0.442	0.500
	IC_2	-0.255	0.298	0.346
	IC_3	-0.014	0.182	0.247
L_2	TC_13	-0.072	0.146	0.176
	IC_1	-0.319	0.333	0.363
	IC_2	-0.131	0.186	0.217
	IC_3	0.114	0.173	0.226

L_3	TC_13	0.025	0.137	0.149
	IC_1	-0.223	0.225	0.268
	IC_2	-0.038	0.133	0.154
	IC_3	0.208	0.212	0.250
L_4	TC_13	0.056	0.169	0.231
	IC_1	-0.204	0.270	0.313
	IC_2	-0.013	0.190	0.228
	IC_3	0.241	0.258	0.316
L_5	TC_13	-0.151	0.243	0.296
	IC_1	-0.389	0.414	0.473
	IC_2	-0.196	0.281	0.334
	IC_3	0.031	0.192	0.233
R_1	TC_13	0.164	0.288	0.361
	IC_1	-0.075	0.270	0.344
	IC_2	0.107	0.276	0.357
	IC_3	0.336	0.404	0.505
R_2	TC_13	0.043	0.181	0.206
	IC_1	-0.211	0.261	0.304
	IC_2	-0.023	0.201	0.214
	IC_3	0.208	0.246	0.321
R_3	TC_13	0.009	0.185	0.233
	IC_1	-0.240	0.297	0.345
	IC_2	-0.049	0.201	0.250
	IC_3	0.158	0.228	0.274
R_4	TC_13	-0.062	0.248	0.294
	IC_1	-0.326	0.396	0.445
	IC_2	-0.134	0.257	0.309
	IC_3	0.072	0.213	0.278
R_5	TC_13	0.161	0.291	0.352
	IC_1	-0.091	0.269	0.336
	IC_2	0.107	0.269	0.325
	IC_3	0.317	0.329	0.415

As shown in Fig. 29 and 30, the value and temporal variation of the simulated surface radiant temperatures of IC_1-3 and TC_13 were very close, and their temperature values were ranked from high to low as IC_3, TC_13, IC_2, and IC_1. To be more specific, as shown in Table 8, the largest difference among the MAEs and RMSEs of IC_1-3 and TC_13 was ranged about 0.06-0.26 °C (about 0.14 °C in average) and 0.09-0.25 °C (about 0.15 °C in average), respectively.

3.2 Multispectral brightness-radiation correlation- and heat transfer-based simulation result

Compared with the measurement-based surface radiant temperature, the results of the simulated surface radiant temperatures (Section 2.5) of case GC_1-4 for the studied regions on G3 NW wall surface are shown in Fig.31, and their MBE, MAE, and RMSE regarding the case GC_1, 2, 3, and 4 were shown in Table 9.

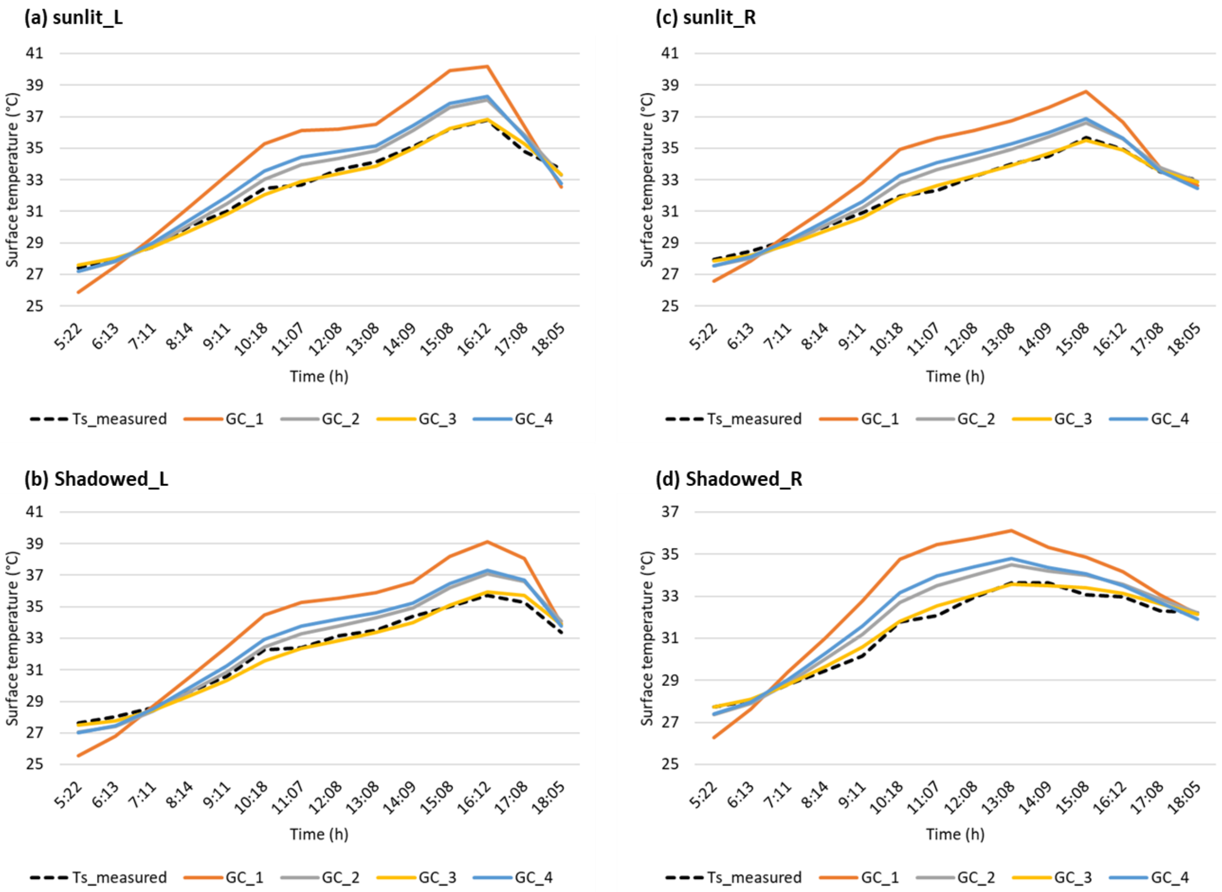

Figure 31. Measurement-simulation comparison for the case GC_1, 2, 3, 4 (shown in Table 2) in terms of the four studied regions (shown in Fig.5)

Table 9. MBE, MAE, and RMSE between the measurement-based and simulated surface temperature of case GC_1, 2, 3, 4.

Studied region	Case	MBE (ºC)	MAE (ºC)	RMSE (ºC)
Sunlit_L	GC_1	1.711	2.167	2.401
	GC_2	0.560	0.677	0.808
	GC_3	-0.064	0.203	0.249
	GC_4	0.764	0.945	1.075
Shadowed_L	GC_1	1.493	1.827	2.139
	GC_2	0.461	0.631	0.749
	GC_3	-0.086	0.174	0.200
	GC_4	0.642	0.829	0.998
Sunlit_R	GC_1	1.534	2.004	2.216
	GC_2	0.463	0.661	0.776
	GC_3	-0.109	0.283	0.328
	GC_4	0.681	0.863	0.976
Shadowed_R	GC_1	1.422	1.697	1.972
	GC_2	0.571	0.641	0.756
	GC_3	0.127	0.175	0.229
	GC_4	0.732	0.832	0.992

Fig. 31 reveals that the simulated radiant temperatures of case GC_3 were the closest to the measured ones with a very small differences, which was followed by GC_2 and GC_4; whereas, the GC_1's results reveal the largest difference from the measured temperatures with lower temperatures in the morning and much higher peak temperatures. To be more specific as shown in Table 9, the MAE and RMSE for Sunlit_L/R and Shadowed_L/R were ranged 0.174-0.283 ^{o}C and 0.2-0.328 ^{o}C for case GC_3, respectively, which were obviously smaller than the 0.631-0.677 ^{o}C (MAE range) and 0.749-0.808^{o}C (RMSE range) for GC_2 as the second closest case to the measured temperatures with a difference of at least about 0.38 ^{o}C and 0.45 ^{o}C for MAE and RMSE, and up to about 0.47 and 0.56 ^{o}C for MAE and RMSE, respectively. When comparing with the GC_1 which was the most different case to the measured temperatures, the error differences were ranged about 1.5-2 ^{o}C and 1.7-2.2 ^{o}C for MAE and RMSE, respectively.

Based on the above results, the general cluster (GC cases) which the target thermal combination belongs to can be determined as GC_3, four specific clusters of TC_13, TC_15, TC_10, and TC_11 included in GC_3 were also figured out to be the possible target thermal combinations for a further test. In terms of the case TC_13, TC_15, TC_10, and TC_11, the region-to-region (Sunlit_L/R and Shadowed_L/R as shown in Fig.5) comparison between the simulation results and the measured surface radiant temperatures were shown in Fig. 32, and their MBE, MAE, and RMSE were shown in Table 10.

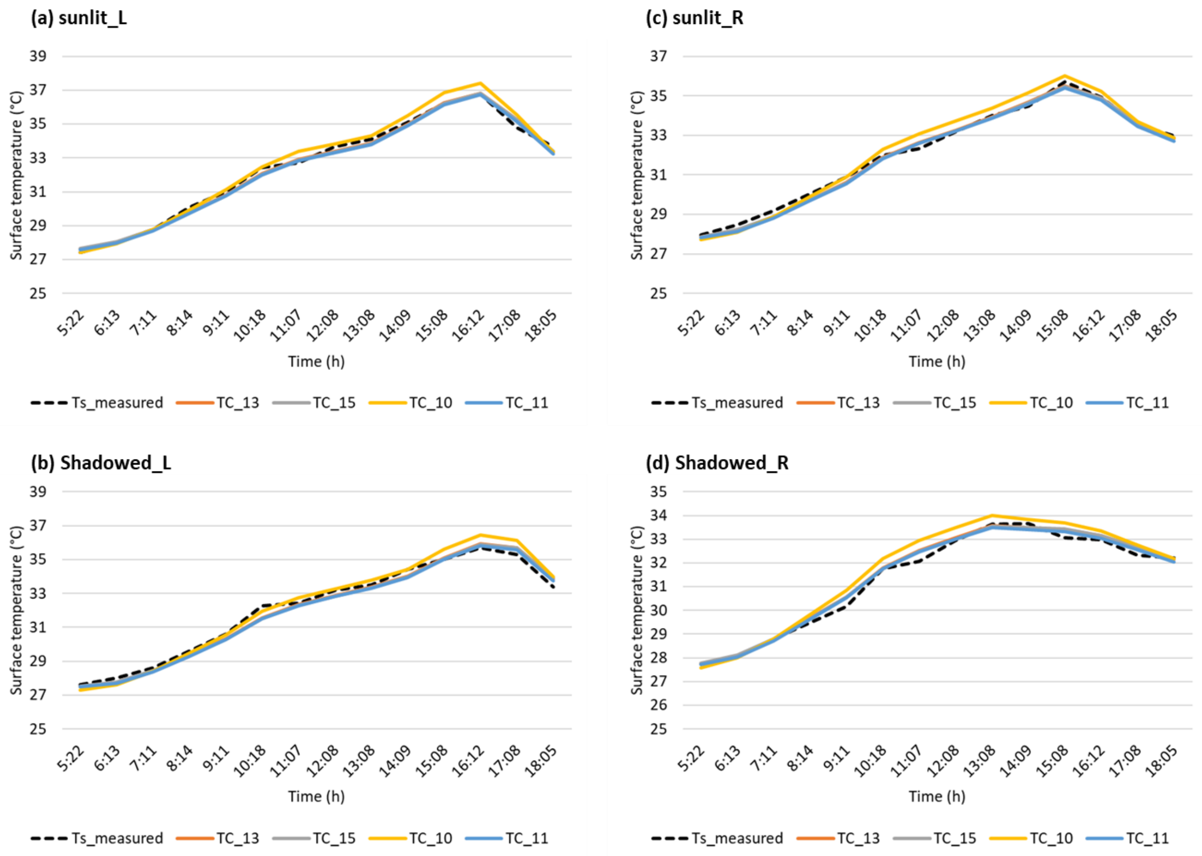

Figure 32. Measurement-simulation comparison for the case TC_13, 15, 10, 11 (shown in Table 1) in terms of the four studied regions (shown in Fig.5)

Table 10. MBE, MAE, and RMSE between the measurement-based and simulated surface temperature of case GC_1, 2, 3, 4

Studied region	Case	MBE (ºC)	MAE (ºC)	RMSE (ºC)
Sunlit_L	TC_13	-0.064	0.203	0.249
	TC_15	-0.077	0.213	0.260
	TC_10	0.218	0.301	0.397
	TC_11	-0.139	0.235	0.275
Shadowed_L	TC_13	-0.086	0.174	0.200
	TC_15	-0.095	0.171	0.196
	TC_10	0.160	0.325	0.383
	TC_11	-0.159	0.214	0.240
Sunlit_R	TC_13	-0.109	0.283	0.328
	TC_15	-0.118	0.288	0.338
	TC_10	0.149	0.355	0.433
	TC_11	-0.178	0.290	0.338
Shadowed_R	TC_13	0.127	0.175	0.229
	TC_15	0.125	0.173	0.224
	TC_10	0.326	0.358	0.440
	TC_11	0.058	0.158	0.200

As shown in Fig. 32, compared with the measured surface radiant temperatures, the TC_10 reveals a bit smaller temperatures in the morning and larger peak temperatures which times for the peak temperatures of the target points can be observed to be a bit earlier than TC_13, 15, and 11. Whereas, the simulated surface radiant temperatures and their temporal variation TC_13, 15, and 11 in terms of the target points were observed significantly close based on Fig. 32. To be more specific, Table 10 reveals that daily average MAEs and RMSEs from sunrise to sunset of the TC_10 were generally larger than the case with second largest MAEs and RMSEs by about 0.07-0.18 and 0.1-0.21, respectively. As shown in Table 5, TC_13 reveals smallest RMSEs for Sunlit_L and R; whereas the TC_15 and TC_11 reveal smallest RMSEs for Shadowed_L and R, respectively.

As mentioned in Section 2.4, considering the RMSE of about 0.03 for estimating total albedo based on the narrowband albedos obtained by multispectral camera (Chapter 3), the sensitivities of the under- and over- estimated shortwave radiations on the simulated surface temperatures were also tested, which results were shown in Fig.33 for the solely case TC_13 and shown in Fig. 34 for TC_13, 15, and 11 compared with the measured surface temperatures in terms of the studied region of Sunlit_R and Shadowed_R (studied regions shown in Fig. 5).

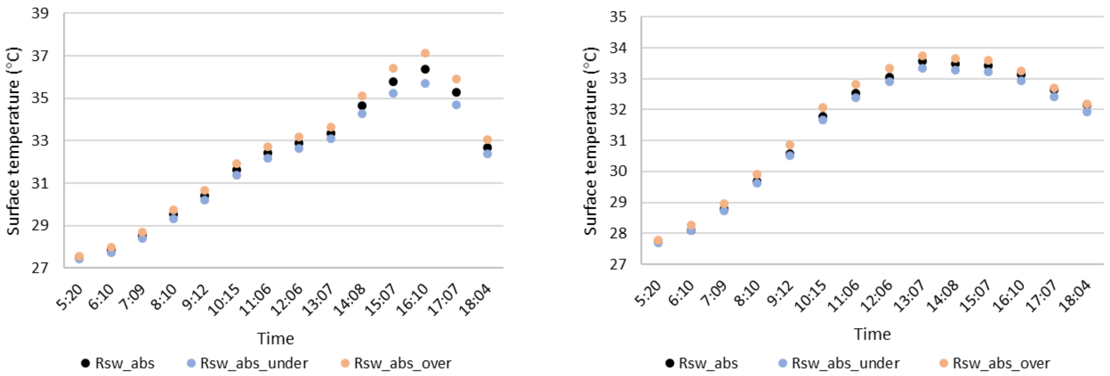

Figure 33. Surface temperature simulated with R_{sw_abs}, $R_{sw\_abs\_over}$, and $R_{sw\_abs\_under}$ for the case TC_13 (shown in Table 1) in terms of the studied region of Sunlit_R and Shadowed_R

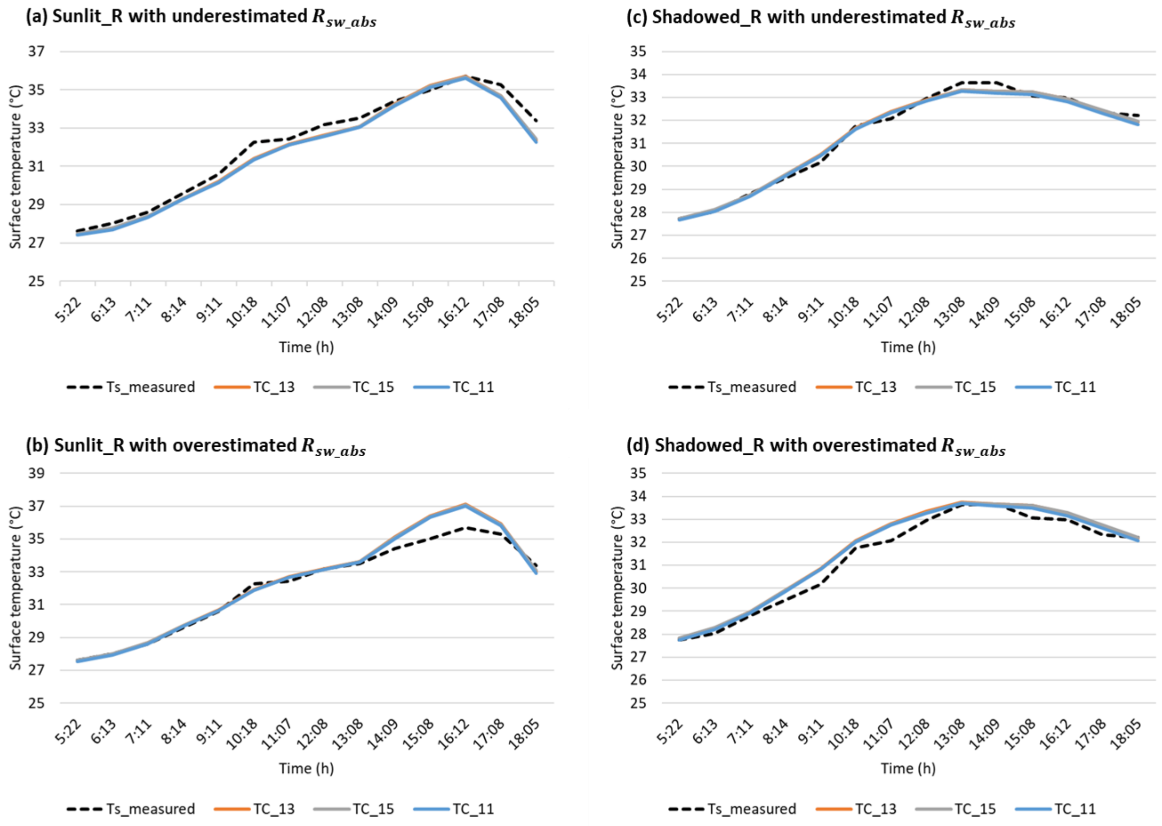

Figure 34. Measurement-simulation comparison for the case TC_13, 15, 11 (shown in Table 1) in terms of the studied region of Sunlit_R and Shadowed_R

Table 11. MBE, MAE, and RMSE between the measurement-based and simulated surface temperatures

Studied region	**Shortwave radiation condition**	**Case**	**MBE (ºC)**	**MAE (ºC)**	**RMSE (ºC)**
Sunlit_R	Normal	TC_13	-0.109	0.283	0.328
		TC_15	-0.118	0.288	0.338
		TC_11	-0.178	0.290	0.338
	Underestimated	TC_13	-0.353	0.384	0.470
		TC_15	-0.361	0.387	0.472
		TC_11	-0.423	0.440	0.527
	Overestimated	TC_13	-0.009	0.171	0.212
		TC_15	-0.012	0.171	0.209
		TC_11	-0.078	0.184	0.233
Shadowed_R	Normal	TC_13	0.127	0.175	0.229
		TC_15	0.125	0.173	0.224
		TC_11	0.058	0.158	0.200
	Underestimated	TC_13	0.294	0.407	0.615
		TC_15	0.281	0.385	0.596
		TC_11	0.220	0.375	0.569
	Overestimated	TC_13	0.310	0.315	0.388
		TC_15	0.305	0.306	0.377
		TC_11	0.238	0.269	0.337

As shown in the left Fig. 33, regarding the Sunlit_R as the region absorbing the largest shortwave radiation (Fig. 11), the normal-underestimated and normal-overestimated absolute gaps were respectively up to about 0.27 °C and

0.3 °C until 13:07, whereas they turned much larger as up to about 0.67 °C and 0.75 °C around 16:10. Whereas, regarding the Shadowed_R as the region absorbing the smallest shortwave radiation, the right Fig.33 reveals that the normal-underestimated and normal-overestimated absolute gaps were respectively up to about 0.23 °C and 0.29 °C. Comparing the Fig. 34 with Fig.32 in terms of the region of Sunlit_R, the underestimated shortwave radiation-based simulated surface temperatures were non-negligibly lower than the normal ones at 11:00-13:00 and 16:00-18:00, whereas those based on the overestimated shortwave radiation were significantly higher than the normal ones between 14:00 and17:00. However, the difference between the normal simulated surface temperature (Fig. 32) and the simulated surface temperatures (Fig. 34) based on the over- or under-estimated shortwave radiation for the region of Shadowed_R was less obvious compared to the Sunlit_R. As shown in Table 11, the over- and under-estimation of shortwave radiation absorbed by the target region would lead to the larger MAEs and RMSEs, except for that the overestimated shortwave radiation-based simulated surface temperatures of TC_13, 15, and 11 were with the lower MAEs and RMSEs for the Sunlit_R. Compared with the normal simulated surface temperature as shown in Table 11, this exception also caused a different determination of the case with lowest MAE and RMSE when applying the over- and under-estimated shortwave radiation; whereas, other case with lowest MAE and RMSE would remain the same when the absorbed shortwave radiation turning to the over- and under-estimated ones.

3.3 Influence of error of estimated albedos in simulation and estimating thermal properties

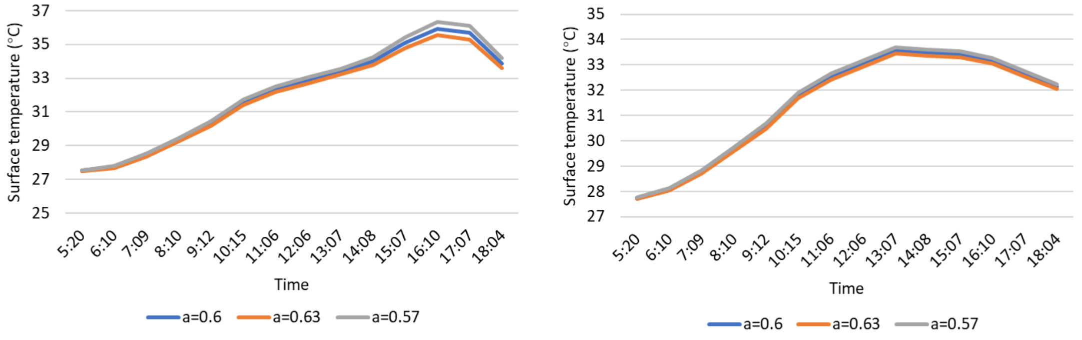

Figure 35. Simulated surface temperatures when albedo is overestimated (0.57) or underestimated (0.63) for R_sunlit and R_shadowed regions.

As shown in Fig.35, compared with the simulated surface temperature of the target regions when albedo is 0.6, their absolute difference is up to about 0.4 and 0.13 ºC, and average in about 0.19 and 0.09 ºC for the R_sunlit and R_shadowed, respectively. Regarding the influence on the estimation of thermal properties, the case TC_15 and 11 were also input to test if the estimation results would be changed. Compared with the measured values, the simulated surface temperatures for case TC_13, 15, and 11 when albedo is overestimated (0.57) or underestimated (0.63) for R_sunlit regions are shown in Fig.36.

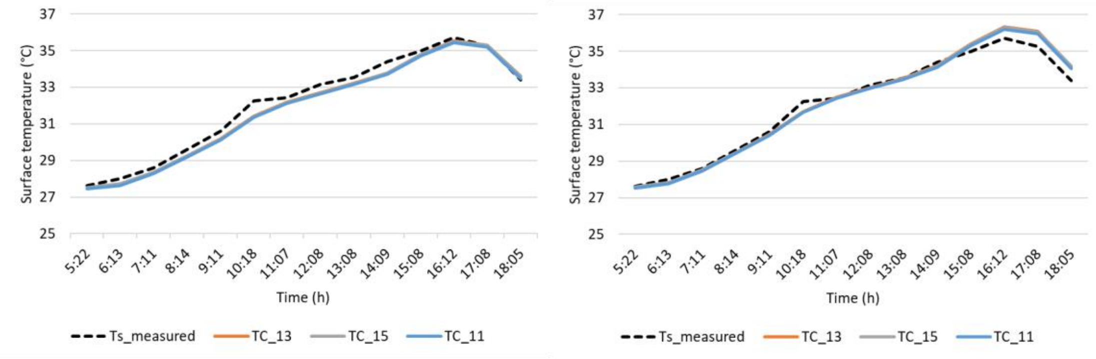

	Albedo (-)	RMSE of TC_13 (°C)	RMSE of TC_15 (°C)	RMSE of TC_11 (°C)
R_sunlit	0.6	0.328	0.338	0.338
	0.63	0.386	0.401	0.433
	0.57	0.403	0.403	0.369
	0.57 (~14:09)	0.215	0.227	0.257

Figure 36. Simulated surface temperatures for case TC_13, 15, and 11 when albedo is underestimated (0.63, left) or overestimated (0.57, right) for R_sunlit, and lower table shows their RMSEs.

As shown in the table of Fig.36, when albedo was overestimated (0.57), case TC_11 revealed the minimum RMSE, which would cause a mistaken estimation different from the estimation result of TC_13 when albedo was 0.6 and when albedo was underestimated (0.63). However, considering that larger error of absorbed shortwave radiation caused by the under- or over-estimated albedos as shown in Fig.35 appeared when absorbed shortwave radiation turned larger, the RMSE of simulated surface temperatures before 15:00 which input absorbed shortwave radiation was lower than 100 W/m^2 was investigated as shown in the table of Fig.36. It reveals that TC_13 was the case with the minimum RMSE, which was in agreement with the results when albedo was 0.6

3.4 Calculated thermal properties based on theoretical method

The calculated thermal properties of the target surface based on theoretical method were about 7.27 W m^{-2} K^{-1} and 418 KJ m^{-2} K^{-1} for thermal conductivity and heat capacity, respectively. Table 12 reveals the error of each typical case compared to these theoretical method-based calculated thermal properties.

Table 12. Error and error percentage of the typical case compared to the theoretical method-based calculated thermal properties

	Thermal conductivity		Heat capacity	
	Error [W m^{-2} K^{-1}]	Error percentage [%]	Error [KJ m^{-2} K^{-1}]	Error percentage [%]
TC_1 (GC_1)	-6.8	-94.0	-397.6	-95.1
TC_2	-6.7	-92.6	-221.0	-52.9
TC_3	-6.7	-92.4	-366.1	-87.6
TC_4	-6.3	-87.2	-4.2	-1.0
TC_5	-6.3	-86.8	-114.5	-27.4
TC_6	-5.9	-81.3	-402.7	-96.3
TC_7	-5.9	-80.5	-332.3	-79.5
TC_8 (GC_2)	-4.6	-62.6	-43.0	-10.3
TC_9	-3.0	-41.2	-390.5	-93.4
TC_10	-2.7	-36.9	-10.6	-2.5
TC_11	-2.4	-33.3	209.1	50.0
TC_12	-0.3	-4.2	-386.0	-92.3
TC_13 (GC_3)	-0.1	-1.1	-1.3	-0.3
TC_14 (GC_4)	1.0	13.4	-334.4	-80.0
TC_15	1.1	15.5	-39.0	-9.3
TC_16	2.2	30.1	-245.3	-58.7
TC_17	5.2	71.5	-403.3	-96.5

4. Discussion

4.1 Evaluation of estimation method

The determination of the typical case of thermal properties closest to the actual thermal properties is suggested to follow two steps: first is to determine the one among four general clusters which the possible cases belong to (as shown in left Fig. 10); second is to determine the specific case which performance on surface temperatures closest to that of the actual thermal properties (as shown in Fig.9 and right Fig.10). Regarding the thermal properties of the target surface estimated in this chapter, the above-proposed first step to determine the one among four general clusters which the possible cases belong to was according to the results of the point-to-point comparison (ten studied points as shown in Fig. 2) between the simulated surface radiant temperatures and measured ones. Based on the comparison results that the simulated surface radiant temperatures of GC_3 were the closest to the measured ones with a very small difference mostly less than 0.3 °C but the GC_2 as the second closest case reveals a difference up to above 1 °C from the measured temperatures (Fig.19 and 20), and the daily MAEs and RMSEs of GC_3 were smaller than those of GC_2 by at least about 0.37 °C for both daily MAEs and RMSEs, and up to about 0.67 and 0.72 respectively for daily MAEs and RMSEs (Table 4), it was simple and clear to determine that the GC_3 was the one which the possible cases belong to. Second step to determine the specific case among TC_13, 15, 10, 11 within the determined cluster (GC_3) closest to the actual thermal properties was based on the results of both the point-to-point comparison (ten studied points as shown in Fig. 2) and grid-to-grid comparison (100*100mm as grid size and 27000-30000 as the total number, process as shown in Fig. 4). As shown in Fig.19 and 20, the TC_10 reveals smaller simulated radiant temperatures in the morning, larger peak temperatures, and a bit earlier time for peak temperatures, compared with the measured ones, demonstrating that TC_10 was not the case which performance on surface temperatures closest to that of the actual thermal properties. It was further proved by the histogram of the AEs within the studied day (Fig. 21) and the relatively large daily RMSE, MBE, and frequency of AEs above 0.5 ^{o}C (Table 6) of TC_10. However, the left three cases of TC_13, 15, and 11 were much difficult to be distinguished, due to their close performance on the simulated surface radiant temperatures and their temporal variations as shown in Fig. 21 and 22 and quite similar daily MAEs and RMSEs as shown in Table 5. However, considering the case dominating the most points among ten studied points with the smallest RMSE, TC_13 was fractionally ahead with smallest RMSEs for 5 points, followed by the TC_11 and TC_15 with smallest RMSEs for 3 and 2 points, respectively. Furthermore, TC_13 with the largest number of the relatively low hourly AEs less than 0.3 ^{o}C and the smallest number of relatively high hourly AEs above 0.5 ^{o}C and 0.7 ^{o}C (Fig. 21 and Table 6) showed a narrow lead compared to TC_11 and 15. Regarding the grid-to-grid comparison results shown in Table 7, TC_13 demonstrates the closest-to-zero MEs and smallest MAEs and RMSEs even though the largest difference of the MAEs and RMSEs among TC_13, 15, and 11 was very small, which was up to only 0.16 ^{o}C except for the moment of 13:08. TC_15 performed best at 13:08 with smaller MAEs and RMSEs by respectively 0.003 ^{o}C and 0.002 ^{o}C compared with TC_13. Hence, TC_13 was regarded as the one with the thermal properties closest to the actual ones due to its limited advantages as discussed above.

The estimated thermal properties of TC_13 was validated by a theoretical method based on ISO 6946, which results demonstrated that the estimation results were representative because the estimated and theoretical values were only 1.1% and 0.3% different respectively for thermal conductivity and heat capacity, which was much less than 20% as the criterium to decide if the estimated thermal properties are representative as stated in section 7.3 of ISO9869-1. As shown in Fig.6, the mean absolute error (MAE) of this estimation method on thermal properties of building surface is theoretically calculated to be about 0.3 W m^{-2} K^{-1} in thermal conductivity and 15 kJ m^{-2} K^{-1} in heat capacity. Compared with a high accuracy with a very low AE of about 0.07-0.1 W m^{-2} K^{-1} by using the QIRT method and 0.03-0.15 W m^{-2} K^{-1} by applying HFM for estimating the U-value of the heavy wall (heat capacity above 150 kJ m^{-2} K^{-1}) studied by R. Albatici, et. al[57], the accuracy of the estimation method on thermal conductivity proposed here is lower than QIRT and HFM by about 0.2-0.23 and 0.15-0.27 W m^{-2} K^{-1} in AE, respectively. However, regarding the HFM method, as mentioned in Introduction (section 1), the required multiple pieces of the equipment and long period for a single building wall cause that it cannot adopt well for neighborhood scale. Regarding the QIRT method, the requirement of environmental conditions are very strict to guarantee the accuracy and reliability of the estimated U-values: measurement performed in the early morning before the sunrise with overcast sky, local wind speed near the building façade lower than 0.5m/s during the monitoring, high air temperature gradient between inside and outside of at least 15 °C, and outdoor temperature with low swing (less than 6 °C) in the 12 hours prior to the monitoring. Actually all these requirements are established to guarantee the environmental conditions to be similar to steady state, but they were not met at all in my study: measurement performed from sunrise to sunset with a clear sky, in-situ wind speed mostly above 0.5m/s, inside-outside temperature gradient lower than 6 °C, and outdoor temperature with a relatively large swing during the monitoring. It suggests that due to the different purpose to develop the methods for estimating thermal properties, the accuracy of this proposed estimation method on thermal properties is lower than commonly used QIRT and HFM methods, but its advantage in time, equipment, and labor saving would bridge the gap of estimating thermal properties in block/neighborhood and even larger scale. However, the findings presented in this chapter show that the typical case with the thermal properties closest to the actual ones could be figured out for the concrete construction (heavy), while further studies are still needed to validate this method for different heavy constructions and to test if it can be applied for light and super-insulated constructions.

Considering the determination on TC_15/11 instead of TC_13, which is very likely to occur, due to their very close performance on the surface radiant temperatures, the estimated and theoretical values were about 15.5% and 9% different respectively for thermal conductivity and heat capacity for TC_15, whereas about 33.3% and 50% for TC_11. According to the ISO9869-1, regarding the TC_15, the difference between the estimated and theoretical thermal properties were still less than 20%, which can be regarded as the representative. However, the large difference of up to 50% between the estimated and theoretical thermal properties cannot be regarded as reliable (more detailed discussion refers to section 4.3). In addition, regarding that the function of the estimated thermal properties in this chapter is to explore the radiative and heat exchange between the urban surfaces and the atmosphere and thus to identify areas with severe outdoor thermal conditions and to examine the potential UHI mitigation strategies, the difference of building surface temperatures and sensible heat flux should be considered when mistaking the TC_15 and 11 instead of the TC_13. Based on the hourly average of surface temperature difference of the ten studied points (left Fig.33) between TC_15/11 and TC_13, the hourly difference of the estimated sensible heat flux emitted from the target wall surface was shown in right Fig. 37 by using the Jurges' model-based calculated convective heat transfer coefficient. As shown in left Fig.37, due to the very close hourly simulated surface temperatures of TC_15 and 11 compared with TC_13 with an absolute difference of up to around 0.1 °C and 0.2 °C, respectively, the absolute difference of the estimated sensible heat flux of TC_15 and 11 compared with TC_13 was up to only around 1 W/m^2 and 1.5 W/m^2. Taking the GC_2 (the second closest case among the four general cases) and GC_4 (the most different case among the four general cases) as examples to indicate how small the difference of sensible heat flux is for TC_15 and 11, the difference of surface temperature was respectively above 1 ºC and 4 ºC from 11:00 to 17:00 for GC_2 and 4 when comparing with the GC_3/TC_13 (Fig.19 and 20), the surface temperature difference of 1 ºC and 4 ºC would cause a difference of sensible heat flux ranged around 11-13 W/m^2 and 44-52 W/m^2 in this period, respectively. Hence, compared with the TC_13 with the thermal properties closest to the theoretical method-based calculated ones for the target surface, the negligible difference of the performance of TC_15 and 11 on surface temperature and emitted sensible heat flux reveals that applying the confusing case in the same season for predicting the surface temperature and sensible heat flux would be also reliable, which error is probably very small and even may be negligible.

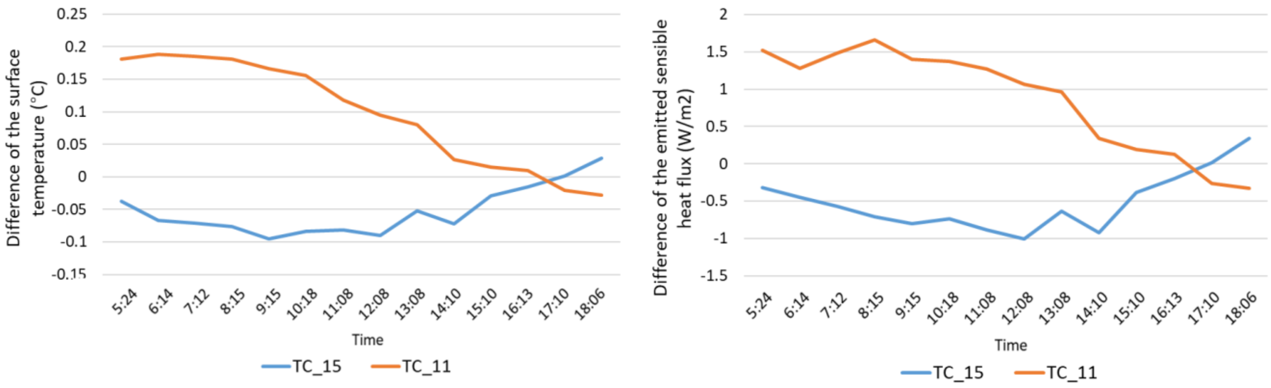

Figure 37. Estimated difference of the surface temperature (left) and emitted sensible heat flux (right) of TC_15 and 13 compared with that of TC_13

The simulation results based on multispectral brightness-radiation correlation and heat transfer model were very similar to the ones based on THERMORender model as discussed above. Based on the region-to-region (four small regions as shown in Fig. 5) difference of the simulated surface temperatures of GC cases compared with measured ones shown in Fig. 33 and Table 9, it was also simple and clear to determine that the GC_3 was the one which the possible cases belong to. However, the largest difference of the MAEs and RMSEs among TC_13, 15, and 11 was very small, which was up to only 0.22 °C, causing the determination on specific case very hard and easy to confuse (Fig.34 and Table 10).

Three considerations to decide the number of points/regions for point-to-point/region-to-region comparison are suggested for other studies or practices using the estimation method developed in this thesis. First, more information should be obtained by the selected points, which include different temporal variation of sunlit and shadowed conditions of the study points (Fig.3) and the points should keep a certain distance to guarantee the different received heat flux. Second, the points should be located systematically which can reduce the influence of the occasional thermal disturbance occurred in some certain regions of target surface. Third, the time and workload efficiency should also be taken into the consideration. If the existing study points already contain the sufficient information of the regions with shadowed-sunlit transitions. Even though we can select more points, they may show very similar variation of surface temperatures as the existing study points which probably not be as needed and representative as the existing study points.

With the selection of the systematic points/small regions avoiding the inappropriate regions involved thermal bridges, thermal anomalies, and hidden by surroundings in the infrared images and involving both the sunlit and shadowed surface regions, the point-to-point/region-to-region comparison is suggested to figure out the general cluster which the possible case belongs to due to its cheaper calculation amount. Furthermore, it is also suggested to primarily figure out the more potential specific cases within the determined general cluster. The grid-to-grid comparison may be useful to determine the case with the thermal properties closest to the actual ones. However, the process for a grid-to-grid comparison is more complicated, and the improved accuracies of the estimated thermal properties probably lead to a small improvement of the accuracies of the surface temperature and emitted sensible heat flux of approximately 0.1-0.2 ºC and 1-1.5 W/m^2 as discussed before (Fig.37). Whether to conduct the grid-to-grid comparison should depend on the requirement of the accuracies of the estimated thermal properties and the time and workload efficiency, how different the potential cases within the determined general cluster are, and how large the difference would be on the surface temperature and emitted sensible heat flux caused by the different thermal properties of these potential cases. In addition, about one point per 25 m^2-surface area in our case was tested to be sufficient, which can be regarded as a rough guide when objective is a relatively large public building. However, if the objective is a small residential building, this guide should be adjusted into one point per 5/10 m^2-surface area.

Regarding the influence of error of estimated albedos (Chapter 3) in the simulation results and estimating thermal properties, case TC_11 revealed the minimum RMSE when albedo was overestimated (Fig.36), which would cause a mistaken estimation different from the estimation result as TC_13 when albedo was not mis-estimated. However, the RMSE of simulated surface temperatures before 15:00 which input absorbed shortwave radiation was lower than 100 W/m2 reveals that TC_13 was the case with the minimum RMSE (table of Fig.36), demonstrating that the mistaken evaluation on thermal properties caused by the error of estimated albedo may be avoided by selecting the target regions with less at-surface solar radiation or the hours being shadowed. In addition, to select more study points/regions and hours can also reduce the errors caused by the mis-estimated albedos.

4.2 Sensitivity analysis

The indoor air temperatures of the target building were measured by setting three thermometers inside the target building in this chapter. Considering the difficulties to put the thermometers inside the target buildings in neighborhood and even larger scale, the assumption of the indoor air temperatures may be needed when applying this estimation method. With the assumption of the indoor air temperature of constant 28, 29, and 30 ºC, the largest difference among the MAEs and RMSEs of IC1-3 and TC_13 was respectively about 0.14 and 0.15 ºC in average, and up to about 0.26 and 0.25 ºC (Table 8), revealing that the wall surface temperature is not very sensitive to the indoor air temperature within 2 ºC. Moreover, the influence of the assumed indoor air temperature can be figured out by the systematic RMSE, because the simulated surface temperatures of IC_1-3 with different indoor air temperatures demonstrate a relatively consistent temporal variation which can be observed by the parallel curves representing the temperature variations of IC_1-3 as shown in Fig. 27 and 28. Hence, the assumption of indoor air temperatures within a limited difference from the actual ones (e.g., a difference within 2 ºC in summer) is probably acceptable when applying this estimation method in practice without accessing the buildings. However, the assumption of the indoor air temperature with a larger difference from the actual ones and other seasons with different indoor-outdoor temperature gradient should be tested to evaluate the sensitivity of the assumed indoor air temperatures on the accuracy of this estimation method. Another possible solution to measure it without accessing the indoors is to measure the window glass surface temperature, which is very close to the indoor air temperature. The common infrared thermal camera with an 8-14μm wavelength cannot accurately measure the glass temperature due to the reflection of temperature from objects behind or near to the glass at longer wavelengths. However, the infrared camera with a wavelength within 6-8μm can eliminate any reflection from other objects, resulting in accurate measurement on glass temperature, such as the thermoIMAGER G7 (Micro-Epsilon, UK) at a wavelength of 7.9μm.

Regarding the sensitivity of the over-and under-estimated shortwave radiation due to the error on estimated albedo on the simulated surface temperature and the determination of the typical case with thermal properties closest to the actual ones, the absolute gaps between the cases with the normal and under- /over-estimated shortwave radiation were up to around 0.3 °C when the target surface region (0.6 in albedo) is shadowed or with shortwave radiation reflected by itself of less than 100W/m^2 (Fig.15 and Fig.31). However, if the shortwave radiation reflected by the target surface region is relatively large as above 100W/m^2, the errors caused by over-/under-estimation of shortwave radiation absorbed by the target surface can cause a temperature difference of up to 0.67/0.75 °C, which may lead to a different determination of the typical case with thermal properties closest to the actual ones (e.g., the case varied when shortwave radiation was overestimated as shown in Table 11). Considering the above-discussed sensitivity of the estimated over-and under-estimated shortwave radiation on the simulated surface temperature and the condition under a clear sky is easier to be reproduced in THERMORender model, this method can be a supplement to be used for the conditions under an overcast or partly cloudy sky.

4.3 Limitation

The estimation method proposed in this chapter is generally limited to the prior known typical combinations of thermal properties of building surfaces. However, once the typical combinations of thermal properties are obtained as the ones in this chapter, they could be used for all the current estimations based on this method. In addition, since this estimation method is limited to the prior known database, another estimation method will be studied for new materials in future. Without the requirement of the database and its clustering, the new estimation method will use the simulated heat flux received by the building surface, internal wall surface temperature, external wall surface temperature to calculate the thermal properties values by using transient heat conduction equation

The case TC_11, which value of the heat capacity and thermal properties were not so close to the TC_13, reveals the closest simulation result as that of TC_13. The reason is due to the larger heat capacity and smaller thermal conductivity of TC_11 case, compared to TC_13. In terms of the summer season, the effect of larger heat capacity of TC_11 is to reduce the external surface temperature, whereas its smaller thermal conductivity can increase the external surface temperature. Hence the compromise caused by the reduction effect of larger heat capacity and increase effect of smaller thermal conductivity of TC_11 leads to its simulation result closest as that of TC_13. This unexpected result demonstrates the limitation of the estimation method on thermal properties proposed here, i.e., regarding the summer season, the compromise effect of the larger heat capacity and smaller thermal conductivity and vice versa. When considering this limitation for the winter season, the larger thermal conductivity leads to the increase of the external surface temperature as the opposite variation compared to the summer. It thus suggests that the hourly variation of surface temperature of the combination of larger thermal conductivity and heat capacity may be close to the combination of lower thermal conductivity and heat capacity, such as the TC_13 and TC_11(Fig.19 and 20), and GC_2 and GC_4 (Fig.17 and 18, not as constant as TC_13 and 11, but their simulated temperatures were much closer than the expectation based on their input thermal properties).

This limitation decides that the estimated thermal properties should be limited to be applied on the same season as the one to conduct this estimation method. However, with the adoption limitation in terms of the season, even though the estimated thermal properties are not close to the actual ones due to the compromise effect as mentioned above, these estimated thermal properties for the target block or neighborhood as the input for SEB simulation would guarantee the very similar-to-actual influence of the target block or neighborhood on their external surface temperature, emitted sensible heat flux, and UHI.

In addition, to break through this limitation, to conduct this estimation method in both summer and winter would be effective. Because the effect of larger thermal properties shows opposite variation in external surface temperature, which can contribute to get rid of the different compromise effect in each season.

5. Summary and future work

An estimation method on thermal properties was proposed in this chapter, coupling the use of multispectral RS and SEB model-based simulation. Taking a concrete building in a block in a university campus (Yokohama city, Japan) as a target building, the multispectral and hourly infrared thermal images from sunrise to sunset of the target building were taken, and meanwhile the indoor air temperature and weather data were measured in site. The typical 7 cases (4 cases of GC_1-4 representing the general clusters and specific 3 cases of TC_15, 10, and 11 within the determined general cluster (TC_13 was not mentioned here because it was the same as GC_3) were input as possible thermal properties of the target building in SEB simulation with other boundary conditions of the measured indoor air temperature and weather data, and the estimated albedo of the target building (Chapter 2). Among these cases, the case TC_13 which simulated radiant surface temperatures of target building revealing the most consistent with the measured temperatures was regarded as the one closest to actual condition, and its thermal properties were regarded as the estimated results. The main findings of this chapter are as follows:

(1) The determination of the typical case with the thermal properties closest to the actual thermal properties is suggested to follow two steps in order to reduce the simulation time and computational cost: first is to determine the one among four general clusters which the possible cases belong to; second is to determine the specific case belonging to the above-determined general cluster which performance on surface temperatures closest to that of the actual thermal properties.

(2) The typical case with the thermal properties closest to the actual ones was figured out for the target concrete wall surface (heavy construction) with a very low AE of only 0.1 W m^{-2} K^{-1} (1.1%) and 1.3 KJ m^{-2} K^{-1} (0.3%) in thermal conductivity and heat capacity, respectively.

(3) The MAE of this estimation method on thermal properties of building surface is theoretically calculated to be about 0.3 W m^{-2} K^{-1} in thermal conductivity and 15 kJ m^{-2} K^{-1} in heat capacity. Due to the different purpose to develop the methods for estimating thermal properties, the accuracy of this proposed estimation method is lower than QIRT and HFM methods, but its advantage in time, equipment, and labor saving would bridge the gap of estimating thermal properties in block and neighborhood scale.

(4) The determination on TC_15/11 instead of TC_13 is very likely to occur, because their performance on the surface radiant temperatures were very similar. The estimated and theoretical values were about 15.5% and 9% different respectively for thermal conductivity and heat capacity for TC_15, whereas about 33.3% and 50% for TC_11. According to the criterium given by ISO9869-1 that the difference between the estimated and theoretical thermal properties should be less than 20%, the TC_15 can be regarded as representative whereas the TC_11 cannot be regarded as reliable which reveals the main limitation of this method.

(5) Regarding the main limitation of this estimation method, the compromise in summer caused by the temperature reduction effect of a larger heat capacity and increase effect of a smaller thermal conductivity as a combination may lead to its simulation result very close to the actual condition but a much larger error of the estimated thermal properties (e.g., when determining on TC_11, the AE percentage is about 33.3% and 50% respectively for thermal conductivity and heat capacity). While considering the winter season, the larger thermal conductivity leads to the increase of the external surface temperature as the opposite variation compared to the summer. Hence the estimated thermal properties are limited to be applied on the same season as the one to conduct this estimation method. With this adoption limitation, even though the estimated thermal properties are not close to the actual ones due to the above-mentioned compromise effect, these estimated thermal properties as the input for SEB simulation would guarantee a similar-to-actual influence of the target block or neighborhood on their external

surface temperature and emitted sensible heat flux (e.g., an absolute difference of up to about 0.2 ºC in surface temperature and 1.5W/m^2 in emitted sensible heat flux of TC_11 compared with TC_13). In addition, to conduct this estimation method in both summer and winter would be effective to breakthrough this limitation.

(6) The assumption of indoor air temperatures within a limited difference from the actual ones (e.g., a difference within 2 ºC in summer) is probably acceptable when applying this estimation method in practice without accessing the buildings.

(7) Regarding the multispectral brightness-radiation correlation- and heat transfer-based simulation, if the shortwave radiation reflected by the target surface region is relatively large as above 100W/m^2, the errors caused by over-/under-estimation of shortwave radiation (due to the RMSE for estimating albedo of about 0.03 as given in Chapter 2) absorbed by the target surface can cause a temperature difference of up to 0.67/0.75 ºC, which may lead to a different determination of the typical case with thermal properties closest to the actual ones. Hence, this method is limited to be applied when the target surface region with a not low albedo (0.6 in this chapter, lower albedos should be tested in future) is shadowed or with shortwave radiation reflected by itself of less than 100W/m^2. Considering the condition under a clear sky is easier to be reproduced in THERMORender model, this method can be a supplement to be used for the conditions under an overcast or partly cloudy sky.

Although the estimation method proposed in this chapter is limited to the prior known typical combinations of thermal properties of building surfaces, with the adoption limitation in terms of the season, and its accuracy is lower than the current in-situ estimation methods, it is time-, equipment-, and labor-saving compared to current in-situ measurement methods for assessing building surface thermal properties. To integrate with the vehicle or unmanned aerial vehicle, this estimation method coupling with the albedo estimation method proposed in Chapter 3 is allowed for obtaining both the actual thermal properties and meanwhile the total global albedo of urban surfaces in order to improve the SEB model performance on an urban block, neighborhood, and even larger scale.

CHAPTER 5: CONCLUSIONS

Surface energy balance (SEB) model is commonly used to explore urban surface-atmosphere heat exchange, which quality is affected by the input of thermophysical properties of urban surface. Coupling the multi-spectral remote sensing and SEB-based numerical simulation, this thesis proposes a new estimation method on thermophysical properties (i.e., albedo, thermal conductivity, and heat capacity) of building surfaces at a block or neighborhood scale.

In Chapter 2, taking a block in university campus in Yokohama city, Japan as a study area, the effect of thermophysical properties of building wall and roof surface were estimated in terms of the surface temperature and sensible heat flux, demonstrating that a non-negligible temperature difference behaved by building surface with different thermophysical properties, suggesting a large potential of the proposed estimation method to be workable. Meanwhile, the SEB model sensitivities of the building surface temperature in terms of the thermophysical properties were also studied, showing that the SEB model sensitivity of the surface temperature to thermal properties for the façade is close to that of the albedo. The sensitivity to $\Delta\lambda_c$ of 1 $\mathrm{Wm^{-2}K^{-1}}$ (1/11 of the civil engineering range) and a ΔC_a of 50 $\mathrm{kJm^{-2}K^{-1}}$ (1/10 of the civil engineering range) are both close to 0.1 ºC, and the difference owing to the orientation is slight. It demonstrates that the SEB model sensitivity is sufficient to distinguish the different thermal properties. In addition, the combined modification of thermal properties can enlarge the accumulated cooling effects of individual modifications but can also reduce or even eliminate their single effects, which depends on how to modify the thermal properties. However, this combined effect would not be a compromise but an accumulated cooling or warming effect in the opposite season, and vice versa, revealing the possible problem (two very different combinations of thermal properties showing similar performance on surface temperatures, which cannot be distinguished) and potential solution (to conduct measurement once more in opposite season) of the estimation method developed in this thesis (Chapter 4.3).

In Chapter 3, the technique process and three narrow-to-broadband (NTB) conversion models were developed to estimate the total shortwave albedo of the building surface based on the multispectral RS (ground-based in this research). Based on the measured spectral reflectances of urban surfaces and simulated at-surface solar spectral irradiances under various conditions (season, solar zenith angle, and horizontal/vertical surface), we simulated datasets of extensive spectral albedos of urban surfaces. Based on the built datasets of various at-surface solar irradiances and spectral albedos, we developed three NTB conversion models following published methodologies for three common UAV-based multispectral cameras, and evaluated their performance as well as the camera capacity to estimate broadband albedo. In addition, the models' sensitivities to the solar conditions and the surface material class were analyzed. These models were also validated using independent sample surfaces covered by different construction materials. Based on the proposed technique process and NTB models, the root mean square error (RMSE) of the estimated albedo is less than 0.033, which are acceptable for SEB modeling. Among the developed three models, Model_phy_reg's performance was the most accurate, stable, and robust, suggesting that the physical constraint used to develop the NTB conversion model may contribute to its applicability and robustness.

In Chapter 4, the thermal properties (i.e., thermal conductivity and heat capacity) of the building surface were estimated based on multispectral RS and SEB model-based simulation. Taking a concrete building in a block in a university campus (Yokohama city, Japan) as a target building, the multispectral images and hourly infrared thermal images from sunrise to sunset of the target building were taken, and meanwhile the indoor air temperature and weather data were measured in site. Typical combinations of thermal properties of building surface were characterized by clustering into 4 general clusters and 17 specific clusters based on a database established here. First the general and then the specific cases were input as possible thermal properties of the target building in SEB simulation with other boundary conditions of the measured indoor air temperature and weather data, and the estimated albedo of the target building (Chapter 2). First, the results showed that the estimated thermal properties based on this developed estimation method were with a very low AE of only 0.1 $\mathrm{Wm^{-2}K^{-1}}$ (1.1%) and 1.3 $\mathrm{KJm^{-2}K^{-1}}$ (0.3%) in thermal conductivity and heat capacity calculated according to the well-documented wall component and theoretical method (ISO6946), respectively. It validates the effectiveness of this developed estimation method on thermal properties of building surfaces. Second, accuracy of applying this developed estimation method in theory is about 0.3 [$\mathrm{Wm^{-2}K^{-1}}$] in λ_c and 15 [$\mathrm{kJm^{-2}K^{-1}}$] in C_a as the mean absolute error. Third, mistaken estimation when applying this estimation method may happen, which estimated combination of thermal properties could be so different from the actual one due to the combined effect of a combination of thermal properties as a compromise as mentioned in Chapter 2. However, these estimated λ_c and C_a are applicable in same season, which error in SEB-based simulated surface temperatures and sensible heat flux can be ignored even though the estimated thermal properties are not close to the actual ones due to the above-mentioned compromise effect. According to some findings in Chapter 2, this limitation due to the compromise effect can be effectively overcome by applying this method once more in opposite season or extending measurement period until night.

As a conclusion, coupling the use of multispectral RS and SEB-based numerical simulation, a new estimation method on thermophysical properties of building surfaces at block and neighborhood scale is proposed and primarily proved to be effective and applicable to obtain thermophysical properties of common heavy wall composed of concrete with a surface reflectance near isotropic. The accuracy of this estimation method on thermal properties (mean AE of about 0.3 [W $m^{-2}K^{-1}$] in λ_c and 15 [kJ $m^{-2}K^{-1}$] in C_a in theory) are relatively lower compared to the in-situ estimation methods, and that for estimating albedo (RMSE of about 0.03) is close to the satellite/airborne RS methods. Both the estimated albedo, thermal conductivity, and heat capacity based on this developed estimation method are sufficient and applicable for SEB modeling at block or neighborhood scale. This estimation method is limited to be applied for estimating the albedos of the Lambertian building surfaces and the estimated thermal properties are limited to be applied on the same season as the one to conduct this estimation method. However, considering the reflectance of most construction materials used for building walls and roofs is near isotropic as Lambertian, to attach an isotropic-reflection material to the limited building surfaces which original materials' reflectance are anisotropic can probably overcome the former limitation. To apply this estimation method on thermal properties once more in the opposite season or extending the measurement period until night may break through the latter limitation. In future, to integrate with the vehicle or unmanned aerial vehicle, this estimation method on thermophysical properties of urban surfaces is allowed for obtaining both the actual thermal properties and meanwhile the total global albedo of urban surfaces in order to improve the SEB model performance at an urban block, neighborhood, and an even larger scale.

REFERENCE

[1] T.R. Oke, G. Mills, A. Christen, J.A. Voogt, Urban Climates, Cambridge University Press, Cambridge, 2017. https://doi.org/10.1017/9781139016476.

[2] I. Harman, S.E. Belcher, The surface energy balance and boundary layer over urban street canyons, Q. J. R. Meteorol. Soc. 132 (2007) 2749–2768. https://doi.org/10.1256/qj.05.185.

[3] P.A. Mirzaei, Recent challenges in modeling of urban heat island §, Sustain. Cities Soc. 19 (2015) 200–206. https://doi.org/10.1016/j.scs.2015.04.001.

[4] J. He, A. Hoyano, A numerical simulation method for analyzing the thermal improvement effect of super-hydrophilic photocatalyst-coated building surfaces with water film on the urban/built environment, Energy Build. 40 (2008) 968–978. https://doi.org/https://doi.org/10.1016/j.enbuild.2007.08.003.

[5] M. Bruse, H. Fleer, with a three dimensional numerical model, 13 (1998) 373–384.

[6] A. Hénon, P.G. Mestayer, D. Groleau, J. Voogt, High resolution thermo-radiative modeling of an urban fragment in Marseilles city center during the UBL-ESCOMPTE campaign, Build. Environ. 46 (2011) 1747–1764. https://doi.org/https://doi.org/10.1016/j.buildenv.2011.02.001.

[7] A. Hénon, P. Mestayer, J.-P. Lagouarde, J. Voogt, An urban neighborhood temperature and energy study from the CAPITOUL experiment with the SOLENE model. Part 2: influence of building surface heterogeneities, Theor. Appl. Climatol. 110 (2012). https://doi.org/10.1007/s00704-012-0616-z.

[8] A. Hénon, P.G. Mestayer, J.-P. Lagouarde, J.A. Voogt, An urban neighborhood temperature and energy study from the CAPITOUL experiment with the SOLENE model, Theor. Appl. Climatol. 110 (2012) 177–196. https://doi.org/10.1007/s00704-012-0615-0.

[9] J. He, A. Hoyano, T. Asawa, A numerical simulation tool for predicting the impact of outdoor thermal environment on building energy performance, Appl. Energy. 86 (2009) 1596–1605. https://doi.org/10.1016/j.apenergy.2008.12.034.

[10] T. Asawa, A. Hoyano, K. Nakaohkubo, Thermal design tool for outdoor spaces based on heat balance simulation using a 3D-CAD system, Build. Environ. 43 (2008) 2112–2123. https://doi.org/10.1016/j.buildenv.2007.12.007.

[11] A. Hoyano, T. Asawa, A. Murakami, R. Sato, K. Nakaohkubo, 3D-CAD MODELING OF A SUBSTANTIAL URBAN AREA AND HEAT ISLAND POTENTIAL OF URBAN BLOCKS IN SUMMER : Analysis of the thermal environment in a substantial urban area with regard to land use and land cover using numerical simulation Part 1, J.Environ.Eng.,AIJ. 72 (2007) 97–104. https://doi.org/https://doi.org/10.3130/aije.72.97_1.

[12] M.H. Elnabawi, N. Hamza, S. Dudek, Numerical modelling evaluation for the microclimate of an outdoor urban form in Cairo, Egypt, HBRC J. 11 (2015) 246–251. https://doi.org/10.1016/j.hbrcj.2014.03.004.

[13] L. Katzschner, S. Thorsson, Microclimatic Investigations as Tool for Urban Design, … Conf. Urban Clim. (2009) 1–4. http://www.ide.titech.ac.jp/~icuc7/extended_abstracts/pdf/397076-1-090514162300-002.pdf.

[14] S. Charisi, T.K. Thiis, P. Stefansson, I. Burud, Prediction model of microclimatic surface conditions on building façades, Build. Environ. 128 (2018) 46–54. https://doi.org/10.1016/J.BUILDENV.2017.11.017.

[15] V. Costanzo, G. Evola, L. Marletta, Energy savings in buildings or UHI mitigation? Comparison between green roofs and cool roofs, Energy Build. 114 (2016) 247–255. https://doi.org/10.1016/J.ENBUILD.2015.04.053.

[16] Y. Wang, U. Berardi, H. Akbari, Comparing the effects of urban heat island mitigation strategies for Toronto, Canada, Energy Build. 114 (2016) 2–19. https://doi.org/10.1016/J.ENBUILD.2015.06.046.

[17] K. Gobakis, D. Kolokotsa, Coupling building energy simulation software with microclimatic simulation for the evaluation of the impact of urban outdoor conditions on the energy consumption and indoor environmental quality, Energy Build. (2017). https://doi.org/10.1016/j.enbuild.2017.02.020.

[18] J. Bouyer, C. Inard, M. Musy, Microclimatic coupling as a solution to improve building energy simulation in an

urban context, Energy Build. 43 (2011) 1549–1559. https://doi.org/10.1016/j.enbuild.2011.02.010.

[19] J. Allegrini, V. Dorer, J. Carmeliet, Coupled CFD , radiation and building energy model for studying heat fluxes in an urban environment with generic building configurations, Sustain. Cities Soc. 19 (2015) 385–394. https://doi.org/10.1016/j.scs.2015.07.009.

[20] M. Idczak, D. Groleau, P. Mestayer, J.-M. Rosant, J.-F. Sini, An application of the thermo-radiative model SOLENE for the evaluation of street canyon energy balance, Build. Environ. 45 (2010) 1262–1275. https://doi.org/https://doi.org/10.1016/j.buildenv.2009.11.011.

[21] L. Shashua-bar, Y. Tzamir, M.E. Hoffman, THERMAL EFFECTS OF BUILDING GEOMETRY AND SPACING ON THE URBAN CANOPY LAYER MICROCLIMATE IN A HOT-HUMID CLIMATE IN SUMMER, 1742 (2004) 1729–1742. https://doi.org/10.1002/joc.1092.

[22] M. Taleghani, L. Kleerekoper, M. Tenpierik, A. Van Den Dobbelsteen, Outdoor thermal comfort within fi ve different urban forms in the Netherlands, Build. Environ. 83 (2015) 65–78. https://doi.org/10.1016/j.buildenv.2014.03.014.

[23] J. Ching, M. Brown, S. Burian, F. Chen, R. Cionco, A. Hanna, T. Hultgren, T. McPherson, D. Sailor, H. Taha And, D. Williams, National urban database and access portal tool, Bull. Am. Meteorol. Soc. 90 (2009) 1157–1168. https://doi.org/10.1175/2009BAMS2675.1.

[24] Y. Xu, C. Ren, P. Ma, J. Ho, W. Wang, K.K.-L. Lau, H. Lin, E. Ng, Urban morphology detection and computation for urban climate research, Landsc. Urban Plan. 167 (2017) 212–224. https://doi.org/https://doi.org/10.1016/j.landurbplan.2017.06.018.

[25] J.D. Hedley, C. Roelfsema, V. Brando, C. Giardino, T. Kutser, S. Phinn, P.J. Mumby, O. Barrilero, J. Laporte, B. Koetz, Coral reef applications of Sentinel-2: Coverage, characteristics, bathymetry and benthic mapping with comparison to Landsat 8, Remote Sens. Environ. 216 (2018) 598–614. https://doi.org/https://doi.org/10.1016/j.rse.2018.07.014.

[26] S. Bonafoni, A. Sekertekin, Albedo Retrieval From Sentinel-2 by New Narrow-to-Broadband Conversion Coefficients, IEEE Geosci. Remote Sens. Lett. (2020) 1–5. https://doi.org/10.1109/LGRS.2020.2967085.

[27] C. Cao, X. Lee, J. Muhlhausen, L. Bonneau, J. Xu, Measuring Landscape Albedo Using Unmanned Aerial Vehicles, Remote Sens. 10 (2018) 1812. https://doi.org/10.3390/rs10111812.

[28] L. Markelin, G.H.S. Simis, D.P. Hunter, E. Spyrakos, N.A. Tyler, D. Clewley, S. Groom, Atmospheric Correction Performance of Hyperspectral Airborne Imagery over a Small Eutrophic Lake under Changing Cloud Cover, Remote Sens. . 9 (2017). https://doi.org/10.3390/rs9010002.

[29] W. Heldens, U. Heiden, T. Esch, A. Mueller, S. Dech, Integration of remote sensing based surface information into a three-dimensional microclimate model, ISPRS J. Photogramm. Remote Sens. 125 (2017) 106–124. https://doi.org/10.1016/j.isprsjprs.2017.01.009.

[30] S. Liang, X. Li, J. Wang, eds., Chapter 7 - Broadband Albedo, in: Adv. Remote Sens., Academic Press, Boston, 2012: pp. 175–233. https://doi.org/https://doi.org/10.1016/B978-0-12-385954-9.00007-1.

[31] T. R. Oke, The energetic basis of the urban heat island, Q. J. R. Meteorol. Soc. 108 (1982).

[32] A. Trlica, L.R. Hutyra, C.L. Schaaf, A. Erb, J.A. Wang, Albedo, Land Cover, and Daytime Surface Temperature Variation Across an Urbanized Landscape, Earth's Futur. 5 (2017) 1084–1101. https://doi.org/10.1002/2017EF000569.

[33] D.J. Sailor, Simulated Urban Climate Response to Modifications in Surface Albedo and Vegetative Cover, J. Appl. Meteorol. 34 (1995) 1694–1704. https://doi.org/10.1175/1520-0450-34.7.1694.

[34] A.L. Pisello, State of the art on the development of cool coatings for buildings and cities, Sol. Energy. 144 (2017) 660–680. https://doi.org/10.1016/j.solener.2017.01.068.

[35] A. Kandya, M. Mohan, Energy & Buildings Mitigating the Urban Heat Island effect through building envelope

modifications, Energy Build. 164 (2018) 266–277. https://doi.org/10.1016/j.enbuild.2018.01.014.

[36] S.J.M. Koenders, R.C.G.M. Loonen, J.L.M. Hensen, Energy & Buildings Investigating the potential of a closed-loop dynamic insulation system for opaque building elements, Energy Build. 173 (2018) 409–427. https://doi.org/10.1016/j.enbuild.2018.05.051.

[37] F. Roberz, R.C.G.M. Loonen, P. Hoes, J.L.M. Hensen, Ultra-lightweight concrete : Energy and comfort performance evaluation in relation to buildings with low and high thermal mass, Energy Build. 138 (2017) 432–442. https://doi.org/10.1016/j.enbuild.2016.12.049.

[38] M. Robati, G. Kokogiannakis, T.J. Mccarthy, Impact of structural design solutions on the energy and thermal performance of an Australian of fi ce building, Build. Environ. 124 (2017) 258–282. https://doi.org/10.1016/j.buildenv.2017.08.018.

[39] J. Yang, Z. Wang, K.E. Kaloush, H. Dylla, Effect of pavement thermal properties on mitigating urban heat islands : A multi-scale modeling case study in Phoenix, Build. Environ. 108 (2016) 110–121. https://doi.org/10.1016/j.buildenv.2016.08.021.

[40] A.G. Klein, J. Stroeve, Development and validation of a snow albedo algorithm for the MODIS instrument, Ann. Glaciol. 34 (2002) 45–52. https://doi.org/DOI: 10.3189/172756402781817662.

[41] S. Liang, Narrowband to broadband conversions of land surface albedo I: Algorithms, Remote Sens. Environ. 76 (2001) 213–238. https://doi.org/https://doi.org/10.1016/S0034-4257(00)00205-4.

[42] C.B. Schaaf, F. Gao, A.H. Strahler, W. Lucht, X. Li, T. Tsang, N.C. Strugnell, X. Zhang, Y. Jin, J.-P. Muller, P. Lewis, M. Barnsley, P. Hobson, M. Disney, G. Roberts, M. Dunderdale, C. Doll, R.P. d'Entremont, B. Hu, S. Liang, J.L. Privette, D. Roy, First operational BRDF, albedo nadir reflectance products from MODIS, Remote Sens. Environ. 83 (2002) 135–148. https://doi.org/https://doi.org/10.1016/S0034-4257(02)00091-3.

[43] G. Smiatek, J. Helmert, E.-M. Gerstner, Impact of land use and soil data specifications on COSMO-CLM simulations in the CORDEX-MED area, Meteorol. Zeitschrift. 25 (2016) 215–230. https://doi.org/10.1127/metz/2015/0594.

[44] K. Liu, H. Su, X. Li, Estimating High-Resolution Urban Surface Temperature Using a Hyperspectral Thermal Mixing (HTM) Approach, IEEE J. Sel. Top. Appl. Earth Obs. Remote Sens. 9 (2016) 804–815. https://doi.org/10.1109/JSTARS.2015.2459375.

[45] W. Xu, M.J. Wooster, C.S.B. Grimmond, Modelling of urban sensible heat flux at multiple spatial scales: A demonstration using airborne hyperspectral imagery of Shanghai and a temperature–emissivity separation approach, Remote Sens. Environ. 112 (2008) 3493–3510. https://doi.org/https://doi.org/10.1016/j.rse.2008.04.009.

[46] S. Liang, J. Stroeve, J.E. Box, Mapping daily snow/ice shortwave broadband albedo from Moderate Resolution Imaging Spectroradiometer (MODIS): The improved direct retrieval algorithm and validation with Greenland in situ measurement, J. Geophys. Res. Atmos. 110 (2005). https://doi.org/10.1029/2004JD005493.

[47] J. Stroeve, J.E. Box, Z. Wang, C. Schaaf, A. Barrett, Re-evaluation of MODIS MCD43 Greenland albedo accuracy and trends, Remote Sens. Environ. 138 (2013) 199–214. https://doi.org/https://doi.org/10.1016/j.rse.2013.07.023.

[48] P. Wright, M. Bergin, J. Dibb, B. Lefer, F. Domine, T. Carman, C. Carmagnola, M. Dumont, Z. Courville, C. Schaaf, Z. Wang, Comparing MODIS daily snow albedo to spectral albedo field measurements in Central Greenland, Remote Sens. Environ. 140 (2014) 118–129. https://doi.org/https://doi.org/10.1016/j.rse.2013.08.044.

[49] G.K. Oral, Z. Yilmaz, The limit U values for building envelope related to building form in temperate and cold climatic zones, Build. Environ. 37 (2002) 1173–1180. https://doi.org/https://doi.org/10.1016/S0360-1323(01)00102-0.

[50] A. Prada, F. Cappelletti, P. Baggio, A. Gasparella, On the effect of material uncertainties in envelope heat

transfer simulations, Energy Build. 71 (2014) 53–60. https://doi.org/https://doi.org/10.1016/j.enbuild.2013.11.083.

[51] D. Majcen, L. Itard, H. Visscher, Theoretical vs. actual energy consumption of labelled dwellings in the Netherlands: Discrepancies and policy implications, Energy Policy. 54 (2013) 125–136. https://doi.org/10.1016/j.enpol.2012.11.008.

[52] D. Bienvenido-Huertas, J. Moyano, D. Marín, R. Fresco-Contreras, Review of in situ methods for assessing the thermal transmittance of walls, Renew. Sustain. Energy Rev. 102 (2019) 356–371. https://doi.org/https://doi.org/10.1016/j.rser.2018.12.016.

[53] A. Rasooli, L. Itard, In-situ characterization of walls' thermal resistance: An extension to the ISO 9869 standard method, Energy Build. 179 (2018) 374–383. https://doi.org/https://doi.org/10.1016/j.enbuild.2018.09.004.

[54] International Standard Organization, ISO 9869-1:2014 Thermal insulation -- Building elements -- In-situ measurement of thermal resistance and thermal transmittance -- Part 1: Heat flow meter method, 2018 (2018).

[55] X. Meng, B. Yan, Y. Gao, J. Wang, W. Zhang, E. Long, Factors affecting the in situ measurement accuracy of the wall heat transfer coefficient using the heat flow meter method, Energy Build. 86 (2015) 754–765. https://doi.org/https://doi.org/10.1016/j.enbuild.2014.11.005.

[56] A. Rasooli, L. Itard, C.I. Ferreira, A response factor-based method for the rapid in-situ determination of wall's thermal resistance in existing buildings, Energy Build. 119 (2016) 51–61. https://doi.org/https://doi.org/10.1016/j.enbuild.2016.03.009.

[57] R. Albatici, A.M. Tonelli, M. Chiogna, A comprehensive experimental approach for the validation of quantitative infrared thermography in the evaluation of building thermal transmittance, Appl. Energy. 141 (2015) 218–228. https://doi.org/10.1016/j.apenergy.2014.12.035.

[58] P.A. Fokaides, S.A. Kalogirou, Application of infrared thermography for the determination of the overall heat transfer coefficient (U-Value) in building envelopes, Appl. Energy. 88 (2011) 4358–4365.

[59] R. Albatici, A.M. Tonelli, Infrared thermovision technique for the assessment of thermal transmittance value of opaque building elements on site, Energy Build. 42 (2010) 2177–2183. https://doi.org/https://doi.org/10.1016/j.enbuild.2010.07.010.

[60] I. ASTM, ASTM C1046(2013) - 95: Standard Practice for In-Situ Measurement of Heat Flux and Temperature on Building Envelope Components, Annu. B. ASTM Stand. (2013). www.astm.org.

[61] I. ASTM, ASTM C1155 - 95(2013): Standard Practice for Determining Thermal Resistance of Building Envelope Components from the In-Situ Data, Annu. B. ASTM Stand. (2013). www.astm.org.

[62] A. International, ASTM C1060-11a(2015): Standard Practice for Thermographic Inspection of Insulation Installations in Envelope Cavities of Frame Buildings, (2015). www.astm.org.

[63] Geneva, ISO 6781:1983 — Thermal insulation — Qualitative detection of thermal irregularities in building envelopes — Infrared method, (1983).

[64] N. Soares, C. Martins, M. Gonçalves, P. Santos, L.S. da Silva, J.J. Costa, Laboratory and in-situ non-destructive methods to evaluate the thermal transmittance and behavior of walls, windows, and construction elements with innovative materials: A review, Energy Build. 182 (2019) 88–110. https://doi.org/https://doi.org/10.1016/j.enbuild.2018.10.021.

[65] C. Flood, L. Scott, W. Gleeson, In-Situ Thermal Transmittance of Case Studies in Dublin, 2016.

[66] P. Baker, Technical Paper 10: U-values and traditional buildings-In situ measurements and their comparisons to calculated values, (2011).

[67] S. Flanders, The Convergence Criterion in Measuring Building R . . Values, in: n.d.

[68] A. Ahmad, M. Maslehuddin, L.M. Al-Hadhrami, In situ measurement of thermal transmittance and thermal resistance of hollow reinforced precast concrete walls, Energy Build. 84 (2014) 132–141.

https://doi.org/https://doi.org/10.1016/j.enbuild.2014.07.048.

[69] P.A. Fokaides, S.A. Kalogirou, Application of infrared thermography for the determination of the overall heat transfer coefficient (U-Value) in building envelopes, Appl. Energy. 88 (2011) 4358–4365. https://econpapers.repec.org/RePEc:eee:appene:v:88:y:2011:i:12:p:4358-4365.

[70] B. Tejedor, M. Casals, M. Gangolells, X. Roca, Quantitative internal infrared thermography for determining in-situ thermal behaviour of façades, Energy Build. 151 (2017) 187–197. https://doi.org/https://doi.org/10.1016/j.enbuild.2017.06.040.

[71] S. Van De Vijver, M. Steeman, N. Bossche, K. Carbonez, A. Janssens, The influence of environmental parameters on the thermographic analysis of the building envelope, Quant. InfraRed Thermogr. (2014).

[72] B. Lehmann, K. Ghazi Wakili, T. Frank, B. Collado, C. Tanner, Effects of individual climatic parameters on the infrared thermography of buildings, Appl. Energy. 110 (2013) 29–43. https://doi.org/10.1016/j.apenergy.2013.03.066.

[73] A. Synnefa, M. Saliari, M. Santamouris, Experimental and numerical assessment of the impact of increased roof reflectance on a school building in Athens, Energy Build. 55 (2012) 7–15. https://doi.org/10.1016/j.enbuild.2012.01.044.

[74] H.M.P.I.K. Herath, R.U. Halwatura, G.Y. Jayasinghe, Modeling a Tropical Urban Context with Green Walls and Green Roofs as an Urban Heat Island Adaptation Strategy, Procedia Eng. 212 (2018) 691–698. https://doi.org/https://doi.org/10.1016/j.proeng.2018.01.089.

[75] P. Wouters, L. Vandaele, P. Voit, N. Fisch, The use of outdoor test cells for thermal and solar building research within the PASSYS project, Build. Environ. 28 (1993) 107–113. https://doi.org/https://doi.org/10.1016/0360-1323(93)90044-4.

[76] P.H. Baker, H.A.L. van Dijk, PASLINK and dynamic outdoor testing of building components, Build. Environ. 43 (2008) 143–151. https://doi.org/https://doi.org/10.1016/j.buildenv.2006.10.009.

[77] G. Stevens, J. Bradford, Do U-value insulation? England's field trial of solid wall insulation, ECEEE Summer Study Proc. 2013. (2013) 1269–1280.

[78] H. Madsen, P. Bacher, G. Bauwens, A.-H. Deconinck, G. Reynders, S. Roels, E. Himpe, G. Lethé, Thermal performance characterisation using time series data - statistical guidelines, 2015. https://doi.org/10.13140/RG.2.1.1564.4241.

[79] E. Johansson, Influence of urban geometry on outdoor thermal comfort in a hot dry climate: A study in Fez, Morocco, Build. Environ. 41 (2006) 1326–1338. https://doi.org/https://doi.org/10.1016/j.buildenv.2005.05.022.

[80] D. Kolokotsa, M. Santamouris, S.C. Zerefos, Green and cool roofs' urban heat island mitigation potential in European climates for office buildings under free floating conditions, Sol. Energy. 95 (2013) 118–130. https://doi.org/https://doi.org/10.1016/j.solener.2013.06.001.

[81] C. Georgakis, S. Zoras, M. Santamouris, Studying the effect of " cool " coatings in street urban canyons and its potential as a heat island mitigation technique, Sustain. Cities Soc. 13 (2014) 20–31. https://doi.org/10.1016/j.scs.2014.04.002.

[82] A. Laura, V. Lucia, C. Piselli, G. Pignatta, Combined thermal effect of cool roof and cool façade on a prototype building, Energy Procedia. 78 (2015) 1556–1561. https://doi.org/10.1016/j.egypro.2015.11.205.

[83] M. Doya, E. Bozonnet, F. Allard, Experimental measurement of cool facades ' performance in a dense urban environment, Energy Build. 55 (2012) 42–50. https://doi.org/10.1016/j.enbuild.2011.11.001.

[84] J. Lucero-Álvarez, M. Alarcón-Herrera, I. Martin-Dominguez, The Effect of Solar Reflectance, Infrared Emissivity, and Thermal Insulation of Roofs on the Annual Thermal Load of Single-family Households in México, in: 2014. https://doi.org/10.18086/eurosun.2014.13.03.

[85] J. Lucero-Álvarez, N. Rodriguez-Muñoz, I. Martin-Dominguez, The Effects of Roof and Wall Insulation on the

Energy Costs of Low Income Housing in Mexico, Sustainability. 8 (2016) 590. https://doi.org/10.3390/su8070590.

[86] J. Yang, M. Kumar, A. Pyrgou, A. Chong, M. Santamouris, D. Kolokotsa, S. Eang, Green and cool roofs ' urban heat island mitigation potential in tropical climate, Sol. Energy. 173 (2018) 597–609. https://doi.org/10.1016/j.solener.2018.08.006.

[87] C. Berger, F. Riedel, J. Rosentreter, E. Stein, S. Hese, C. Schmullius, Fusion of Airborne Hyperspectral and LiDAR Remote Sensing Data to Study the Thermal Characteristics of Urban Environments, Comput. Approaches Urban Environ. Geotechnol. Environ. Vol 13. Springer, Cham. (2015) 273–292. https://doi.org/10.1007/978-3-319-11469-9_11.

[88] W.H. (William H. McAdams, Heat transmission, 3d ed, New York : McGraw-Hill, 1954.

[89] E.M. Sparrow, J.W. Ramsey, E.A. Mass, Effect of Finite Width on Heat Transfer and Fluid Flow about an Inclined Rectangular Plate, J. Heat Transfer. 101 (1979) 199–204. http://dx.doi.org/10.1115/1.3450946.

[90] S.E.G. Jayamaha, N.E. Wijeysundera, S.K. Chou, Measurement of the heat transfer coefficient for walls, Build. Environ. 31 (1996) 399–407. https://doi.org/https://doi.org/10.1016/0360-1323(96)00014-5.

[91] N.E. Wijeysundera, S.K. Chou, S.E.G. Jayamaha, Heat Flow through Walls under Transient Rain Conditions, J. Therm. Insul. Build. Envel. 17 (1993) 118–141. https://doi.org/10.1177/109719639301700105.

[92] International Standard Organization, ISO 6946:2017 - Building components and building elements - Thermal resistance and thermal transmittance, Int. Organ. Stand. Geneva, Switz. (2017).

[93] BRE, DETR Framework Project Report: Field investigations of the thermal performance of construction elements as built, (2001) 93.

[94] K. Nakaohkubo, A. Hoyano, Development of support tool for thermal and luminous environmental design in outdoor and semi-outdoor living space using numerical analysis, IBPSA 2009 - Int. Build. Perform. Simul. Assoc. 2009. (2009).

[95] H. Akbari, Measured energy savings from the application of reflective roofs in two small non-residential buildings, 28 (2003) 953–967. https://doi.org/10.1016/S0360-5442(03)00032-X.

[96] J.H. Jo, J.D. Carlson, J.S. Golden, H. Bryan, An integrated empirical and modeling methodology for analyzing solar reflective roof technologies on commercial buildings, Build. Environ. 45 (2010) 453–460. https://doi.org/10.1016/j.buildenv.2009.07.001.

[97] B. Ken, C. Bonnie, Environmental design, London : Chartered Institution of Building Services Engineers, [2015] ©2015, 2015.

[98] H.T. Ã, M. Moriyama, Surface heat budget on green roof and high reflection roof for mitigation of urban heat island, 42 (2007) 2971–2979. https://doi.org/10.1016/j.buildenv.2006.06.017.

[99] Architectural Institute of Japan, Handbook of environmental design, Revised, MARUZEN-YUSHODO Company, Limited, 2007. http://ci.nii.ac.jp/ncid/BA80278078.

[100] D.G. Erbs, S.A. Klein, J.A. Duffie, Estimation of the diffuse radiation fraction for hourly, daily and monthly-average global radiation, Sol. Energy. 28 (1982) 293–302. https://doi.org/https://doi.org/10.1016/0038-092X(82)90302-4.

[101] J. He, A. Hoyano, A 3D CAD-based simulation tool for prediction and evaluation of the thermal improvement effect of passive cooling walls in the developed urban locations, Sol. Energy. 83 (2009) 1064–1075. https://doi.org/https://doi.org/10.1016/j.solener.2009.01.006.

[102] A. Hénon, P.G. Mestayer, A Method for Monitoring the Heat Flux from an Urban District with a Single Infrared Remote Sensor, (2014) 277–303. https://doi.org/10.1007/s10546-014-9943-1.

[103] S. Jung, S. Yoon, Deduction of optimum surface design factors for enhancement of outdoor thermal environment in a micro-scale unit, Sustain. 9 (2017). https://doi.org/10.3390/su9081381.

[104] A. Gagliano, M. Detommaso, F. Nocera, G. Evola, A multi-criteria methodology for comparing the energy and environmental behavior of cool , green and traditional roofs, Build. Environ. 90 (2015) 71–81. https://doi.org/10.1016/j.buildenv.2015.02.043.

[105] J. Yang, M. Kumar, A. Pyrgou, A. Chong, M. Santamouris, D. Kolokotsa, S. Eang, Green and cool roofs ' urban heat island mitigation potential in tropical climate, Sol. Energy. 173 (2018) 597–609. https://doi.org/10.1016/j.solener.2018.08.006.

[106] J.F. Calleja, C. Recondo, J. Peón, S. Fernández, F. la Cruz, J. González-Piqueras, A New Method for the Estimation of Broadband Apparent Albedo Using Hyperspectral Airborne Hemispherical Directional Reflectance Factor Values, Remote Sens. 8 (2016). https://doi.org/10.3390/rs8030183.

[107] F. Canisius, S. Wang, H. Croft, G.S. Leblanc, A.J.H. Russell, J. Chen, R. Wang, A UAV-Based Sensor System for Measuring Land Surface Albedo: Tested over a Boreal Peatland Ecosystem, Drones . 3 (2019). https://doi.org/10.3390/drones3010027.

[108] J. Fernandez Calleja, C. Hellmann, G. Mendiguren González, S. Punalekar, J. Peón, A. MacArthur, L. Alonso, Relating Hyperspectral Airborne Data to Ground Measurements in a Complex and Discontinuous Canopy, Acta Geophys. (2015). https://doi.org/10.1515/acgeo-2015-0036.

[109] J. Arroyo-Mora, M. Kalacska, D. Inamdar, R. Soffer, O. Lucanus, J. Gorman, T. Naprstek, E. Schaaf, G. Ifimov, K. Elmer, G. Leblanc, Implementation of a UAV–Hyperspectral Pushbroom Imager for Ecological Monitoring, Drones. 3 (2019) 12. https://doi.org/10.3390/drones3010012.

[110] L. Deng, Z. Mao, X. Li, Z. Hu, F. Duan, Y. Yan, UAV-based multispectral remote sensing for precision agriculture: A comparison between different cameras, ISPRS J. Photogramm. Remote Sens. 146 (2018) 124–136. https://doi.org/10.1016/j.isprsjprs.2018.09.008.

[111] S. Liang, D. Wang, T. He, Y. Yu, Remote sensing of earth's energy budget: synthesis and review, Int. J. Digit. Earth. 12 (2019) 737–780. https://doi.org/10.1080/17538947.2019.1597189.

[112] E.S. Krayenhoff, J.A. Voogt, A microscale three-dimensional urban energy balance model for studying surface temperatures, Boundary-Layer Meteorol. 123 (2007) 433–461. https://doi.org/10.1007/s10546-006-9153-6.

[113] S. Liang, C.J. Shuey, A.L. Russ, H. Fang, M. Chen, C.L. Walthall, C.S.T. Daughtry, R. Hunt, Narrowband to broadband conversions of land surface albedo: II. Validation, Remote Sens. Environ. 84 (2003) 25–41. https://doi.org/https://doi.org/10.1016/S0034-4257(02)00068-8.

[114] Y. Qu, S. Liang, Q. Liu, T. He, S. Liu, X. Li, Mapping Surface Broadband Albedo from Satellite Observations: A Review of Literatures on Algorithms and Products, Remote Sens. 7 (2015) 990–1020. https://doi.org/10.3390/rs70100990.

[115] Z. Wang, A.M. Erb, C.B. Schaaf, Q. Sun, Y. Liu, Y. Yang, Y. Shuai, K.A. Casey, M.O. Román, Early spring post-fire snow albedo dynamics in high latitude boreal forests using Landsat-8 OLI data, Remote Sens. Environ. 185 (2016) 71–83. https://doi.org/https://doi.org/10.1016/j.rse.2016.02.059.

[116] Y. Shuai, J.G. Masek, F. Gao, C.B. Schaaf, An algorithm for the retrieval of 30-m snow-free albedo from Landsat surface reflectance and MODIS BRDF, Remote Sens. Environ. 115 (2011) 2204–2216. https://doi.org/https://doi.org/10.1016/j.rse.2011.04.019.

[117] T. Hakala, J. Suomalainen, J.I. Peltoniemi, Acquisition of Bidirectional Reflectance Factor Dataset Using a Micro Unmanned Aerial Vehicle and a Consumer Camera, Remote Sens. 2 (2010) 819–832. https://doi.org/10.3390/rs2030819.

[118] A.H. Strahler, MODIS BRDF Albedo Product : Algorithm Theoretical Basis Document, (n.d.) 1–53.

[119] K. Nakaohkubo, A. Hoyano, T. Asawa, H. Fukasawa, Development of outdoor heat balance simulation considering directional characteristics of reflected solar radiation from the building external surfaces, J. Environ. Eng. (Transactions AIJ). 73 (2008) 275–282. https://doi.org/10.3130/aije.73.275.

[120] J.C. Ryan, A. Hubbard, J.E. Box, S. Brough, K. Cameron, J.M. Cook, M. Cooper, S.H. Doyle, A. Edwards, T. Holt, T.D.L. Irvine-Fynn, C. Jones, L. Pitcher, A.K. Rennermalm, L.C. Smith, M. Stibal, N. Snooke, Derivation of High Spatial Resolution Albedo from UAV Digital Imagery: Application over the Greenland Ice Sheet, in: Front. Earth Sci., 2017.

[121] J.A. Valiente, M. Nunez, E. Lopez-Baeza, J.F. Moreno, Narrow-band to broad-band conversion for Meteosat-visiible channel and broad-band albedo using both AVHRR-1 and -2 channels, Int. J. Remote Sens. 16 (1995) 1147–1166. https://doi.org/10.1080/01431169508954468.

[122] T. Akkermans, N. Clerbaux, Narrowband-to-Broadband Conversions for Top-of-Atmosphere Reflectance from the Advanced Very High Resolution Radiometer (AVHRR), Remote Sens. 12 (2020) 305. https://doi.org/10.3390/rs12020305.

[123] J. Song, W. Gao, E. Research, N.I. Univ., An improved method to derive surface albedo from narrowband AVHRR satellite data : narrowband to broadband conversion., (1999). https://doi.org/10.1175/1520-0450(1999)038<0239:AIMTDS>2.0.CO;2.

[124] S. Peng, J. Wen, Q. Xiao, D. You, B. Dou, Q. Liu, Y. Tang, Multi-Staged NDVI Dependent Snow-Free Land-Surface Shortwave Albedo Narrowband-to-Broadband (NTB) Coefficients and Their Sensitivity Analysis, Remote Sens. 9 (2017) 93.

[125] M. Tasumi, A.R. G., T. Ricardo, At-Surface Reflectance and Albedo from Satellite for Operational Calculation of Land Surface Energy Balance, J. Hydrol. Eng. 13 (2008) 51–63. https://doi.org/10.1061/(ASCE)1084-0699(2008)13:2(51).

[126] Z. Li, A. Erb, Q. Sun, Y. Liu, Y. Shuai, Z. Wang, P. Boucher, C. Schaaf, Preliminary assessment of 20-m surface albedo retrievals from sentinel-2A surface reflectance and MODIS/VIIRS surface anisotropy measures, Remote Sens. Environ. 217 (2018) 352–365. https://doi.org/https://doi.org/10.1016/j.rse.2018.08.025.

[127] W. Ying, H. Wu, Z. Li, Net Surface Shortwave Radiation Retrieval Using Viirs Data, in: IGARSS 2018 - 2018 IEEE Int. Geosci. Remote Sens. Symp., 2018: pp. 2623–2626. https://doi.org/10.1109/IGARSS.2018.8518858.

[128] Y. Liu, Z. Wang, Q. Sun, A.M. Erb, Z. Li, C.B. Schaaf, X. Zhang, M.O. Román, R.L. Scott, Q. Zhang, K.A. Novick, M.S. Bret-Harte, S. Petroy, M. SanClements, Evaluation of the VIIRS BRDF, Albedo and NBAR products suite and an assessment of continuity with the long term MODIS record, Remote Sens. Environ. 201 (2017) 256–274. https://doi.org/https://doi.org/10.1016/j.rse.2017.09.020.

[129] M. Mori, T. Iwata, Y. Minami, S. Kato, Y. Akamatsu, Spectral Analysis of Building Materials Used in Japan, Int. Arch. Photogramm. Remote Sens. Spat. Inf. Sci. XXXVII (2004) 49–54.

[130] S.K. Von Bueren, A. Burkart, A. Hueni, U. Rascher, M.P. Tuohy, I.J. Yule, Deploying four optical UAV-based sensors over grassland :, (2015) 163–175. https://doi.org/10.5194/bg-12-163-2015.

[131] G. Baldinelli, S. Bonafoni, A. Rotili, Albedo Retrieval From Multispectral Landsat 8 Observation in Urban Environment: Algorithm Validation by in situ Measurements, IEEE J. Sel. Top. Appl. Earth Obs. Remote Sens. 10 (2017) 4504–4511. https://doi.org/10.1109/JSTARS.2017.2721549.

[132] S. Kotthaus, T.E.L. Smith, M.J. Wooster, C.S.B. Grimmond, Derivation of an urban materials spectral library through emittance and reflectance spectroscopy, ISPRS J. Photogramm. Remote Sens. 94 (2014) 194–212. https://doi.org/10.1016/j.isprsjprs.2014.05.005.

[133] E.A. Cloutis, Spectral Reflectance Properties of Hydrocarbons: Remote-Sensing Implications, Science (80-.). 245 (1989) 165 LP – 168. https://doi.org/10.1126/science.245.4914.165.

[134] C.A. Gueymard, Parameterized transmittance model for direct beam and circumsolar spectral irradiance, Sol. Energy. 71 (2001) 325–346. https://doi.org/https://doi.org/10.1016/S0038-092X(01)00054-8.

[135] C. Gueymard, SMARTS2 , A Simple Model of the Atmospheric Radiative Transfer of Sunshine : Algorithms and performance assessment, (1995).

[136] C. Gueymard, The SMARTS spectral irradiance model after 25 years: New developments and validation of reference spectra, Sol. Energy. 187 (2019) 233–253. https://doi.org/10.1016/j.solener.2019.05.048.

[137] C.A. Gueymard, Interdisciplinary applications of a versatile spectral solar irradiance model: A review, Energy. 30 (2005) 1551–1576. https://doi.org/https://doi.org/10.1016/j.energy.2004.04.032.

[138] C. Gueymard, Prediction and validation of cloudless shortwave solar spectra incident on horizontal, tilted, or tracking surfaces, Sol. Energy. 82 (2008) 260–271. https://doi.org/10.1016/j.solener.2007.04.007.

[139] J. Cierniewski, A. Karnieli, C. Kaźmierowski, S. Królewicz, J. Piekarczyk, K. Lewińska, A. Goldberg, R. Wesołowski, M. Orzechowski, Effects of Soil Surface Irregularities on the Diurnal Variation of Soil Broadband Blue-Sky Albedo, IEEE J. Sel. Top. Appl. Earth Obs. Remote Sens. 8 (2015) 493–502. https://doi.org/10.1109/JSTARS.2014.2330691.

[140] MicaSense-RedEdge^{TM}, User Manual Multispectral Camera, (2015) 1–27.

[141] M. Gul, Y. Kotak, T. Muneer, S. Ivanova, Enhancement of albedo for solar energy gain with particular emphasis on overcast skies, Energies. 11 (2018) 1–17. https://doi.org/10.3390/en11112881.

[142] C.L. BREST, S.N. GOWARD, Deriving surface albedo measurements from narrow band satellite data, Int. J. Remote Sens. 8 (1987) 351–367. https://doi.org/10.1080/01431168708948646.

[143] B. Franch, E. Vermote, S. Skakun, J.-C. Roger, A. Santamaria-Artigas, J.L. Villaescusa-Nadal, J. Masek, Toward Landsat and Sentinel-2 BRDF Normalization and Albedo Estimation: A Case Study in the Peruvian Amazon Forest, Front. Earth Sci. 6 (2018) 185. https://doi.org/10.3389/feart.2018.00185.

[144] X. Xu, T. Asawa, Systematic numerical study on the effect of thermal properties of building surface on its temperature and sensible heat flux, Build. Environ. 168 (2020) 106485. https://doi.org/https://doi.org/10.1016/j.buildenv.2019.106485.

[145] T. Nagata, Y. Sawada, Estimation of diffuse radiation on horizontal surface for clear sky, in: 1978: pp. 519–520.

[146] A. Pérez-Burgos, M. Díez-Mediavilla, C. Alonso-Tristán, M.C. Rodríguez-Amigo, Analysis of solar direct irradiance models under clear-skies: Evaluation of the improvements for locally adapted models, J. Renew. Sustain. Energy. 9 (2017) 23703. https://doi.org/10.1063/1.4981798.

[147] X. Zhao, H. Wei, Y. Shen, K. Zhang, Real-time Clear-sky Model and Cloud Cover for Direct Normal Irradiance Prediction, J. Phys. Conf. Ser. 1072 (2018) 12003. https://doi.org/10.1088/1742-6596/1072/1/012003.

[148] A. Matzarakis, F. Rutz, H. Mayer, Modelling radiation fluxes in simple and complex environments - Application of the RayMan model, Int. J. Biometeorol. 51 (2007) 323–334. https://doi.org/10.1007/s00484-006-0061-8.

[149] C. Chen, Determining the leaf emissivity of three crops by infrared thermometry, Sensors (Basel). 15 (2015) 11387–11401. https://doi.org/10.3390/s150511387.

ACKNOWLEDGEMENTS

This dissertation is based on the research work of my Doctor Course at the School of Environment and Society, Tokyo Institute of Technology. Here, I would like to thank the following people, without whom I would not have been able to complete this research, and without whom I would not have made it through my Ph.D. degree!

First and foremost, I am extremely grateful to my supervisor, Prof. Takashi Asawa for his invaluable advice, continuous support, and patience during my Ph.D. study. His immense knowledge and plentiful experience have largely encouraged me in all the time of current and future academic research and daily life.

I would like to extend my sincere thanks to Dr. Hideki Kobayashi, Dr. Tomoki Kiyono, and Dr. Chen Kan for their technical support and advice on my research.

I would like to offer my special thanks to Prof. Tsubasa Okaze, Prof. Yoshiki Nakamura, Prof. Masashi Matsuoka, Prof. Hiroaki Yamanaka for their patient reviews and insightful comments.

I would like to thank Ms. Hinako Abe and Mr. Hideyuki Fukasawa for their contributions to data collection. I would also like to thank Dr. Maria Alejandra Del Rio, Ms. Qin Beilei, and other members of the Asawa Lab. It is their kind help and support that have made my study and life in Japan a wonderful time.

Furthermore, I want to thank Prof. He Jiang and Dr. Luo Yanwen who give me a lot of support and encouragement during my study life in China as well as in Japan.

Last but not the least, I would like to give my deep appreciation to the following people who always give me endless love and support:

My parents, who support me financially and mentally to pursue my academic dream.

My partner, Dr. Yang Mingcong-you have been amazing feeding me all the time, and we will now lose some weight as promised. Special thanks.

My close friends who are near, soon-to-be Dr. Wu Tong, Dr. Ananya Roy, Dr. Soo Peng, and Dr. Cao Yong, and who are not near, Dr. Qin Lang and Dr. Zeng Qilin, Ms. Cai Xintian, and Ms. Li Jia-thank you for all the unconditional support and sorry for being less caring about you when I wrote this dissertation.